CONTACT DYNAMICS AND FORCE CONTROL OF FLEXIBLE MULTI-BODY SYSTEMS

Sun-Wook Kim

B.Eng (McGill University) 1992
M.Eng (McGill University) 1994

Department of Mechanical Engineering
McGill University
Montreal, Quebec, Canada

A thesis submitted to the Faculty of Graduate Studies and Research
in partial fulfilment of the requirements for the degree of
Doctor of Philosophy

August 1999

National Library of Canada
Acquisitions and Bibliographic Services
395 Wellington Street
Ottawa ON K1A 0N4
Canada

Bibliothèque nationale du Canada
Acquisitions et services bibliographiques
395, rue Wellington
Ottawa ON K1A 0N4
Canada

Your file Votre référence

Our file Notre référence

0-612-64588-6

Abstract

A detailed modelling of contact dynamics involving general flexible multi-body systems of arbitrary kinematic architecture is considered. The components undergoing direct contact (e.g., the end-effector of a manipulator and a satellite) are modelled using the finite element method and the Lagrange multiplier technique. Special attention is paid to dynamic fidelity of contact dynamics. Contact geometric constraints and corresponding contact forces are analysed and incorporated into the dynamical equations. This model takes into account structural deformations and oscillations, friction, time-varying contact area, and repeated contact/impact. Multi-body systems, on the other hand, are handled by a modified Euler-Lagrange method based on the Natural Orthogonal Complement (NOC). Thus, the system dynamics is composed of a set of differential equations (either multi-body formulations or finite element nodal displacement formulations) subjected to sets of algebraic equations expressing kinematic or contact constraints. A systematic procedure for solving this system of equations is formulated with special emphasis on computational efficiency.

This dynamic model is then used to design a *composite* controller which must simultaneously achieve three goals: (1) trajectory tracking, (2) force control, and (3) stabilization of the flexible degrees of freedom of the multibody system. The *singular perturbation method* is used to obtain two reduced order models. Subsequently, the slow subsystem is used to design a simultaneous position/force controller based on impedance control, where an optimization method is incorporated to accommodate manipulator redundancy. The fast subsystem is used to design a Linear Quadratic

Regulator (LQR) to suppress structural vibrations.

A simulation environment is developed based on the above procedures and formulations for the planar case. It is used to perform dynamic and control simulations of a variety of contact scenarios involving multi-body systems. A comparative study of the results indicates that a detailed contact dynamics model may be essential for a realistic simulation of contact/impact, capture, and force control operations.

Résumé

Une modélisation détaillée de la dynamique de contact est considérée pour des systèmes de corps multiples généralement flexibles et d'architecture cinématique donnée. Les composants soumis à des contacts directs (par exemple entre l'organe terminal d'un robot manipulateur et un satellite) sont modélisés en utilisant la méthode des éléments finis et la technique du multiplicateur de Lagrange. Une attention particulière est portée à l'exactitude de la dynamique de contact. Les contraintes géométriques de contact et les forces de contact associées sont analysées et intégrées dans les équations de la dynamique. Ce modèle prend en compte des déformations et oscillations de la structure, la friction, la zone de contact variant avec le temps, les impacts et contacts répétés. D'autre part, les systèmes de corps multiples sont analysés avec la méthode modifiée d'Euler-Lagrange basée sur le Complément Naturel Orthogonal (CNO). Ainsi, la dynamique du système est composée d'un ensemble d'équations différentielles (régissant la dynamique des corps multiples ou les déplacements des nœuds des éléments finis) sujettes à des ensembles d'équations algébriques représentant les contraintes de cinématique ou de contact. Une procédure systématique pour résoudre ce système d'équations est détaillée en mettant l'accent sur son efficacité numérique.

Ce modèle dynamique est alors utilisé pour concevoir un contrôleur hybride qui doit atteindre trois objectifs en même temps: (1) suivre une trajectoire, (2) contrôler la force, et (3) stabiliser les degrés de liberté flexibles du système de corps multiples. La méthode des perturbations singulières est utilisée pour obtenir deux modèles d'ordre réduit. Par conséquent, le sous-système lent est utilisé pour contrôler simultanément la position et la force en fonction du contrôle d'impédance, où une méthode d'optimisation est incorporée pour prendre en compte la redondance du robot manipulateur. Le sous-système rapide est utilisé pour créer une Commande Linéaire Quadratique (CLQ) pour supprimer les vibrations de la structure.

Un environnement de simulation est développé en fonction des procédures précédentes et des formulations pour le cas plan. Il est utilisé pour obtenir des simulations de dynamique et de contrôle à travers différents scénarios de contact impliquant des systèmes de corps multiples. Une étude comparative des résultats montre qu'un modèle détaillé de la dynamique de contact peut être primordial pour une simulation réaliste des opérations de contact et d'impact, de capture et de contrôle de force.

Claim of Originality

The major contribution of this thesis is the development of a general formulation for a detailed and efficient model of contact dynamics involving flexible multi-body systems. Specific contributions of this work are:

- Development of an efficient methodology for the formulation of a finite element model of contacting bodies undergoing large displacements, with the use of the symbolic software MAPLE V.
- Development of a systematic procedure for solving the equations of motion of flexible multi-body systems of arbitrary kinematic architecture subjected to sets of kinematic or contact constraints, with special emphasis on computational efficiency.
- Design of a *composite* controller for trajectory tracking, force and vibration control of a spacecraft-mounted manipulator operating on a free-floating system.
- Development of a computer code for the simulation of contact dynamics and force control of multi-body systems.

These contributions have been partly reported in preliminary form in Kim & Misra (1997), Kim et al. (1997), Kim et al. (1998a), and Kim et al. (1998b).

Acknowledgements

I would like to express my sincere gratitude to my supervisor, Professor A. K. Misra, for his excellent guidance, support and encouragement throughout the course of this work. I am also deeply grateful to Professor V. J. Modi of the University of British Columbia (UBC) for inviting me to spend six memorable months at his facility and giving me the opportunity to share in his work.

I would like to express my appreciation to my colleagues and friends at the Department of Mechanical Engineering and the Centre for Intelligent Machines (CIM). I am truly thankful to Byung No Min for many years of generous advice, help and discussions concerning this research work. I am grateful to Professor Modi's students at UBC, especially Mathieu Caron for his patience in helping me clarify many questions regarding his work. Special thanks to Bertrand Petermann for translating my abstract into French.

Last, but not least, I would like to thank my parents for their great patience, support and encouragement. This work would indeed not have been possible without them.

Contents

List of Figures

List of Tables

Nomenclature

In this thesis, bold-face, lower-case, Latin and Greek letters denote vectors: bold-face, upper-case, Latin and Greek letters denote matrices; and calligraphic and italic letters generally represent scalar quantities such as material or geometric properties, points, or indices. The term *element* refers to a finite element of a contacting body (addressed in Chapter 2), *link* refers to a body in a multi-body system (addressed in Chapter 3), and *subsystem* refers to either a contacting body or a multi-body system (addressed in Chapter 4).

Latin Symbols

$a_0, \cdots, a_7$: Newmark integration parameters.

$\mathbf{A}$: in Chapter 3, kinematic velocity constraint matrix; in Chapter 5, desired apparent mass matrix in impedance control.

$\mathbf{b}_i$: generalized coordinates associated with the bending of link i.

$\mathbf{B}$: in Chapter 2, strain-displacement transformation matrix; in Chapter 3, matrix of shape functions.

$\mathbf{c}_i$: generalized nonlinear force vector of element, link, or subsystem i containing the Coriolis and centrifugal forces.

$\mathbf{C}_i$: damping matrix of element, link, or subsystem i.

C_s : spacecraft's centre of mass.

$\mathbf{C}_s$: linear interpolation matrix of segment s.

$\mathbf{e}$: tracking error vector in impedance control.

E : modulus of elasticity.

$\mathbf{E}_i$: stress-strain constitutive matrix of element i.

$\mathbf{f}_i$: generalized external force vector of element, link, or subsystem i.

$\mathbf{f}_{c_i}$: constraint force vector of element i.

$\mathbf{F}$: vibration control state feedback gain matrix of reduced-order model.

$\mathbf{g}_j$: j-th constraint vector.

$\mathbf{G}$: Guyan reduction matrix.

I : area moment of inertia.

$\mathbf{I}_{nn}$: $n \times n$ identity matrix.

$\mathbf{I}_{h_i}$: inertia matrix of the hub of link i.

$\mathbf{J}_i$: in Chapter 2, Jacobian of element i relating the natural coordinate derivatives to the local coordinate derivatives; in Chapter 5, Jacobian of the manipulator system.

$\mathbf{K}_i$: stiffness matrix of element, link, or subsystem i.

$\mathbf{K}_d$: desired apparent damping matrix in impedance control.

$\mathbf{K}_p$: desired apparent stiffness matrix in impedance control.

$\mathbf{L}$: transformation matrix from $\dot{\mathbf{q}}$ to $\boldsymbol{\omega}$.

M_i : concentrated mass at the tip of link i.

$\mathbf{M}_i$: generalized mass matrix of element, link, or subsystem i.

$\mathbf{M}$: generalized mass matrix of a contacting body.

$\bar{\mathbf{M}}$: generalized mass matrix of a multi-body system.

$\mathbf{n}_k$: unit normal to the *target* surface for *contactor* node k.

$\mathbf{N}$: Natural Orthogonal Complement of the velocity constraint matrix of a multi-body system.

$\mathbf{N}_i$: matrix of interpolating functions of element i.

$\mathbf{p}$: inertial position vector of the origin of the local frame xyz of a contacting body.

$\tilde{\mathbf{p}}_i$: position vector of the origin of (X_i, Y_i, Z_i) with respect to (X_o, Y_o, Z_o).

$\mathbf{p}_h$: position vector of the tip of a multi-body/manipulator system with respect to its base.

$\mathbf{P}_{ji}$: constraint matrix resulting from the relationship between constraint j and subsystem i.

$\mathbf{q}_i$: generalized coordinates of element, link, or subsystem i.

$\hat{\mathbf{q}}$: quaternion formed by either the Euler parameters or the linear invariants describing the orientation of a contacting body with respect to an inertial frame.

$\hat{\mathbf{q}}_i$: quaternion describing the orientation of (X_i, Y_i, Z_i) with respect to (X_o, Y_o, Z_o).

$\mathbf{r}_i$: in Chapter2, inertial position vector of a point on element i; in Chapter 3, position vector of a point on link i measured with respect to the (X_i, Y_i, Z_i) frame.

$\mathbf{R}_i$: rotation matrix describing the orientation of frame (X_i, Y_i, Z_i) with respect to $(X_{i-1}, Y_{i-1}, Z_{i-1})$.

$\mathbf{R}$: rotation matrix describing the orientation of the local frame xyz of a contacting body with respect to XYZ.

t : time variable.

$\mathbf{t}_k$: unit tangential to the *target* surface for *contactor* node k.

T_i : kinetic energy of element or link i.

$\mathbf{T}$: *connectivity* matrix.

U_i : potential energy of element or link i.

$\mathbf{u}_i$: elastic displacement with respect to the undeformed position of a point in element i measured in the local frame xyz.

$\hat{\mathbf{u}}_i^j$: elastic displacement of node j in element i measured in the local frame xyz.

$\mathbf{v}_i$: *extended* velocity vector of link i.

$\tilde{\mathbf{v}}_i$: velocity vector of the origin of (X_i, Y_i, Z_i) with respect to (X_o, Y_o, Z_o).

W_j, W_k, W_l : weighting factors in Gaussian Quadrature.

$\mathbf{x}_i$: undeformed position vector of a point in element i with respect to the local frame xyz.

$\hat{\mathbf{x}}_i^j$: position vector of node j in element i with respect to the local frame xyz.

$\mathbf{x}_{ref}$: reference or nominal trajectory of the end-effector.

xyz : local frame of a contacting body.

XYZ : inertial frame of a contacting body.

(X_i, Y_i, Z_i) : local frame of link i.

(X_I, Y_I, Z_I) : inertial frame at the center of Earth.

(X_o, Y_o, Z_o) : orbital frame at the spacecraft's center of mass.

Greek Symbols

α, β, γ : Euler angles.

$\boldsymbol{\gamma}_i$: i-th contact force vector.

$\boldsymbol{\delta}_i$: angular rotation vector of the tip of link i about the (X_i, Y_i, Z_i) axes due to bending.

ϵ : perturbation parameter in singular perturbation control.

$\boldsymbol{\epsilon}_i$: vector comprising the components of the strain tensor of element i.

$\boldsymbol{\eta}$: fast state variables in singular perturbation control.

θ_i : joint rotation of link i measured along the positive direction of the Z_i axis.

$\boldsymbol{\lambda}_j$: Lagrange multipliers corresponding to the j-th constraint.

$\boldsymbol{\Lambda}$: transformation matrix from $\boldsymbol{\omega}$ to $\dot{\mathbf{q}}$.

$\boldsymbol{\mu}_i$: deflection of link i due to bending.

ξ, η, ζ : natural coordinates of an element.

ρ_i : in Chapter 2, mass per unit volume of element i; in Chapter 3, mass per unit length of link i.

$\boldsymbol{\sigma}_i$: vector comprising the components of the stress tensor of element i.

$\boldsymbol{\tau}$: control torque vector.

ϕ_{ij} : shape function of link i corresponding to the j-th mode of the flexibility model.

$\boldsymbol{\phi}_i^C$: generalized extended constraint forces of link i.

$\boldsymbol{\phi}_i^E$: generalized extended external forces of link i.

$\boldsymbol{\phi}_i^S$: generalized extended system forces of link i.

$\boldsymbol{\chi}_i$: non-conservative generalized forces of element or link i.

$\boldsymbol{\psi}_i$: independent generalized coordinates of link i.

$\boldsymbol{\psi}$: independent generalized coordinates of a multi-body system.

$\boldsymbol{\omega}$: angular velocity of a contacting body measured in the xyz frame.

$\boldsymbol{\omega}_i$: angular velocity of (X_i, Y_i, Z_i) with respect to (X_o, Y_o, Z_o).

$\boldsymbol{\omega}_h$: angular velocity vector of the tip of a multi-body/manipulator system with respect to its base.

Ω : orbital rate.

Chapter 1

Introduction

1.1 Background and Motivation

Contact dynamics is becoming an important issue in space operations. Berthing or docking of two spacecraft systems will become routine operations in the near future; the Shuttle will dock with the Space Station during the latter's construction and operation, and malfunctioning satellites will be serviced by the Shuttle or other free flyers. These operations are likely to involve a velocity differential between the two contacting bodies, which can result in dynamic disturbances. It is important to assess the effect of these disturbances to determine whether they endanger structural safety and attitude stability of the space systems. After the initial impact. sustained contact is desired in most operations. In this case, the control system must have the capability to damp out the vibrations generated during impact, apply a desired amount of force and prevent damage of parts due to overload.

Space robots are expected to play an increasingly significant role in these contact operations. A major motivation behind this is to minimize the need for astronaut Extra Vehicular Activity (EVA), which would greatly reduce mission costs and hazards to the astronauts involved. The Canadian Shuttle Remote Manipula-

Figure 1.1: Shuttle-mounted CANADARM preparing to capture a payload

tor System (SRMS, also known as CANADARM (Figure 1.1*)) represents state of the art technology in the field of space-based, flexible manipulators. It has been operational on board the Shuttle since 1981, and has been used for such activities as payload berthing, deployment, and positioning, docking of the Shuttle with the space station Mir, and such unexpected tasks as breaking of ice around a vent nozzle (Nguyen et al. 1991). The Mobile Servicing System (MSS) (Figure 1.2†), which is the Canadian contribution to the International Space Station (ISS), includes a large, 7 degree-of-freedom self-relocatable manipulator arm called the Space Station Remote Manipulator System (SSRMS), and a smaller, dual-arm robot attached to the tip of the SSRMS known as the Special Purpose Dextrous Manipulator (SPDM). The SSRMS is designed to perform the gross motions such as capture, manipulation and berthing operations, while the SPDM satisfies those operations requiring dextrous

---

[*] Figure downloaded from http://www.spar.ca/space/images/

[†] Figure downloaded from http://spaceflight.nasa.gov/medialibrary/

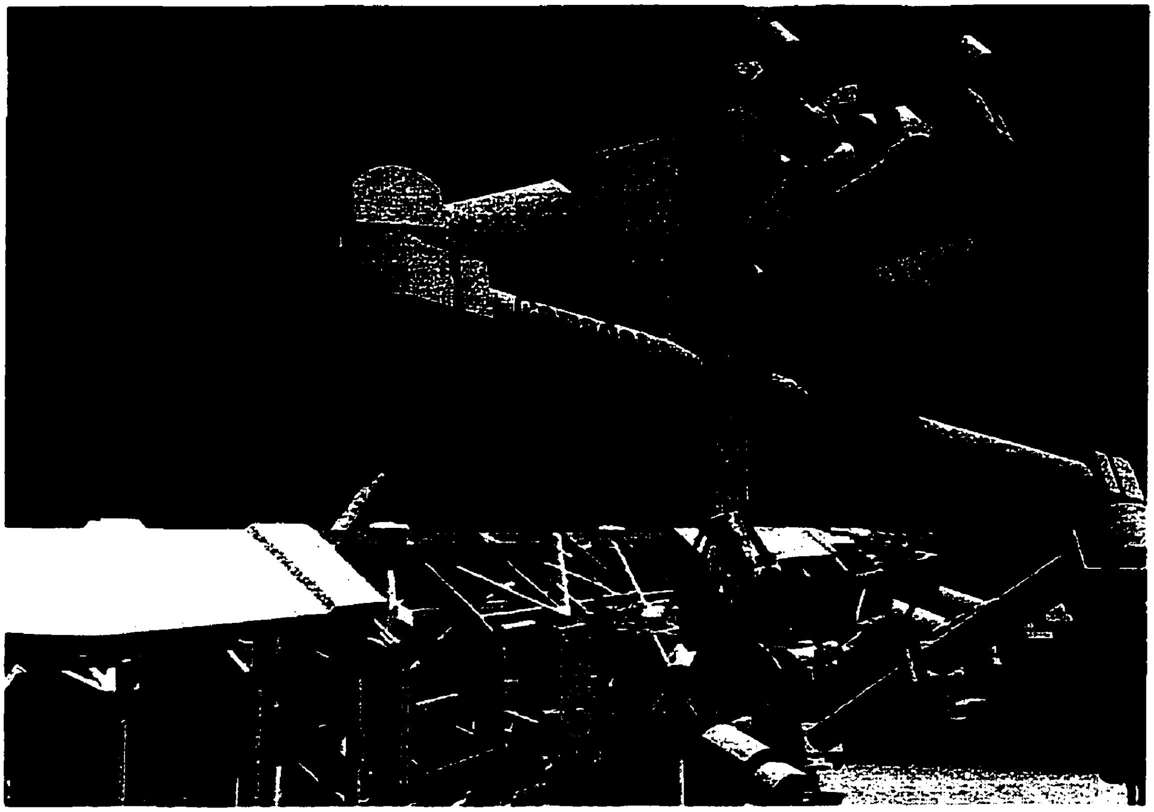

Figure 1.2: The Mobile Servicing System (MSS)

capabilities. The MSS is expected to play a major role in the assembly and external maintenance of the Space Station. Some of its functions are: (*i*) removal of Space Station elements and equipment from the shuttle cargo bay, (*ii*) Space Station external maintenance including changeout of Orbit Replaceable Units (ORU), actuation of mechanisms, mating/demating utilities, (*iii*) transportation on the Space Station of payloads such as Space Station elements, attached payloads and ORU's, (*iv*) deployment and retrieval of free flyers by capturing and maneuvering to appropriate sites on the Space Station or deploying from the Station, and (*v*) EVA support including transporting or positioning of EVA crew (Stieber et al. 1998).

Most of these operations inevitably involve contact or constrained motions. But contact maneuvers are generally recognized to be difficult operations for robotic manipulators (Ma & Carr 1998). The contact dynamics behaviour is coupled with the entire manipulator and base dynamics, as well as the control system dynamics. Furthermore, space manipulators have some unique characteristics such as joint flexibility, link flexibility, large size, absence of a fixed base, and the microgravity environment of space. The CANADARM, for example, was designed to manipulate payload masses of up to 30,000 kg in space, but is unable to lift its own weight on Earth. These features make it difficult to conduct experiments with space manipulators in an Earth laboratory environment, and simplified ground-based tests may not be representative of the actual system in the space environment. Therefore, computer simulation analyses become all the more essential to perform such tasks as engineering design, feasibility, along with operations analysis and training.

During contact operations involving the CANADARM, which is the only operational space manipulator available today, all contact activities are performed very slowly, without any sensing capability to inform the operator of the magnitude of the forces that the arm exerts on its surroundings. A force feedback control can therefore be a welcome addition to the existing CANADARM or the new SSRMS control architecture to improve their performance for the current operational activities, as well as to meet emerging requirements for Space Station operations. Most simulation efforts on force control, however, have relied on quite simple contact models for verification of the control schemes. As with most contact activities in space, an accurate contact model can add to a more reliable and sophisticated validation tool for candidate force control algorithms.

The contact dynamical model used for analysis and simulation must then have sufficiently high dynamic fidelity to represent the reality. With the steady increase of computer power over the years (according to Moore's law, it doubles every 18 months), it is possible to use increasingly accurate and sophisticated models. However, computational efficiency is still important since some simulations will include hardware-in-the-loop or human-in-the-loop components, which will require the capability for real-time simulation. In accordance with these considerations, the main interest of this thesis lies in developing a dynamic formulation capable of simulating the detailed contact dynamics involving multi-body systems and control systems.

But at the same time, special attention will be paid to computational efficiency so as to explore the possibility of real-time implementation.

1.2 Contact Dynamics

Most methods of contact modelling that have appeared in the literature can be classified into two main categories: impulse-momentum based methods and contact force based methods. The impulse-momentum based methods assume that impact occurs *instantaneously* and separate the dynamic analysis of the system into two intervals: before and after impact. Given the state of the system just before impact, principles of energy and momentum are used to obtain rebound states at the end of impact. Contact force based methods, on the other hand, analyse the contact geometric constraints and corresponding contact forces, and incorporate them into the dynamical equations.

Among impulse-momentum approaches, the problem of a robotic manipulator impacting the environment has been studied by several researchers. Zheng & Hemami (1985) analyzed the dynamics of a robot colliding with the environment; a mathematical model was derived to establish a relationship between the abrupt velocity changes and the impulsive forces. Wang & Mason (1987) modelled the impact dynamics with friction in the planar case using a graphical method. Yoshida et al. (1992) used the extended generalized inertia tensor (Ex-GIT) and the virtual mass concept to formulate the impact dynamics of a system of free-floating links. All these works were restricted to rigid multi-body systems. Kim (1994) extended the work to flexible multi-body systems. Impact was modelled from fully elastic to fully plastic by introducing two parameters characterizing the impact: the energy loss parameter and the friction parameter. Due to the complexity of actual physical processes of impact, some general simplifying assumptions were made in all the above works in order to render the problem amenable to mathematical treatment. Some of these assumptions are: (1) impact duration is instantaneous; (2) generalized coordinates remain unchanged during impact; (3) impact occurs at a point rather than a time-varying area. Another major weakness of the impulse-momentum approach is that it is not directly applicable to problems of sustained contact and friction between the contacting bodies.

The contact-force based methods, on the other hand, do not make the assumption of instantaneous impact duration and can naturally handle problems of sustained contact and friction. This method can again be subdivided into three types: the spring-dashpot approach, the classical Hertz contact theory approach, and the finite element approach. The spring-dashpot approach, also referred to as the Kelvin-Voigt model, is the simplest one, where the contact interface is modelled by a parallel and (usually) linear spring-dashpot element. Because of its simplicity, this model has been the preferred choice in most works on force control of manipulator systems (section 1.5).

The Hertz contact theory describes a relationship between the normal contact force and the local contact deformation by means of material stiffness properties of the contacting bodies and local contact surface geometry (Johnson 1985). Using this simple relationship, the contact problem of complex multi-body systems undergoing complicated contact tasks can be analysed with minimal computational cost (Ma 1995, Vallejo et al. 1992). This theory assumes that local contact deformations can be described in a quasi-static manner and neglects the effects of elastic structural oscillations. However, in all contact operations, initial impact is almost unavoidable, where elastic waves are excited that interact with structural deformations as well as local contact deformations. As time progresses, geometric and material dispersion of waves occurs, diminishing initial peak response. This early time response is important for prediction of the dynamics of impacting structures. Some researchers have attempted to add certain features absent in the original Hertz model. The lack of an energy dissipation function, for example, was accounted for by Lankarani & Nikravesh (1990) by including a hysteresis damping function.

Among finite element approaches, several formulation methodologies have been advanced in the literature for solving contact problems. One approach is based on the use of special *gap* or *interface* elements intervening between the surfaces of the bodies in contact (Cook 1981). This approach is straightforward but in cases where the contacting bodies are of complex or irregular shape or undergo large displacements, it is inadequate and hence its use is restricted to simple geometries (Tissakht 1995). More general approaches for solving contact problems in finite element analyses are those based on the variational formulations. These approaches can generally be classified into two types (Cook 1981, Bathe 1982): (*i*) the Lagrange multiplier methods, and (*ii*) the penalty method. Some variations or combinations of these two approaches have also appeared in the literature, such as the augmented Lagrangian method (Simo & Laursen 1992) and the mixed method (Shyu et al. 1989).

In the Lagrange multiplier method (Bathe & Chaudhary 1985, Chaudhary & Bathe 1986, Hughes et al. 1976), the contact constraints are satisfied *exactly* by introducing into the equations of motion a set of Lagrange multipliers representing contact forces. Both the generalized coordinates and Lagrange multipliers are treated as unknown variables, and therefore, the size of the resulting system of equations increases due to the additional variables, i.e., the Lagrange multipliers.

The penalty method easily eliminates this drawback by assuming that the contact pressure is equal to the amount of material penetration times a certain penalty parameter (Oden & Kikuchi 1982, de la Fuente & Felippa 1991). However, the contact constraints are satisfied *exactly only* in the limit of infinite penalty values, while it is well-known that penalty methods suffer from ill-conditioning that worsens as penalty values are increased. Other weaknesses of the penalty method are: (1) the solution strongly depends on the particular choice of the penalty parameter, and (2) it violates the principle of conservation of energy of the systems in contact because some of the energy is stored in the 'penalty spring'.

All the above-mentioned studies dealt with two *single-body* systems. Some researchers extended the finite element formulation of contact problems to general multi-body systems (Wu & Haug 1990, Wasfy 1995). However, due to the complexity and computational cost involved in a full finite element contact model, some simplifying assumptions and procedures were used. Wu & Haug (1990) used a substructure technique to analyse *frictionless* contact-impact of flexible multi-body systems. In this approach, components that may come into contact are divided into substructures, on each of which deformation modes are defined to account for elastic deformations and vibrations. A constraint addition-deletion technique based on Lagrange multipliers is used to account for contact and separation between a pair of contact nodes. However, the contact nodes are predetermined, and thus large displacements and sliding while in contact are not allowed. Wasfy (1995) presented a finite element based technique for modeling contact-impact of flexible manipulators with a fixed rigid surface. The conservation of energy and momentum, or Newton's collision rule and conservation of momentum, are used as velocity constraints on individual mass-lumped nodes in contact with the rigid surface to obtain the post-impact velocities of the nodes.

In this thesis, the Lagrange multiplier technique based on the finite element method was chosen to model contact dynamics of contacting bodies. This method represents, to the author's knowledge, the most detailed formulation of contact dynamics, capable of modeling such phenomena as structural deformations, friction, time-varying contact area, repeated contact/impact, and others, without making doubtful assumptions about the nature of the physical contact mechanics. Its main disadvantage compared with the penalty methods, namely increase in the number of equations to be solved, is a minor inconvenience since at most, only 3 equations (3D sticking case) are added for each node in contact.

Note that only the contacting bodies will be modelled using the above-mentioned approach. These bodies may well be connected to other bodies, as is the case of the end-effector (a contacting body) with the rest of the manipulator (a multi-body system). The dynamical formulation of multi-body systems are discussed in the following section.

1.3 Dynamics of Multi-Body Systems

Methods of formulation and simulation of the dynamics of multi-body systems are extensive. A detailed literature review, however, is beyond the scope of this thesis. Only those works directly relevant to this thesis are described here.

The Newton-Euler method lends itself to very efficient recursive computations for solving dynamics problems of serial, rigid-link multi-body systems. However, this method is not convenient for application to systems containing kinematic loops or flexible links. On the other hand, the Euler-Lagrange method is conceptually much simpler, with the added advantage of not requiring the calculation of the constraint forces. However, this method requires the evaluation of derivatives of energy terms which are very lengthy for multibody systems.

Some energy based methods, however, are capable of circumventing these difficulties. In Kane's method (Kane & Levinson 1983), the constraint forces are eliminated from the equations of motion with the introduction of *partial velocities* and *partial angular velocities*. Similarly, in the method of Natural Orthogonal Complement (NOC) (Angeles & Lee 1988, Cyril 1988, Cyril et al. 1991), the Lagrange equations are derived for each individual component and then assembled to obtain the equations of motion of the whole system. This approach, however, introduces the non-working constraint forces which are eliminated later by using the Natural Orthogonal Complement (NOC) of the kinematic velocity constraint matrix. This method has the simplicity of the Newton-Euler formulations which permit the analysis of one body at a time, while it avoids the disadvantages of the usual Lagrange formulations, namely evaluation of derivatives of lengthy energy terms. Various types of flexible systems have been analysed using this method: serial-type multibody systems (Cyril et al. 1989), manipulators with kinematic loops (Fattah 1995, Cho 1995), and articulating truss structures (Boutin 1995).

Other energy methods attempt to develop $O(N)$ algorithms, where N is the number of bodies comprising the system. In other words, in an $O(N)$ algorithm, the number of arithmetic operations increases linearly with the number of bodies. Most formulations are of $O(N^3)$ because the computation of the inverse of the global mass matrix requires $O(N^3)$ arithmetic operations. Pradhan et al. (1997) developed an $O(N)$ algorithm where the kinetic and potential energy are derived for each individual body using a decoupled set of coordinates and then assembled to form the kinetic and potential energy of the *whole* system. Next, a coordinate transformation is made where the new set of coupled coordinates facilitates the expression of physical constraints between adjacent bodies. A unique feature of this transformation process is that the new mass matrix can be factorized in terms of block diagonal matrices such that its inversion is an $O(N)$ process. One disadvantage of this method, however, is that constraint forces are not eliminated but are treated as variables; therefore, the number of equations increases with the number of constraint equations. This method was applied to planar dynamics of flexible manipulators with N slewing deployable links (Caron et al. 1998) and the dynamics of N-body tethered systems (Kalantzis et al. 1998).

In this thesis, the modified Euler-Lagrange method based on NOC was chosen to model multi-body systems. This method is conceptually simple, systematic, computationally efficient, and combines the advantages of the Newton-Euler and Euler-Lagrange methods. Further incentive for this choice was provided by the availability of FLEXLINK (Cyril et al. 1989), an in-house general-purpose software package for the dynamic simulation of serial-link flexible manipulators.

1.4 Integration of Contact Dynamics with Multi-body System Dynamics

In this thesis, the main objective is a detailed modelling of contact dynamics involving general multi-body systems of arbitrary kinematic architecture. It is thus necessary to bring together two fields of work: contact dynamics and multi-body system dynamics.

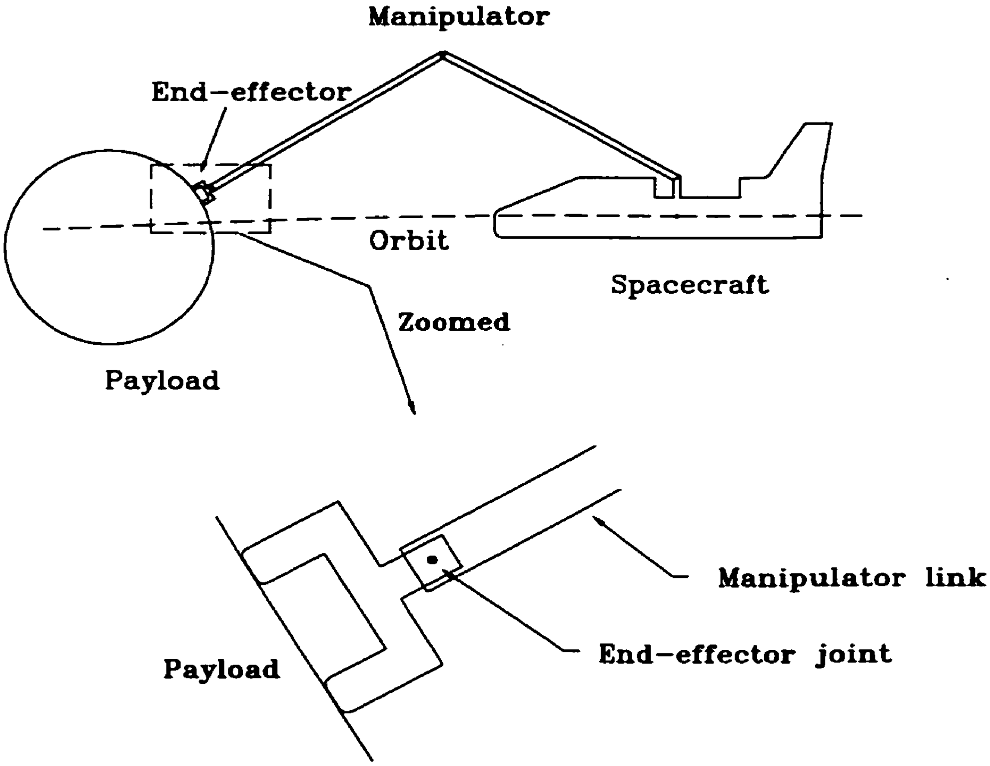

Figure 1.3: Schematic diagram of a typical system under study

The bodies which undergo direct contact (such as the end-effector and payload) are modelled using the finite element method (FEM) since contact effects such as local contact deformations and friction occur near the area of contact, while the rest of the multi-body systems are modelled using a flexible multi-body formulation based on the method of Natural Orthogonal Complement (NOC) (Cyril et al. 1991). The resulting equations of motion are then integrated by taking into account the kinematic constraints at mechanical joints and contact surfaces. A schematic diagram of a typical system under study is shown in Figure 1.3: a manipulator mounted on a spacecraft is capturing a satellite (payload). In this case, the end-effector and satellite (contacting bodies) are modelled using FEM while the rest of the system is modelled using a multi-body formulation.

These systems of equations are usually *stiff* (in the numerical analysis sense) and nonlinear, and the number of finite element equations that describe the deformations of the contacting bodies is large. In fact, the enormous computational cost involved in simulating the dynamics of a full finite element contact model is the major reason for resorting to less computationally demanding and simplified methods reviewed in Section 1.2. Therefore, one of the major objectives of this thesis is to explore and develop computationally efficient methods and procedures without sacrificing modelling accuracy.

For large systems of equations, several *reduction methods* are available in the literature (for a comprehensive survey, see Noor (1994)). The response of the system, which is originally described in terms of a large number of generalized coordinates, $\mathbf{q}_n$, is approximated by a combination of preselected global approximation vectors. The problem is then reformulated in terms of a few discrete variables $\boldsymbol{\psi}_r$ given by

$$\mathbf{q}_n = \boldsymbol{\Gamma}_{n \times r} \boldsymbol{\psi}_r \tag{1.1}$$

where $\boldsymbol{\Gamma}$ is an $n \times r$ transformation matrix. The crux of reduction methods is the proper selection of global approximation methods. An ideal set of global approximation vectors was defined by Noor & Peters (1980) as one which maximizes the quality of the results and minimizes the total effort in obtaining them. This criteria depends on the particular application, as well as on the system response characteristics being approximated. Two commonly used reduction methods are modal truncation and Guyan reduction. In modal truncation, the approximation matrix is made up of columns of eigenvectors which, based on certain criteria, provide the most significant contributions to the system dynamics. Usually, the higher the eigenfrequency, the less is its contribution to the overall dynamics. Therefore, it is common practice to discard the higher frequency eigenvectors and retain the lower ones (e.g. Ma et al. (1997), Boutin (1995)). In Guyan reduction (Cook 1981, Guyan 1965), also known as the *mass condensation* method, the degrees of freedom are subdivided into two types – *slaves* and *masters* where the slaves are dependent on the masters and thus disappear from the final reduced set of equations. Several general methods for choosing slaves and masters are available in the literature (Cook 1981, Noor 1994), but this criteria is ultimately problem dependent.

The equations of motion of dynamical systems are usually second-order nonlinear differential equations which require taking the inverse of a time-varying, configuration-dependent mass matrix in some manner. In this thesis, there is particular interest in inverting the mass matrix of a single contacting body but whose order is large because of the large number of nodal degrees of freedom involved. Several methods have been proposed to compute the inverse of the mass matrix ranging from taking an algebraic inverse, to using traditional numerical inverse methods such as Cholesky Decomposition (CD)(Bathe 1982). The algebraic inverse is only feasible for relatively small systems, even with powerful symbolic manipulation programs such as Mathematica, Maple, or AUTOLEV. Taking a numerical inverse at each integration step is the most generally applicable method, but even CD requires $O(N^3)$ arithmetic operations to invert a symmetric and positive definite $N \times N$ mass matrix. In the field of multibody dynamics, some novel techniques of formulating the dynamics have been developed with the express purpose of finding a more efficient way of taking care of this operation. In the $O(N)$ algorithms discussed in Section 1.3 (Pradhan et al. 1997, Caron et al. 1998, Kalantzis et al. 1998), the mass matrix of each body is inverted separately such that the overall effort of inverting the global mass matrix is $O(N)$. Junkins & Schaub (1997) presented a technique for deriving the equations of motion which yields a dynamical system with an identity mass matrix by introducing a quasivelocity vector. The problem of inverting a complicated mass matrix is thus replaced by the problem of solving the corresponding eigenfactor differential equations.

The above-mentioned methods and other procedures are investigated in this thesis to reduce the overall computational cost involved in the solution.

1.5 Trajectory, Force, and Vibration Control

The problem of force control of robotic manipulators has been widely studied by many researchers (Raibert & Craig 1981, Craig 1986, Matsuno & Yamamoto 1994, Hogan 1987, Lasky & Hsia 1991, Seraji & Colbaugh 1993, Nguyen et al. 1991, Khatib

1987). Among the various force control schemes, the hybrid position/force control and impedance control are the two unified (position and force) control algorithms. The hybrid position/force scheme attempts to directly control the end-effector's position and applied force. At a typical contact point, the contact direction and end-effector motion direction are approximately orthogonal to each other. Therefore, along the motion direction, a pure position control is activated, and along the contact direction, a pure force control is applied. The scheme is implemented by individually designing a position and a force control law for each degree of freedom of the task space and then integrating the overall control law through the use of so-called selection matrices, which basically represent switches that set the mode of control to be used for each degree of freedom. One of the disadvantages of the hybrid position/control is that it requires specific knowledge of the motion and force directions of the task space.

Impedance control easily eliminates this problem; while most control schemes are based on directly controlling position or force, impedance control assumes that the control should be designed, not to control motion or force alone, but rather to modulate and regulate the interaction between force and motion; in other words, to regulate the mechanical impedance of the manipulator. This controller is Cartesian task-space based (or operational space as in Khatib (1987)), which eliminates the task of solving the inverse kinematics problem. It also uses a *nonlinear dynamic decoupling approach*, equivalent to joint-space based *computed torque control* or *feedback linearization technique*, which fully exploits the knowledge of the dynamic model, so that linear and decoupled control structures can be obtained. Impedance control works well where the characteristics of the environment are exactly known; in the presence of parameter uncertainties, force-tracking becomes poor and additional schemes must be incorporated into the control scheme to rectify this problem. Lasky & Hsia (1991) proposed a double-loop controller where a conventional impedance controller is implemented in the inner loop and a simple force-feedback controller in the outer loop. Seraji & Colbaugh (1993) presented adaptive strategies to estimate the environmental parameters and adjust *online* the required reference trajectory.

The main concern in all these works, however, was on terrestrial rigid manipulators. A major problem with controlling flexible manipulators is that in many cases the flexible degrees of freedom become unstable and the control maneuver fails. Thus, for a fully flexible manipulator system, the controller must not only track a certain desired trajectory and apply a desired amount of force but must also stabilize the vibrations which are naturally excited, damping them out as fast as possible during its path. However, these multiple objectives cannot be met with the use of conventional rigid-manipulator controllers since there are not as many control inputs as output variables.

Attempts to control a flexible multi-link manipulator using rigid manipulator control by simply ignoring the flexible effects are unsatisfactory when link deflections are substantial. They either result in gross inaccuracies in the positioning of the end-effector, or instability due to elastic effects. Bayo (1988) presented a feedforward approach where an inverse dynamics problem is solved to calculate the joint torques which would produce zero tip deflection of the manipulator links. Some researchers (Baruh & Tadikonda 1989, Jaar et al. 1995, Caron et al. 1998) used the feedback linearization technique or the computed torque method to control multi-link robotic systems where the flexible dynamics were treated as 'disturbances' but were not explicitly controlled. However, these schemes may fail for fast joint manoeuvres, as the flexible dynamic 'disturbances' become large and unstable. Carusone & D'Eleuterio (1993) employed gain scheduling of a series of steady-state optimal regulators based on linearized dynamical equations about stationary configurations along the desired manipulator trajectory. Others proposed the use of smart structures such as piezo-ceramic actuators capable of applying transverse forces to the links, to damp out the undesirable vibrations of the flexible links (Modi et al. 1993, Kalaycioglu et al. 1997). However, this scheme necessitates the use of additional (piezo-ceramic) actuators besides the conventional joint controllers.

One scheme that has been used to circumvent the difficulty of achieving stabilization of the elastic effects using only conventional joint control is the *singular per-*

turbation method (for a detailed theoretical presentation, see Kokotovic (1984)). The technique exploits the property that elastic vibration frequencies are usually greater than the frequency content of the rigid body motion trajectory. Hence, highly coupled differential equations of motion can be rearranged into two reduced-order systems, consisting of a "slow" (rigid) subsystem and a "fast" (flexible) subsystem, for which the latter possesses a much faster time scale. The control scheme for each subsystem may then be addressed separately, to establish a *composite control* design. The attractive feature of this strategy is that the control system can be designed separately using well-established control schemes suitable for each subsystem. For the slow subsystem, any of the conventional control techniques used for rigid manipulators can be applied, such as the computed torque or impedance control. The fast subsystem turns out to be a linear time-varying system where the slow state variables act as parameters. Then, a linear state feedback control based on either the Linear Quadratic Regulator (LQR) or the pole placement technique can be applied to damp out the flexible variables. This control was designed for serial-type flexible-link manipulators by Siciliano & Book (1988). Matsuno & Yamamoto (1994) demonstrated its use to simultaneously control position and force of a two-degree-of-freedom flexible manipulator where the hybrid position/force control was used for the slow subsystem. Boutin (1995) applied this control technique to articulating truss structures.

Manipulators may also be redundant, i.e., the joint space dimension may be greater than that of the end-effector task space (as in the case of the 7-joint SSRMS). Manipulator redundancy has been exploited to achieve such goals as minimization of a quadratic criterion (Whitney 1969), minimization of joint torques (Chung et al. 1993), or avoidance of joint limits, obstacles, or kinematic singularities. Extending Whitney's work, Khatib (1987) designed an operational-space based controller that minimizes the instantaneous kinetic energy of the system to obtain an effective inverse of the manipulator Jacobian, known as the *inertia-weighted pseudoinverse.*

1.6 Scope and Organization of the Thesis

In this thesis, an efficient solution procedure of a detailed contact dynamics model of general multi-body systems of arbitrary kinematic architecture is considered. The bodies which undergo direct contact, referred to as *contacting bodies*, are modelled using the Lagrange Multiplier technique based on the Finite Element Method. The modified Euler-Lagrange method based on the Natural Orthogonal Complement (NOC) was chosen to model multi-body systems. These systems, by the nature of the kinematic or contact constraints acting between them, may form arbitrary kinematic configurations such as kinematic loops, or chains of tree- or serial-type topology. The dynamics of the individual systems are then globally coupled, and are accounted for in a general integration of all the systems.

In order to render the dynamic simulation computationally efficient, the following solution procedures are used in this thesis. Firstly, the computationally straightforward and economical Newmark method is used for the time integration of the equations of motion, with which the second order dynamical equations can be converted into algebraic form. Secondly, algebraic manipulations are made of the resulting equations in order to exploit the positive definite and positive semi-definite character of the mass, damping and stiffness matrices and use the efficient Cholesky Decomposition (CD) method for the inversion of matrices. Thirdly, the Guyan reduction method is applied to the sets of finite element equations in order to obtain a reduced set of equations. Finally, efficient methods of obtaining the inverse of a configuration dependent and time-varying mass matrix of large size are investigated and their relative merits analysed and weighed against compromises in modelling accuracy.

This dynamic model is then used to design a *composite* controller which must simultaneously achieve three goals: (1) trajectory tracking, (2) force control, and (3) stabilization of the flexible degrees of freedom of the multibody system. The *singular perturbation method* is used to obtain two reduced order models; subsequently, the slow subsystem is used to design a position/force controller based on impedance control, and the fast linear subsystem is used to design a Linear Quadratic Regulator (LQR).

The detailed presentation of the above thesis description is organized into seven chapters in the following manner:

Chapter 2 deals with the dynamical formulation of the contacting bodies using the Finite Element Method (FEM). The dynamical equations of each element are derived individually using the symbolic manipulator software Maple V. Then these equations are assembled using the method of NOC to form the equations of motion of an entire contacting body.

Chapter 3 presents the dynamical formulation of multi-body systems using the method of NOC. The kinematics formulation is first presented. Then the dynamical equations of each body is derived separately. Finally, the equations of motion of the multi-body system are assembled using the method of NOC.

Chapter 4 deals with problems of integrating the various systems formulated in Chapters 2 and 3. An arbitrary interconnecting assembly of these systems is considered. Several solution strategies are presented with a view to increasing the computational efficiency without sacrificing dynamic fidelity.

Chapter 5 is concerned with the implementation of a trajectory, force, and vibration control of the dynamical model. A *composite* control strategy is presented based on the Singular Perturbation method. Impedance control is used for the slow subsystem and the Linear Quadratic Regulator (LQR) is used for the fast subsystem. Manipulator redundancy is exploited to minimize the instantaneous kinetic energy of the system.

Chapter 6 presents the computer code description, simulations, validations, results and discussions.

Chapter 7 is devoted to conclusions and recommendations for further work.

Appendices provide some basic information and the details of certain derivations.

Chapter 2

Finite Element Model of Contacting Bodies

2.1 Introduction

This chapter describes the dynamical formulation of contacting bodies such as end-effectors and payloads. The local contact phenomena such as contact deformations. elastic oscillations and friction are modelled based on the finite element method. A linear finite element model can be used when both strains and displacements of the body to be modelled can be assumed to be infinitesimal. Most space contact activities are performed slowly and the generated forces are not severe. thus the infinitesimal strain assumption holds good. However, for contact operations where the end-effector and payload undergo prolonged contact with significant rigid-body motion, such as when the end-effector is sliding along a path on the target body, the second assumption, i.e. the infinitesimal displacement assumption is not valid. Thus, a nonlinear finite element model which incorporates large rigid-body displacements but assumes infinitesimal strains is presented here.

The simulations and results presented in this thesis are confined to planar (2D) motion. However, the formulations and notation presented in this thesis maintain the generality of a spatial (3D) motion, unless otherwise explicitly stated. Note that in this thesis, bold-face, lower-case, Latin and Greek letters denote vectors; bold-face, upper-case, Latin and Greek letters denote matrices; and calligraphic and italic letters generally represent scalar quantities such as material or geometric properties or indices.

A schematic diagram of the end-effector, which is a typical contacting body in contact operations, is shown in Figure 2.1. Two reference frames are chosen as shown: the inertial frame XYZ, and the local frame xyz, or body-fixed frame, which is defined as one having the same rigid-body motion as the body to which it is attached. The rigid-body motion can then be fully described by the position and orientation of the local frame xyz with respect to XYZ. The position of the origin of the xyz frame can be described by the position vector $\mathbf{p}$, while its orientation can be represented by the rotation tensor $\mathbf{R}$. The nine elements of matrix $\mathbf{R}$ are the direction cosines which describe the orientation of xyz axes with respect to XYZ axes. Due to the orthogonality property of $\mathbf{R}$, there are six constraint equations involving the nine elements:

$$\mathbf{R}^T\mathbf{R} = \mathbf{I}_{33} \tag{2.1}$$

where $\mathbf{I}_{33}$ is a 3 × 3 identity matrix. Hence there are 3 independent parameters which can be represented as generalized coordinates, $\hat{\mathbf{q}}$, using a three-component representation such as the Euler angles, or roll, yaw, and pitch angles, such that

$$\hat{\mathbf{q}} = \{\alpha \;\; \beta \;\; \gamma\}^T \tag{2.2}$$

In the planar case illustrated in Figure 2.1, γ is the same as θ (shown in Figure 2.1), while α and β are both zero. The orientation vector $\hat{\mathbf{q}}$ can also be represented by a four-parameter set or *quaternion* such as Euler parameters or linear invariants (Cyril 1988). If a three-component representation is chosen, the three coordinates are independent, but singularity problems are introduced. On the other hand, if a four-parameter set is chosen, then the four components of the orientation vector $\hat{\mathbf{q}}$

are not independent but constrained by

$$\hat{\mathbf{q}}^T\hat{\mathbf{q}} = 1 \tag{2.3}$$

The angular velocity of the body, $\boldsymbol{\omega}$, and the time derivative of $\hat{\mathbf{q}}$ are related by

$$\boldsymbol{\omega} = \mathbf{L}\dot{\hat{\mathbf{q}}} \tag{2.4}$$

$$\dot{\hat{\mathbf{q}}} = \boldsymbol{\Lambda}\boldsymbol{\omega} \tag{2.5}$$

where $\mathbf{L}$ and $\boldsymbol{\Lambda}$ are 3×3 matrices if $\hat{\mathbf{q}}$ is made up of Euler angles, and 3×4 and 4×3 respectively if $\hat{\mathbf{q}}$ is made up of a four-parameter set. For ease of mathematical representation as well as physical interpretation, Euler angles are chosen here to represent body orientation.

The position of an arbitrary point on element i given by $\mathbf{x}_i$ and elastic displacement given by $\mathbf{u}_i$ are measured with respect to the local frame xyz. With this kinematic representation, the nodal positions will not change and all volume integrations, which are nodal-position dependent, will need to be computed (symbolically) only once. The reference frames and coordinates for other contacting bodies are chosen in the same way.

The basic procedure in the derivation of the equations of motion of each contacting body is as follows: The equations of motion of each element are derived symbolically using the symbolic manipulator software Maple V and the equations of motion of the whole system are assembled using a method which is a simplified application of the method of Natural Orthogonal Complement (NOC) (Cyril et al. 1991). The use of Maple V lends to computational efficiency because computations such as volume integrations and algebraic manipulations and simplifications can be done *off-line*. The results of the Maple program can be input to a FORTRAN code where the individual sets of equations of motion are assembled.

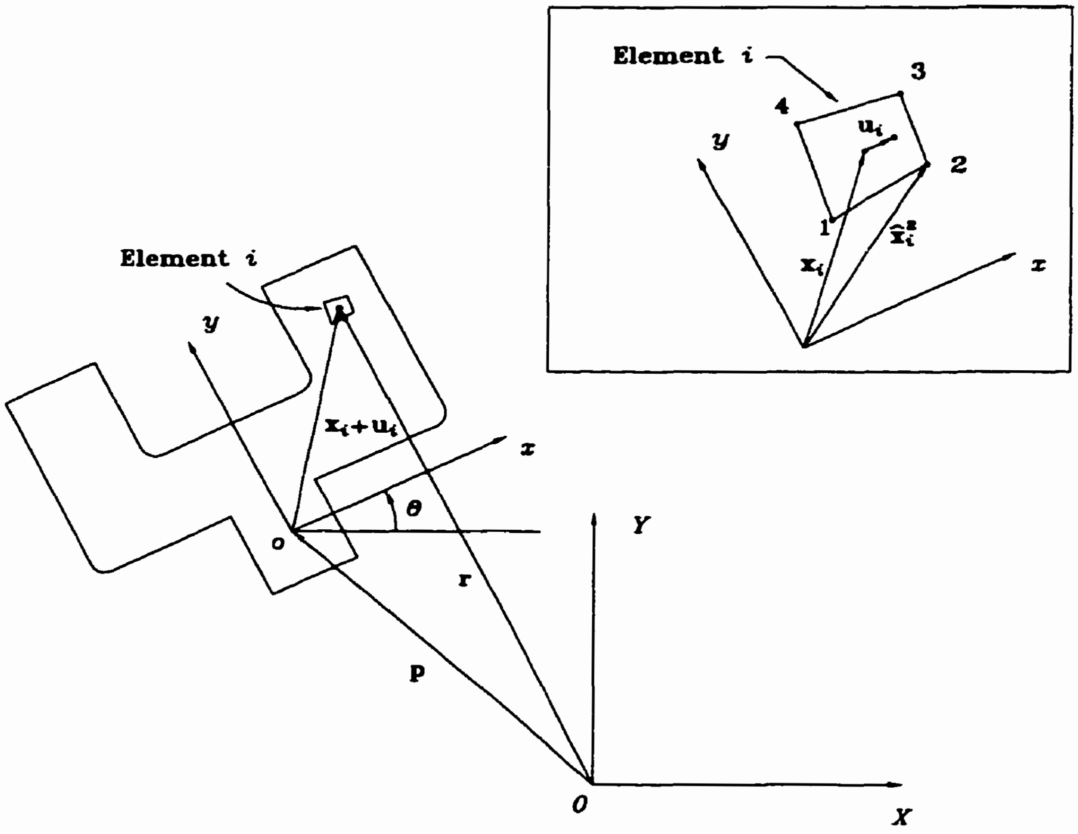

Figure 2.1: Coordinate Systems of a Typical Contacting Body

2.2 Dynamics of an Individual Element

The equations of motion of a single element can be derived using the Lagrangian formulation. The position of an arbitrary point in an element i can be expressed as:

$$\mathbf{r}_i = \mathbf{p} + \mathbf{R}(\mathbf{x}_i + \mathbf{u}_i) \tag{2.6}$$

where $\mathbf{r}_i$ is the inertial position vector of the point, $\mathbf{p}$ is the inertial position vector of the origin of the local frame xyz, $\mathbf{x}_i$ and $\mathbf{u}_i$ are respectively the undeformed position vector and the elastic displacement with respect to the undeformed position of the point measured in the xyz coordinate frame (see Figure 2.1), and $\mathbf{R}$ is the rotation matrix which describes the orientation of the local frame with respect to the inertial frame. The velocity of the point can be obtained by differentiation with respect to time:

$$\dot{\mathbf{r}}_i = \dot{\mathbf{p}} + \mathbf{R}\boldsymbol{\omega}\times(\mathbf{x}_i + \mathbf{u}_i) + \mathbf{R}\dot{\mathbf{u}}_i \tag{2.7}$$

where $\boldsymbol{\omega}$ is measured in the xyz coordinate system.

The system must be discretized before Lagrange's equations can be applied. Isoparametric finite elements are used in this spatial discretization, i.e., the same shape functions are used for the interpolations of the element displacements and the element coordinates. Using this approach,

$$\mathbf{x}_i = \mathbf{N}_i\hat{\mathbf{x}}_i \tag{2.8}$$

$$\mathbf{u}_i = \mathbf{N}_i\hat{\mathbf{u}}_i \tag{2.9}$$

where, if m is the number of nodes of the i-th element, and $\hat{\mathbf{x}}_i^j$ and $\hat{\mathbf{u}}_i^j$ are position vectors and elastic displacements of node j of element i, then $\hat{\mathbf{x}}_i$, and $\hat{\mathbf{u}}_i$ are $3m\times1$ vectors of nodal coordinates and displacements given by

$$\hat{\mathbf{x}}_i = \left\{\begin{matrix} \hat{\mathbf{x}}_i^1 \\ \hat{\mathbf{x}}_i^2 \\ \vdots \\ \hat{\mathbf{x}}_i^j \\ \vdots \\ \hat{\mathbf{x}}_i^m \end{matrix}\right\} \; ; \; \hat{\mathbf{u}}_i = \left\{\begin{matrix} \hat{\mathbf{u}}_i^1 \\ \hat{\mathbf{u}}_i^2 \\ \vdots \\ \hat{\mathbf{u}}_i^j \\ \vdots \\ \hat{\mathbf{u}}_i^m \end{matrix}\right\} \; ; \; \hat{\mathbf{x}}_i^j = \left\{\begin{matrix} \hat{x}_i^j \\ \hat{y}_i^j \\ \hat{z}_i^j \end{matrix}\right\} \; ; \; \hat{\mathbf{u}}_i^j = \left\{\begin{matrix} \hat{u}_i^j \\ \hat{v}_i^j \\ \hat{w}_i^j \end{matrix}\right\}$$

and $\mathbf{N}_i$ is a $3\times3m$ matrix of interpolating functions. Appendix A.1 discusses isoparametric interpolating functions of various types of elements. Substituting equations (2.4), (2.8) and (2.9) into equation (2.7):

$$\dot{\mathbf{r}}_i = \dot{\mathbf{p}} - \mathbf{R}\tilde{\mathbf{N}}_i\mathbf{L}\dot{\mathbf{q}} + \mathbf{R}\mathbf{N}_i\dot{\hat{\mathbf{u}}}_i \tag{2.10}$$

where $\tilde{\mathbf{N}}_i$ is the cross-product matrix associated with $(\mathbf{x}_i + \mathbf{u}_i)$. Here, the cross-product matrix $\mathbf{A}$ associated with a vector $\mathbf{a} = [a_x \; a_y \; a_z]^T$ is the skew-symmetric matrix of $\mathbf{a}$ given by

$$\mathbf{A} = \begin{bmatrix} 0 & -a_z & a_y \\ a_z & 0 & -a_x \\ -a_y & a_x & 0 \end{bmatrix}$$

so that for an arbitrary vector $\mathbf{b}$,

$$\mathbf{a} \times \mathbf{b} \equiv \mathbf{A}\mathbf{b}$$

Then, matrix $\tilde{\mathbf{N}}_i$ can be expressed as

$$\tilde{\mathbf{N}}_i = \begin{bmatrix} 0 & -\mathbf{N}_{i3}(\hat{\mathbf{x}}_i + \hat{\mathbf{u}}_i) & \mathbf{N}_{i2}(\hat{\mathbf{x}}_i + \hat{\mathbf{u}}_i) \\ \mathbf{N}_{i3}(\hat{\mathbf{x}}_i + \hat{\mathbf{u}}_i) & 0 & -\mathbf{N}_{i1}(\hat{\mathbf{x}}_i + \hat{\mathbf{u}}_i) \\ -\mathbf{N}_{i2}(\hat{\mathbf{x}}_i + \hat{\mathbf{u}}_i) & \mathbf{N}_{i1}(\hat{\mathbf{x}}_i + \hat{\mathbf{u}}_i) & 0 \end{bmatrix}$$

where

$$\mathbf{N}_i = \begin{bmatrix} \mathbf{N}_{i1} \\ \mathbf{N}_{i2} \\ \mathbf{N}_{i3} \end{bmatrix}$$

Equation (2.10) can further be expressed in compact form:

$$\dot{\mathbf{r}}_i = \mathbf{W}_i \dot{\mathbf{q}}_i \tag{2.11}$$

where

$$\mathbf{W}_i = \begin{bmatrix} \mathbf{I} & -\mathbf{R}\tilde{\mathbf{N}}_i\mathbf{L} & \mathbf{R}\mathbf{N}_i \end{bmatrix} \tag{2.12}$$

and $\dot{\mathbf{q}}_i$ is the vector of generalized velocities given by

$$\dot{\mathbf{q}}_i = \begin{Bmatrix} \dot{\mathbf{p}} \\ \dot{\mathbf{q}} \\ \dot{\hat{\mathbf{u}}}_i \end{Bmatrix} \tag{2.13}$$

The kinetic energy of element i can be expressed as

$$T_i = \frac{1}{2}\int \dot{\mathbf{r}}_i \cdot \dot{\mathbf{r}}_i dm_i$$

which can be recast in matrix form as

$$T_i = \frac{1}{2}\dot{\mathbf{q}}_i^T \mathbf{M}_i \dot{\mathbf{q}}_i \tag{2.14}$$

where $\mathbf{M}_i$ is the mass matrix given by

$$\mathbf{M}_i = \int \mathbf{W}_i^T \mathbf{W}_i dm_i \tag{2.15}$$

$$= \int \begin{bmatrix} \mathbf{I} & -\mathbf{R}\tilde{\mathbf{N}}_i\mathbf{L} & \mathbf{R}\mathbf{N}_i \\ -\mathbf{L}^T\tilde{\mathbf{N}}_i^T\mathbf{R}^T & \mathbf{L}^T\tilde{\mathbf{N}}_i^T\tilde{\mathbf{N}}_i\mathbf{L} & -\mathbf{L}^T\tilde{\mathbf{N}}_i^T\mathbf{N}_i \\ \mathbf{N}_i^T\mathbf{R}^T & -\mathbf{N}_i^T\tilde{\mathbf{N}}_i\mathbf{L} & \mathbf{N}_i^T\mathbf{N}_i \end{bmatrix} dm_i \tag{2.16}$$

The mass matrix can also be expressed in the following block form:

$$\mathbf{M}_i = \begin{bmatrix} \mathbf{M}_i^{pp} & \mathbf{M}_i^{p\theta} & \mathbf{M}_i^{pu} \\ \mathbf{M}_i^{p\theta^T} & \mathbf{M}_i^{\theta\theta} & \mathbf{M}_i^{\theta u} \\ \mathbf{M}_i^{pu^T} & \mathbf{M}_i^{\theta u^T} & \mathbf{M}_i^{uu} \end{bmatrix} \tag{2.17}$$

The above sub-matrices may be partitioned as

$$\mathbf{M}_i^{pp} = m_i\mathbf{I} \tag{2.18}$$

$$\mathbf{M}_i^{p\theta} = \mathbf{R}\bar{\mathbf{M}}_i^{p\theta}\mathbf{L} \tag{2.19}$$

$$\mathbf{M}_i^{pu} = \mathbf{R}\bar{\mathbf{M}}_i^{pu} \tag{2.20}$$

$$\mathbf{M}_i^{\theta\theta} = \mathbf{L}^T\bar{\mathbf{M}}_i^{\theta\theta}\mathbf{L} \tag{2.21}$$

$$\mathbf{M}_i^{\theta u} = \mathbf{L}^T\bar{\mathbf{M}}_i^{\theta u} \tag{2.22}$$

$$\mathbf{M}_i^{uu} = \int \mathbf{N}_i^T\mathbf{N}_i dm_i \tag{2.23}$$

where

$$\bar{\mathbf{M}}_i^{p\theta} = -\int \tilde{\mathbf{N}}_i dm_i \tag{2.24}$$

$$\bar{\mathbf{M}}_i^{pu} = \int \mathbf{N}_i dm_i \tag{2.25}$$

$$\begin{aligned} \bar{\mathbf{M}}_i^{\theta\theta} &= \int \tilde{\mathbf{N}}_i^T\tilde{\mathbf{N}}_i dm_i \\ &= \int \left[(\hat{\mathbf{x}}_i + \hat{\mathbf{u}}_i)^T\mathbf{N}_i^T\mathbf{N}_i(\hat{\mathbf{x}}_i + \hat{\mathbf{u}}_i)\mathbf{I} - \mathbf{N}_i(\hat{\mathbf{x}}_i + \hat{\mathbf{u}}_i)(\hat{\mathbf{x}}_i + \hat{\mathbf{u}}_i)^T\mathbf{N}_i^T\right] dm_i \end{aligned} \tag{2.26}$$

$$\bar{\mathbf{M}}_i^{\theta u} = -\int \tilde{\mathbf{N}}_i\mathbf{N}_i dm_i \tag{2.27}$$

This unique partitioned representation of the mass matrix will be used later in Section 4.3.1 to develop an efficient method of inversion of a large matrix.

The differential mass of the element dm_i can be expressed in terms of natural coordinates (Appendix A.1), $\xi\eta\zeta$, such that a certain integral

$$\mathbf{M}^{ab} = \int \mathbf{\Phi}^{ab} dm_i \tag{2.28}$$

may be rewritten as

$$\mathbf{M}^{ab} = \rho_i \int_{-1}^{1} \int_{-1}^{1} \int_{-1}^{1} \mathbf{\Phi}^{ab}(\xi,\eta,\zeta) J_i(\xi,\eta,\zeta) d\xi d\eta d\zeta \tag{2.29}$$

where ρ_i is the density of the element (which, assuming constant, may be taken out of the integral) and J_i is the determinant of $\mathbf{J}_i$ which is the Jacobian relating the natural coordinate derivatives to the local coordinate derivatives:

$$\mathbf{J}_i = \begin{bmatrix} \frac{\partial x_i}{\partial \xi} & \frac{\partial x_i}{\partial \eta} & \frac{\partial x_i}{\partial \zeta} \\ \frac{\partial y_i}{\partial \xi} & \frac{\partial y_i}{\partial \eta} & \frac{\partial y_i}{\partial \zeta} \\ \frac{\partial z_i}{\partial \xi} & \frac{\partial z_i}{\partial \eta} & \frac{\partial z_i}{\partial \zeta} \end{bmatrix} \; ; \; \mathbf{x}_i = \begin{Bmatrix} x_i \\ y_i \\ z_i \end{Bmatrix}$$

Volume integrations expressed in this form can be carried out using the n-point Gaussian Quadrature (Cook 1981), given by

$$\mathbf{M}^{ab} \approx \rho_i \sum_{j}^{n} \sum_{k}^{n} \sum_{l}^{n} W_j W_k W_l \mathbf{\Phi}^{ab}(\xi_j, \eta_k, \zeta_l) J_i(\xi_j, \eta_k, \zeta_l) \tag{2.30}$$

where ξ_j, η_k and ζ_l are appropriate sampling points, and W_j, W_k, and W_l are corresponding weighting factors. Volume integrals of equations (2.23–2.27) are carried out using this method.

The potential energy of element i can be expressed as

$$U_i = \frac{1}{2} \int \boldsymbol{\epsilon}_i^T \boldsymbol{\sigma}_i dV \tag{2.31}$$

where $\boldsymbol{\epsilon}_i$ and $\boldsymbol{\sigma}_i$ are vectors comprising the components of the strain and stress tensors. The stresses and strains are related by a constitutive equation, known as the generalized Hooke's law:

$$\boldsymbol{\sigma}_i = \mathbf{E}_i \boldsymbol{\epsilon}_i \tag{2.32}$$

where $\mathbf{E}_i$ is the stress-strain constitutive matrix. The displacements and strains are related by

$$\boldsymbol{\epsilon}_i = \boldsymbol{\partial} \mathbf{u}_i \tag{2.33}$$

where $\boldsymbol{\partial}$ denotes a matrix of function derivatives:

$$\boldsymbol{\sigma}_i = \begin{Bmatrix} \sigma_x \\ \sigma_y \\ \sigma_z \\ \tau_{xy} \\ \tau_{yz} \\ \tau_{zx} \end{Bmatrix}_i \quad ; \quad \boldsymbol{\epsilon}_i = \begin{Bmatrix} \epsilon_x \\ \epsilon_y \\ \epsilon_z \\ \gamma_{xy} \\ \gamma_{yz} \\ \gamma_{zx} \end{Bmatrix}_i \quad ; \quad \boldsymbol{\partial} = \begin{bmatrix} \frac{\partial}{\partial x} & 0 & 0 \\ 0 & \frac{\partial}{\partial y} & 0 \\ 0 & 0 & \frac{\partial}{\partial z} \\ \frac{\partial}{\partial y} & \frac{\partial}{\partial x} & 0 \\ 0 & \frac{\partial}{\partial z} & \frac{\partial}{\partial y} \\ \frac{\partial}{\partial z} & 0 & \frac{\partial}{\partial x} \end{bmatrix}$$

Using equation (2.9), equation (2.33) becomes

$$\boldsymbol{\epsilon}_i = \mathbf{B}_i \hat{\mathbf{u}}_i \tag{2.34}$$

where

$$\mathbf{B}_i = \boldsymbol{\partial} \mathbf{N}_i \tag{2.35}$$

Using equations (2.32) and (2.34), the potential energy of element i can be expressed in matrix form as

$$U_i = \frac{1}{2} \mathbf{q}_i^T \mathbf{K}_i \mathbf{q}_i \tag{2.36}$$

Vector $\mathbf{q}_i$ is the set of generalized coordinates of element i given by

$$\mathbf{q}_i = \begin{Bmatrix} \mathbf{p} \\ \hat{\mathbf{q}} \\ \hat{\mathbf{u}}_i \end{Bmatrix} \tag{2.37}$$

and $\mathbf{K}_i$ is the stiffness matrix given by

$$\mathbf{K}_i = \begin{bmatrix} \mathbf{0} & \mathbf{0} & \mathbf{0} \\ \mathbf{0} & \mathbf{0} & \mathbf{0} \\ \mathbf{0} & \mathbf{0} & \mathbf{K}_i^{uu} \end{bmatrix} \tag{2.38}$$

where

$$\mathbf{K}_i^{uu} = \int_{-1}^{1} \int_{-1}^{1} \int_{-1}^{1} \mathbf{B}_i^T \mathbf{E}_i \mathbf{B}_i J_i d\xi d\eta d\zeta \tag{2.39}$$

As already mentioned with respect to the computation of the mass matrix, the volume integration of equation (2.39) is carried out using the n-point Gaussian Quadrature.

The equations of motion of the element can be obtained using Lagrange's equations:

$$\frac{d}{dt}\left(\frac{\partial T_i}{\partial \dot{\mathbf{q}}_i}\right) - \frac{\partial T_i}{\partial \mathbf{q}_i} + \frac{\partial U_i}{\partial \mathbf{q}_i} = \boldsymbol{\chi}_i \tag{2.40}$$

where $\boldsymbol{\chi}_i$ contains all the non-conservative generalized forces. The final form of the equations of motion for an element i can then be written as

$$\mathbf{M}_i\ddot{\mathbf{q}}_i + \mathbf{K}_i\mathbf{q}_i + \mathbf{c}_i(\mathbf{q}_i, \dot{\mathbf{q}}_i) = \mathbf{f}_i + \mathbf{f}_{c_i} \tag{2.41}$$

where $\mathbf{M}_i$ is the mass matrix, $\mathbf{K}_i$ is the stiffness matrix, $\mathbf{c}_i$ is the nonlinear vector comprising the centrifugal and Coriolis forces, $\mathbf{f}_i$ is the external force vector and $\mathbf{f}_{c_i}$ represents the nonworking constraint forces acting on interelement nodes. Note that equation (2.41) is computed in its entirety in symbolic form in the Maple V program and is done *off-line*.

2.3 Dynamics of an Entire Contacting Body

The equations of motion of a whole contacting body can be assembled as follows:

$$\breve{\mathbf{M}}\ddot{\breve{\mathbf{q}}} + \breve{\mathbf{K}}\breve{\mathbf{q}} + \breve{\mathbf{c}}(\breve{\mathbf{q}}, \dot{\breve{\mathbf{q}}}) = \breve{\mathbf{f}} + \breve{\mathbf{f}}_c \tag{2.42}$$

where

$$\breve{\mathbf{M}} = \begin{bmatrix} \mathbf{M}_1 & \mathbf{0} & \cdots & \mathbf{0} \\ \mathbf{0} & \mathbf{M}_2 & \cdots & \mathbf{0} \\ \vdots & \vdots & \ddots & \vdots \\ \mathbf{0} & \mathbf{0} & \cdots & \mathbf{M}_N \end{bmatrix} ; \quad \breve{\mathbf{K}} = \begin{bmatrix} \mathbf{K}_1 & \mathbf{0} & \cdots & \mathbf{0} \\ \mathbf{0} & \mathbf{K}_2 & \cdots & \mathbf{0} \\ \vdots & \vdots & \ddots & \vdots \\ \mathbf{0} & \mathbf{0} & \cdots & \mathbf{K}_N \end{bmatrix} ; \tag{2.43}$$

$$\breve{\mathbf{q}} = \begin{Bmatrix} \mathbf{q}_1 \\ \mathbf{q}_2 \\ \vdots \\ \mathbf{q}_N \end{Bmatrix} ; \quad \breve{\mathbf{c}} = \begin{Bmatrix} \mathbf{c}_1 \\ \mathbf{c}_2 \\ \vdots \\ \mathbf{c}_N \end{Bmatrix} ; \quad \breve{\mathbf{f}} = \begin{Bmatrix} \mathbf{f}_1 \\ \mathbf{f}_2 \\ \vdots \\ \mathbf{f}_N \end{Bmatrix} ; \quad \breve{\mathbf{f}}_c = \begin{Bmatrix} \mathbf{f}_{c_1} \\ \mathbf{f}_{c_2} \\ \vdots \\ \mathbf{f}_{c_N} \end{Bmatrix} \tag{2.44}$$

and N is the number of elements of the contacting body. Many nodal coordinates repeat themselves in the $\breve{\mathbf{q}}$ vector, and the relationship between $\breve{\mathbf{q}}$ and $\mathbf{q}$, which represents a set of minimum number of independent nodal coordinates, can be expressed as

$$\breve{\mathbf{q}} = \mathbf{T}\mathbf{q} \tag{2.45}$$

where $\mathbf{T}$ is a constant *connectivity* matrix made up of *ones* and *zeros*. Hence,

$$\dot{\breve{\mathbf{q}}} = \mathbf{T}\dot{\mathbf{q}} \text{ and } \ddot{\breve{\mathbf{q}}} = \mathbf{T}\ddot{\mathbf{q}} \tag{2.46}$$

Representing the equations of motion in terms of the new set of coordinates $\mathbf{q}$ we have

$$\breve{\mathbf{M}}\mathbf{T}\ddot{\mathbf{q}} + \breve{\mathbf{K}}\mathbf{T}\mathbf{q} + \breve{\mathbf{c}}(\mathbf{q}, \dot{\mathbf{q}}) = \breve{\mathbf{f}} + \breve{\mathbf{f}}_c \tag{2.47}$$

Premultiplying the above equation by $\mathbf{T}^T$ we obtain

$$\mathbf{M}\ddot{\mathbf{q}} + \mathbf{K}\mathbf{q} + \mathbf{c}(\mathbf{q}, \dot{\mathbf{q}}) = \mathbf{f} \tag{2.48}$$

where

$$\begin{aligned}
\mathbf{M} &= \mathbf{T}^T\breve{\mathbf{M}}\mathbf{T} \\
\mathbf{K} &= \mathbf{T}^T\breve{\mathbf{K}}\mathbf{T} \\
\mathbf{c} &= \mathbf{T}^T\breve{\mathbf{c}} \\
\mathbf{f} &= \mathbf{T}^T\breve{\mathbf{f}}
\end{aligned}$$

The term $\mathbf{T}^T\breve{\mathbf{f}}_c$, which does not appear in the equations of motion, is eliminated because the constraint forces $\breve{\mathbf{f}}_c$ do not generate any power in the system, i.e.,

$$\dot{\breve{\mathbf{q}}}^T\breve{\mathbf{f}}_c = \mathbf{0} \tag{2.49}$$

$$\text{or } \dot{\mathbf{q}}^T\mathbf{T}^T\breve{\mathbf{f}}_c = \mathbf{0} \tag{2.50}$$

Since the elements of the vector $\dot{\mathbf{q}}$ are independent, equation (2.50) leads to

$$\mathbf{T}^T\breve{\mathbf{f}}_c = \mathbf{0}$$

Damping effects are complex phenomena which are not simple to model mathematically. Since damping characteristics depend on the overall frequency content of the system, the damping matrix is in general not assembled from element damping matrices, but is constructed using the mass and stiffness matrices of the complete element assemblage together with experimental results on the amount of damping (Bathe 1982). One practical approach to modelling damping is Rayleigh's *proportional damping* (Bathe 1982, James et al. 1989), where it is assumed that the damping matrix is proportional to either or both the mass and stiffness matrices:

$$\mathbf{C} = \alpha\mathbf{M} + \beta\mathbf{K} \tag{2.51}$$

Here, α and β are constants which can be obtained for two typical values of natural frequencies ω_i and corresponding damping factors ζ_i, by performing a modal analysis on the linear elastic equations of motion where rigid body modes and nonlinear forces are removed:

$$\mathbf{M}\ddot{\mathbf{q}} + \mathbf{C}\dot{\mathbf{q}} + \mathbf{K}\mathbf{q} = \mathbf{0} \tag{2.52}$$

The modal transformation is given by:

$$\mathbf{q} = \mathbf{U}\boldsymbol{\delta} \quad ; \quad \dot{\mathbf{q}} = \mathbf{U}\dot{\boldsymbol{\delta}} \quad ; \quad \ddot{\mathbf{q}} = \mathbf{U}\ddot{\boldsymbol{\delta}}$$

where $\mathbf{U}$ is the modal matrix and $\boldsymbol{\delta}$ is the vector of principal coordinates. Substituting the above equations into equation (2.52) and premultiplying by $\mathbf{U}^T$,

$$\mathbf{U}^T\mathbf{M}\mathbf{U}\ddot{\boldsymbol{\delta}} + \mathbf{U}^T\mathbf{C}\mathbf{U}\dot{\boldsymbol{\delta}} + \mathbf{U}^T\mathbf{K}\mathbf{U}\boldsymbol{\delta} = \mathbf{0} \tag{2.53}$$

Using the orthogonality relationships between the eigenvectors relative to the mass and stiffness matrices, the following relationship can be obtained:

$$2\zeta_r\omega_r = \alpha + \beta\omega_r^2, \quad r = 1, \cdots, n \tag{2.54}$$

where n is the number of independent generalized coordinates. For two known sets of values of ω_r and ζ_r we can obtain α and β. Then, equation (2.48) can be rewritten with the inclusion of damping effects as

$$\mathbf{M}\ddot{\mathbf{q}} + \mathbf{C}\dot{\mathbf{q}} + \mathbf{K}\mathbf{q} + \mathbf{c}(\mathbf{q}, \dot{\mathbf{q}}) = \mathbf{f} \tag{2.55}$$

2.4 Contact Constraints

This section describes the kinematics associated with contact constraints. These constraints are then incorporated into the equations of motion using Lagrange multipliers. The basic conditions of contact along the contact surfaces are that no material overlap can occur; this is also called the *impenetrability* condition. As a result, contact forces develop on the surface of contact upon the contacting bodies, which are equal and opposite. The local normal forces can only exert compressive action; the tangential tractions satisfy a law of frictional resistance.

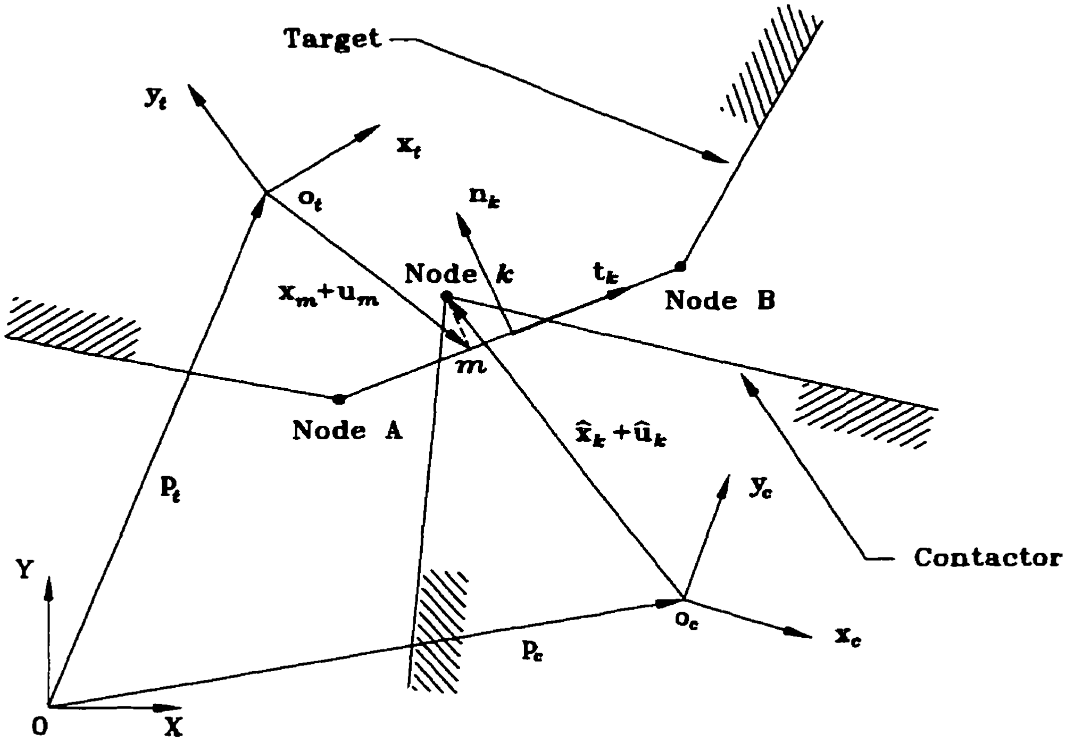

Figure 2.2: Schematic diagram of nodes in contact

Contact between two bodies can be determined by checking whether the minimum distance between them is zero (Ma 1995). For two arbitrarily given bodies, there always exists a unique minimum distance between them, which can be found using the following optimization problem:

$$\min\{\frac{1}{2}(\mathbf{r}_i - \mathbf{r}_j)^T(\mathbf{r}_i - \mathbf{r}_j)\} \tag{2.56}$$

where $\mathbf{r}_i$ and $\mathbf{r}_j$ are the position vectors of points i and j on the surface of each contacting body. Consider Figure 2.2, which shows in a schematic diagram a typical contact problem. Two generic contacting bodies are shown, where arbitrarily one is called *contactor* and the other *target*. Coordinate XYZ represents the inertial frame whereas $x_c y_c z_c$ and $x_t y_t z_t$ are local axes of the *contactor* and *target* respectively. To simplify the formulation, it is assumed that the *contactor* contains the finite element boundary nodes that come into contact with the *target* segments or nodes; i.e., the compatibility of surface displacements is only enforced at the discrete locations corresponding to the *contactor* nodes. For a certain *contactor* node k in contact with the *target* surface, a local contact frame can be identified, where $\mathbf{n}_k$ denotes the unit normal to the *target* surface and $\mathbf{t}_k$ denotes a unit tangential vector. The position of node k can be described by the summation*

$$\mathbf{r}_k = \mathbf{p}_c + \mathbf{R}_c(\hat{\mathbf{x}}_k + \hat{\mathbf{u}}_k) \tag{2.57}$$

whereas a *target* point m can be expressed by

$$\mathbf{r}_m = \mathbf{p}_t + \mathbf{R}_t(\mathbf{x}_m + \mathbf{u}_m) \tag{2.58}$$

where $\mathbf{R}_c$ and $\mathbf{R}_t$ denote rotation matrices describing the orientation of the *contactor* and *target* bodies respectively with respect to the inertial frame. The contact conditions can be established by calculating the distance of *contactor* node k on the *contactor* boundary to the *target* boundary, as

$$g_n = \mathbf{n}_k^T(\mathbf{r}_k - \mathbf{r}_m) \tag{2.59}$$

where m is the point on the *target* boundary such that $(\mathbf{r}_k - \mathbf{r}_m)^T(\mathbf{r}_k - \mathbf{r}_m)$ is minimum.

2.4.1 Frictionless Contact

In the absence of friction, the contact conditions can be expressed in mathematical form using the so-called Kuhn-Tucker conditions (Parisch & Lubbing 1997) (also

---

*Note here that, consistent with the notation used in Section 2.2, $\hat{\mathbf{x}}$ and $\hat{\mathbf{u}}$ denote vectors corresponding to discrete nodal points, whereas $\mathbf{x}$ and $\mathbf{u}$ denote vectors corresponding to arbitrary points.

known as Signorini conditions (Tissakht 1995)):

$$g_n = 0 \tag{2.60}$$

$$t_n \leq 0 \tag{2.61}$$

$$t_n g_n = 0 \tag{2.62}$$

The first statement, equation (2.60), defines the impenetrability condition and states that the bodies are allowed to separate but not to penetrate. The second, equation (2.61), defines that the normal traction, t_n, can only exert compressive action. The third, equation (2.62), states that the normal traction is non-zero only when the gap becomes zero, and vice-versa.

Vectors $\mathbf{x}_m$ and $\mathbf{u}_m$ can be obtained by linear interpolation between nodes that make up the segment s on which point m lies (Figure 2.3 for 2D case); hence

$$\mathbf{x}_m = \sum_{r=1}^{p} \beta_{sr} \hat{\mathbf{x}}_{sr} \tag{2.63}$$

$$\mathbf{u}_m = \sum_{r=1}^{p} \beta_{sr} \hat{\mathbf{u}}_{sr} \tag{2.64}$$

where p is the number of nodes making up the segment s, $\hat{\mathbf{x}}_{sr}$ and $\hat{\mathbf{u}}_{sr}$ represent the positions and deformations of the said nodes, and β_{sr} are interpolating functions constrained by

$$\sum_{r=1}^{p} \beta_{sr} = 1 \tag{2.65}$$

In matrix form,

$$\mathbf{x}_m = \mathbf{C}_s \hat{\mathbf{x}}_s \tag{2.66}$$

$$\mathbf{u}_m = \mathbf{C}_s \hat{\mathbf{u}}_s \tag{2.67}$$

where

$$\hat{\mathbf{x}}_s = \left\{ \begin{array}{c} \hat{\mathbf{x}}_{s1} \\ \hat{\mathbf{x}}_{s2} \\ \vdots \\ \hat{\mathbf{x}}_{sp} \end{array} \right\} \quad ; \quad \hat{\mathbf{u}}_s = \left\{ \begin{array}{c} \hat{\mathbf{u}}_{s1} \\ \hat{\mathbf{u}}_{s2} \\ \vdots \\ \hat{\mathbf{u}}_{sp} \end{array} \right\}$$

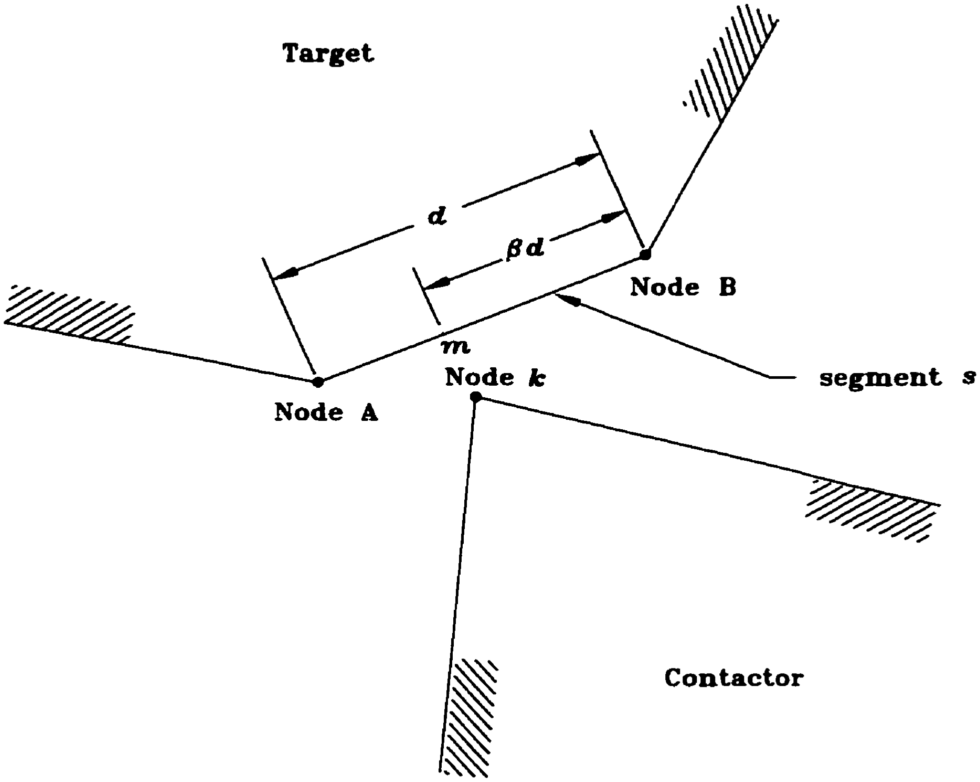

Figure 2.3: Definition of variables

$$\mathbf{C}_s = \begin{bmatrix} \beta_{s1} & 0 & 0 & \beta_{s2} & 0 & 0 & & \beta_{sp} & 0 & 0 \\ 0 & \beta_{s1} & 0 & 0 & \beta_{s2} & 0 & \cdots & 0 & \beta_{sp} & 0 \\ 0 & 0 & \beta_{s1} & 0 & 0 & \beta_{s2} & & 0 & 0 & \beta_{sp} \end{bmatrix}$$

In the 2D case illustrated in Figure 2.3,

$$\hat{\mathbf{x}}_s = \left\{ \begin{array}{c} \hat{\mathbf{x}}_A \\ \hat{\mathbf{x}}_B \end{array} \right\} \; ; \; \hat{\mathbf{u}}_s = \left\{ \begin{array}{c} \hat{\mathbf{u}}_A \\ \hat{\mathbf{u}}_B \end{array} \right\} \; ; \; \mathbf{C}_s = \begin{bmatrix} \beta & 0 & 1-\beta & 0 \\ 0 & \beta & 0 & 1-\beta \end{bmatrix} \qquad (2.68)$$

where

$$\beta = \mathbf{t}_k^T(\mathbf{x}_m - \hat{\mathbf{x}}_B)/d \qquad (2.69)$$

$$d = \mathbf{t}_k^T(\hat{\mathbf{x}}_A - \hat{\mathbf{x}}_B) \qquad (2.70)$$

Appendix A.2 provides details on the derivation of the corresponding matrix $\mathbf{C}_s$ for 3D elements.

2.4.2 Contact with Friction

Using Coulomb's law, two states of friction can be identified: sticking and sliding. The procedure used to decide whether a contact node is sticking, sliding or separating will be discussed in Chapter 4.

When node k is sticking, constraints are enforced in both the normal and tangential directions:

$$\mathbf{g} = \mathbf{r}_k - \mathbf{r}_m = \mathbf{0} \tag{2.71}$$

If node k is in sliding contact, a constraint is enforced only in the local normal direction, as in equation (2.60) for frictionless contact:

$$g_n = \mathbf{n}_k^T(\mathbf{r}_k - \mathbf{r}_m) = 0 \tag{2.72}$$

while in the tangential direction, Coulomb's law of frictional resistance is satisfied. If the normal traction becomes tensile, then no constraints are enforced and node k is separated from point m.

2.5 Equations of Motion with Contact Constraints

For a generic *contactor* node k in contact with a point m on a *target* segment s, the material overlap $\mathbf{g}^k$ for a general sticking contact can be expressed using equations (2.71), (2.57), and (2.58):

$$\mathbf{g}^k = \mathbf{p}_c + \mathbf{R}_c(\hat{\mathbf{x}}_k + \hat{\mathbf{u}}_k) - \{\mathbf{p}_t + \mathbf{R}_t(\mathbf{x}_m + \mathbf{u}_m)\} = \mathbf{0} \tag{2.73}$$

The Lagrange multiplier technique is used to take this constraint into account, and from equation (2.55), the equations of motion of the *contactor* and *target* can be expressed as follows:

$$\mathbf{M}_c\ddot{\mathbf{q}}_c + \mathbf{C}_c\dot{\mathbf{q}}_c + \mathbf{K}_c\mathbf{q}_c + \mathbf{c}_c(\mathbf{q}_c, \dot{\mathbf{q}}_c) + \mathbf{P}_c^{k^T}\boldsymbol{\lambda}^k = \mathbf{f}_c \tag{2.74}$$

$$\mathbf{M}_t\ddot{\mathbf{q}}_t + \mathbf{C}_t\dot{\mathbf{q}}_t + \mathbf{K}_t\mathbf{q}_t + \mathbf{c}_t(\mathbf{q}_t, \dot{\mathbf{q}}_t) + \mathbf{P}_t^{k^T}\boldsymbol{\lambda}^k = \mathbf{f}_t \tag{2.75}$$

Here, $\boldsymbol{\lambda}^k$ is the vector of Lagrange multipliers representing contact forces which enforce the associated contact constraints with respect to node k, subscripts c and t denote *contactor* and *target* values respectively, and

$$\mathbf{P}_c^k = \frac{\partial \mathbf{g}^k}{\partial \mathbf{q}_c} = \frac{\partial \dot{\mathbf{g}}^k}{\partial \dot{\mathbf{q}}_c} = \begin{bmatrix} \frac{\partial \dot{\mathbf{g}}^k}{\partial \dot{\mathbf{p}}_c} & \frac{\partial \dot{\mathbf{g}}^k}{\partial \dot{\hat{\mathbf{q}}}_c} & \frac{\partial \dot{\mathbf{g}}^k}{\partial \dot{\hat{\mathbf{u}}}_c} \end{bmatrix} \tag{2.76}$$

$$\mathbf{P}_t^k = \frac{\partial \mathbf{g}^k}{\partial \mathbf{q}_t} = \frac{\partial \dot{\mathbf{g}}^k}{\partial \dot{\mathbf{q}}_t} = \begin{bmatrix} \frac{\partial \dot{\mathbf{g}}^k}{\partial \dot{\mathbf{p}}_t} & \frac{\partial \dot{\mathbf{g}}^k}{\partial \dot{\hat{\mathbf{q}}}_t} & \frac{\partial \dot{\mathbf{g}}^k}{\partial \dot{\hat{\mathbf{u}}}_t} \end{bmatrix} \tag{2.77}$$

Differentiation of equation (2.73) and use of equation (2.67) lead to

$$\begin{aligned} \dot{\mathbf{g}}^k &= \dot{\mathbf{p}}_c + \mathbf{R}_c \boldsymbol{\omega}_c \times (\hat{\mathbf{x}}_k + \hat{\mathbf{u}}_k) + \mathbf{R}_c \dot{\hat{\mathbf{u}}}_k \\ &\quad - \dot{\mathbf{p}}_t - \mathbf{R}_t \boldsymbol{\omega}_t \times (\mathbf{x}_m + \mathbf{u}_m) - \mathbf{R}_t \mathbf{C}_s \dot{\hat{\mathbf{u}}}_s = \mathbf{0} \end{aligned} \tag{2.78}$$

where

$$\boldsymbol{\omega}_c = \mathbf{L}_c \dot{\hat{\mathbf{q}}}_c \tag{2.79}$$

$$\boldsymbol{\omega}_t = \mathbf{L}_t \dot{\hat{\mathbf{q}}}_t \tag{2.80}$$

Then, from equations (2.76) and (2.77)

$$\mathbf{P}_c^k = \begin{bmatrix} \mathbf{I}_{3\times 3} & -\mathbf{R}_c(\mathbf{X}_k + \mathbf{U}_k)\mathbf{L}_c & \mathbf{R}_c & \mathbf{0}_c \end{bmatrix} \tag{2.81}$$

$$\mathbf{P}_t^k = -\begin{bmatrix} \mathbf{I}_{3\times 3} & -\mathbf{R}_t(\mathbf{X}_m + \mathbf{U}_m)\mathbf{L}_t & \mathbf{R}_t\mathbf{C}_s & \mathbf{0}_t \end{bmatrix} \tag{2.82}$$

where matrices $\mathbf{0}_c$ and $\mathbf{0}_t$ denote zero elements belonging respectively to all nodes of the *contactor* other than node k, and all nodes of the *target* other than nodes si, $(i = 1, \cdots, p)$. Also, $\mathbf{X}_k$, $\mathbf{U}_k$, $\mathbf{X}_m$ and $\mathbf{U}_m$ are the cross-product skew-symmetric matrices of $\hat{\mathbf{x}}_k$, $\hat{\mathbf{u}}_k$, $\mathbf{x}_m$ and $\mathbf{u}_m$ respectively.

When node k is in sliding contact, the constraint is expressed by equation (2.72):

$$g_n^k = \mathbf{n}_k^T \mathbf{g}^k = 0 \tag{2.83}$$

$$\dot{g_n}^k = \mathbf{n}_k^T \dot{\mathbf{g}}^k + (\boldsymbol{\omega}_t \times \mathbf{n}_k)^T \mathbf{g}^k = 0 \tag{2.84}$$

where it is assumed that the angular velocity of the normal vector $\mathbf{n}_k$ is identical to that of the *target*. Hence,

$$\mathbf{P}_c^{k,(slide)} = \begin{bmatrix} \mathbf{n}_k^T & -\mathbf{n}_k^T \mathbf{R}_c(\mathbf{X}_k + \mathbf{U}_k)\mathbf{L}_c & \mathbf{n}_k^T \mathbf{R}_c & \mathbf{0}_c \end{bmatrix} \tag{2.85}$$

$$\mathbf{P}_t^{k,(slide)} = -\begin{bmatrix} \mathbf{n}_k^T & -\mathbf{n}_k^T \mathbf{R}_t(\mathbf{X}_m + \mathbf{U}_m)\mathbf{L}_t + \mathbf{g}^{k^T} \bar{\mathbf{N}}_k & \mathbf{n}_k^T \mathbf{R}_t \mathbf{C}_s & \mathbf{0}_t \end{bmatrix} \tag{2.86}$$

where $\bar{\mathbf{N}}_k$ is the cross-product skew-symmetric matrix associated with $\mathbf{n}_k$.

So far, the problem of accounting for the contact constraints due to a single arbitrary node k was presented. The constraint equations with respect to all n^* contacting nodes can be assembled as follows:

$$\mathbf{P}_c = \begin{bmatrix} \mathbf{P}_c^1 \\ \mathbf{P}_c^2 \\ \vdots \\ \mathbf{P}_c^{n^*} \end{bmatrix} \; ; \; \mathbf{P}_t = \begin{bmatrix} \mathbf{P}_t^1 \\ \mathbf{P}_t^2 \\ \vdots \\ \mathbf{P}_t^{n^*} \end{bmatrix} \; ; \; \boldsymbol{\lambda} = \begin{Bmatrix} \boldsymbol{\lambda}^1 \\ \boldsymbol{\lambda}^2 \\ \vdots \\ \boldsymbol{\lambda}^{n^*} \end{Bmatrix} \; ; \; \mathbf{g} = \begin{Bmatrix} \mathbf{g}^1 \\ \mathbf{g}^2 \\ \vdots \\ \mathbf{g}^{n^*} \end{Bmatrix}$$

Matrices $\mathbf{P}_c^k$ and $\mathbf{P}_t^k$, and vectors $\boldsymbol{\lambda}^k$, and $\mathbf{g}^k$ in equations (2.73) . (2.74) and (2.75) are then substituted by $\mathbf{P}_c$, $\mathbf{P}_t$, $\boldsymbol{\lambda}$, and $\mathbf{g}$ respectively.

Chapter 3

Dynamics of Multi-Body Systems

The method of derivation of the dynamical equations of multi-body systems presented by Cyril (1988) and Cyril et al. (1991) will be used in this work. A summary is presented in this chapter but Cyril (1988) should be referred to for further details.

3.1 Kinematics

3.1.1 General Description

A typical multi-body system may consist of a main body (a spacecraft) that serves as a platform on which other bodies (such as a multi-link robotic manipulator) are mounted. As an example, a spacecraft with a 2-link robotic manipulator capturing a payload is shown in Figure 3.1. The inertial frame (X_I, Y_I, Z_I) is located at the center of the Earth. The orbital frame (X_o, Y_o, Z_o) is located at the spacecraft's center of mass C_s and rotates at the orbital rate Ω. The system frame (X_1, Y_1, Z_1) is engraved on the spacecraft so that its orientation relative to the orbital frame defines the attitude of the spacecraft, represented by the pitch, roll and yaw angles. Finally,

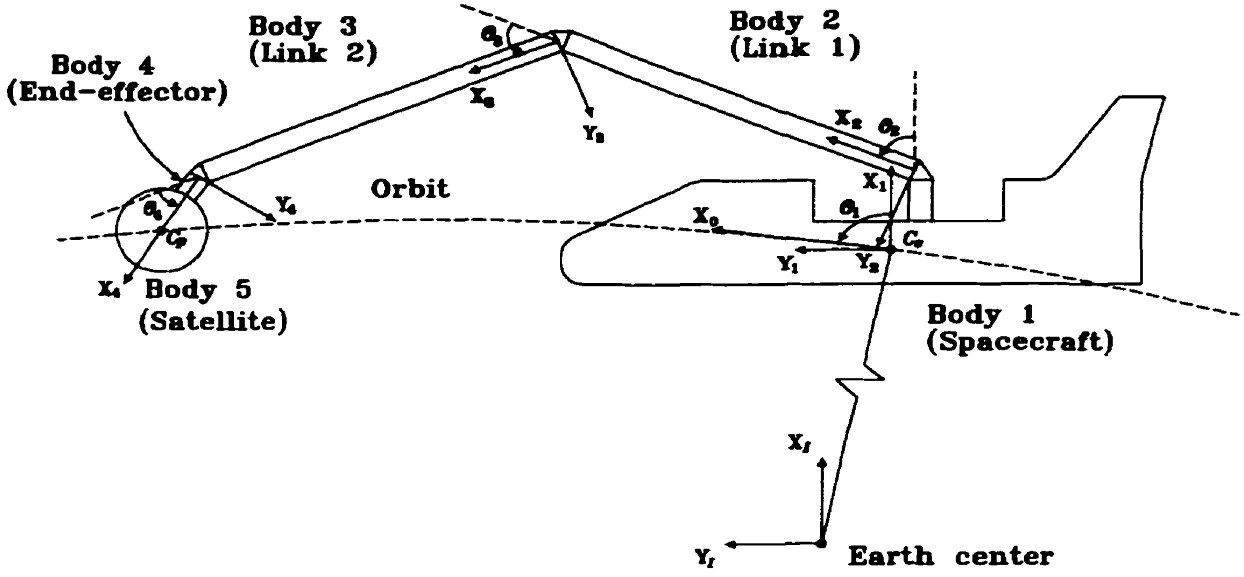

Figure 3.1: Schematic diagram of a typical multi-body system

a local frame*, (X_i, Y_i, Z_i), is attached to each individual body i, as shown in Figure 3.1.

To describe the kinematics of an individual body i, the so-called *extended* vectors are used. The *extended position* vector of body i is defined as

$$\mathbf{q}_i = \{\tilde{\mathbf{p}}_i^T \;\; \hat{\mathbf{q}}_i^T \;\; \mathbf{b}_i^T\}^T \tag{3.1}$$

where

- $\tilde{\mathbf{p}}_i$ = the position vector of the origin of the local frame (X_i, Y_i, Z_i) with respect to (X_o, Y_o, Z_o) (see Figure 3.2).
- $\hat{\mathbf{q}}_i$ = a vector defining the orientation of (X_i, Y_i, Z_i) with respect to (X_o, Y_o, Z_o). As discussed in Section 2.1, either a three parameter set of Euler angles or a four parameter set of *quaternions* may be used.
- $\mathbf{b}_i$ = a finite-dimensional vector of discretized deformation coordinates of the flexible body with respect to (X_i, Y_i, Z_i).

---

*A local frame is defined as one which has the same rigid-body motion as the body to which it is attached (Section 2.1).

The *extended velocity* vector is defined as

$$\mathbf{v}_i = \{\bar{\mathbf{v}}_i^T \ \ \boldsymbol{\omega}_i^T \ \ \dot{\mathbf{b}}_i^T\}^T \tag{3.2}$$

where

- $\bar{\mathbf{v}}_i$ = the velocity of the origin of the body-fixed axes (X_i, Y_i, Z_i) with respect to (X_o, Y_o, Z_o).
- $\boldsymbol{\omega}_i$ = the angular velocity of (X_i, Y_i, Z_i) with respect to (X_o, Y_o, Z_o).
- $\dot{\mathbf{b}}_i$ = the time derivative of $\mathbf{b}_i$ relative to the (X_i, Y_i, Z_i) frame.

3.1.2 Discretization of Flexible Links

Let $\mathbf{r}_i$ be the position vector of an arbitrary point on the flexible body i with respect to the (X_i, Y_i, Z_i) axes (Figure 3.2). If we define $\mathbf{i}_i$, $\mathbf{j}_i$ and $\mathbf{k}_i$ as unit vectors parallel to axes X_i, Y_i and Z_i respectively and x_i, y_i and z_i as the coordinates of any point in the (X_i, Y_i, Z_i) frame, then $\mathbf{r}_i$ can be expressed as

$$\mathbf{r}_i = x_i\mathbf{i}_i + y_i\mathbf{j}_i + z_i\mathbf{k}_i + \boldsymbol{\mu}_i \tag{3.3}$$

where $\boldsymbol{\mu}_i$ denotes the displacement of the point due to structural deformation. If the link is modelled as a slender beam, y_i and z_i can be approximated as zero. The component of $\boldsymbol{\mu}_i$ in the X_i direction is due to the axial shortening effect, that is related to centrifugal stiffening, which can be assumed negligible for small rotation rates. Its two other components in the Y_i and Z_i directions, which are due to displacements in bending, can be discretized using different methods, among which are: (*i*) the assumed modes method (Cyril 1988), (*ii*) the cubic-splines method (Cho 1995), and (*iii*) the finite element method (Fattah 1995). The finite element method and the cubic splines method allow the modelling of complicated structures having nonhomogeneous material properties and nonuniform cross-sections. However, these methods generally require a large number of generalized coordinates. The assumed modes method, on the other hand, requires only a small number of lower frequency modes to model the system with sufficient accuracy, although the calculation of exact shape functions is restricted to relatively simple systems. Since flexible manipulator links can usually be approximated as slender beams, the assumed modes method is chosen here for the discretization of the flexible links. The bending displacements can thus be written as

$$\mu_{i(2)}(x,t) = \sum_{j=1}^{m} \phi_{ij}(x_i) b_{ij}(t) \tag{3.4}$$

$$\mu_{i(3)}(x,t) = \sum_{j=1}^{m} \phi_{ij}(x_i) b_{i(m+j)}(t) \tag{3.5}$$

where ϕ_{ij} stands for a shape function of link i, and m is the number of shape functions used to model the elastic deformation of the flexible body in each direction. The shape functions must be admissible functions, i.e., they must satisfy at least the geometric boundary conditions (Meirovitch 1967). In compact form,

$$\boldsymbol{\mu}_i = \mathbf{B}_i(x_i)\mathbf{b}_i \tag{3.6}$$

where $\mathbf{B}_i(x_i)$ is a $3 \times 2m$ matrix of shape functions and $\mathbf{b}_i$ is the vector of elastic generalized coordinates given by

$$\mathbf{B}_i(x_i) = \begin{bmatrix} 0 & \cdots & 0 & 0 & \cdots & 0 \\ \phi_{i1}(x_i) & \cdots & \phi_{im}(x_i) & 0 & \cdots & 0 \\ 0 & \cdots & 0 & \phi_{i1}(x_i) & \cdots & \phi_{im}(x_i) \end{bmatrix} \tag{3.7}$$

$$\mathbf{b}_i = \{b_{i1} \;\; b_{i2} \;\; \cdots \;\; b_{im} \;\; b_{i(m+1)} \;\; \cdots \;\; b_{i(2m)}\}^T \tag{3.8}$$

The rotation of the tip of the link with respect to (X_i, Y_i, Z_i) due to its structural deformation, $\boldsymbol{\delta}_i$ (its z-component is shown in Figure 3.2), can be expressed as

$$\boldsymbol{\delta}_i = \mathbf{D}_i(l_i)\mathbf{b}_i \tag{3.9}$$

where

$$\mathbf{D}_i(l_i) = \begin{bmatrix} 0 & \cdots & 0 & 0 & \cdots & 0 \\ 0 & \cdots & 0 & -\phi'_{i1}(l_i) & \cdots & -\phi'_{im}(l_i) \\ \phi'_{i1}(l_i) & \cdots & \phi'_{im}(l_i) & 0 & \cdots & 0 \end{bmatrix}, \tag{3.10}$$

l_i is the length of the beam, and $(\;)'$ represents differentiation with respect to x_i.

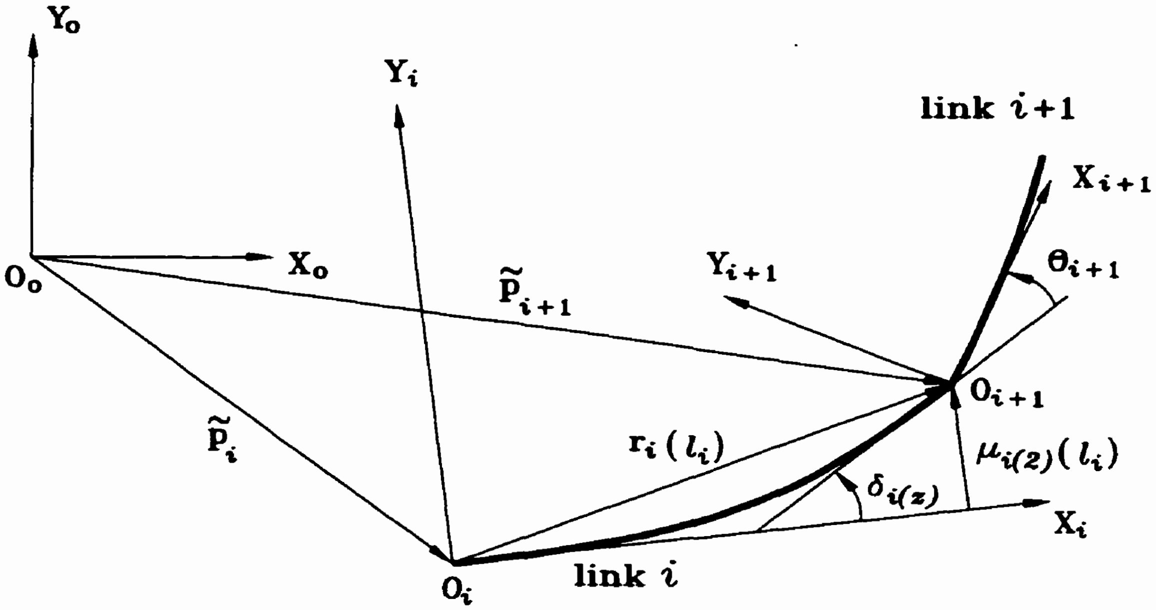

Figure 3.2: 2D schematic diagram of the i-th body and its coordinates

3.1.3 Recursive Relations

The rotation matrix describing the orientation of the local frame (X_i, Y_i, Z_i) with respect to the orbital frame (X_o, Y_o, Z_o) is defined as follows:

$$\mathbf{Q}_i = \mathbf{R}_1 \mathbf{R}_2 \cdots \mathbf{R}_{i-1} \mathbf{R}_i \tag{3.11}$$

where $\mathbf{R}_i$ describes the orientation of (X_i, Y_i, Z_i) with respect to $(X_{i-1}, Y_{i-1}, Z_{i-1})$.

For each body, the position of its origin (X_i, Y_i, Z_i) with respect to that of (X_o, Y_o, Z_o) is defined by the following recursive relation:

$$\bar{\mathbf{p}}_i = \bar{\mathbf{p}}_{i-1} + \mathbf{r}_{i-1}(l_{i-1}) \tag{3.12}$$

The corresponding translational and angular velocities can be written as:

$$\bar{\mathbf{v}}_i = \bar{\mathbf{v}}_{i-1} + \boldsymbol{\omega}_{i-1} \times \mathbf{r}_{i-1}(l_{i-1}) + \dot{\boldsymbol{\mu}}_{i-1}, \tag{3.13}$$

$$\boldsymbol{\omega}_i = \boldsymbol{\omega}_{i-1} + \dot{\boldsymbol{\delta}}_{i-1} + \dot{\theta}_i \mathbf{z}_i \tag{3.14}$$

where θ_i is the angle between X_i and X_{i-1} under rigid body conditions (i.e. no deformations in flexible links). It is assumed here that joints between adjacent links are revolute (refer to Cyril (1988) for corresponding expressions with prismatic joints). Further differentiation of equations (3.13) and (3.14) lead to the corresponding linear and angular accelerations:

$$\begin{aligned}\dot{\tilde{\mathbf{v}}}_i = \dot{\tilde{\mathbf{v}}}_{i-1} + \boldsymbol{\omega}_{i-1} \times \boldsymbol{\omega}_{i-1} \times \mathbf{r}_{i-1}(l_{i-1}) + \dot{\boldsymbol{\omega}}_{i-1} \times \mathbf{r}_{i-1}(l_{i-1}) \\ +2\boldsymbol{\omega}_{i-1} \times \dot{\boldsymbol{\mu}}_{i-1} + \ddot{\boldsymbol{\mu}}_{i-1}\end{aligned} \tag{3.15}$$

$$\dot{\boldsymbol{\omega}}_i = \dot{\boldsymbol{\omega}}_{i-1} + \ddot{\boldsymbol{\delta}}_{i-1} + \boldsymbol{\omega}_{i-1} \times \dot{\boldsymbol{\delta}}_{i-1} + \ddot{\theta}_i \mathbf{z}_i + (\boldsymbol{\omega}_{i-1} + \boldsymbol{\delta}_{i-1}) \times \dot{\theta}_i \mathbf{z}_i \tag{3.16}$$

3.2 Dynamics

The usual practice in Lagrangian dynamics is to consider the dynamical system as a whole, i.e., the potential and kinetic energy expressions of the system are obtained entirely and used to derive the equations of motion of the whole system. In the method of Natural Orthogonal Complement (NOC) used here, the Lagrange equations are obtained for each body separately and then assembled to derive the equations of motion of the system. The resulting nonworking constraint forces are conveniently eliminated using the NOC of the kinematic velocity constraint matrix. This method combines the advantages of the Newton-Euler and Lagrange methods, namely, capability for systematic analysis of each body separately, and convenient application to systems containing flexible bodies.

3.2.1 Dynamics of an Individual Body

The position of an arbitrary point on body i can be expressed as

$$\mathbf{p}_i = \tilde{\mathbf{p}}_i + \mathbf{r}_i \tag{3.17}$$

Differentiating, its velocity is given by

$$\dot{\mathbf{p}}_i = \tilde{\mathbf{v}}_i + \boldsymbol{\omega}_i \times \mathbf{r}_i + \dot{\mathbf{r}}_i \tag{3.18}$$

where $\dot{\mathbf{r}}_i$ is the derivative of $\mathbf{r}_i$ relative to the (X_i, Y_i, Z_i) frame.

Using equations (3.3) and (3.6), the above equation may be expressed as

$$\dot{\mathbf{p}}_i = \tilde{\mathbf{v}}_i - \tilde{\mathbf{R}}_i \boldsymbol{\omega}_i + \mathbf{B}_i \dot{\mathbf{b}}_i \tag{3.19}$$

where $\tilde{\mathbf{R}}_i$ is the cross-product skew symmetric matrix associated with the local position vector $\mathbf{r}_i$. This equation may further be expressed in matrix form as follows:

$$\dot{\mathbf{p}}_i = \mathbf{W}_i \mathbf{v}_i \tag{3.20}$$

where

$$\mathbf{W}_i = [\mathbf{I}_{3\times3} \quad -\tilde{\mathbf{R}}_i \ \ \mathbf{B}_i] \tag{3.21}$$

and $\mathbf{v}_i$ is the *extended velocity* vector as defined in equation (3.2).

The kinetic energy of a flexible link i can be expressed as:

$$T_i = \frac{1}{2}\int_0^{l_i} \rho_i(x)\dot{\mathbf{p}}_i^T \dot{\mathbf{p}}_i dx + \frac{1}{2} M_i \dot{\mathbf{p}}_i^T(l_i)\dot{\mathbf{p}}_i(l_i) + \frac{1}{2}\boldsymbol{\omega}_i^T \mathbf{I}_{h_i} \boldsymbol{\omega}_i \tag{3.22}$$

where ρ_i is the mass per unit length, M_i is the concentrated mass (if any) at the tip of the link, and $\mathbf{I}_{h_i}$ is the hub moment of inertia. Also, assuming that links are long and slender, the effects of rotary inertia can be neglected according to *Euler-Bernoulli* beam theory. Letting

$$\boldsymbol{\omega}_i = \mathbf{H}\mathbf{v}_i \tag{3.23}$$

where

$$\mathbf{H} = [\mathbf{0}_{3\times3} \ \ \mathbf{I}_{3\times3} \ \ \mathbf{0}_{3\times2m}] \tag{3.24}$$

and using equation (3.20), equation (3.22) may be rewritten as

$$T_i = \frac{1}{2}\mathbf{v}_i^T \mathbf{M}_i \mathbf{v}_i \tag{3.25}$$

where the *extended* mass matrix $\mathbf{M}_i$ can be obtained from

$$\mathbf{M}_i = \int_0^{l_i} \rho(x)\mathbf{W}_i^T \mathbf{W}_i dx + M_i \mathbf{W}_i^T \mathbf{W}_i \Big|_{x=l_i} + \mathbf{H}^T \mathbf{I}_{h_i} \mathbf{H} \tag{3.26}$$

Neglecting gravity, the potential energy due to the elastic strain energy stored in a flexible beam i can be written as:

$$U_i = \frac{1}{2}\int_0^{l_i} EI(\frac{\partial^2 \mu_{i(2)}}{\partial x^2})^2 dx + \frac{1}{2}\int_0^{l_i} EI(\frac{\partial^2 \mu_{i(3)}}{\partial x^2})^2 dx \tag{3.27}$$

where E and I are the modulus of elasticity and the area moment of inertia respectively. Again using *Euler-Bernoulli* beam theory, the effects of shear deformations have been neglected. Then, letting

$$\boldsymbol{\mu}_i'' = \mathbf{B}_i''\mathbf{b}_i \tag{3.28}$$

where

$$\mathbf{B}_i'' = \begin{bmatrix} 0 & \cdots & 0 & 0 & \cdots & 0 \\ \phi_{i1}'' & \cdots & \phi_{im}'' & 0 & \cdots & 0 \\ 0 & \cdots & 0 & \phi_{i1}'' & \cdots & \phi_{im}'' \end{bmatrix} \tag{3.29}$$

and the symbol $'$ denotes differentiation with respect to x_i, the potential energy can be rewritten in matrix form as

$$U_i = \frac{1}{2}\mathbf{b}_i^T\mathbf{K}_i^*\mathbf{b}_i \tag{3.30}$$

where

$$\mathbf{K}_i^* = EI\int_0^{l_i} \mathbf{B}_i''^T(x)\mathbf{B}_i''(x)dx \tag{3.31}$$

If structural damping of the links is to be incorporated in the model, the modulus of elasticity, E, may be replaced by the modified modulus of elasticity, E^* (James et al. 1989), defined as follows:

$$E^* = E(1 + \nu\frac{\partial}{\partial t}) \tag{3.32}$$

where ν is a damping parameter which can be found experimentally.

Having obtained the kinetic and potential energy expressions of body i, the dynamical equations of motion of body i are derived using Lagrange's equations:

$$\frac{d}{dt}(\frac{\partial T_i}{\partial \dot{\mathbf{q}}_i}) - \frac{\partial T_i}{\partial \mathbf{q}_i} = \boldsymbol{\chi}_i - \frac{\partial U_i}{\partial \mathbf{q}_i}, \quad i = 1, \cdots, N. \tag{3.33}$$

where χ_i contains all the non-conservative generalized forces. Upon substitution of the kinetic and potential energy expressions into the above equation, the equations of motion of body i can be derived in the following form:

$$\mathbf{M}_i\dot{\mathbf{v}}_i = \boldsymbol{\phi}_i^E + \boldsymbol{\phi}_i^S + \boldsymbol{\phi}_i^C \tag{3.34}$$

where $\boldsymbol{\phi}_i^E$ is the vector of generalized external forces, $\boldsymbol{\phi}_i^S$ contains the system forces such as centrifugal and Coriolis forces as well as stiffness and dissipative forces, and $\boldsymbol{\phi}_i^C$ contains the generalized constraint forces (Cyril 1988). Note that if *quaternions* are used for the representation of body orientation, an algebraic constraint force also will result. The means to eliminate it was presented by Cyril (1988), by virtue of which the said constraint does not appear in equation (3.34).

3.2.2 Dynamics of an Entire Multi-Body System

Upon assembling the equations of motion of an N-body multi-body system, the constrained equations of motion of the system can be written as:

$$\mathbf{M}\dot{\mathbf{v}} = \boldsymbol{\phi}^E + \boldsymbol{\phi}^S + \boldsymbol{\phi}^C \tag{3.35}$$

where

$$\mathbf{M} = \begin{bmatrix} \mathbf{M}_1 & \mathbf{0} & \cdots & \mathbf{0} \\ \mathbf{0} & \mathbf{M}_2 & \cdots & \mathbf{0} \\ \vdots & \vdots & \ddots & \vdots \\ \mathbf{0} & \mathbf{0} & \cdots & \mathbf{M}_N \end{bmatrix} \tag{3.36}$$

is the generalized *extended* mass matrix of the system and $\dot{\mathbf{v}}, \boldsymbol{\phi}^E, \boldsymbol{\phi}^S$, and $\boldsymbol{\phi}^C$ represent the generalized extended acceleration vector, the generalized extended external, system, and constraint forces, respectively:

$$\dot{\mathbf{v}} = \begin{Bmatrix} \dot{\mathbf{v}}_1 \\ \dot{\mathbf{v}}_2 \\ \vdots \\ \dot{\mathbf{v}}_N \end{Bmatrix} \; ; \; \boldsymbol{\phi}^E = \begin{Bmatrix} \boldsymbol{\phi}_1^E \\ \boldsymbol{\phi}_2^E \\ \vdots \\ \boldsymbol{\phi}_N^E \end{Bmatrix} \; ; \; \boldsymbol{\phi}^S = \begin{Bmatrix} \boldsymbol{\phi}_1^S \\ \boldsymbol{\phi}_2^S \\ \vdots \\ \boldsymbol{\phi}_N^S \end{Bmatrix} \; ; \; \boldsymbol{\phi}^C = \begin{Bmatrix} \boldsymbol{\phi}_1^C \\ \boldsymbol{\phi}_2^C \\ \vdots \\ \boldsymbol{\phi}_N^C \end{Bmatrix} \tag{3.37}$$

The kinematic constraints acting at joints between adjacent links can be derived from linear and angular velocity constraint relations which can be written in the following compact form:

$$\mathbf{A}\mathbf{v} = \mathbf{0} \tag{3.38}$$

where **A** is the kinematic velocity constraint matrix, and **0** is a zero vector.

It is preferable to express the equations of motion in term of a minimum set of independent generalized coordinates, which can be defined as follows:

$$\boldsymbol{\psi} = \{\boldsymbol{\psi}_1^T \;\; \boldsymbol{\psi}_2^T \;\; \cdots \;\; \boldsymbol{\psi}_N^T\}^T \tag{3.39}$$

where $\boldsymbol{\psi}_1$ represents the spacecraft's attitude degrees of freedom, for example, pitch, yaw, and roll. For the remaining $N-1$ bodies, $\boldsymbol{\psi}_i$ for a flexible body i which is linked to the preceding body by a revolute joint can be written as:

$$\boldsymbol{\psi}_i = \{\theta_i \;\; \mathbf{b}_i^T\}^T \tag{3.40}$$

Using kinematic relations (3.13) and (3.14), the generalized extended velocity **v** can be expressed in terms of the independent generalized velocities $\dot{\boldsymbol{\psi}}$ as

$$\mathbf{v} = \mathbf{N}\dot{\boldsymbol{\psi}} \tag{3.41}$$

Upon substitution of equation (3.41) into equation (3.38), we obtain

$$\mathbf{A}\mathbf{N}\dot{\boldsymbol{\psi}} = \mathbf{0} \tag{3.42}$$

This relation must hold for any vector $\dot{\boldsymbol{\psi}}$, hence,

$$\mathbf{A}\mathbf{N} = \mathbf{0}^* \tag{3.43}$$

where $\mathbf{0}^*$ is a zero matrix. By virtue of the above relationship, **N** is called the Natural Orthogonal Complement of the velocity constraint matrix **A**.

By definition, the constraint forces $\boldsymbol{\phi}^C$ do zero work, i.e., they do not introduce any power onto the system. Hence,

$$\Pi = \mathbf{v}^T\boldsymbol{\phi}^C = 0 \tag{3.44}$$

$$\text{i.e.,}\quad \Pi = \dot{\boldsymbol{\psi}}^T\mathbf{N}^T\boldsymbol{\phi}^C = 0 \tag{3.45}$$

Since $\dot{\boldsymbol{\psi}}$ is an independent vector, it follows that

$$\mathbf{N}^T\boldsymbol{\phi}^C = \mathbf{0} \tag{3.46}$$

Furthermore, differentiating equation (3.41), $\dot{\mathbf{v}}$ can be obtained as follows:

$$\dot{\mathbf{v}} = \mathbf{N}\ddot{\boldsymbol{\psi}} + \dot{\mathbf{N}}\dot{\boldsymbol{\psi}} \tag{3.47}$$

Pre-multiplying equation (3.35) by $\mathbf{N}^T$, the constraint forces can be eliminated by virtue of equation (3.46); then using equation (3.47) the independent dynamical equation of motion of the multi-body system can be expressed as follows:

$$\tilde{\mathbf{M}}\ddot{\boldsymbol{\psi}} = \mathbf{c}(\boldsymbol{\psi}, \dot{\boldsymbol{\psi}}) + \mathbf{f} \tag{3.48}$$

where

$$\tilde{\mathbf{M}} = \mathbf{N}^T\mathbf{M}\mathbf{N} \tag{3.49}$$

$$\mathbf{c} = \mathbf{N}^T[\boldsymbol{\phi}_S - \mathbf{M}\dot{\mathbf{N}}\dot{\boldsymbol{\psi}}] \tag{3.50}$$

$$\mathbf{f} = \mathbf{N}^T\boldsymbol{\phi}^E \tag{3.51}$$

Here, $\tilde{\mathbf{M}}$ is the generalized mass matrix of the system, which is symmetric and positive definite. Vector $\mathbf{f}$ represents the generalized external forces, and the vector $\mathbf{c}$ contains the Coriolis, centrifugal, stiffness, and damping terms.

If forces are applied at the tip of the multi-body system (e.g., the end-effector of a manipulator), then the equations of motion may be rewritten as

$$\tilde{\mathbf{M}}\ddot{\boldsymbol{\psi}} = \mathbf{c}(\boldsymbol{\psi}, \dot{\boldsymbol{\psi}}) + \mathbf{f} + \mathbf{P}^T\boldsymbol{\lambda} \tag{3.52}$$

where $\boldsymbol{\lambda}$ represents a vector of forces and moments in Cartesian coordinates associated with applied loads and $\mathbf{P}$ is the system Jacobian, which can be expressed as

$$\mathbf{P} = \begin{bmatrix} \mathbf{P}_1 \\ \mathbf{P}_2 \end{bmatrix} \tag{3.53}$$

where

$$\mathbf{P}_1 = \begin{bmatrix} \frac{\partial \mathbf{p}_h}{\partial \boldsymbol{\psi}_1} & \frac{\partial \mathbf{p}_h}{\partial \boldsymbol{\psi}_2} & \cdots & \frac{\partial \mathbf{p}_h}{\partial \boldsymbol{\psi}_N} \end{bmatrix} \tag{3.54}$$

$$\mathbf{P}_2 = \begin{bmatrix} \frac{\partial \boldsymbol{\omega}_h}{\partial \dot{\boldsymbol{\psi}}_1} & \frac{\partial \boldsymbol{\omega}_h}{\partial \dot{\boldsymbol{\psi}}_2} & \cdots & \frac{\partial \boldsymbol{\omega}_h}{\partial \dot{\boldsymbol{\psi}}_N} \end{bmatrix} \tag{3.55}$$

and $\mathbf{p}_h$ and $\boldsymbol{\omega}_h$ are the position and angular velocity vectors of the tip with respect to the base of the multi-body/manipulator system.

Chapter 4

Integration of System Equations

4.1 Introduction

The goal of this chapter is to describe the integration of general multibody systems of arbitrary kinematic architecture as shown in Figure 4.1. The whole system is made up of *subsystems* each of which may be a contacting body or a multi-body system of serial- or tree-type kinematic chains and open- or closed-loop configurations. The equations of motion for contacting bodies are derived in Chapter 2 and expressed in the form of equations (2.74) and (2.75) and those for multi-body systems are presented in Chapter 3 and expressed in the form of equation (3.52). Different constraint relationships are associated with each *subsystem*. Constraints which result from the *impenetrability* condition when one body contacts another are generally temporary and time-dependent because the contact surface may be in sticking or sliding contact, its geometry and area may change, or may completely separate. Such constraints are hereafter referred to as **contact constraints**. On the other hand, constraints existing at joints between subsystems (such as the joint connecting the end-effector and a manipulator system) are permanent and depend on the particular kinematic architecture of a system. Such constraints will be referred to as **kinematic constraints**. A *subsystem*, whether a contacting body or a multi-body system, may be constrained by either or both of these two types of constraints. Letting N and n be respectively the number of subsystems and constraint relations of a system, the equations of motion of each subsystem and associated constraints can be recast in the following general form:

$$\mathbf{M}_i\ddot{\mathbf{q}}_i + \mathbf{C}_i\dot{\mathbf{q}}_i + \mathbf{K}_i\mathbf{q}_i + \mathbf{c}_i(\mathbf{q}_i, \dot{\mathbf{q}}_i) + \sum_{j=1}^{n} \mathbf{P}_{ji}^T \boldsymbol{\lambda}_j = \mathbf{f}_i, \quad i = 1 \cdots N \tag{4.1}$$

with the constraint relations given by

$$\mathbf{g}_k = f(\mathbf{q}_{r_k}, \mathbf{q}_{s_k}) = \mathbf{p}_{r_k}(\mathbf{q}_{r_k}) - \mathbf{p}_{s_k}(\mathbf{q}_{s_k}) = \mathbf{0}, \quad k = 1 \cdots n \tag{4.2}$$

where r_k and s_k are the two subsystems which are involved in the k-th constraint, and $\mathbf{p}_{r_k}$ and $\mathbf{p}_{s_k}$ are the respective position vectors of the point of application of the k-th constraint expressed in $\mathbf{q}_{r_k}$ and $\mathbf{q}_{s_k}$ coordinates. If subsystem i is a multi-body system, the stiffness and dissipative forces may be taken out of the nonlinear force vector $\mathbf{c}$ in equation (3.52) and expressed separately as done in equation (4.1). In equation (4.1)

$$\text{if } \ i = r_j, s_j \ \text{ then } \ \mathbf{P}_{ji} = \frac{\partial \mathbf{g}_j}{\partial \mathbf{q}_i}, \quad \text{else } \ \mathbf{P}_{ji} = \mathbf{0} \tag{4.3}$$

In other words, matrix $\mathbf{P}_{ji}$ exists only if subsystem i is involved in the j-th constraint; otherwise it is zero.

When k stands for a constraint corresponding to contact, equation (4.2) is a **contact constraint** and expresses the basic contact condition of no material overlap, and both $\mathbf{g}_k$ and $\mathbf{P}_{ki}$ depend on those time-dependent conditions such as which nodes are in contact and which of these nodes are in sticking or sliding friction. However, this information is not known *a priori*; thus the solution procedure is iterative (Bathe & Chaudhary 1985, Chaudhary & Bathe 1986). This procedure is described in detail in the following sections.

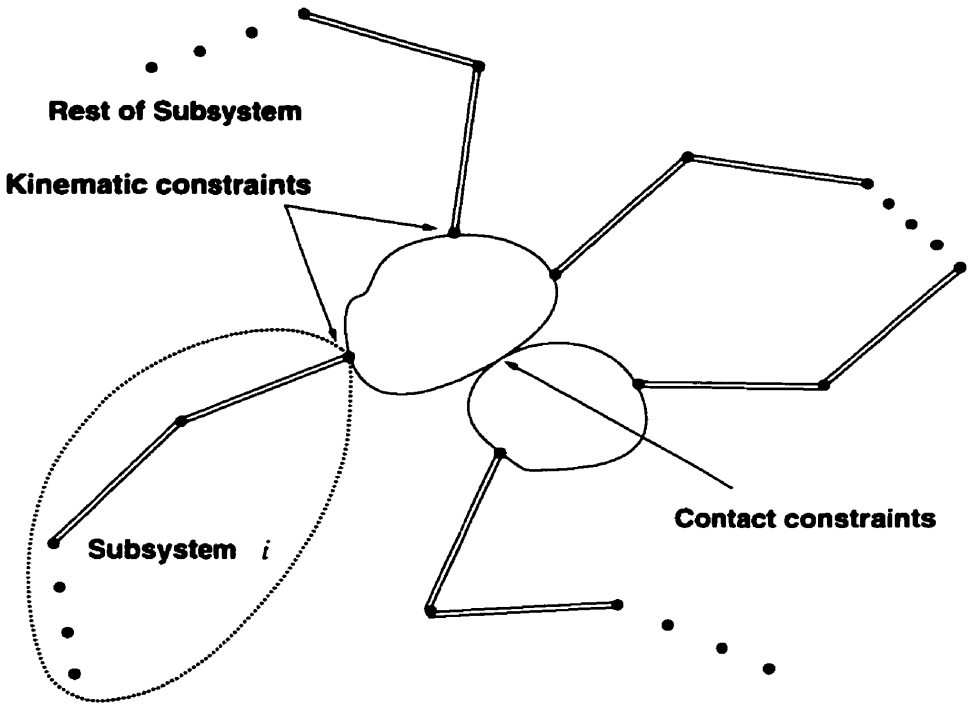

Figure 4.1: General multibody systems in contact

4.2 Full Solution of Equations of Motion

4.2.1 Time Integration

The differential equations of motion given by equation (4.1) are nonlinear and may be *stiff* [*], such that an integration method which efficiently takes these characteristics into account such as *Gear's* method would be ideal. However, due to the large number of equations which are usually encountered in finite element analysis, a computationally less expensive route offered by the *Newmark* method is used here. In this method, the following propagation schemes are used:

$$\dot{\mathbf{q}}_{t+\Delta t} = \dot{\mathbf{q}}_t + [(1-\delta)\ddot{\mathbf{q}}_t + (\delta)\ddot{\mathbf{q}}_{t+\Delta t}]\Delta t \tag{4.4}$$

$$\mathbf{q}_{t+\Delta t} = \mathbf{q}_t + \dot{\mathbf{q}}_t\Delta t + [(\frac{1}{2}-\alpha)\ddot{\mathbf{q}}_t + \alpha\ddot{\mathbf{q}}_{t+\Delta t}]\Delta t^2 \tag{4.5}$$

where α and δ are parameters that can be selected to obtain integration accuracy and stability. The Newmark method is a *direct implicit* integration algorithm which

---

[*] A system is said to be stiff if the ratio between its largest and smallest eigenvalues is large.

is unconditionally stable and introduces no artificial damping if $\alpha \geq 1/4$ and $\delta = 1/2$ are used. It was shown by Chaudhary & Bathe (1986) that $\alpha = 1/2$ and $\delta = 1/2$ are effective choices for time integration of dynamic contact equations because both the criteria of energy and momentum conservation are satisfied by the solution, provided that the time step employed, Δt, is sufficiently small.

Using these two equations (4.4) and (4.5), $\ddot{\mathbf{q}}_{t+\Delta t}$ and $\dot{\mathbf{q}}_{t+\Delta t}$ can be expressed in terms of the unknown displacement vector $\mathbf{q}_{t+\Delta t}$ only. Therefore, these expressions of $\ddot{\mathbf{q}}_{t+\Delta t}$ and $\dot{\mathbf{q}}_{t+\Delta t}$ can now be substituted into the differential equations (4.1) and converted into algebraic ones:

$$\hat{\mathbf{K}}_{i(t+\Delta t)}\mathbf{q}_{i(t+\Delta t)} + \sum_{j=1}^{n} \mathbf{P}^T_{ji(t+\Delta t)}\boldsymbol{\lambda}_{j(t+\Delta t)} = \hat{\mathbf{r}}_{i(t+\Delta t)}, \quad i = 1 \cdots N \tag{4.6}$$

where

$$\hat{\mathbf{K}}_{i(t+\Delta t)} = \mathbf{K}_{i(t+\Delta t)} + a_0\mathbf{M}_{i(t+\Delta t)} + a_1\mathbf{C}_{i(t+\Delta t)} \tag{4.7}$$

$$\begin{aligned}\hat{\mathbf{r}}_{i(t+\Delta t)} &= \mathbf{f}_{i(t+\Delta t)} + \mathbf{M}_i(a_0\mathbf{q}_{i(t)} + a_2\dot{\mathbf{q}}_{i(t)} + a_3\ddot{\mathbf{q}}_{i(t)}) \\ &\quad + \mathbf{C}_i(a_1\mathbf{q}_{i(t)} + a_4\dot{\mathbf{q}}_{i(t)} + a_5\ddot{\mathbf{q}}_{i(t)}) - \mathbf{c}_{i(t+\Delta t)}\end{aligned} \tag{4.8}$$

and $a_0, \cdots, a_7$ are Newmark integration parameters given by

$$\begin{aligned} &a_0 = \frac{1}{\alpha\Delta t^2}; \quad a_1 = \frac{\delta}{\alpha\Delta t}; \quad a_2 = \frac{1}{\alpha\Delta t}; \quad a_3 = \frac{1}{2\alpha} - 1; \\ &a_4 = \frac{\delta}{\alpha} - 1; \quad a_5 = \frac{\Delta t}{2}(\frac{\delta}{\alpha} - 2); \quad a_6 = \Delta t(1-\delta); \quad a_7 = \delta\Delta t \end{aligned}$$

4.2.2 Solution of a System of Nonlinear Equations

Both equations (4.2) and (4.6) are now in algebraic form but are nonlinear. These nonlinearities are introduced not only by the term $\mathbf{c}_{i(t+\Delta t)}$ appearing in $\hat{\mathbf{r}}_{i(t+\Delta t)}$ of equation (4.8), but also by the nonlinear nature of the contact problem: boundary conditions at the contact surface change during the motion of the contact body under consideration, and these conditions are not known *a priori*. Therefore, a nonlinear solver must be used to solve for unknown vectors $\mathbf{q}_{i(t+\Delta t)}$ and $\boldsymbol{\lambda}_{j(t+\Delta t)}$ from equations

(4.6) and (4.2). The Newton-Raphson method is chosen to carry out this task. This method is an iterative algorithm which attempts to find the solution of a nonlinear algebraic equation of the form given by

$$\mathbf{h}(\mathbf{x}) = \mathbf{0} \tag{4.9}$$

Assuming that in the iterative solution we have evaluated $\mathbf{x}^{(i-1)}$, then a Taylor series expansion gives

$$\mathbf{h}(\mathbf{x}^{i}) = \mathbf{h}(\mathbf{x}^{(i-1)}) + \left.\frac{\partial \mathbf{h}}{\partial \mathbf{x}}\right|_{\mathbf{x}^{(i-1)}} \Delta\mathbf{x}^{(i)} = \mathbf{0} \tag{4.10}$$

or

$$\left.\frac{\partial \mathbf{h}}{\partial \mathbf{x}}\right|_{\mathbf{x}^{(i-1)}} \Delta\mathbf{x}^{(i)} = -\mathbf{h}(\mathbf{x}^{(i-1)}) \tag{4.11}$$

where higher order terms were neglected and

$$\Delta\mathbf{x}^{(i)} = \mathbf{x}^{(i)} - \mathbf{x}^{(i-1)}$$

By expressing equations (4.6) in the form of equation (4.9) we have

$$\hat{\mathbf{f}}_{i(t+\Delta t)} = \hat{\mathbf{K}}_{i(t+\Delta t)}\mathbf{q}_{i(t+\Delta t)} + \sum_{j=1}^{n} \mathbf{P}^{T}_{ji(t+\Delta t)}\boldsymbol{\lambda}_{j(t+\Delta t)} - \hat{\mathbf{r}}_{i(t+\Delta t)} = \mathbf{0}, \quad i = 1 \cdots N \tag{4.12}$$

The Newton-Raphson method can now be applied. However, for the above equations, it is not easy to evaluate the derivative term $\frac{\partial \mathbf{h}}{\partial \mathbf{x}}$ in equation (4.11). But since the Newton-Raphson method is an iterative procedure (reason for which higher order terms in the Taylor series are neglected), it is not absolutely necessary to obtain the derivative exactly. An approximate term will also work although at the cost of slower convergence. Also, with this approach, care must be taken so that the approximated derivative is close enough to the exact one such that the solution does not diverge. Some assumptions are now made to facilitate the computation of the derivative term. The matrices and vectors in equations (4.2) and (4.12) which are dependent on the unknown variables $\mathbf{q}_i$ are:

$$\hat{\mathbf{K}}_i(\mathbf{q}_i), \quad \hat{\mathbf{r}}_i(\mathbf{q}_i, \dot{\mathbf{q}}_i), \quad \mathbf{P}_{ki}(\mathbf{q}_{r_k}, \mathbf{q}_{s_k}), \quad \mathbf{p}_{r_k}(\mathbf{q}_{r_k}), \quad \mathbf{p}_{s_k}(\mathbf{q}_{s_k})$$

It is assumed that all the above vectors and matrices are "weakly" dependent such that they may be considered constant during $t \rightarrow t + \Delta t$, except vectors $\mathbf{p}_{r_k}$ and $\mathbf{p}_{s_k}$ whose derivative terms are $\mathbf{P}_{ki}$, $(i = r_k, s_k)$. With this assumption, we can now apply the Newton-Raphson method for the l-th iteration as given by equation (4.11). Omitting the subscript $t + \Delta t$, equations (4.6) and (4.2) may be expressed as:

$$\hat{\mathbf{K}}_i^{l-1}\Delta\mathbf{q}_i^l + \sum_{j=1}^{n} \mathbf{P}_{ji}^{l-1^T}\Delta\boldsymbol{\lambda}_j^l = -\hat{\mathbf{f}}_i^{l-1}, \quad i = 1\cdots N \tag{4.13}$$

$$\mathbf{P}_{kr_k}^{l-1}\Delta\mathbf{q}_{r_k}^l + \mathbf{P}_{ks_k}^{l-1}\Delta\mathbf{q}_{s_k}^l = -\mathbf{g}_k^{l-1}, \quad k = 1\cdots n \tag{4.14}$$

Equations (4.13) and (4.14) may now be solved simultaneously. It follows from equation (4.7) that since matrix $\mathbf{M}_i$ is positive definite, and $\mathbf{K}_i$ and $\mathbf{C}_i$ are positive semi-definite, $\hat{\mathbf{K}}_i$ results in a positive definite matrix. An efficient method which exploits the symmetry and positive definiteness of the $\hat{\mathbf{K}}_i$ matrices is now presented.

The efficient Cholesky Decomposition is used to invert the $\hat{\mathbf{K}}_i$ matrices in equation (4.13):

$$\Delta\mathbf{q}_i = -\hat{\mathbf{K}}_i^{-1}\left(\sum_{j=1}^{n} \mathbf{P}_{ji}^T\Delta\boldsymbol{\lambda}_j + \hat{\mathbf{f}}_i\right), \quad i = 1\cdots N \tag{4.15}$$

where the superscript l was removed for convenience. Inserting the above equation for $i = r_k$ and $i = s_k$ into equation (4.14), the resulting equation can be expressed in the form given by

$$\sum_{j=1}^{n} \bar{\mathbf{R}}_{kj}\Delta\boldsymbol{\lambda}_j = \hat{\mathbf{g}}_k, \quad k = 1\cdots n \tag{4.16}$$

where

$$\bar{\mathbf{R}}_{kj} = \mathbf{P}_{kr_k}\hat{\mathbf{K}}_{r_k}^{-1}\mathbf{P}_{jr_k}^T + \mathbf{P}_{ks_k}\hat{\mathbf{K}}_{s_k}^{-1}\mathbf{P}_{js_k}^T \tag{4.17}$$

$$\hat{\mathbf{g}}_k = \mathbf{g}_k - \mathbf{P}_{kr_k}\hat{\mathbf{K}}_{r_k}^{-1}\hat{\mathbf{f}}_{r_k} - \mathbf{P}_{ks_k}\hat{\mathbf{K}}_{s_k}^{-1}\hat{\mathbf{f}}_{s_k} \tag{4.18}$$

Equation (4.17) is expressed in a general form. In light of equation (4.3), the following observations can be made about $\bar{\mathbf{R}}_{kj}$. If $k = j$ then both terms on the right hand side of equation (4.17) exist, thus

$$\bar{\mathbf{R}}_{kk} = \mathbf{P}_{kr_k}\hat{\mathbf{K}}_{r_k}^{-1}\mathbf{P}_{kr_k}^T + \mathbf{P}_{ks_k}\hat{\mathbf{K}}_{s_k}^{-1}\mathbf{P}_{ks_k}^T \tag{4.19}$$

If $k \neq j$ then either one or both terms will be equal to zero. One term will be nonzero if either r_k or s_k is equal to either r_j or s_j; in other words, a common subsystem is involved in the k-th and j-th constraint equations. Denoting the common subsystem by c_{kj},

$$\begin{aligned} \text{if } c_{kj} \text{ exists, then } \bar{\mathbf{R}}_{kj} &= \mathbf{P}_{kc_{kj}} \hat{\mathbf{K}}_{c_{kj}}^{-1} \mathbf{P}_{jc_{kj}}^{T} \\ \text{else } \bar{\mathbf{R}}_{kj} &= \mathbf{0}. \end{aligned} \tag{4.20}$$

Equation (4.16) may also be expressed in the following matrix form:

$$\bar{\mathbf{R}} \Delta \boldsymbol{\lambda} = \hat{\mathbf{g}} \tag{4.21}$$

where

$$\Delta\boldsymbol{\lambda} = \begin{Bmatrix} \Delta\boldsymbol{\lambda}_1 \\ \Delta\boldsymbol{\lambda}_2 \\ \vdots \\ \Delta\boldsymbol{\lambda}_n \end{Bmatrix} \; ; \; \hat{\mathbf{g}} = \begin{Bmatrix} \hat{\mathbf{g}}_1 \\ \hat{\mathbf{g}}_2 \\ \vdots \\ \hat{\mathbf{g}}_n \end{Bmatrix} \; ; \; \bar{\mathbf{R}} = \begin{bmatrix} \bar{\mathbf{R}}_{11} & \bar{\mathbf{R}}_{12} & \cdots & \bar{\mathbf{R}}_{1n} \\ \bar{\mathbf{R}}_{21} & \bar{\mathbf{R}}_{22} & \cdots & \bar{\mathbf{R}}_{2n} \\ \vdots & \vdots & \ddots & \vdots \\ \bar{\mathbf{R}}_{n1} & \bar{\mathbf{R}}_{n2} & \cdots & \bar{\mathbf{R}}_{nn} \end{bmatrix}$$

It turns out that matrix $\bar{\mathbf{R}}$ is both symmetric and positive definite: the proofs are presented in Appendix B. Thus, the $\Delta\boldsymbol{\lambda}_i$'s can be obtained from equation (4.21) by the inversion of $\bar{\mathbf{R}}$ using Cholesky Decomposition, and the $\Delta\mathbf{q}_i$'s can then be obtained from equation (4.15). Then, variables for the l-th iteration may be updated to

$$\mathbf{q}_i^l = \mathbf{q}_i^{l-1} + \Delta\mathbf{q}_i^l, \quad i = 1 \cdots N \tag{4.22}$$

$$\boldsymbol{\lambda}_k^l = \boldsymbol{\lambda}_k^{l-1} + \Delta\boldsymbol{\lambda}_k^l, \quad k = 1 \cdots n \tag{4.23}$$

The acceleration and velocity terms of each subsystem at $t + \Delta t$ are calculated by rearranging the Newmark propagation schemes (4.4) and (4.5), such that,

$$\ddot{\mathbf{q}}_{i(t+\Delta t)} = a_0(\mathbf{q}_{i(t+\Delta t)} - \mathbf{q}_{i(t)}) - a_2\dot{\mathbf{q}}_{i(t)} - a_3\ddot{\mathbf{q}}_{i(t)}, \quad i = 1 \cdots N \tag{4.24}$$

$$\dot{\mathbf{q}}_{i(t+\Delta t)} = \dot{\mathbf{q}}_{i(t)} + a_6\ddot{\mathbf{q}}_{i(t)} + a_7\ddot{\mathbf{q}}_{i(t+\Delta t)}, \quad i = 1 \cdots N \tag{4.25}$$

4.2.3 Updated Contact Conditions after Iteration $l-1$

The contact conditions after iteration $l-1$, represented by the constraint vector $\mathbf{g}_\tau^{l-1}$, the contact matrix $\mathbf{P}_{\tau i}^{l-1}$ and the contact force vector $\boldsymbol{\gamma}_\tau^{l-1}$ given by

$$\boldsymbol{\gamma}_\tau^{l-1} = \mathbf{P}_{\tau i}^{l-1^T} \boldsymbol{\lambda}_\tau^{l-1} \tag{4.26}$$

where τ denotes a contact constraint and i a contacting body, are included in equations (4.13) and (4.14). It is discussed by Chaudhary & Bathe (1986) that the direct use of these contact conditions can lead to serious errors of linearization. Furthermore, it is also argued that although the decision on whether a *contactor* node is releasing or is in sticking or sliding conditions is perhaps most quickly determined based on considering the total and relative magnitudes of the calculated nodal point forces, this method can lead to some numerical difficulties. It is deemed more effective to establish the condition at a *contactor* node from the accumulated effects and conditions of the *contactor* segments adjacent to the node. Then, a new set of updated contact conditions is obtained by the following procedure:

- The distributed segment tractions, $\mathbf{T}$, are recovered on the *contactor* surface such that they are equivalent (in the virtual work sense) to the nodal contact forces, $\boldsymbol{\gamma}_\tau^{l-1}$.

- New distributed segment tractions, $\bar{\mathbf{T}}$, are updated to satisfy Coulomb's law of friction, which is further discussed in Section 4.2.4. The updated *contactor* surface nodal forces, $\bar{\boldsymbol{\gamma}}_\tau^{l-1}$, are obtained as consistent nodal loads corresponding to the updated segment tractions. The updated states of *contactor* nodes, represented by sticking, sliding and tension release, are determined based on the states of adjoining *contactor* segments. These updated nodal states are then used to obtain the updated constraint vector and contact matrix, $\bar{\mathbf{g}}_\tau^{l-1}$ and $\bar{\mathbf{P}}_{\tau i}^{l-1}$.

- The corresponding *target* surface updated nodal contact forces are obtained from the *contactor* surface updated nodal forces by considering static equilibrium of the contact region (as described in Section 2.4).

The above procedure for updating the contact conditions is presented in detail for the two-dimensional and the general three-dimensional cases in Appendix C. These updated contact conditions, namely $\bar{\mathbf{g}}_{\tau}^{l-1}$ and $\bar{\mathbf{P}}_{\tau i}^{l-1}$ and $\bar{\gamma}_{\tau}^{l-1}$, are incorporated into equations (4.13) and (4.14) before proceeding with the l-th iteration.

4.2.4 Contact Friction

In some previous work on friction (Karnopp 1985, Haessig & Friedland 1991), it was decided that the best friction model was one which assigns a certain small region of velocity $-v_h < v < v_h$, such that if the relative velocity between two sliding bodies falls inside this region, the sliding friction switches to sticking and $v = 0$. This model is not only amenable to computational treatment but also accounts for the discontinuous manner in which real systems become stuck. Then, when the sticking friction force becomes greater than the limiting friction force f_h, the friction mode switches back to sliding. Thus, it is assumed here that the decision from sliding to sticking is solely dependent on the velocity v_h, which may be found experimentally. This model may be accurate enough for simple bodies subject to friction, but for complicated systems where the normal force and contact area change over time, the limiting velocity v_h may depend on these and other factors as well, such that it is no longer safe to predetermine a constant value of v_h. Therefore, a different model is proposed here, as described below.

At every time step, where the system may be in sticking or sliding contact, a test is done and the force which will bring the system to a sticking contact for the current time step is calculated. If this calculated force is greater than the limiting friction force f_h, then the system is sliding, if not then sticking. This model can be thought to be similar to the previous models except that the concept of the limiting velocity v_h is only implicitly used, and this value is dependent on the various dynamic conditions of the system such as acceleration, velocity, normal force, and contact area. This model is used to simulate the dynamics of a simple system undergoing friction, and the results are compared with those found in previous work. The system is illustrated in Figure 4.2, where $m = 0.1kg$ and $K = 100N/m$. The nominal and constant sliding friction force is chosen as $0.2N$ and the limiting sticking friction force as $0.25N$. The system is initially at rest and the point P undergoes motion as $x_0(t) = v_0 t$, where $v_0 = 0.002m/s$. The results for the motion and friction force of mass m are shown in Figure 4.3. For this simple system, both the proposed model and previous models (such as Karnopp and the bristle models (Haessig & Friedland 1991)) yield similar results. However, in this system neither normal force nor contact area are time-dependent. For the proposed model, if, for example, the normal force changes for the same mass (as in impact dynamics), the limiting velocity v_h will adjust itself *online* and become larger as the force becomes larger, which is in agreement with intuition. Changes in other parameters which become a factor in friction can be accounted for in the same way. In previous models, v_h will have to be found experimentally every time these parameters change and must be done *off-line*.

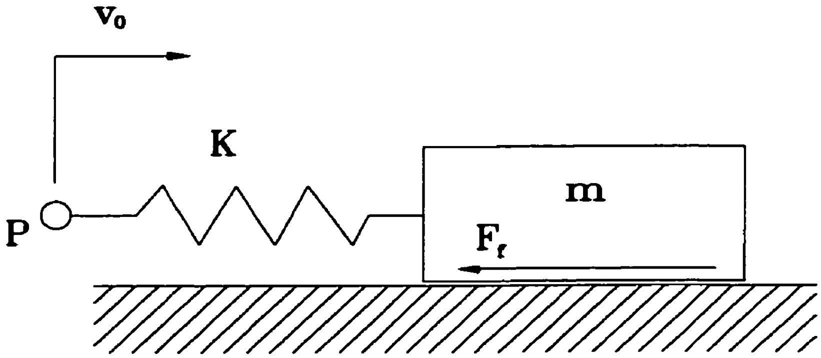

Figure 4.2: Single body in friction

Another issue of interest in modelling friction is how to represent the transitional phases when friction changes from sticking to sliding and when the relative sliding velocity changes sign. The classical friction model shown in Figure (4.4 a) shows the friction force and direction changing instantaneously at $v = 0$. However, in reality they cannot change instantaneously but must occur over a finite period of time, though this duration may be extremely small. This transitional period of time

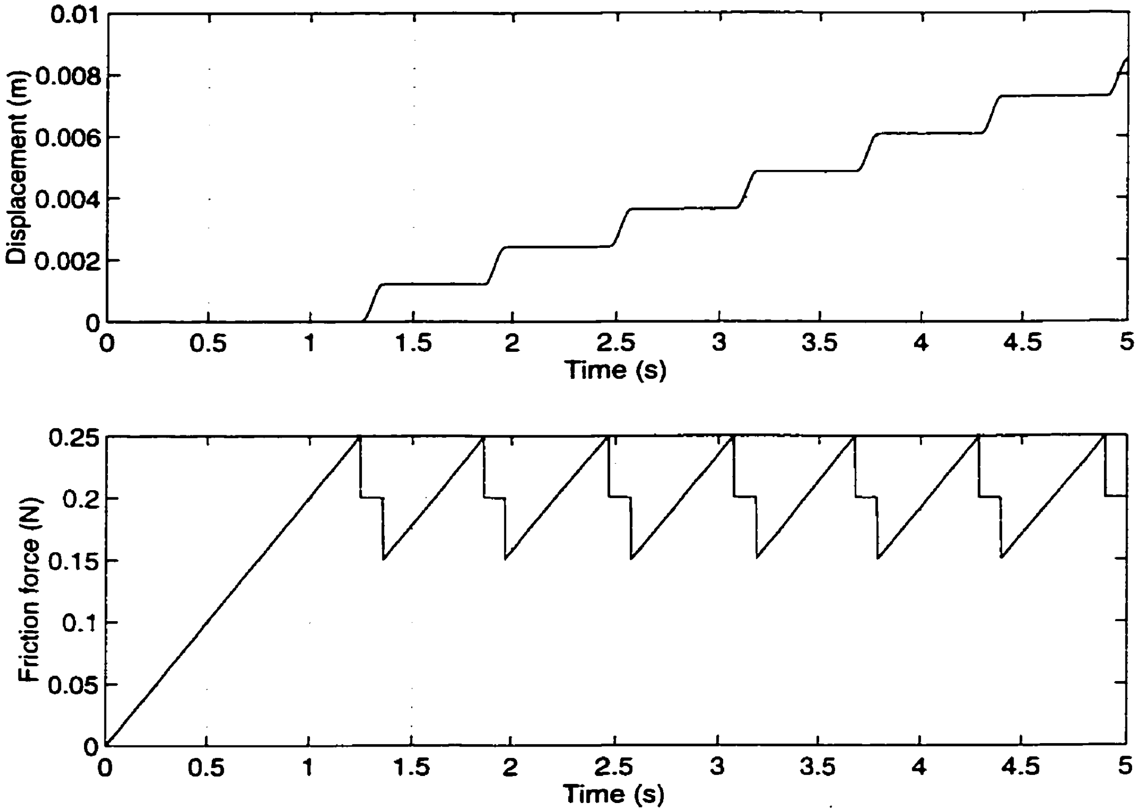

Figure 4.3: The motion and friction force of the mass

should be modelled not only for physical accuracy but also for numerical stability. Changes during this transition ($-v_s < v < v_s$) are represented linearly as shown in Figure (4.4 b). Four regions or modes of friction can be identified: (0) is the sticking region, (1) is the sliding region of transition from sticking to sliding, (2) is the sliding region, and (3) is the sliding region of transition when the relative velocity changes sign. Switches from one region to another must follow some rules. For example, the friction mode may switch from the sticking region (0) to sliding region (1) but not to region (3). With a view to a systematic procedure, some rules are defined. From the proposed model discussed above one may infer that the friction mode can switch from any region to region (0), i.e., sticking is allowed from any sliding region as long as the test for stiction (discussed above) is satisfied. Furthermore, the rules presented in Table (4.1) also apply.

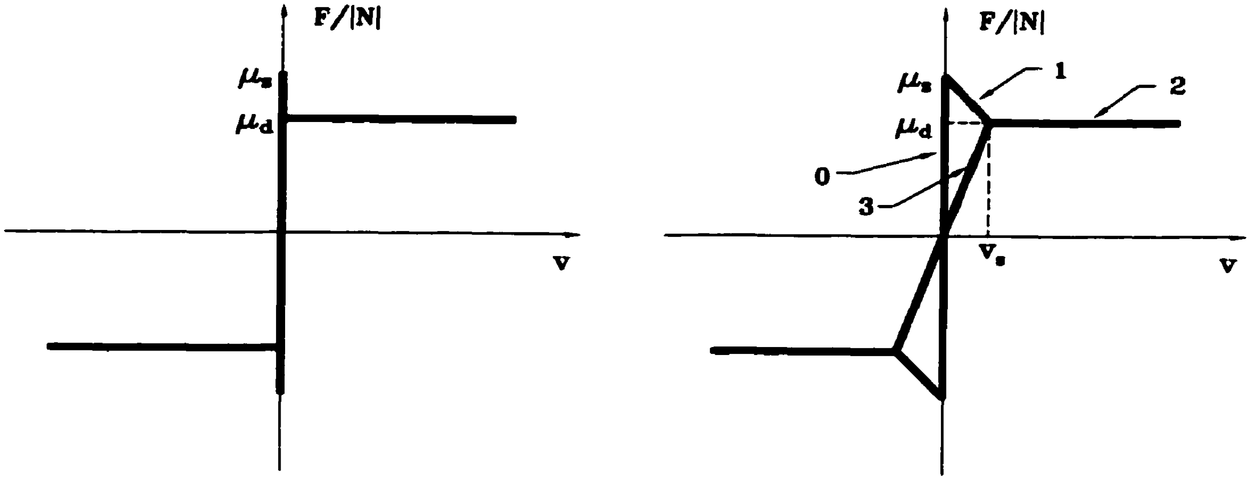

(a) (b)

Figure 4.4: Two friction models: (a) Classical, (b) Proposed

Table 4.1: Rules on switching from one region to another

From region	Allowed to go to region
0	0, 1
1	0, 1, 2
2	0, 2, 3
3	0, 2, 3

4.2.5 Convergence Criteria

Convergence of solution is accepted after iteration l if the following criteria are simultaneously satisfied:

- **Energy convergence criterion**. The energy due to the unbalanced force at iteration l is small in comparison to the energy at first iteration:

$$\frac{\Delta\mathbf{q}_i^{l^T}\{\mathbf{M}_i\ddot{\mathbf{q}}_i^{l-1}+\mathbf{C}_i\dot{\mathbf{q}}_i^{l-1}+\mathbf{K}_i\mathbf{q}_i^{l-1}+\mathbf{c}_i(\mathbf{q}_i,\dot{\mathbf{q}}_i)^{l-1}+\sum\mathbf{P}_{ji}^T\boldsymbol{\lambda}_j^{l-1}-\mathbf{f}_i\}}{\Delta\mathbf{q}_i^{1^T}\{\mathbf{M}_i\ddot{\mathbf{q}}_i^{1}+\mathbf{C}_i\dot{\mathbf{q}}_i^{1}+\mathbf{K}_i\mathbf{q}_i^{1}+\mathbf{c}_i(\mathbf{q}_i,\dot{\mathbf{q}}_i)^{1}+\sum\mathbf{P}_{ji}^T\boldsymbol{\lambda}_j^{1}-\mathbf{f}_i\}}=\epsilon_E \quad (4.27)$$

- **Force convergence criterion.** The Euclidean norm of the unbalanced force is small in comparison to that of the total external load:

$$\frac{||\mathbf{M}_i\ddot{\mathbf{q}}_i^{l-1} + \mathbf{C}_i\dot{\mathbf{q}}_i^{l-1} + \mathbf{K}_i\mathbf{q}_i^{l-1} + \mathbf{c}_i(\mathbf{q}_i, \dot{\mathbf{q}}_i)^{l-1} + \sum \mathbf{P}_{ji}^T\boldsymbol{\lambda}_j^{l-1} - \mathbf{f}_i||}{||\sum \mathbf{P}_{ji}^T\boldsymbol{\lambda}_j^{l-1} - \mathbf{f}_i||} = \epsilon_F \qquad (4.28)$$

- **Contact force convergence criterion.** The change in the contact force vector prior to updating, $\boldsymbol{\gamma}$, is small:

$$\frac{||\boldsymbol{\gamma}^{l-1} - \boldsymbol{\gamma}^{l-2}||}{||\boldsymbol{\gamma}^{l-1} + 0.001||} = \epsilon_C \qquad (4.29)$$

Constants ϵ_E, ϵ_F and ϵ_C are the energy, force and contact force convergence tolerances, respectively. In equation (4.29), a small number of 0.001 makes the denominator non-zero in case no contact conditions exist during iteration $l-1$.

4.3 Simplified Solutions of Equations for Contacting Bodies

4.3.1 Efficient Computation of the Inverse of Matrix $\hat{\mathbf{K}}$

The inverse of matrix $\hat{\mathbf{K}}_i$ in equation (4.15), where i belongs to a contacting body and henceforth omitted for brevity, can be computed using 3 methods. The first method is the simple inversion of the positive definite and symmetric matrix $\hat{\mathbf{K}}$ using the Cholesky Decomposition (CD). This procedure requires about $C_1 = n_t^3/6$ operations where n_t is the order of the matrix to be inverted. It is therefore computationally quite expensive.

To formulate the second and third methods, matrices **M**, **K** and **C** can be recast, using the partitioned representation of equations (2.17)–(2.27), (2.38), and (2.51), as follows:

$$\mathbf{M} = \begin{bmatrix} \mathbf{T} & \mathbf{0}_{ou} \\ \mathbf{0}_{ou}^T & \mathbf{I}_{uu} \end{bmatrix} \begin{bmatrix} \bar{\mathbf{M}}_{oo} & \bar{\mathbf{M}}_{ou} \\ \bar{\mathbf{M}}_{ou}^T & \mathbf{M}_{uu} \end{bmatrix} \begin{bmatrix} \mathbf{T} & \mathbf{0}_{ou} \\ \mathbf{0}_{ou}^T & \mathbf{I}_{uu} \end{bmatrix}^T \qquad (4.30)$$

$$\mathbf{C} = \begin{bmatrix} \mathbf{0}_{oo} & \mathbf{0}_{ou} \\ \mathbf{0}_{ou}^T & \mathbf{C}_{uu} \end{bmatrix} \tag{4.31}$$

$$\mathbf{K} = \begin{bmatrix} \mathbf{0}_{oo} & \mathbf{0}_{ou} \\ \mathbf{0}_{ou}^T & \mathbf{K}_{uu} \end{bmatrix} \tag{4.32}$$

where

$$\bar{\mathbf{M}}_{oo} = \begin{bmatrix} \mathbf{M}_{pp} & \bar{\mathbf{M}}_{p\theta} \\ \bar{\mathbf{M}}_{p\theta}^T & \bar{\mathbf{M}}_{\theta\theta} \end{bmatrix} \tag{4.33}$$

$$\bar{\mathbf{M}}_{ou} = \begin{bmatrix} \bar{\mathbf{M}}_{pu} \\ \bar{\mathbf{M}}_{\theta u} \end{bmatrix} \tag{4.34}$$

$$\mathbf{T} = \begin{bmatrix} \mathbf{R} & \mathbf{0} \\ \mathbf{0} & \mathbf{L}^T \end{bmatrix} \tag{4.35}$$

and the orthogonality property of the rotation matrix ($\mathbf{R}\mathbf{R}^T = \mathbf{I}$) was used in equation (4.30). Equation (4.30) can further be expressed in compact form as

$$\mathbf{M} = \mathbf{T}_G \bar{\mathbf{M}} \mathbf{T}_G^T \tag{4.36}$$

where

$$\mathbf{T}_G = \begin{bmatrix} \mathbf{T} & \mathbf{0}_{ou} \\ \mathbf{0}_{ou}^T & \mathbf{I}_{uu} \end{bmatrix} \tag{4.37}$$

$$\bar{\mathbf{M}} = \begin{bmatrix} \bar{\mathbf{M}}_{oo} & \bar{\mathbf{M}}_{ou} \\ \bar{\mathbf{M}}_{ou}^T & \mathbf{M}_{uu} \end{bmatrix} \tag{4.38}$$

Also note that

$$\mathbf{K} = \mathbf{T}_G \mathbf{K} \mathbf{T}_G^T \tag{4.39}$$

$$\mathbf{C} = \mathbf{T}_G \mathbf{C} \mathbf{T}_G^T \tag{4.40}$$

In light of equations (4.36), (4.39), and (4.40), equation (4.7) may be recast as

$$\hat{\mathbf{K}} = \mathbf{T}_G \bar{\mathbf{K}} \mathbf{T}_G^T$$

where

$$\bar{\mathbf{K}} = \mathbf{K} + a_0\bar{\mathbf{M}} + a_1\mathbf{C} \tag{4.41}$$

Matrix $\hat{\mathbf{K}}$ may be inverted in symbolic form as

$$\hat{\mathbf{K}}^{-1} = \mathbf{T}_G^{-T}\bar{\mathbf{K}}^{-1}\mathbf{T}_G^{-1} = \bar{\mathbf{T}}_G\mathbf{H}\bar{\mathbf{T}}_G^T \tag{4.42}$$

where

$$\mathbf{H} = \bar{\mathbf{K}}^{-1} = \begin{bmatrix} \mathbf{H}_{oo} & \mathbf{H}_{ou} \\ \mathbf{H}_{ou}^T & \mathbf{H}_{uu} \end{bmatrix} \tag{4.43}$$

$$\bar{\mathbf{T}}_G = \mathbf{T}_G^{-T} = \begin{bmatrix} \bar{\mathbf{T}} & \mathbf{0}_{ou} \\ \mathbf{0}_{ou}^T & \mathbf{I}_{uu} \end{bmatrix} \tag{4.44}$$

and using the relationship $\mathbf{R}^{-1} = \mathbf{R}^T$ and equations (2.4)–(2.5):

$$\bar{\mathbf{T}} = \mathbf{T}^{-T} = \begin{bmatrix} \mathbf{R} & \mathbf{0} \\ \mathbf{0} & \mathbf{\Lambda} \end{bmatrix} \tag{4.45}$$

Noting that matrices $\mathbf{K}$ and $\mathbf{C}$ are constant, the only time-varying quantity that matrix $\bar{\mathbf{K}}$ is dependent on is the independent nodal displacement vector $\hat{\mathbf{u}}$. The second method consists in realizing that for most contacting bodies of interest, $\hat{\mathbf{u}} << \hat{\mathbf{x}}$. Then, we can assume that $\hat{\mathbf{x}} + \hat{\mathbf{u}} \approx \hat{\mathbf{x}}$ such that $\bar{\mathbf{K}}$ now becomes a constant matrix and may be inverted *offline* only once. Thus, from equation (4.42)

$$\hat{\mathbf{K}}^{-1} = \begin{bmatrix} \bar{\mathbf{T}}\mathbf{H}_{oo}\bar{\mathbf{T}}^T & \bar{\mathbf{T}}\mathbf{H}_{ou} \\ \mathbf{H}_{ou}^T\bar{\mathbf{T}}^T & \mathbf{H}_{uu} \end{bmatrix} \tag{4.46}$$

where $\bar{\mathbf{T}}$ is the only time-varying quantity in the expression. The inversion of matrix $\hat{\mathbf{K}}$ therefore requires only $C_2 = 2(n_p + n_\theta)^3 + (n_p + n_\theta)^2 n_u$ operations to compute *online*, where n_p, n_θ and n_u are respectively the number of translational, rotational and elastic degrees of freedom of the contacting body.

If, however, the elastic deflections are substantial and cannot be neglected, we pursue the third method. It can easily be verified from equations (2.17) and (2.18)–

(2.27) that out of the 6 independent sub-matrices of $\bar{\mathbf{K}}$ given by

$$\bar{\mathbf{K}} = \begin{bmatrix} \bar{\mathbf{K}}_{pp} & \bar{\mathbf{K}}_{p\theta} & \bar{\mathbf{K}}_{pu} \\ \bar{\mathbf{K}}_{p\theta}^T & \bar{\mathbf{K}}_{\theta\theta} & \bar{\mathbf{K}}_{\theta u} \\ \bar{\mathbf{K}}_{pu}^T & \bar{\mathbf{K}}_{\theta u}^T & \bar{\mathbf{K}}_{uu} \end{bmatrix} \tag{4.47}$$

only $\bar{\mathbf{K}}_{\theta\theta}$, $\bar{\mathbf{K}}_{p\theta}$ and $\bar{\mathbf{K}}_{\theta u}$ are dependent on $\hat{\mathbf{u}}$ and the others are constant. We can rearrange $\bar{\mathbf{K}}$ as

$$\bar{\mathbf{K}} = \begin{bmatrix} \bar{\mathbf{K}}_{\theta\theta} & \bar{\mathbf{K}}_{\theta c} \\ \bar{\mathbf{K}}_{\theta c}^T & \bar{\mathbf{K}}_{cc} \end{bmatrix}$$

where the subscript c comprises terms related to p and u, i.e., the translational and elastic degrees of freedom. Given an equation of the form

$$\begin{bmatrix} \bar{\mathbf{K}}_{\theta\theta} & \bar{\mathbf{K}}_{\theta c} \\ \bar{\mathbf{K}}_{\theta c}^T & \bar{\mathbf{K}}_{cc} \end{bmatrix} \begin{Bmatrix} \mathbf{x}_\theta \\ \mathbf{x}_c \end{Bmatrix} = \begin{Bmatrix} \mathbf{b}_\theta \\ \mathbf{b}_c \end{Bmatrix} \tag{4.48}$$

the solution may be obtained in symbolic form as

$$\begin{Bmatrix} \mathbf{x}_\theta \\ \mathbf{x}_c \end{Bmatrix} = \begin{bmatrix} \mathbf{H}_{\theta\theta} & \mathbf{H}_{\theta c} \\ \mathbf{H}_{\theta c}^T & \mathbf{H}_{cc} \end{bmatrix} \begin{Bmatrix} \mathbf{b}_\theta \\ \mathbf{b}_c \end{Bmatrix} \tag{4.49}$$

From equation (4.48) we can obtain

$$\bar{\mathbf{K}}_{\theta\theta}\mathbf{x}_\theta + \bar{\mathbf{K}}_{\theta c}\mathbf{x}_c = \mathbf{b}_\theta \tag{4.50}$$

$$\bar{\mathbf{K}}_{\theta c}^T\mathbf{x}_\theta + \bar{\mathbf{K}}_{cc}\mathbf{x}_c = \mathbf{b}_c \tag{4.51}$$

From equation (4.51), $\mathbf{x}_c$ may be isolated as

$$\mathbf{x}_c = \bar{\mathbf{K}}_{cc}^{-1}(\mathbf{b}_c - \bar{\mathbf{K}}_{\theta c}^T\mathbf{x}_\theta) \tag{4.52}$$

where we note that $\bar{\mathbf{K}}_{cc}$ is a constant matrix and may be inverted *offline* only once. Substituting the above into equation (4.50),

$$\mathbf{x}_\theta = \mathbf{\Delta}^{-1}\mathbf{b}_\theta - \mathbf{\Delta}^{-1}\mathbf{\Gamma}\mathbf{b}_c \tag{4.53}$$

where

$$\mathbf{\Gamma} = \bar{\mathbf{K}}_{\theta c}\bar{\mathbf{K}}_{cc}^{-1} \tag{4.54}$$

$$\mathbf{\Delta} = \bar{\mathbf{K}}_{\theta\theta} - \mathbf{\Gamma}\bar{\mathbf{K}}_{\theta c}^T \tag{4.55}$$

Table 4.2: Comparison of required operations for the three methods of inversion

Method	2D	3D
1	$(3+n_u)^3/6$	$(6+n_u)^3/6$
2	$9n_u+54$	$36n_u+432$
3	$3n_u^2+18n_u+38$	$7n_u^2+69n_u+212$

Substituting equation (4.53) into equation (4.52),

$$\mathbf{x}_c = -\mathbf{\Gamma}^T\mathbf{\Delta}^{-1}\mathbf{b}_\theta + (\bar{\mathbf{K}}_{cc}^{-1} + \mathbf{\Gamma}^T\mathbf{\Delta}^{-1}\mathbf{\Gamma})\mathbf{b}_c \tag{4.56}$$

Comparing equation (4.49) with equations (4.53) and (4.56), the inverse of matrix $\bar{\mathbf{K}}$ may be expressed as

$$\bar{\mathbf{K}}^{-1} = \mathbf{H} = \begin{bmatrix} \mathbf{\Delta}^{-1} & -\mathbf{\Delta}^{-1}\mathbf{\Gamma} \\ -\mathbf{\Gamma}^T\mathbf{\Delta}^{-1} & \bar{\mathbf{K}}_{cc}^{-1} + \mathbf{\Gamma}^T\mathbf{\Delta}^{-1}\mathbf{\Gamma} \end{bmatrix} \tag{4.57}$$

The *online* computation of matrix $\mathbf{H}$ requires the calculation of the inverse of only one $n_\theta \times n_\theta$ matrix, namely $\mathbf{\Delta}$. We may now use equation (4.46) to calculate $\hat{\mathbf{K}}^{-1}$. In total, this method of computing $\hat{\mathbf{K}}^{-1}$ requires $C_3 = 2n_\theta n_c^2 + 2n_\theta^2 n_c + n_\theta^2 + n_c^2 + n_\theta^3/6 + 2n_p^3 + n_p^2(n_\theta + n_u)$ operations.

Table 4.2 compares the 3 methods in terms of required operations in 2D ($n_p = 2, n_\theta = 1$) and 3D ($n_p = 3, n_\theta = 3$) cases. The computational cost of method 1 is proportional to n_u^3, method 2 to n_u, and method 3 to n_u^2. Figure 4.5 shows ratios of the computational cost of methods 1 and 2 over method 3 (C_1/C_3 and C_2/C_3). As expected, method 2 is by far the most efficient in most cases. For 2D cases, method 3 becomes more efficient than method 1 if $n_u > 14$, or the number of finite element nodes exceeds 7. For 3D cases, this is so if $n_u > 34$, or the number of finite element nodes exceeds 11. From these comparisons, it can be concluded that if the contacting body's elastic displacements are very small compared with its physical dimensions, method 2 should be used for maximum computational efficiency. Otherwise, method 3 should be used where the number of nodes is greater than 7 for 2D cases and 11 for 3D cases, which are the usual situations in finite element analysis.

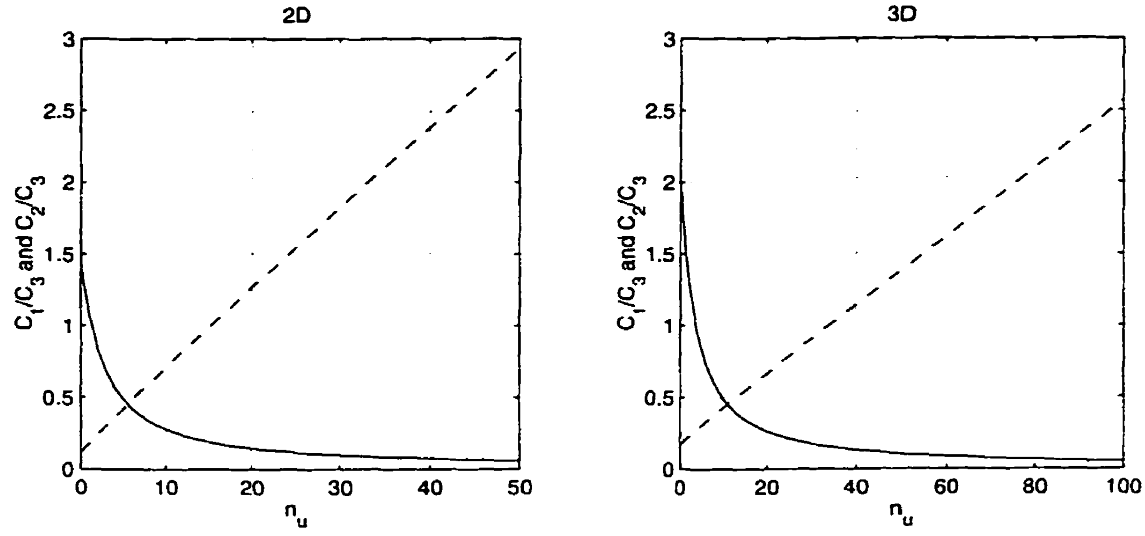

Figure 4.5: Comparison of the three methods of inversion for 2D and 3D cases (C_1/C_3 - - - ; C_2/C_3 —)

4.3.2 Guyan Reduction

Due to the large order of the sets of finite element equations for contacting bodies, use of a reduction method is desirable in order to obtain a smaller set of equations of motion and thus increase computational efficiency. The *Guyan reduction* method, also known as the *mass condensation* method (Guyan 1965, Cook 1981), is appropriate in systems where two different types of degrees of freedom (d.o.f.) can be readily identified, namely "slaves" and "masters". The slaves are chosen from the set of d.o.f.'s on which no external forces are applied, and likely candidates are those with high K_{ii}/M_{ii} ratio. The equations of motion (4.1) corresponding to contacting bodies can then be rearranged in terms of master and slave d.o.f.'s in the following form:

$$\begin{bmatrix} \mathbf{M}_{ss} & \mathbf{M}_{sm} \\ \mathbf{M}_{ms} & \mathbf{M}_{mm} \end{bmatrix} \begin{Bmatrix} \ddot{\mathbf{q}}_s \\ \ddot{\mathbf{q}}_m \end{Bmatrix} + \begin{bmatrix} \mathbf{C}_{ss} & \mathbf{C}_{sm} \\ \mathbf{C}_{ms} & \mathbf{C}_{mm} \end{bmatrix} \begin{Bmatrix} \dot{\mathbf{q}}_s \\ \dot{\mathbf{q}}_m \end{Bmatrix}$$

$$+ \begin{bmatrix} \mathbf{K}_{ss} & \mathbf{K}_{sm} \\ \mathbf{K}_{ms} & \mathbf{K}_{mm} \end{bmatrix} \begin{Bmatrix} \mathbf{q}_s \\ \mathbf{q}_m \end{Bmatrix} + \begin{Bmatrix} \mathbf{c}_s \\ \mathbf{c}_m \end{Bmatrix} + \sum_{j=1}^{n} \begin{bmatrix} \mathbf{P}_s^T \\ \mathbf{P}_m^T \end{bmatrix} \boldsymbol{\lambda}_j = \begin{Bmatrix} \mathbf{f}_s \\ \mathbf{f}_m \end{Bmatrix} \quad (4.58)$$

The first set of equations in equation (4.58) pertaining to the slave d.o.f.'s can be taken out as

$$\mathbf{M}_{ss}\ddot{\mathbf{q}}_s + \mathbf{M}_{sm}\ddot{\mathbf{q}}_m + \mathbf{C}_{ss}\dot{\mathbf{q}}_s + \mathbf{C}_{sm}\dot{\mathbf{q}}_m + \mathbf{K}_{ss}\mathbf{q}_s + \mathbf{K}_{sm}\mathbf{q}_m + \mathbf{c}_s = \mathbf{0}. \tag{4.59}$$

where $\sum_{j=1}^{n}\mathbf{P}_s^T$ and $\mathbf{f}_s$ are both zero and hence do not appear in the above equation. The principal assumption of the *Guyan reduction* method is that in the above system of equations, which carries no external load, the elastic forces play the dominant role and inertia, damping and nonlinear forces are negligible. In other words, the stiffness matrix $\mathbf{K}$ alone dictates how slaves will follow masters. Hence, $\mathbf{q}_s$ can be expressed as a function of $\mathbf{q}_m$:

$$\mathbf{q}_s = -\mathbf{K}_{ss}^{-1}\mathbf{K}_{sm}\mathbf{q}_m \tag{4.60}$$

Therefore,

$$\left\{ \begin{array}{c} \mathbf{q}_s \\ \mathbf{q}_m \end{array} \right\} = \mathbf{G}\mathbf{q}_m \tag{4.61}$$

where

$$\mathbf{G} = \begin{bmatrix} -\mathbf{K}_{ss}^{-1}\mathbf{K}_{sm} \\ \mathbf{I} \end{bmatrix} \tag{4.62}$$

Substituting the above equation and its first and second time derivatives into the original equations and premultiplying by $\mathbf{G}^T$, we obtain

$$\mathbf{M}_R\ddot{\mathbf{q}}_m + \mathbf{C}_R\dot{\mathbf{q}}_m + \mathbf{K}_R\mathbf{q}_m + \mathbf{c}_R(\mathbf{q},\dot{\mathbf{q}}) + \sum_{j=1}^{n}\mathbf{P}_R^T\boldsymbol{\lambda}_j = \mathbf{f}_R \tag{4.63}$$

where

$$\mathbf{M}_R = \mathbf{G}^T\mathbf{M}\mathbf{G}; \quad \mathbf{C}_R = \mathbf{G}^T\mathbf{C}\mathbf{G}; \quad \mathbf{K}_R = \mathbf{G}^T\mathbf{K}\mathbf{G};$$
$$\mathbf{c}_R = \mathbf{G}^T\mathbf{c}; \quad \mathbf{P}_R^T = \mathbf{G}^T\mathbf{P}^T = \mathbf{P}_m^T; \quad \mathbf{f}_R = \mathbf{G}^T\mathbf{f} = \mathbf{f}_m.$$

Note that $\mathbf{G}$ is a constant matrix. Thus, matrices $\mathbf{M}_R$, $\mathbf{C}_R$, and $\mathbf{K}_R$ retain the same structure as the original matrices, so that the same computationally efficient methods presented in section 4.3.1 are still valid with respect to the new Guyan-reduced forms.

The constraint equations are dependent only on the master d.o.f.'s and thus, these equations can be rewritten as

$$\mathbf{g}_k = f(\mathbf{q}_{m,r_k}, \mathbf{q}_{m,s_k}) = \mathbf{p}_{r_k}(\mathbf{q}_{m,r_k}) - \mathbf{p}_{s_k}(\mathbf{q}_{m,s_k}) = \mathbf{0} \tag{4.64}$$

The equations of motion of the contacting bodies and the contact constraint relations are now expressed in terms of the master d.o.f.'s and the order of the equations are reduced to the number of master d.o.f.'s.

4.3.3 Elimination of the Flexible Portion of the Nonlinear Forces

Contacting bodies are generally solid objects with high stiffness to mass ratio. Vibrations and deformations of such bodies are negligible under normal conditions, unless they are acted upon by large contact forces or undergoing impact of short duration. Rayleigh showed that very little vibration is induced in a body under the influence of forces of duration long in comparison with its natural periods. Therefore, under no-contact conditions, the contacting bodies may be considered rigid, and only rigid body motion need be included in the equations of motion:

$$\mathbf{M}_{rr}\mathbf{q}_r + \mathbf{c}_r(\mathbf{q}_r, \dot{\mathbf{q}}_r) = \mathbf{f} \tag{4.65}$$

where subscript r denotes rigid terms. When contact occurs, however, large contact forces of short duration make flexibility and vibration effects important, such that flexible variables must be included in the dynamical model:

$$\begin{bmatrix} \mathbf{M}_{rr} & \mathbf{M}_{rf} \\ \mathbf{M}_{fr} & \mathbf{M}_{ff} \end{bmatrix} \begin{Bmatrix} \ddot{\mathbf{q}}_r \\ \ddot{\mathbf{q}}_f \end{Bmatrix} + \begin{bmatrix} \mathbf{0}_{rr} & \mathbf{0}_{rf} \\ \mathbf{0}_{fr} & \mathbf{K}_{ff} \end{bmatrix} \begin{Bmatrix} \mathbf{q}_r \\ \mathbf{q}_f \end{Bmatrix} + \begin{Bmatrix} \mathbf{c}_r \\ \mathbf{c}_f \end{Bmatrix} = \begin{Bmatrix} \mathbf{f}_r \\ \mathbf{f}_f \end{Bmatrix} \tag{4.66}$$

where subscript f denotes flexible terms. The inertia and stiffness forces are large: however, the contribution of the flexible coordinates on the nonlinear forces due to centrifugal and coriolis forces, $\mathbf{c}_f$, remains relatively small. The validity of this assumption was further verified through comparisons of various simulation results

(Chapter 6). This means that one may safely eliminate the nonlinear force vector $\mathbf{c}_f$ both in contact and no-contact cases, without compromising accuracy; on the other hand, a great deal of computer time is saved.

Note that the three simplifying methods presented in Section 4.3 apply only to the finite element models of contacting bodies, not to multi-body systems.

Chapter 5

Force Control

5.1 Introduction

This chapter is devoted to the design of a controller for flexible multi-body systems. Of particular interest is the case where the multi-body system is a multi-link manipulator with an end-effector at its tip for performing a variety of contact tasks. A typical control task would be to maneuver the end-effector along a given path, position it at a particular location, such as a grapple fixture of a payload, and apply desired amounts of force on the surface. The design of a controller for such a task is applicable to rigid manipulators as well. However, flexible manipulators present another concern not shared by the counterpart rigid manipulators: instability in the elastic vibrations of the links.

It has been reported by several researchers (e.g., Chiou & Shahinpoor (1989), Modi et al. (1993)) that for a manipulator system with link and/or joint flexibility, the flexible degrees of freedom can become unstable and cause maneuver failure. The discontinuous repeated contact/impact between the manipulator and the environment can further contribute to the instability of the system. Thus, for a fully flexible manipulator system, the controller must not only achieve trajectory tracking and force control on the contact surface but must also stabilize the vibrations which are naturally excited during its operation. However, a flexible manipulator system is characterized by having a greater number of generalized coordinates than control inputs. This problem leads to consideration of a *singular perturbation control* as discussed in Section 1.5. According to the *singular perturbation theory*, two reduced order systems can be identified: a slow subsystem whose state variables turn out to be those of the rigid manipulator, and a fast subsystem whose states are composed of the flexible coordinates and velocities. In other words, the gross motion of the system is approximated by the slow reduced subsystem, while the discrepancy between the full model and the slow subsystem represents the fast subsystem. Then, the design of the full flexible model can be split into two separate designs of the two reduced-order systems, i.e., a *composite control* can be pursued (Siciliano & Book 1988).

For the slow subsystem, any of the well-established control techniques developed for rigid manipulators can be applied. In this thesis, a position and force controller based on impedance control is used. Impedance control is a *model-based* control scheme: it attempts to make the physical system behave like a desired model (target impedance) by linearizing and decoupling the actual dynamics using a combination of feedback (servo) and feedforward (model-based) control. As such, it suffers from some common disadvantages of model-based controllers. Firstly, impedance control requires exact knowledge of the dynamic and kinematic parameters of the manipulator system to design its control law and achieve decoupling and linearizing of the closed-loop error dynamics. In reality, however, it is often not possible to obtain an exact model, especially such effects as high-frequency unmodelled dynamics, measurement noise, and joint friction. Secondly, the dynamics of the system must be computed and fed *online* into the controller. In order to alleviate computational demands, a two-level control system architecture may be used: the model-based portion of the controller may be taken out of the servo loop and run at a slower rate. Both these defects lead to a nonlinear and coupled error dynamics which may behave in a complicated way. These considerations also leave open such issues as robustness and sensitivity of the controller. However, for simplicity, these issues will not be addressed in this thesis; i.e., it is assumed that the dynamic and kinematic parameters are known exactly and that the computational power is sufficient to meet the demands of *online* computatation of inverse dynamics.

Another disadvantage exclusively pertinent to impedance control is that it requires exact knowledge of environment parameters in order to achieve good force tracking. In this thesis, it is again assumed for simplicity that these parameters are indeed known exactly. However, in practical situations where this is not the case, additional strategies must be implemented to provide improved force tracking capability (Lasky & Hsia 1991, Seraji & Colbaugh 1993).

The fast subsystem turns out to be a *linear time-varying system* where the slow state variables play the role of parameters. Therefore, any linear controller may be designed to damp out the flexible variables of the system. In the present work, the Linear Quadratic Regulator (LQR) was chosen to meet this objective. The control strategy selected involves feedback of the full state, which is not usually available in practice, such that implementation of state observers is recommended for future work. Also, ideal actuators with no torque limitations were assumed.

5.2 Singular Perturbation Method

The singular perturbation method described in this section is based on the work by Siciliano & Book (1988), where the technique was successfully applied to the control of a two-link flexible manipulator.

The dynamical equations of motion of the multi-link manipulator system to be controlled can be cast as:

$$\mathbf{M}\ddot{\mathbf{q}} + \mathbf{K}\mathbf{q} = \mathbf{c} + \boldsymbol{\tau}_t - \mathbf{J}^T\mathbf{f}_{ext} \tag{5.1}$$

where $\mathbf{M}$ is the mass matrix, $\mathbf{q}$ is the vector of generalized co-ordinates, the vector $\mathbf{c}$ contains the velocity dependent inertia terms as well as damping terms, $\boldsymbol{\tau}_t$ represents the control torques, $\mathbf{J}$ is the Jacobian of the manipulator, and $\mathbf{f}_{ext}$ is the external force vector. Equation (5.1) may be partitioned in terms of rigid and flexible variables as

$$\begin{bmatrix} \mathbf{M}_{rr} & \mathbf{M}_{rf} \\ \mathbf{M}_{fr} & \mathbf{M}_{ff} \end{bmatrix} \left\{ \begin{array}{c} \ddot{\mathbf{q}}_r \\ \ddot{\mathbf{q}}_f \end{array} \right\} + \left\{ \begin{array}{c} \mathbf{0} \\ \mathbf{K}_{ff}\mathbf{q}_f \end{array} \right\} = \left\{ \begin{array}{c} \bar{\mathbf{f}}_r(\mathbf{q}_r, \dot{\mathbf{q}}_r, \mathbf{q}_f, \dot{\mathbf{q}}_f) \\ \bar{\mathbf{f}}_f(\mathbf{q}_r, \dot{\mathbf{q}}_r, \mathbf{q}_f, \dot{\mathbf{q}}_f) \end{array} \right\} + \left\{ \begin{array}{c} \boldsymbol{\tau} \\ \mathbf{0} \end{array} \right\} \quad (5.2)$$

where

$$\bar{\mathbf{f}}_r = \mathbf{c}_r - \mathbf{J}_r^T \mathbf{f}_{ext};$$
$$\bar{\mathbf{f}}_f = \mathbf{c}_f - \mathbf{J}_f^T \mathbf{f}_{ext}.$$

Subscripts r and f denote rigid and flexible terms respectively. The inverse of the mass matrix may be expressed as

$$\mathbf{M}^{-1}(\mathbf{q}_r, \mathbf{q}_f) = \mathbf{H}(\mathbf{q}_r, \mathbf{q}_f) = \begin{bmatrix} \mathbf{H}_{rr}(\mathbf{q}_r, \mathbf{q}_f) & \mathbf{H}_{rf}(\mathbf{q}_r, \mathbf{q}_f) \\ \mathbf{H}_{fr}(\mathbf{q}_r, \mathbf{q}_f) & \mathbf{H}_{ff}(\mathbf{q}_r, \mathbf{q}_f) \end{bmatrix}$$

and equation (5.2) may be recast as

$$\begin{aligned} \ddot{\mathbf{q}}_r = {} & \mathbf{H}_{rr}(\mathbf{q}_r, \mathbf{q}_f)\bar{\mathbf{f}}_r(\mathbf{q}_r, \dot{\mathbf{q}}_r, \mathbf{q}_f, \dot{\mathbf{q}}_f) + \mathbf{H}_{rf}(\mathbf{q}_r, \mathbf{q}_f)\bar{\mathbf{f}}_f(\mathbf{q}_r, \dot{\mathbf{q}}_r, \mathbf{q}_f, \dot{\mathbf{q}}_f) \\ & -\mathbf{H}_{rf}(\mathbf{q}_r, \mathbf{q}_f)\mathbf{K}_{ff}\mathbf{q}_f + \mathbf{H}_{rr}(\mathbf{q}_r, \mathbf{q}_f)\boldsymbol{\tau} \qquad (5.3) \\ \ddot{\mathbf{q}}_f = {} & \mathbf{H}_{fr}(\mathbf{q}_r, \mathbf{q}_f)\bar{\mathbf{f}}_r(\mathbf{q}_r, \dot{\mathbf{q}}_r, \mathbf{q}_f, \dot{\mathbf{q}}_f) + \mathbf{H}_{ff}(\mathbf{q}_r, \mathbf{q}_f)\bar{\mathbf{f}}_f(\mathbf{q}_r, \dot{\mathbf{q}}_r, \mathbf{q}_f, \dot{\mathbf{q}}_f) \\ & -\mathbf{H}_{ff}(\mathbf{q}_r, \mathbf{q}_f)\mathbf{K}_{ff}\mathbf{q}_f + \mathbf{H}_{fr}(\mathbf{q}_r, \mathbf{q}_f)\boldsymbol{\tau} \qquad (5.4) \end{aligned}$$

Provided that the stiffness coefficients are of the same order of magnitude, it is appropriate to extract a common scale factor k such that

$$\tilde{\mathbf{K}} = (1/k)\mathbf{K}_{ff}, \quad k \gg 1$$

and the elastic forces are defined as

$$\boldsymbol{\xi} = k\tilde{\mathbf{K}}\mathbf{q}_f$$

Defining

$$\mu = \frac{1}{k},$$

and premultiplying equation (5.4) by $\tilde{\mathbf{K}}$ we obtain

$$\begin{aligned}\ddot{\mathbf{q}}_r &= \mathbf{H}_{rr}(\mathbf{q}_r, \mu\boldsymbol{\xi})\bar{\mathbf{f}}_r(\mathbf{q}_r, \dot{\mathbf{q}}_r, \mu\boldsymbol{\xi}, \mu\dot{\boldsymbol{\xi}}) + \mathbf{H}_{rf}(\mathbf{q}_r, \mu\boldsymbol{\xi})\bar{\mathbf{f}}_f(\mathbf{q}_r, \dot{\mathbf{q}}_r, \mu\boldsymbol{\xi}, \mu\dot{\boldsymbol{\xi}}) \\ &\quad -\mathbf{H}_{rf}(\mathbf{q}_r, \mu\boldsymbol{\xi})\boldsymbol{\xi} + \mathbf{H}_{rr}(\mathbf{q}_r, \mu\boldsymbol{\xi})\boldsymbol{\tau} \qquad (5.5) \\ \mu\ddot{\boldsymbol{\xi}} &= \mathbf{H}'_{fr}(\mathbf{q}_r, \mu\boldsymbol{\xi})\bar{\mathbf{f}}_r(\mathbf{q}_r, \dot{\mathbf{q}}_r, \mu\boldsymbol{\xi}, \mu\dot{\boldsymbol{\xi}}) + \mathbf{H}'_{ff}(\mathbf{q}_r, \mu\boldsymbol{\xi})\bar{\mathbf{f}}_f(\mathbf{q}_r, \dot{\mathbf{q}}_r, \mu\boldsymbol{\xi}, \mu\dot{\boldsymbol{\xi}}) \\ &\quad -\mathbf{H}'_{ff}(\mathbf{q}_r, \mu\boldsymbol{\xi})\boldsymbol{\xi} + \mathbf{H}'_{fr}(\mathbf{q}_r, \mu\boldsymbol{\xi})\boldsymbol{\tau} \qquad (5.6)\end{aligned}$$

where

$$\mathbf{H}'_{fr} = \tilde{\mathbf{K}}\mathbf{H}_{fr}$$
$$\mathbf{H}'_{ff} = \tilde{\mathbf{K}}\mathbf{H}_{ff}$$

To establish the two reduced subsystems, equations (5.5) and (5.6) will be written in the state space form. The following state variables are defined:

$$\left\{ \begin{array}{c} \mathbf{x}_1 \\ \mathbf{x}_2 \end{array} \right\} = \left\{ \begin{array}{c} \mathbf{q}_r \\ \dot{\mathbf{q}}_r \end{array} \right\}, \quad \left\{ \begin{array}{c} \mathbf{z}_1 \\ \mathbf{z}_2 \end{array} \right\} = \left\{ \begin{array}{c} \boldsymbol{\xi} \\ \epsilon\dot{\boldsymbol{\xi}} \end{array} \right\} \qquad (5.7)$$

where the perturbation parameter ϵ is defined as

$$\epsilon = \sqrt{\mu} \qquad (5.8)$$

With these forms, equations (5.5) and (5.6) become

$$\begin{aligned}\dot{\mathbf{x}}_1 &= \mathbf{x}_2 \qquad (5.9) \\ \dot{\mathbf{x}}_2 &= \mathbf{H}_{rr}(\mathbf{x}_1, \epsilon^2\mathbf{z}_1)\bar{\mathbf{f}}_r(\mathbf{x}_1, \mathbf{x}_2, \epsilon^2\mathbf{z}_1, \epsilon\mathbf{z}_2) + \mathbf{H}_{rf}(\mathbf{x}_1, \epsilon^2\mathbf{z}_1)\bar{\mathbf{f}}_f(\mathbf{x}_1, \mathbf{x}_2, \epsilon^2\mathbf{z}_1, \epsilon\mathbf{z}_2) \\ &\quad -\mathbf{H}_{rf}(\mathbf{x}_1, \epsilon^2\mathbf{z}_1)\mathbf{z}_1 + \mathbf{H}_{rr}(\mathbf{x}_1, \epsilon^2\mathbf{z}_1)\boldsymbol{\tau} \qquad (5.10) \\ \epsilon\dot{\mathbf{z}}_1 &= \mathbf{z}_2 \qquad (5.11) \\ \epsilon\dot{\mathbf{z}}_2 &= \mathbf{H}'_{fr}(\mathbf{x}_1, \epsilon^2\mathbf{z}_1)\bar{\mathbf{f}}_r(\mathbf{x}_1, \mathbf{x}_2, \epsilon^2\mathbf{z}_1, \epsilon\mathbf{z}_2) + \mathbf{H}'_{ff}(\mathbf{x}_1, \epsilon^2\mathbf{z}_1)\bar{\mathbf{f}}_f(\mathbf{x}_1, \mathbf{x}_2, \epsilon^2\mathbf{z}_1, \epsilon\mathbf{z}_2) \\ &\quad -\mathbf{H}'_{ff}(\mathbf{x}_1, \epsilon^2\mathbf{z}_1)\mathbf{z}_1 + \mathbf{H}'_{fr}(\mathbf{x}_1, \epsilon^2\mathbf{z}_1)\boldsymbol{\tau} \qquad (5.12)\end{aligned}$$

Now using the basic assumption of singular perturbation theory of large time scale separation between the two subsystems, we obtain the slow subsystem equations of motion by letting the perturbation $\epsilon \rightarrow 0$. Formally setting $\epsilon = 0$ in equations (5.9) and (5.10):

$$\dot{\bar{\mathbf{x}}}_1 = \bar{\mathbf{x}}_2 \tag{5.13}$$

$$\begin{aligned}\dot{\bar{\mathbf{x}}}_2 = {} & \mathbf{H}_{rr}(\bar{\mathbf{x}}_1, \mathbf{0})\bar{\mathbf{f}}_r(\bar{\mathbf{x}}_1, \bar{\mathbf{x}}_2, \mathbf{0}, \mathbf{0}) + \mathbf{H}_{rf}(\bar{\mathbf{x}}_1, \mathbf{0})\bar{\mathbf{f}}_f(\bar{\mathbf{x}}_1, \bar{\mathbf{x}}_2, \mathbf{0}, \mathbf{0}) \\ & -\mathbf{H}_{rf}(\bar{\mathbf{x}}_1, \mathbf{0})\bar{\mathbf{z}}_1 + \mathbf{H}_{rr}(\bar{\mathbf{x}}_1, \mathbf{0})\bar{\boldsymbol{\tau}}\end{aligned} \tag{5.14}$$

where the overbars are used to indicate that the system with $\epsilon = 0$ is considered. The *quasi-static* elastic force $\bar{\mathbf{z}}_1$ may be obtained from equation (5.12) as

$$\bar{\mathbf{z}}_1 = \mathbf{H}_{ff}^{-1}(\bar{\mathbf{x}}_1, \mathbf{0})\mathbf{H}_{fr}(\bar{\mathbf{x}}_1, \mathbf{0})\{\bar{\mathbf{f}}_r(\bar{\mathbf{x}}_1, \dot{\bar{\mathbf{x}}}_1, \mathbf{0}, \mathbf{0}) + \bar{\boldsymbol{\tau}}\} + \bar{\mathbf{f}}_f(\bar{\mathbf{x}}_1, \dot{\bar{\mathbf{x}}}_1, \mathbf{0}, \mathbf{0}) \tag{5.15}$$

To obtain the fast subsystem, a new time scale $\tilde{t}$ is defined as

$$\tilde{t} = t/\epsilon$$

and implemented into equations (5.9)–(5.12) to obtain

$$\frac{d\mathbf{x}_1}{d\tilde{t}} = \epsilon\mathbf{x}_2 \tag{5.16}$$

$$\begin{aligned}\frac{d\mathbf{x}_2}{d\tilde{t}} = {} & \epsilon\{\mathbf{H}_{rr}(\mathbf{x}_1, \epsilon^2\mathbf{z}_1)\bar{\mathbf{f}}_r(\mathbf{x}_1, \mathbf{x}_2, \epsilon^2\mathbf{z}_1, \epsilon\mathbf{z}_2) + \mathbf{H}_{rf}(\mathbf{x}_1, \epsilon^2\mathbf{z}_1)\bar{\mathbf{f}}_f(\mathbf{x}_1, \mathbf{x}_2, \epsilon^2\mathbf{z}_1, \epsilon\mathbf{z}_2) \\ & -\mathbf{H}_{rf}(\mathbf{x}_1, \epsilon^2\mathbf{z}_1)\mathbf{z}_1 + \mathbf{H}_{rr}(\mathbf{x}_1, \epsilon^2\mathbf{z}_1)\boldsymbol{\tau}\}\end{aligned} \tag{5.17}$$

$$\frac{d\mathbf{z}_1}{d\tilde{t}} = \mathbf{z}_2 \tag{5.18}$$

$$\begin{aligned}\frac{d\mathbf{z}_2}{d\tilde{t}} = {} & \mathbf{H'}_{fr}(\mathbf{x}_1, \epsilon^2\mathbf{z}_1)\bar{\mathbf{f}}_r(\mathbf{x}_1, \mathbf{x}_2, \epsilon^2\mathbf{z}_1, \epsilon\mathbf{z}_2) + \mathbf{H'}_{ff}(\mathbf{x}_1, \epsilon^2\mathbf{z}_1)\bar{\mathbf{f}}_f(\mathbf{x}_1, \mathbf{x}_2, \epsilon^2\mathbf{z}_1, \epsilon\mathbf{z}_2) \\ & -\mathbf{H'}_{ff}(\mathbf{x}_1, \epsilon^2\mathbf{z}_1)\mathbf{z}_1 + \mathbf{H'}_{fr}(\mathbf{x}_1, \epsilon^2\mathbf{z}_1)\boldsymbol{\tau}\end{aligned} \tag{5.19}$$

Now, as $\epsilon \rightarrow 0$, only equations (5.18) and (5.19) remain, and by defining the fast state variables as

$$\left\{ \begin{array}{c} \boldsymbol{\eta}_1 \\ \boldsymbol{\eta}_2 \end{array} \right\} = \left\{ \begin{array}{c} \mathbf{z}_1 - \bar{\mathbf{z}}_1 \\ \mathbf{z}_2 \end{array} \right\} \tag{5.20}$$

the fast subsystem is described by

$$\frac{d\boldsymbol{\eta}_1}{d\tilde{t}} = \boldsymbol{\eta}_2 \tag{5.21}$$

$$\begin{aligned}\frac{d\boldsymbol{\eta}_2}{d\tilde{t}} = {} & \mathbf{H'}_{fr}(\mathbf{x}_1, \mathbf{0})\bar{\mathbf{f}}_r(\mathbf{x}_1, \mathbf{x}_2, \mathbf{0}, \mathbf{0}) + \mathbf{H'}_{ff}(\mathbf{x}_1, \mathbf{0})\bar{\mathbf{f}}_f(\mathbf{x}_1, \mathbf{x}_2, \mathbf{0}, \mathbf{0}) \\ & -\mathbf{H'}_{ff}(\mathbf{x}_1, \mathbf{0})\mathbf{z}_1 + \mathbf{H'}_{fr}(\mathbf{x}_1, \mathbf{0})\boldsymbol{\tau}\end{aligned} \tag{5.22}$$

where, for differentiations with respect to the fast time scale, the quasi-static force varies slowly such that

$$\frac{d\bar{\mathbf{z}}_l}{d\tilde{t}} \approx \mathbf{0} \tag{5.23}$$

If we substitute $\bar{\mathbf{z}}_l$ from equation (5.15) into equation (5.22), the fast subsystem simplifies to

$$\frac{d\boldsymbol{\eta}_1}{d\tilde{t}} = \boldsymbol{\eta}_2 \tag{5.24}$$

$$\frac{d\boldsymbol{\eta}_2}{d\tilde{t}} = -\mathbf{H}'_{ff}(\bar{\mathbf{x}}_1, \mathbf{0})\boldsymbol{\eta}_1 + \mathbf{H}'_{fr}(\bar{\mathbf{x}}_1, \mathbf{0})\boldsymbol{\tau}_f \tag{5.25}$$

which is expressed in a linear state form where the slow variables $\bar{\mathbf{x}}_1$ act as parameters. The control input for the fast subsystem $\boldsymbol{\tau}_f$, is given by

$$\boldsymbol{\tau}_f = \boldsymbol{\tau} - \bar{\boldsymbol{\tau}}.$$

5.3 Composite Control

Once the full flexible system has been split into two reduced-order models, the design of the feedback control for the full system can be split into two separate controls $\bar{\boldsymbol{\tau}}$ and $\boldsymbol{\tau}_f$, and the composite control torque for the full-order system can then be obtained from

$$\boldsymbol{\tau} = \bar{\boldsymbol{\tau}} + \boldsymbol{\tau}_f. \tag{5.26}$$

Figure 5.1 shows the following composite control approach in a block diagram. The overall control diagram is divided into two boxes (in dashed lines): slow control and fast control.

5.3.1 Slow Control

For the slow control, using equation (5.15), equation (5.14) may be recast as

$$\mathbf{M}_{rr}(\bar{\mathbf{q}}_r)\ddot{\mathbf{q}}_r = \mathbf{c}_r(\bar{\mathbf{q}}_r, \dot{\mathbf{q}}_r, \mathbf{0}, \mathbf{0}) + \bar{\boldsymbol{\tau}} - \mathbf{J}_r^T\mathbf{f}_{ext} \tag{5.27}$$

where the following easily verifiable relation was used:

$$\mathbf{M}_{rr}^{-1}(\bar{\mathbf{q}}_r) = \mathbf{H}_{rr}(\bar{\mathbf{q}}_r, \mathbf{0}) - \mathbf{H}_{rf}(\bar{\mathbf{q}}_r, \mathbf{0})\mathbf{H}_{ff}^{-1}(\bar{\mathbf{q}}_r, \mathbf{0})\mathbf{H}_{fr}(\bar{\mathbf{q}}_r, \mathbf{0}).$$

It is realized that equation (5.27) is equivalent to equation (5.1) with flexible terms neglected. Equation (5.27) may now be used to design a position/force controller based on well-established control schemes suitable for rigid manipulators.

Most control schemes are *joint-based*, i.e., the desired trajectory is specified in terms of time histories of joint position, velocity and acceleration, and trajectory errors are developed by differencing these values from the corresponding desired ones. However, in typical contact operations of a manipulator, it is desirable to specify the manipulator's task in terms of appropriate motions of its end-point (end-effector). This means that it is necessary to translate the end-point motion into a corresponding set of joint motion specifications, i.e., *inverse kinematics* must be carried out, which is known to be a difficult computational problem. Impedance control avoids this difficulty by specifying the manipulator's behaviour in Cartesian space: the measured joint position of the manipulator is transformed by means of *direct kinematics* into a Cartesian description of the end-effector position, and tracking errors are specified in Cartesian space. The velocity and acceleration of the end-effector in Cartesian space can be approximated respectively by

$$\dot{\mathbf{x}} = \mathbf{J}_r(\mathbf{q}_r)\dot{\mathbf{q}}_r \tag{5.28}$$

$$\ddot{\mathbf{x}} = \mathbf{J}_r(\mathbf{q}_r)\ddot{\mathbf{q}}_r + \dot{\mathbf{J}}_r(\mathbf{q}_r, \dot{\mathbf{q}}_r)\dot{\mathbf{q}}_r \tag{5.29}$$

For non-redundant manipulators, the generalized accelerations may readily be obtained by straightforward inversion of the Jacobian as

$$\ddot{\mathbf{q}}_r = \mathbf{J}_r^{-1}(\mathbf{q}_r)\{\ddot{\mathbf{x}} - \dot{\mathbf{J}}_r(\mathbf{q}_r, \dot{\mathbf{q}}_r)\dot{\mathbf{q}}_r\} \tag{5.30}$$

However, manipulator systems may be redundant, i.e., there is an infinite number of joint motions which can achieve a certain end-effector trajectory (e.g. the 7-joint SSRMS). This is because the manipulator has more than the minimum number of mechanical degrees of freedom to perform tasks. For redundant manipulators, the inverse of the Jacobian, $\mathbf{J}_r^{-1}$ in equation (5.30) does not exist; in this case, redundancy may be exploited to satisfy a certain optimality criterion such as minimization of actuator joint torques or a quadratic criterion. One such optimization method was developed by Khatib (1987) which minimizes the instantaneous kinetic energy

$$\frac{1}{2}\dot{\mathbf{q}}_r^T \mathbf{M}_{rr} \dot{\mathbf{q}}_r$$

constrained by

$$\dot{\mathbf{x}} - \mathbf{J}_r \dot{\mathbf{q}}_r = \mathbf{0}$$

The effective inverse of the Jacobian which satisfies the above optimization is called the *inertia-weighted pseudoinverse* (Khatib 1987) which can be expressed as

$$\mathbf{J}_{M_r}^{+} = \mathbf{M}_{rr}^{-1}\mathbf{J}_r^T(\mathbf{J}_r\mathbf{M}_{rr}^{-1}\mathbf{J}_r^T)^{-1} \tag{5.31}$$

Therefore, the generalized accelerations can be expressed using equation (5.31) as

$$\ddot{\mathbf{q}}_r = \mathbf{M}_{rr}^{-1}\mathbf{J}_r^T(\mathbf{J}_r\mathbf{M}_{rr}^{-1}\mathbf{J}_r^T)^{-1}(\ddot{\mathbf{x}} - \dot{\mathbf{J}}_r\dot{\mathbf{q}}_r) \tag{5.32}$$

Impedance control is based on specifying the desired behaviour of the system with respect to the external force exerted by the end-effector on the environment, which is referred to as the target impedance. Since the dominant behaviour of manipulator systems along each degree of freedom is that of a second order system, a reasonable target impedance is usually also chosen as second order (Hogan 1987):

$$\mathbf{A}\ddot{\mathbf{e}} + \mathbf{K}_d\dot{\mathbf{e}} + \mathbf{K}_p\mathbf{e} = -\mathbf{f}_{ext} \tag{5.33}$$

where $\mathbf{e}$ is the tracking error vector defined as the difference between the actual end-effector trajectory $\mathbf{x}$ and its reference (or nominal) trajectory $\mathbf{x}_{ref}$:

$$\mathbf{e} = \mathbf{x} - \mathbf{x}_{ref} \tag{5.34}$$

and $\mathbf{A}$, $\mathbf{K}_d$ and $\mathbf{K}_p$ are matrices representing respectively the desired apparent mass, damping, and stiffness of the manipulator tip. These matrices are usually chosen as constant and diagonal to provide system decoupling. The desired external force is achieved indirectly by an appropriate choice of the reference position trajectory. If the boundary of the environment to be contacted is known to be $\mathbf{x}_w$, then the steady-state reference position of the end-effector normal to the contact surface may be chosen as

$$x^n_{ref} = x^n_w + k_p^{-1} f^n_{ext,d} \tag{5.35}$$

where the superscript n denotes the normal to the contact surface, $f^n_{ext,d}$ is the desired contact force on the environment, and k_p is a diagonal element of $\mathbf{K}_p$.

Letting

$$\begin{aligned} \boldsymbol{\Gamma}_r &= (\mathbf{J}_r \mathbf{M}_{rr}^{-1} \mathbf{J}_r^T)^{-1} \\ \mathbf{d}_r &= \mathbf{J}_r^T \boldsymbol{\Gamma}_r \dot{\mathbf{J}}_r \dot{\mathbf{q}}_r + \mathbf{c}_r \end{aligned}$$

the control torques which provide linearizing and nonlinear decoupling action on the system dynamics can be obtained by selecting the following control structure:

$$\bar{\boldsymbol{\tau}} = \hat{\mathbf{J}}_r^T \hat{\boldsymbol{\Gamma}}_r \boldsymbol{\tau}' - \hat{\mathbf{d}}_r + \hat{\mathbf{J}}_r^T \mathbf{f}_{ext} \tag{5.36}$$

Vector $\boldsymbol{\tau}'$ is sometimes referred to as the *servo* portion of the control law and the rest as the *model-based* portion (Craig 1986). $\hat{\boldsymbol{\Gamma}}_r$, $\hat{\mathbf{d}}_r$, and $\hat{\mathbf{J}}_r$ are estimates of $\boldsymbol{\Gamma}_r$, $\mathbf{d}_r$, and $\mathbf{J}_r$ respectively. Assuming exact measurement of system parameters, the estimated values are identical to the real ones, and the symbol $\hat{}$ can henceforth be dropped. The servo portion of the control law can be selected as

$$\boldsymbol{\tau}' = \ddot{\mathbf{x}}^* \tag{5.37}$$

where $\ddot{\mathbf{x}}^*$ is selected to satisfy the target impedance (equation (5.33)):

$$\ddot{\mathbf{x}}^* = \ddot{\mathbf{x}}_{ref} + \mathbf{A}^{-1}\mathbf{K}_d(\dot{\mathbf{x}}_{ref} - \dot{\mathbf{x}}) + \mathbf{A}^{-1}\mathbf{K}_p(\mathbf{x}_{ref} - \mathbf{x}) - \mathbf{A}^{-1}\mathbf{f}_{ext} \tag{5.38}$$

Substituting equations (5.37) and (5.38) into equation (5.36), the control torques for the slow subsystem can be expressed as

$$\begin{aligned}\bar{\boldsymbol{\tau}} = \mathbf{J}_r^T\boldsymbol{\Gamma}_r\{\ddot{\mathbf{x}}_{ref} + \mathbf{A}^{-1}\mathbf{K}_d(\dot{\mathbf{x}}_{ref} - \dot{\mathbf{x}}) + \mathbf{A}^{-1}\mathbf{K}_p(\mathbf{x}_{ref} - \mathbf{x}) - \mathbf{A}^{-1}\mathbf{f}_{ext}\}\\ -\mathbf{d}_r + \mathbf{J}_r^T\mathbf{f}_{ext}\end{aligned} \tag{5.39}$$

It is worth noting that although these torques are calculated based on the rigid model, the effectiveness of the control scheme is assessed based on the original flexible system.

5.3.2 Fast Control

For the fast control, equations (5.24) and (5.25) may be expressed as

$$\dot{\boldsymbol{\eta}} = \mathbf{D}\boldsymbol{\eta} + \mathbf{E}\boldsymbol{\tau}_f \tag{5.40}$$

where $\boldsymbol{\eta} = [\boldsymbol{\eta}_1^T \;\; \boldsymbol{\eta}_2^T]^T$, and if m and n are respectively the number of flexible degrees of freedom and the number of actuator torques, then

$$\mathbf{D} = \begin{bmatrix} \mathbf{0}_{mm} & \mathbf{I}_{mm} \\ -\mathbf{H}'_{ff} & \mathbf{0}_{mm} \end{bmatrix}; \quad \mathbf{E} = \begin{bmatrix} \mathbf{0}_{mn} \\ \mathbf{H}'_{fr} \end{bmatrix}.$$

Provided that matrix **E** insures controllability of the states (Readman 1994), the Linear Quadratic Regulator (LQR) can now be applied to this system. The LQR performance index which optimizes tracking error and energy expenditure may be expressed as

$$J = \int_0^{\infty}(\boldsymbol{\eta}^T\mathbf{Q}\boldsymbol{\eta} + \boldsymbol{\tau}_f^T\mathbf{R}\boldsymbol{\tau}_f)dt \tag{5.41}$$

where **Q** and **R** are symmetric weighting matrices which must be positive semi-definite and positive definite respectively. Expressing the feedback control law as

$$\boldsymbol{\tau}_f = -\mathbf{F}\boldsymbol{\eta} \tag{5.42}$$

the optimal control gain which minimizes the performance index J is given by

$$\mathbf{F} = \mathbf{R}^{-1}\mathbf{E}^T\mathbf{P} \tag{5.43}$$

where matrix **P** is the solution to the matrix Ricatti equation,

$$\mathbf{D}^T\mathbf{P} + \mathbf{P}\mathbf{D} - \mathbf{P}\mathbf{E}\mathbf{R}^{-1}\mathbf{E}^T\mathbf{P} + \mathbf{Q} = \mathbf{0}. \tag{5.44}$$

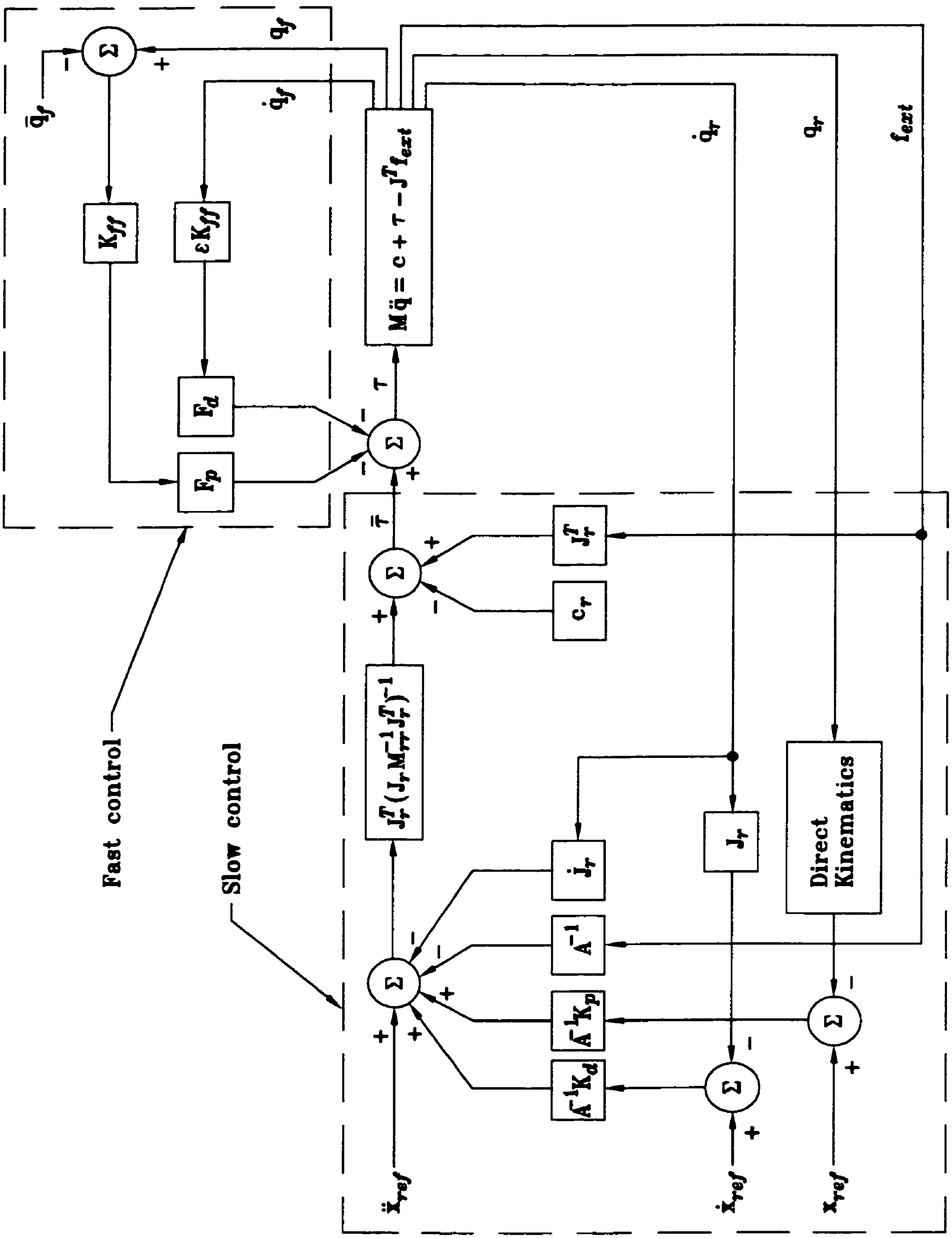

Figure 5.1: Block diagram of the composite control strategy

Chapter 6

Simulations, Discussions and Results

6.1 Program Description

The program developed to perform the dynamic simulations involving contact of multi-body systems was written in the FORTRAN language. Although the formulations described in this thesis were for general spatial (3-dimensional) motion, the simulation program is restricted to planar dynamics. It is felt that the study of planar dynamic simulations alone will give sufficient insight into the formulation presented in this thesis, and also provide a solid basis for a full 3D implementation of contact dynamics of multi-body systems.

Also, as already mentioned in Chapter 2, the computation of the equations of motion of individual finite elements of contacting bodies were carried out in symbolic form using the symbolic manipulator software MAPLE V. In the program, computations to be performed for dynamic simulation may be divided into *offline* and *online* operations.

Offline computations

Initial operations before time integration:

- Read input file: structure definition (length, mass, type of joints, kinematic architecture, finite element mesh, etc), initial conditions ($\mathbf{q}_{t=0}$, $\dot{\mathbf{q}}_{t=0}$), simulation specifications (t_f, Δt, tolerances, etc).
- For each subsystem, compute initial mass and stiffness matrices.
- For each subsystem, compute representative values of natural frequencies; then compute damping constants and damping matrix.
- For contacting bodies, if Guyan reduction method is used, compute matrix $\mathbf{G}$ of equation (4.62), and new matrices $\tilde{\mathbf{M}}$, $\tilde{\mathbf{C}}$ and $\tilde{\mathbf{K}}$ of equation (4.63).
- For contacting bodies, if 2^{nd} or 3^{rd} methods (described in Section 4.3.1) are used to calculate matrix $\hat{\mathbf{K}}^{-1}$ of equation (4.15), perform necessary matrix algebra to compute constant terms included in equations (4.46) and (4.57), respectively.

Online computations

Integrating from time t to $t + \Delta t$:

- Newton-Raphson iteration:
  1. For each subsystem, compute or assemble, depending on method used (Section 4.3.1) and whether Guyan reduction is used (Section 4.3.2), the mass, damping and stiffness matrices, and matrices $\hat{\mathbf{K}}$ and $\hat{\mathbf{K}}^{-1}$.
  2. For contacting bodies, update the conditions of contact*, based on the procedure described in Section 4.2.3.
  3. For each subsystem, update $\hat{\mathbf{K}}$ and $\hat{\mathbf{f}}$ of equation (4.13), and for each constraint set, update $\mathbf{g}$ of equation (4.14).

---

*In the first iteration, assume sticking contact, as discussed in Section 4.2.4.

4. For each subsystem, compute $\Delta\boldsymbol{\lambda}$ and $\Delta\mathbf{q}$ from equations (4.21) and (4.15) respectively. Update $\mathbf{q}$ and $\boldsymbol{\lambda}$ from equations (4.22) and (4.23) respectively.
5. If convergence criteria outlined in Section 4.2.5 is satisfied, stop iteration; otherwise, go back to step 1. Usually, 2 or 3 iterations are found to be sufficient for convergence.

- If composite control is used for force, trajectory and vibration control, slow control torques are obtained from equation (5.39), and fast control from equation (5.42), where $\mathbf{F}$ is the matrix of LQR control gains.
- Output results: generalized coordinates and velocities, forces, torques, etc.
- Go to next time step.

Apart from the use of FLEXLINK (Cyril et al. 1989) to model multi-body systems, a few other external subroutines were included in this program:

- Natural frequencies of subsystems are calculated using the EISPACK library of FORTRAN subroutines.
- The solution of the Ricatti equation (5.44) and of the optimal LQR control gain $\mathbf{F}$ in equation (5.43) are obtained by calls to a FORTRAN subroutine library created by CASCADE (Computer-Aided Systems and Control Analysis and Design Environment) and found in *Netlib*, a repository of public domain mathematical software. The LQR control gains, which are manipulator-configuration dependent, can therefore be calculated on-line at any desired sampling rate.

6.2 Program Validation

As validation tests of the FEM program, the impact problems of simple structures that can be handled analytically using Hertz's theory are simulated and the results compared. An example considered by Chaudhary & Bathe (1986) is used here for the sake of comparison. The direct impact of two spheres is shown in Figure 6.1. Due to the symmetrical nature of the problem and contacting bodies, axisymmetric elements may be used to model a single sphere which is considered to come into contact with a flat rigid surface. A final grid size of 128 elements was chosen (comparable to the example in Chaudhary & Bathe (1986)), which satisfies the requirements for good convergence of results[†] and sufficient number of contact nodes in the contact area. Figure 6.2 shows the finite element mesh used, where a finer grid was constructed near the contact area.

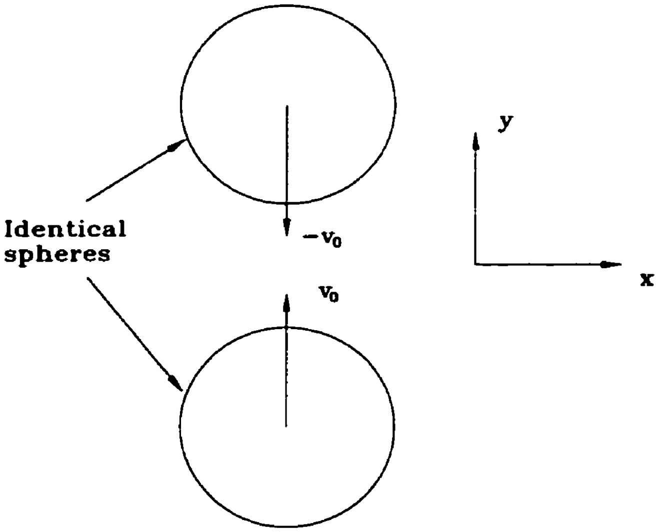

Figure 6.1: Impact of identical spheres

The radius of each sphere is taken as $R = 5$, the Poisson's ratio $\nu = 0.3$, the mass density $\rho = 0.01$, and the initial speed of impact as $v_0 = 3$ (values have no units, as in Chaudhary & Bathe (1986)). The Young's modulus was varied between 10^2 to 10^5. The quasi-static description of elastic impact between two spheres (or bodies which make contact over a circular area), based on Hertz theory, can be found in Johnson (1985) and is given in Appendix D. The impact dynamic simulation results obtained using the present finite element formulation are compared with those calculated using Hertz theory. Figures 6.3 and 6.4 show the force and displacement of the center of

---

[†] Further grid refinement (increase in the number of elements) did not yield appreciably better results.

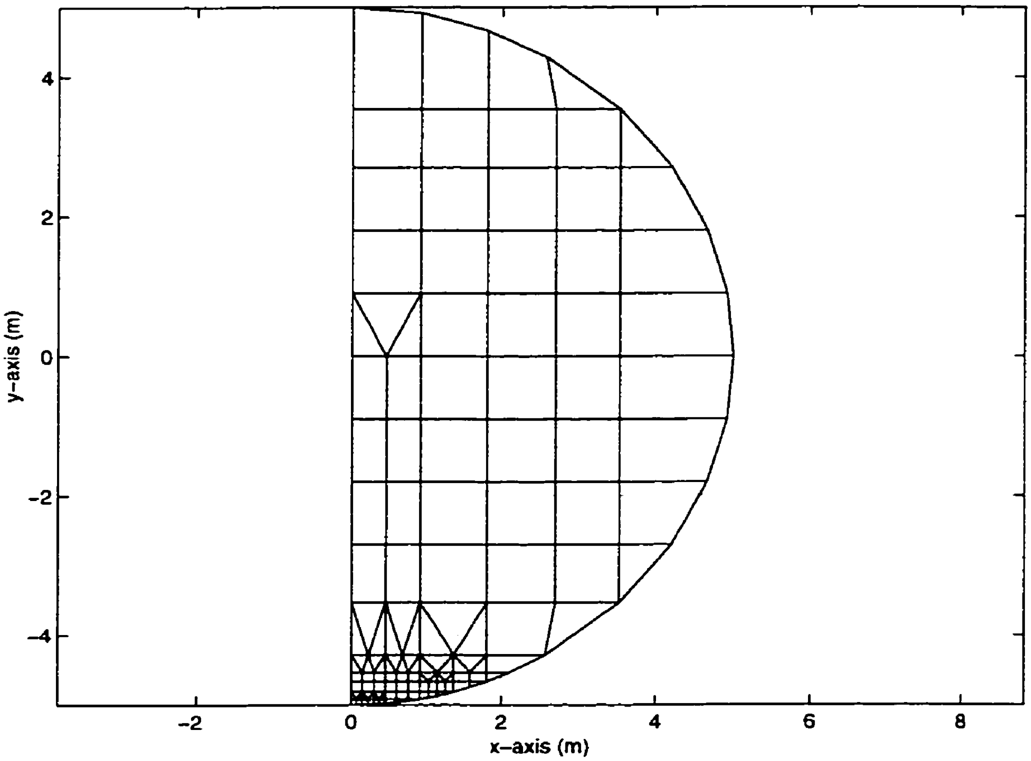

Figure 6.2: Finite element mesh of half a radial cross-section of a sphere

mass of one of the spheres through the duration of impact, and Figure 6.5 shows the developed normal contact tractions along the contact surface from the center to its boundary at the time of maximum deformation (which occurs at half the total impact time). All values are nondimensionalized as follows:

$$\frac{f}{f^*}, \ \frac{u}{u^*}, \ \frac{t}{t^*}, \ \frac{p}{p_0}, \ \frac{r}{a}$$

where f^* and u^* are respectively the contact force and displacement of a sphere at half the impact time t^*, which are also the maximum values because t^* is the time of maximum elastic compression before rebound starts. Pressure p_0 is the contact traction at the center of the contact circle of radius a at t^*. All these values pertain to those of the quasi-static Hertz theory (see Appendix D for further details). It is interesting to note in Figures 6.3 and 6.4 that as the Young's modulus E is increased, the results obtained from the present formulation approach those obtained using

Hertz theory. This is so even though as E is increased, the contact radius decreases and fewer number of nodes are available to represent the details of contact mechanics (see Figure 6.5). This is to be expected because Hertz theory is based on a quasi-static nature of contact which means that the deformation is assumed to be restricted to the vicinity of the contact area and to be given by the statical theory: elastic wave motion in the bodies is ignored and the total mass of each body is assumed to be moving at any instant with the velocity of its centre of mass (Johnson 1985). This quasi-static assumption can be used if the duration of the impact is long enough to permit stress waves to traverse the length of the contact body many times. In other words, Hertz theory is valid only if the ratio of contact time to wave time, which is of the order of $(\sqrt{E/\rho}/v_0)^{1/5}$, is much greater than unity. Thus, it makes sense that as E increases and the ratio increases, the results found using the two methods approach one another. Table 6.1 compares values of f^*, u^*, and t^* obtained using the present formulation and Hertz theory for different values of Young's modulus. It clearly shows that the difference decreases as E increases.

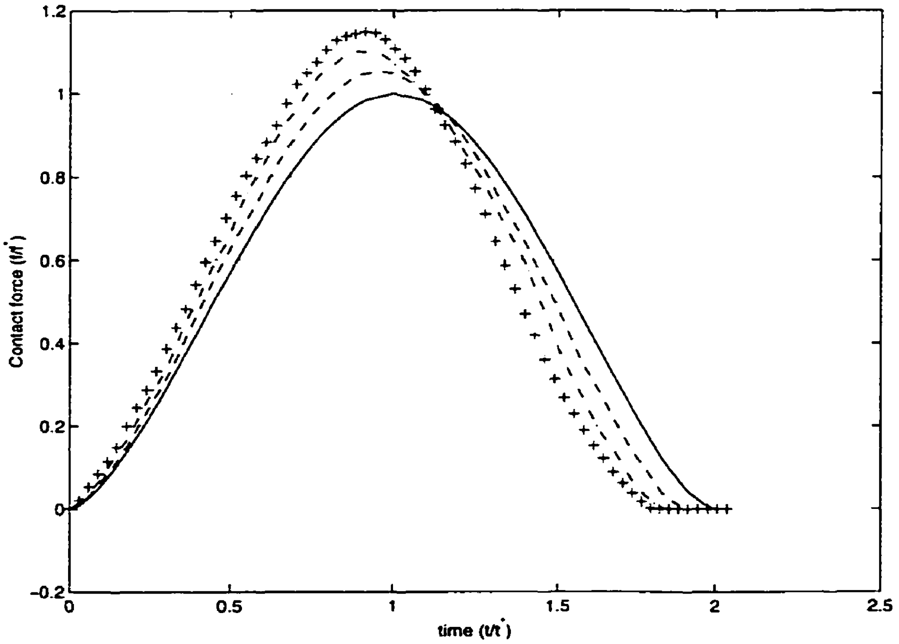

Figure 6.3: Contact force during impact (— Hertz; + $E = 10^2$; $- \cdot -$ $E = 10^3$; $--$ $E = 10^5$)

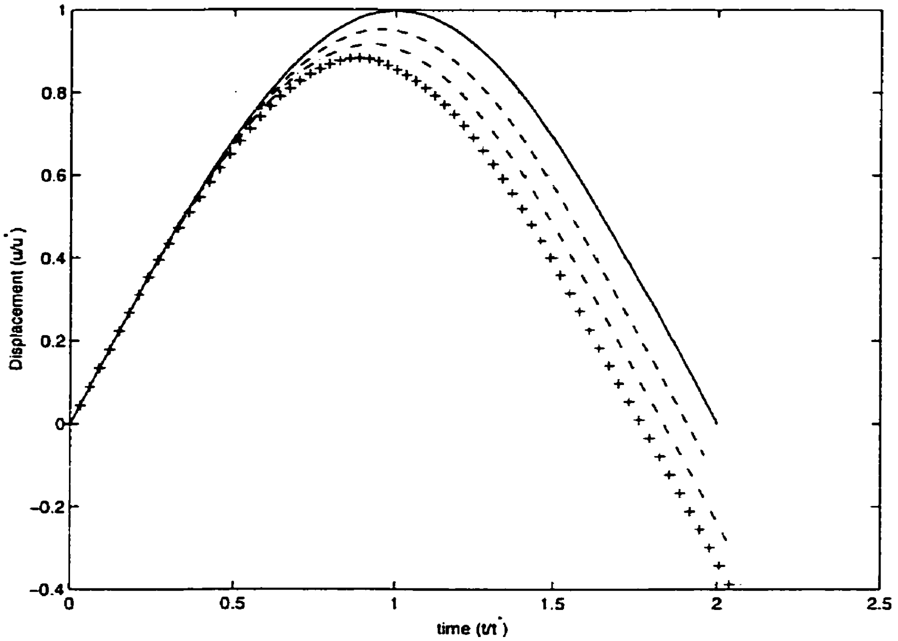

Figure 6.4: Displacement of the center of mass during impact (— Hertz; + $E = 10^2$; $- \cdot -$ $E = 10^3$; $--$ $E = 10^5$)

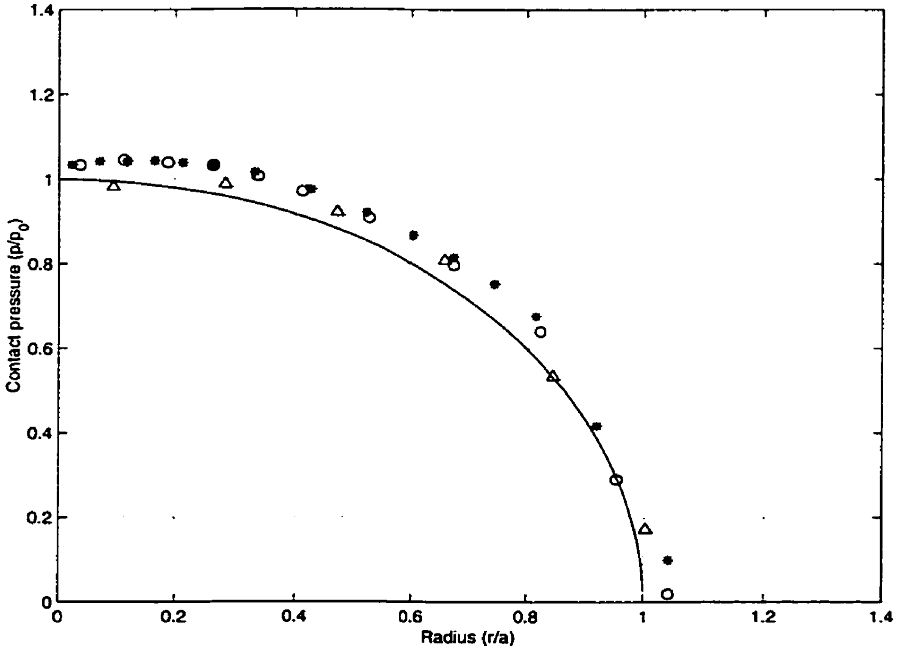

Figure 6.5: Pressure distribution along the contact surface (— Hertz; $*$ $E = 10^2$; $\circ$ $E = 10^3$; $\triangle$ $E = 10^5$)

Table 6.1: Comparison of results obtained from the present formulation and Hertz theory

E	Present Formulation	Hertz theory	Percent Difference
10^2	$f^* = 134.4$	$f^* = 117.0$	14.9 %
	$u^* = 0.4434$	$u^* = 0.5034$	11.3 %
	$t^* = 0.2250$	$t^* = 0.2467$	8.8 %
10^3	$f^* = 323.1$	$f^* = 293.9$	9.9 %
	$u^* = 0.1838$	$u^* = 0.2004$	8.3 %
	$t^* = 0.090$	$t^* = 0.0982$	8.3 %
10^5	$f^* = 1952.0$	$f^* = 1854.6$	5.2 %
	$u^* = 0.0303$	$u^* = 0.0318$	4.7 %
	$t^* = 0.0150$	$t^* = 0.0156$	3.8 %

As mentioned in Section 1.3, the subsystems which are categorized under "multi-body systems" are modelled using FLEXLINK (Cyril et al. 1989), an in-house general-purpose software package for the dynamic simulation of serial-link flexible manipulators. Substantial program verification was carried out by Cyril (1988), and subsequent users of the program (Jaar 1993, Kim 1994).

Partial verification of the program as a whole was done by comparison of results of the system rebound dynamics with those obtained using an impulse-momentum approach described in Section 1.2 (Kim 1994). However, no simulation result was found available in the literature on impact or sustained-contact dynamics of multi-body systems that studies what happens **during** impact or sustained contact. Generally, impulse-momentum approaches assume that impact occurs *instantaneously* and use principles of energy and momentum conservations, along with certain assumptions about the energy loss (e.g. coefficient of restitution) and friction during impact, to obtain rebound states at the end of impact. For certain assumed values of these parameters, the rebound dynamics results may agree quite well with those obtained using the finite element formulation. However, the choice of these parameters is arbitrary, and is usually determined based on experimental results. Thus, one of the benefits of carrying out a full finite element simulation of impact/contact dynamics, despite its computational cost, is that such impact characteristics as energy loss and friction can be obtained without the need of elaborate experiments, by using more commonly available material properties such as damping ratios and coefficients of friction.

Three efficient solution methods for contacting bodies which do not compromise solution accuracy are used: (*i*) the second method of computing $\hat{\mathbf{K}}$ and $\hat{\mathbf{K}}^{-1}$ presented in Section 4.3.1; (*ii*) Guyan reduction method (Section 4.3.2); and (*iii*) elimination of the flexible portion of the nonlinear forces (Section 4.3.3). The validity of these methods have been verified through comparative studies of the simulation results of various scenarios (most of the simulation cases described later in this chapter); it was found that in all cases the use of these methods produce very close results to those obtained using the full solution method.

With respect to the second method of computing $\hat{\mathbf{K}}$ and $\hat{\mathbf{K}}^{-1}$, the validity of the assumption that deformations are negligible compared to the dimensions of the body and thus can be eliminated from the mass matrix, is further demonstrated using a problem addressed by Misra et al. (1998). This paper considers the dynamics of flexible appendages connected to a spinning rigid spacecraft with an offset from the spacecraft center of mass, as shown in Figure 6.6. It was observed that neglecting second and higher order terms in elastic displacements and velocities from the equations of motion resulted in an inaccurate and different response from that of the full nonlinear analysis. In fact, the response turned out to become unstable for positive offset (Figure 6.6-(a)). The present method was applied to this system, i.e., only the elastic displacements from the mass matrix were removed from the equations of motion: the response of the system turned out to be indistinguishable from that of the full nonlinear analysis. This result further demonstrates the validity of the present method, even for different and more sensitive systems, where the elastic displacements are relatively larger than those dealt with in this thesis.

Finally, in all uncontrolled simulation cases where there is no energy input into the system, the total energy of the system was plotted against time to verify the principle of energy conservation.

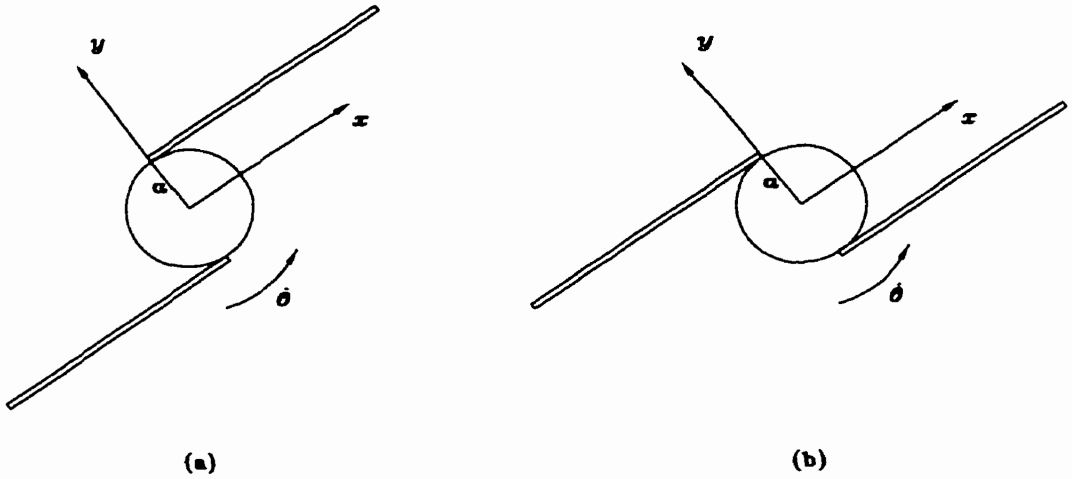

(a) (b)

Figure 6.6: Spinning spacecraft and appendages with an offset a

6.3 Impact Dynamics

First, the frictionless case of impact dynamics is considered, followed by the case of impact with friction. Control is not applied in the following cases, except in Section 6.5.

6.3.1 Frictionless Case

The problem of a spacecraft-mounted two-link flexible manipulator system impacting a satellite is considered here, as seen in Figure 6.7. No friction is assumed to be acting at the contact surfaces. The spacecraft and the manipulator system are treated as "multi-body systems", and the end-effector and satellite to be captured as "contacting bodies". The spacecraft is assumed rigid, and its orbital rate Ω (angular velocity of the orbital frame with respect to the inertial frame) is taken as $1.157 \times 10^{-3} rad/sec$. The problem of orbit maintenance is not considered, i.e., it is assumed that the center of mass of the spacecraft follows a prescribed orbital trajectory. The satellite, however, is modelled as a free-floating body. The manipulator links are modelled as *Euler-Bernoulli* beams, and the assumed modes method (Meirovitch 1967) is used for the discretization of the bending motion, where eigenfunctions of a cantilever beam are chosen as the admissible functions (Section 3.1.2). One mode was used to model each link. It has been reported by some researchers (Cyril 1988, Fattah 1995, Jaar 1993) that the first one or two modes play the dominant roles in many situations; thus, fairly good accuracy can be achieved with only one mode.

The satellite is modelled as an octagonal body and the end-effector as a U-shaped gripper. The end-effector is chosen to play the role of *contactor*, and the satellite the role of *target*. A finite element mesh, made up of 4-node quadrilateral (QUAD4) and 3-node triangular (CST) elements, is constructed on these two bodies, where a finer grid is applied near contact surfaces, as shown in Figures 6.8 and 6.9. The Young's modulus of the end-effector and payload were taken as $E = 7 \times 10^{10} (N/m^2)$.

The three computationally efficient solution methods for contacting bodies, mentioned in Section 6.2, were applied on the end-effector and payload after verification of their validity. For Guyan reduction, the *master* degrees of freedom, comprising approximately 35% of the total number of degrees of freedom, were chosen to include those pertaining to potential contacting nodes and those with lower K_{ii}/M_{ii} ratio. This arrangement yielded a computer simulation time of less than 20% of that of the full model, with negligible discrepancy in the results. The elimination of the flexible portion of the nonlinear forces, discussed in Section 4.3.3, further contributed to an additional 30% reduction in simulation time.

The contact scenario (Figure 6.7) is as follows: the manipulator system reaches out to capture the satellite but rebounds with almost no loss of energy. The only source of energy loss is in the form of structural damping of 1% of the critical damping for contacting bodies and flexible links. The material specification of the system is given in Table 6.2. The non-zero initial conditions immediately before impact are given in Table 6.3. All the generalized coordinates and velocities corresponding to the flexible degrees of freedom are initially assumed to be equal to zero. The manipulator joint rates are such that just before impact with the payload, the end-effector moves in the local horizontal direction with a speed of 0.1 m/sec (Figure 6.7). The basic solution methods, system specifications, configurations and initial conditions outlined above apply throughout this chapter unless otherwise stated, in which case some features may be added or modified to the existing system description.

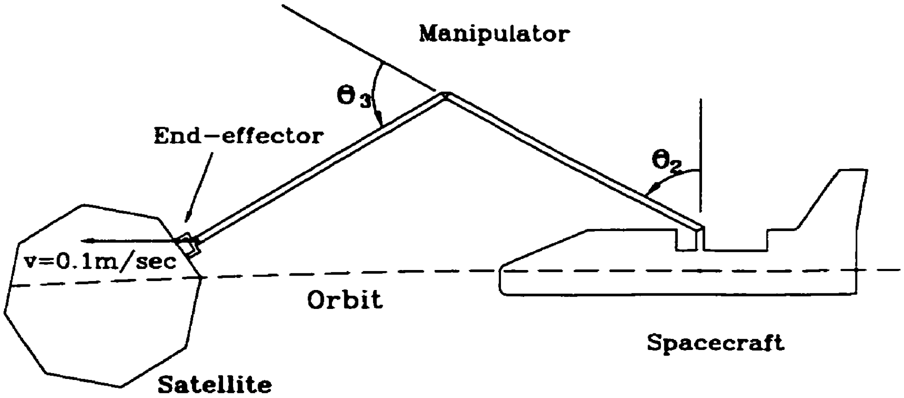

Figure 6.7: Impact scenario

Table 6.2: Material specification of the system

Body	length (m)	mass (kg)	EI (Nm^2)	J_{zz} (kgm^2)
Spacecraft	N/A	1×10^5	N/A	8×10^5
Link 1	8.13	163	88,100	3591
Link 2	8.13	163	88,100	3591
End-effector	N/A	2.3	N/A	0.18
Payload	N/A	884.3	N/A	2495

$EI =$ Flexural stiffness

$J_{zz} =$ Moment of inertia about origin (joint)

The forces acting at the end-effector joint during impact are shown in Figure 6.10. All x and y directions in these figures refer to those of the corresponding local reference

Table 6.3: Initial conditions of the system

Body	Generalized Coordinates (°)	Generalized Velocities (°/s)
Spacecraft	θ_1=0	$\dot{\theta}_1$=0
Link 1	θ_2=67.3	$\dot{\theta}_2$=0.911
Link 2	θ_3=45.4	$\dot{\theta}_3$=-1.82
End-effector	θ_4=0	$\dot{\theta}_4$=0.911
Payload	θ_p=0	$\dot{\theta}_p$=0

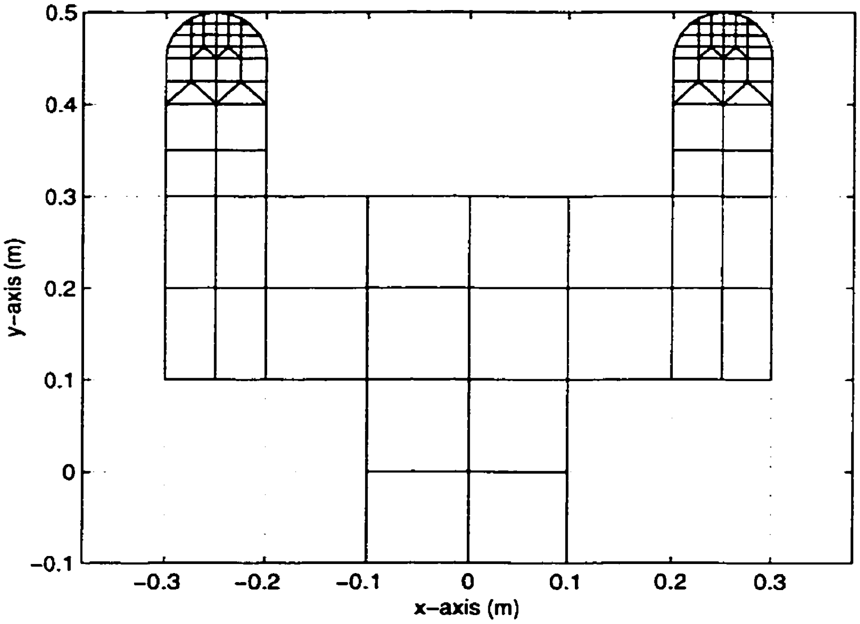

Figure 6.8: Finite element mesh of the end-effector

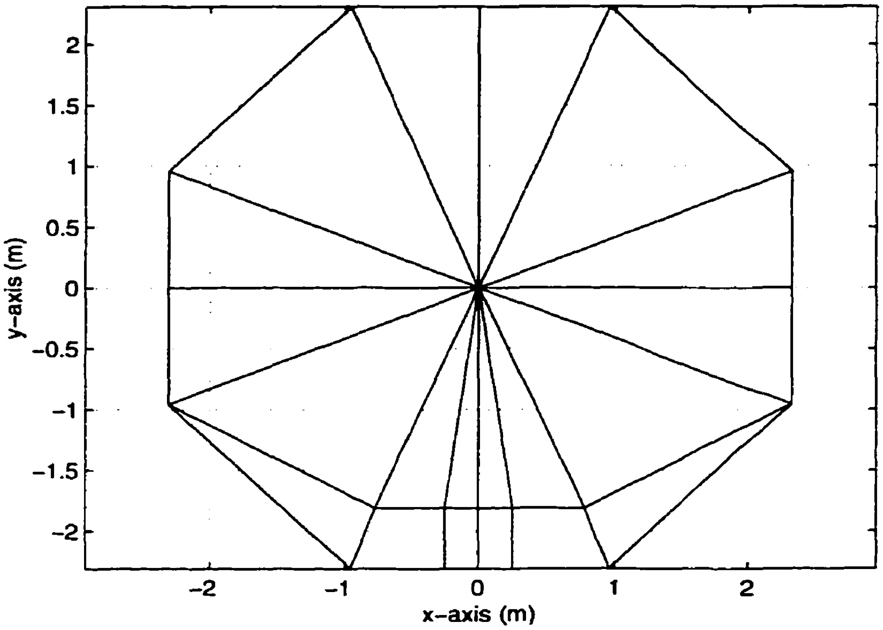

Figure 6.9: Finite element mesh of the payload

frames (Figures 6.8 and 6.9). It can be seen that the duration of impact is about $3.5 \times 10^{-4} sec$. As expected, the end-effector joint force is quite high in the y-direction (normal to the contact surface) and reaches a maximum of approximately $15 \times 10^4 N$ at half the impact time, which is also the point of maximum compression. It can also be observed that the force due to elastic vibrations of the end-effector resulting from impact is non-negligible even after impact, which is contrary to the assumption of Hertz theory. In the x-direction (tangential to the contact surface) the force is relatively insignificant due to the assumption of frictionless contact ($f_t/f_n \approx 0.002$). The total energy of each of the three subsystems (spacecraft-mounted manipulator system, end-effector and payload) are plotted in Figure 6.11 (orbital energy is not included). The end-effector initially has negligible total energy but builds potential energy as it deforms until a maximum is reached at half the impact time and then returns to its initial condition at the end of impact. The manipulator, on the other hand, starts out with a sizeable kinetic energy, loses some of it until half impact-time where it is mostly made up of elastic energy due to the deflections of the links, and regains some kinetic energy during the rebound phase of impact. The payload initially has no energy but gains some kinetic energy imparted by the manipulator during impact. The addition of all three plots is equal to the total energy of the whole system which must be a constant as shown in Figure 6.12. The displacements of the end-effector joint and payload-center are shown in Figure 6.13. In the y-direction, the displacement of the end-effector is comparable in profile to that of the elastic sphere presented in Section 6.2, while in the x-direction, the displacement profiles of both the end-effector and payload are scarcely affected by the impact, due to the assumption of frictionless surfaces. The velocities of the end-effector joint and payload-center are shown in Figure 6.14. The rotation angle of the end-effector with respect to the payload and the rotation angle of the payload are shown in Figure 6.15. With respect to the motion of the end-effector joint, unlike its displacement profiles (Figure 6.13) which do not show oscillatory behaviour because its motion is constrained by the tip of the manipulator, its rotational motion contains oscillatory behaviour. However, these angles, along with the payload displacement in the x direction, are quite small with both bodies because the resultant impact force acts approximately along the line joining their centers of mass. The rotation rates are shown in Figure 6.16.

The post-impact simulation results are shown in Figures 6.17 - 6.20. Figure 6.17 shows the joint angles of the manipulator during the first 50 seconds after impact, where θ_1 is the attitude drift of the spacecraft, while θ_2 and θ_3 are the angles of rotation of the two links. Structural damping was included in the system (1 % of critical damping), which has the effect of damping out the vibrations of the links (Figure 6.19), and also results in the gradual decay of the total energy of the multi-body system (Figure 6.18). Figure 6.20 shows snapshots of the post-impact rebound motion of the manipulator system and payload at every 10 seconds. The manipulator stretches out to impact against the payload, and rebounds as it folds back on itself.

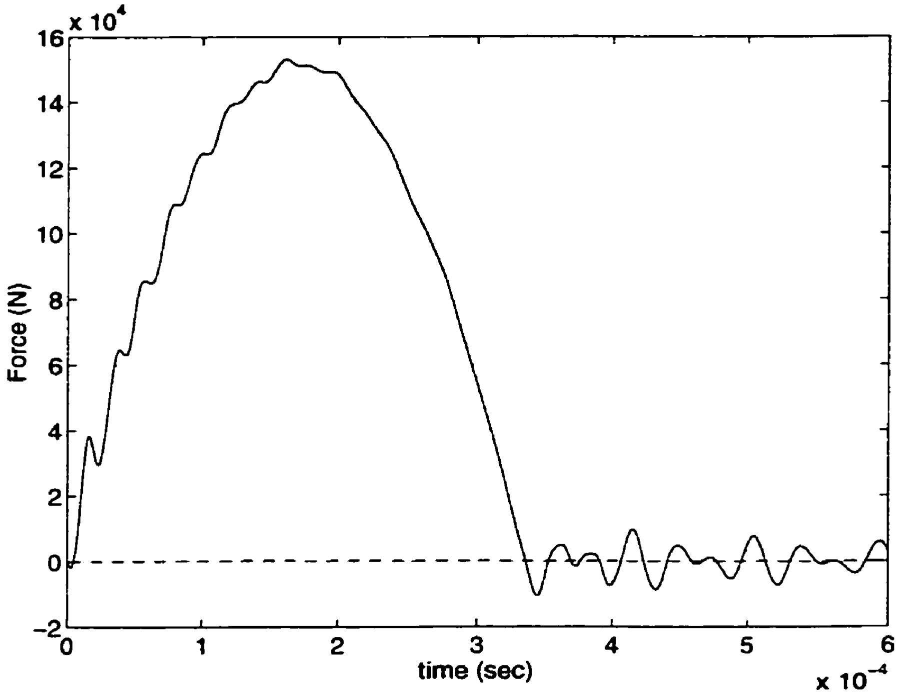

Figure 6.10: End-effector joint forces: frictionless case. (—— x-dir, — y-dir)

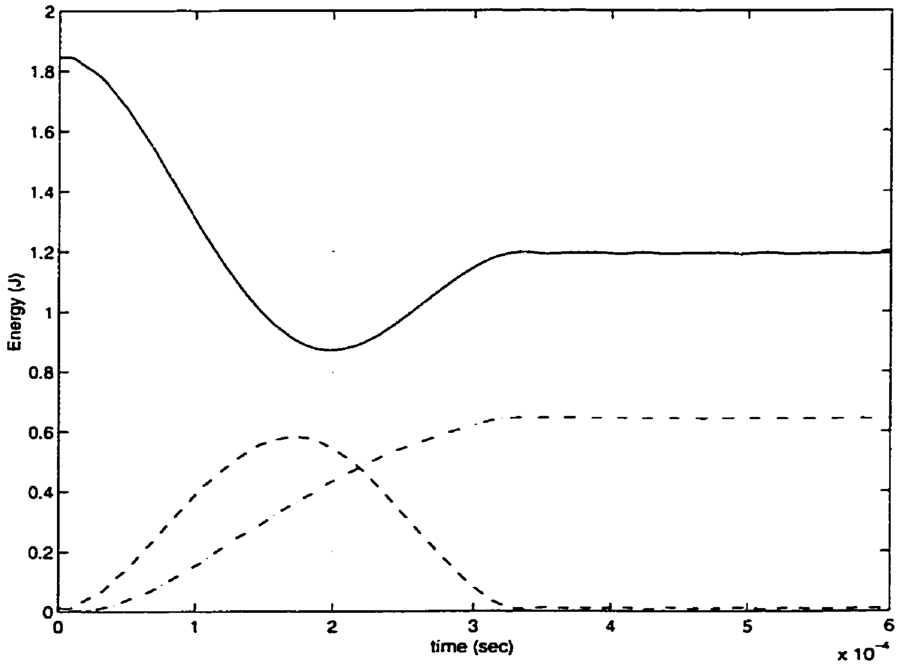

Figure 6.11: Energy: frictionless case. (— • — Payload, —— End-effector, — Manipulator)

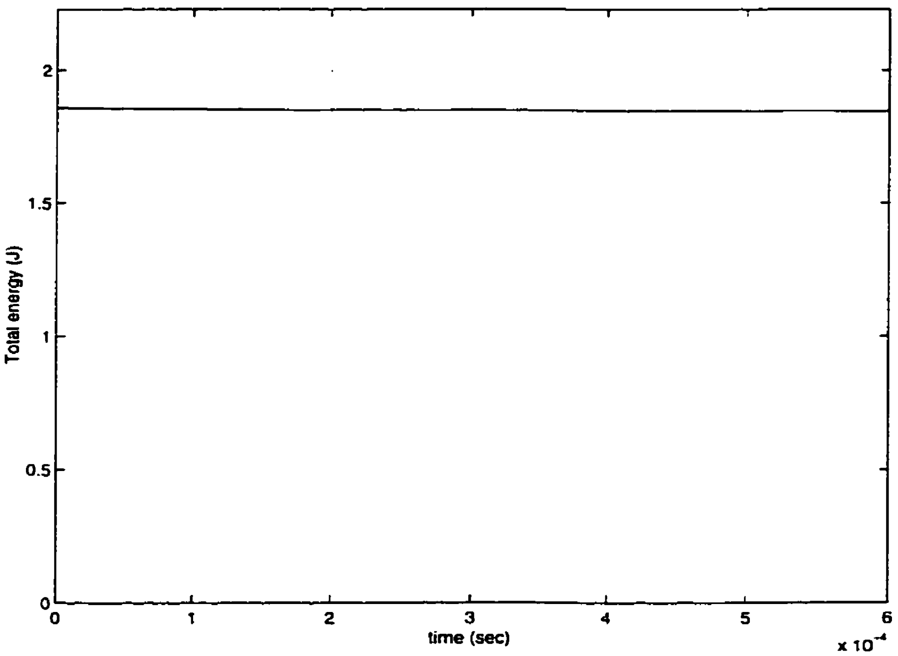

Figure 6.12: Total Energy: frictionless case.

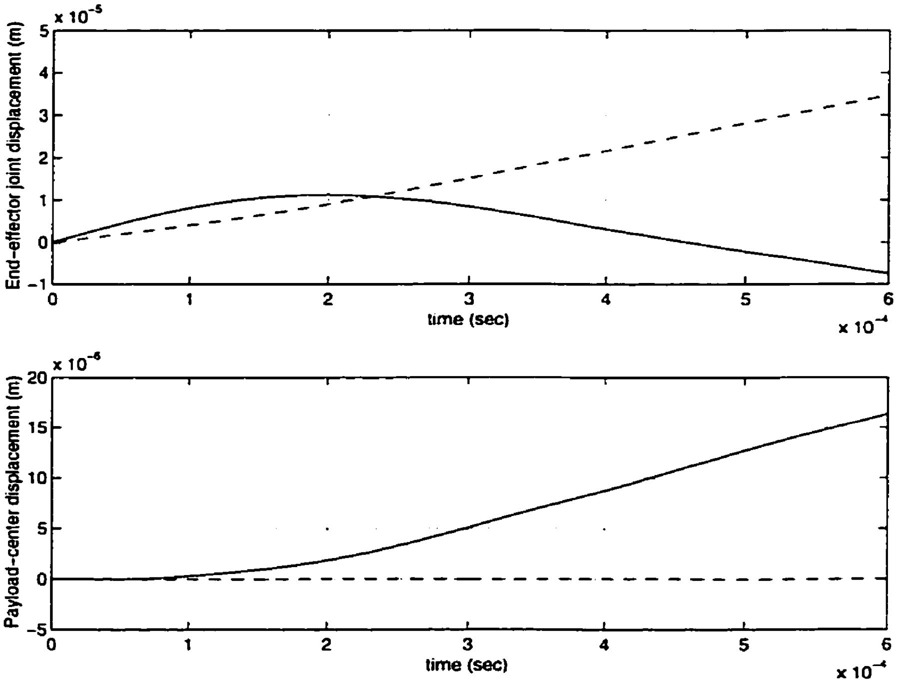

Figure 6.13: Displacements of contacting bodies: frictionless case. (-- x-dir, — y-dir)

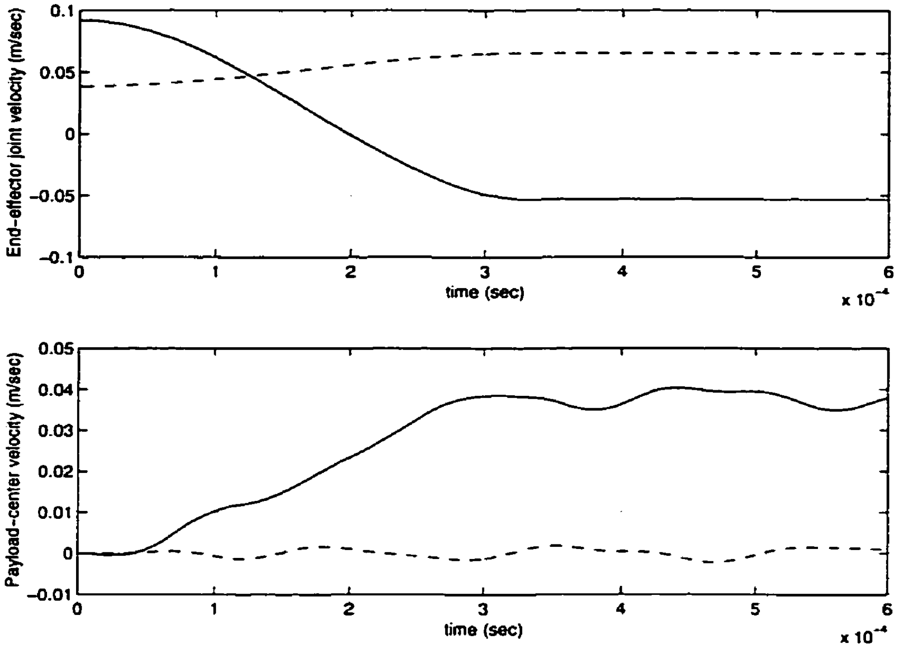

Figure 6.14: Velocities of contacting bodies: frictionless case. (-- x-dir, — y-dir)

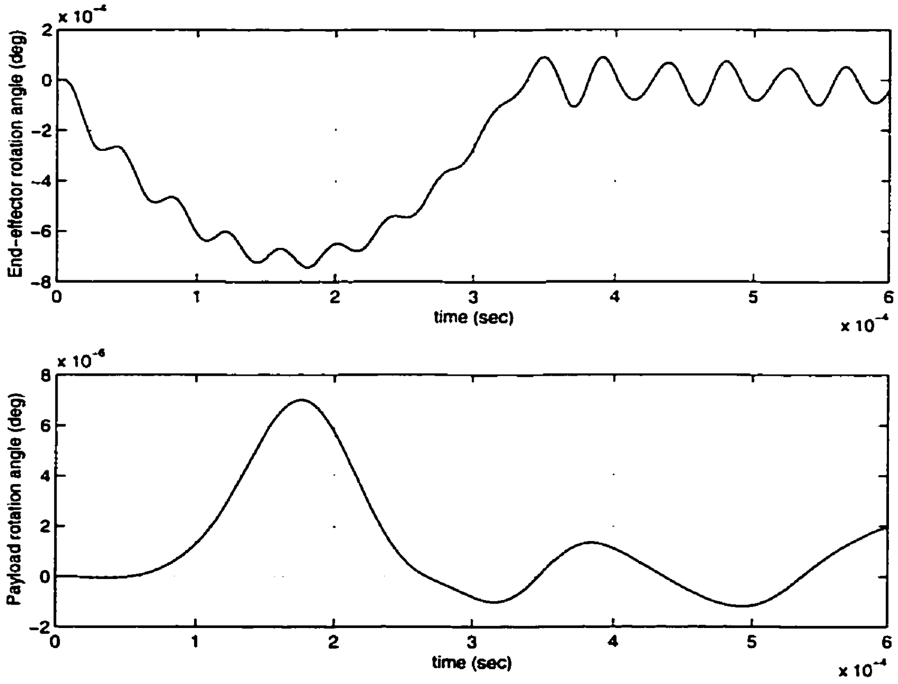

Figure 6.15: Rotation angle of the end-effector with respect to the payload and the rotation angle of the payload: frictionless case.

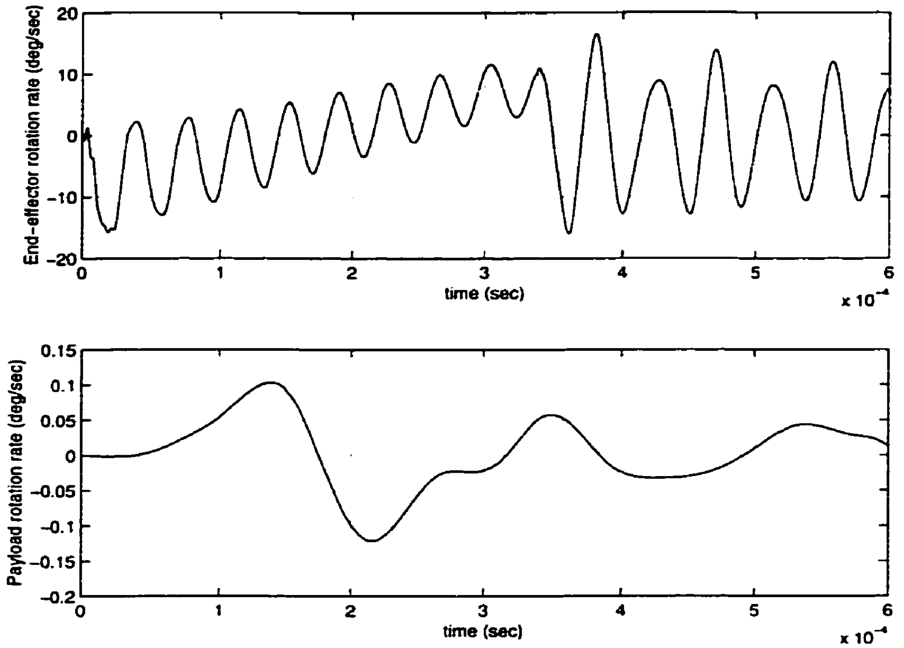

Figure 6.16: Rotation rates of contacting bodies: frictionless case.

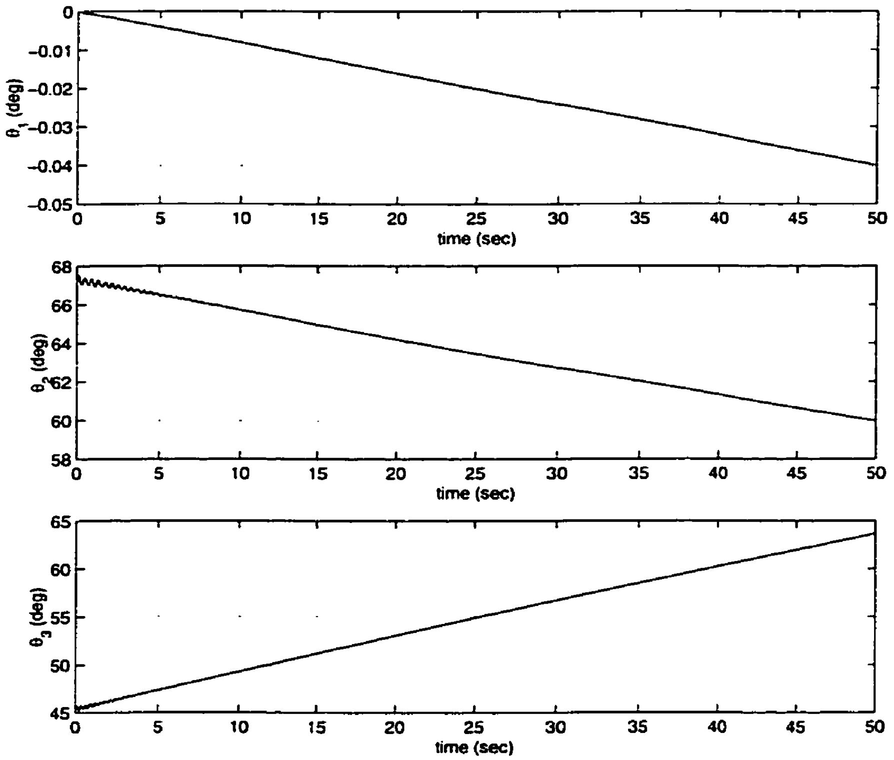

Figure 6.17: Joint angles of multi-body system vs. time: frictionless case.

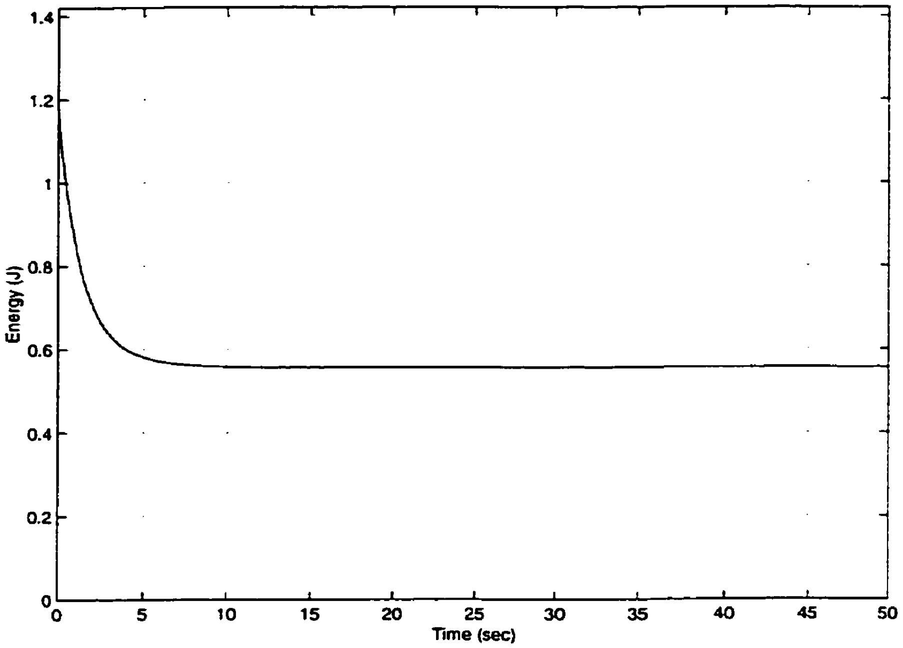

Figure 6.18: Total energy of multi-body system vs. time: frictionless case.

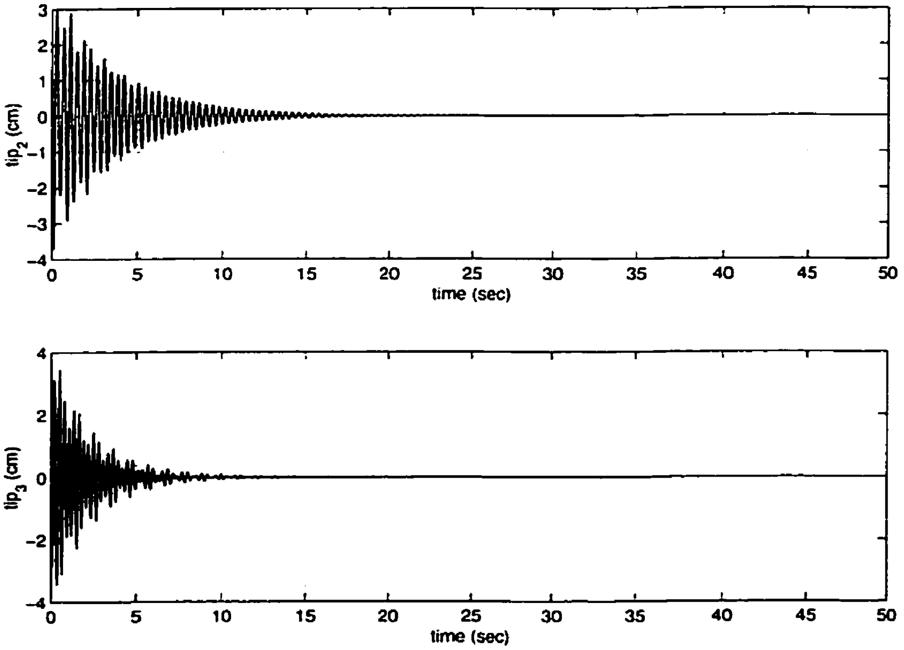

Figure 6.19: Tip deflections of manipulator links vs. time: frictionless case.

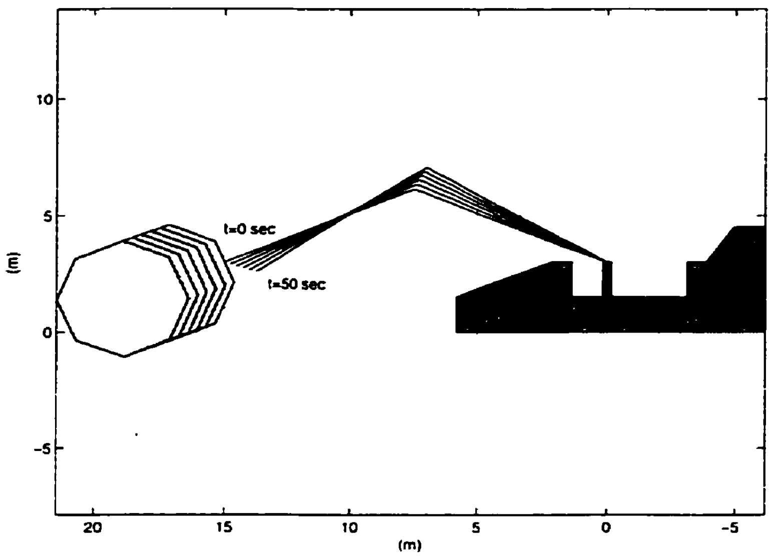

Figure 6.20: Configuration of the system from time = 0 to 50 sec: frictionless case.

6.3.2 Impact with Friction

In this case, it is assumed that there is friction acting at the contact surfaces. Coulomb friction, based on the model described in Sections 4.2.3 and 4.2.4, is applied on the contact surfaces with $\mu_s = 0.2$ and $\mu_d = 0.15$. The forces acting at the end-effector joint during impact are shown in Figure 6.21. In the y direction, the force profile is similar to that of the frictionless case, but in the x direction, unlike the frictionless case, substantial force is observed due to the frictional effects. The total energy of each of the three systems are plotted in Figure 6.22 and the addition of all three plots is shown in Figure 6.23. The displacements of the end-effector joint and payload-center are shown in Figure 6.24. Also, the velocities of the end-effector joint and payload-center are shown in Figure 6.25. The rotation angles of the respective bodies are shown in Figure 6.26. When comparing these results with those of the frictionless case, one can observe a substantial change in displacement of the payload in the x-direction, and also an increase in the rotation of the contacting bodies because in this case there is a friction force acting in the local x-direction at the contact surfaces, which provides a moment about their centers of mass. The rotation rates are shown

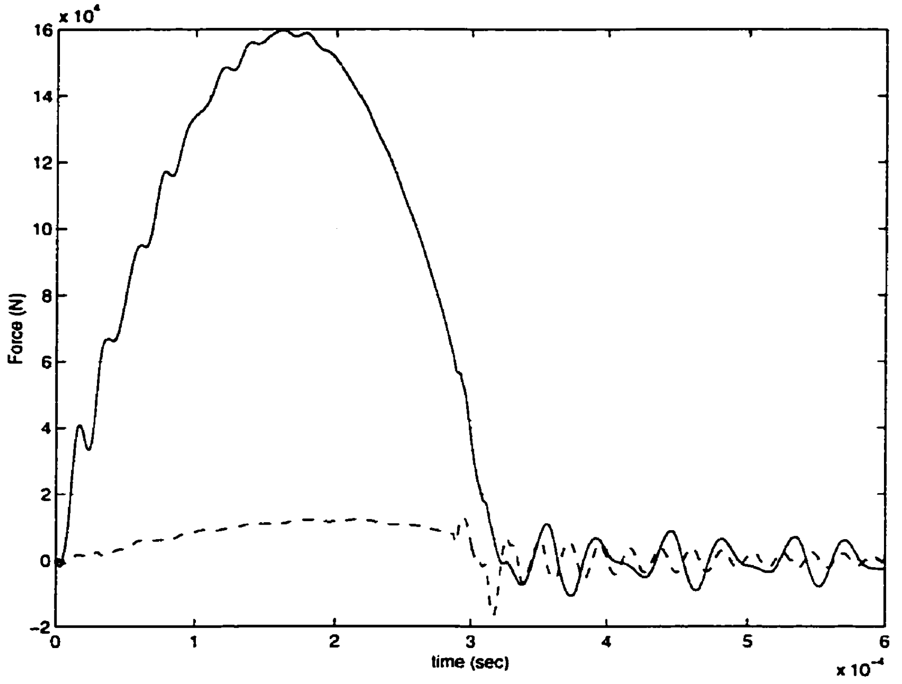

Figure 6.21: End-effector joint forces: friction case. (— — x-dir, — y-dir)

in Figure 6.27.

The post-impact simulation results are shown in Figures 6.28–6.31. The results are similar to the frictionless case of Section 6.3.1, but due to the tangential contact force component resulting from friction, the payload acquires a small counterclockwise rotational speed and the manipulator system rebound trajectory is also influenced by this frictional force (see Figure 6.31 and compare with 6.20). Comparing the energy decay of the two cases (Figures 6.18 and 6.29), the frictionless impact case seems to excite more link vibrations for link 3, so that a higher percentage of post-impact energy decay is observed in this case.

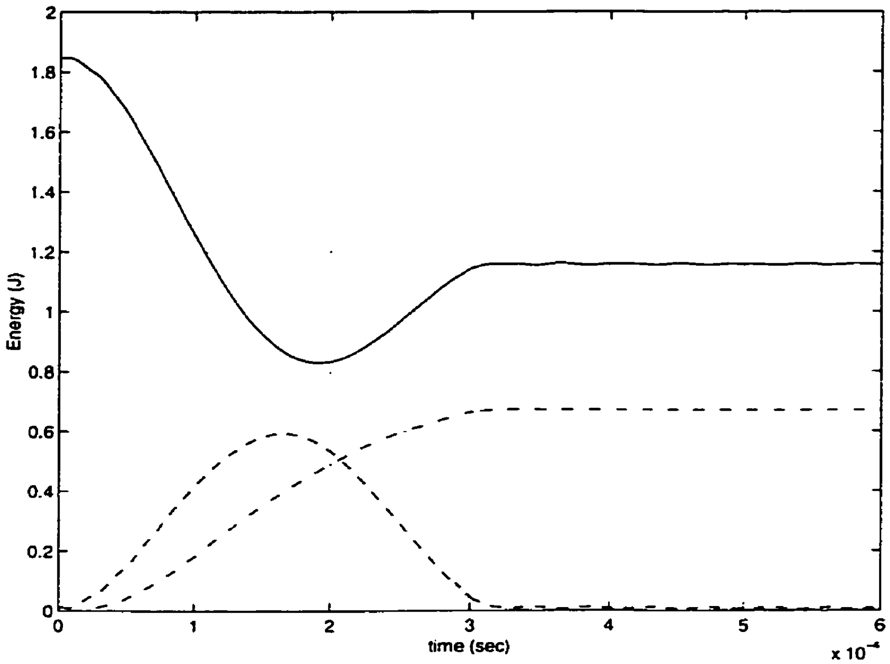

Figure 6.22: Energy: friction case. (—·— Payload, –– End-effector, — Manipulator)

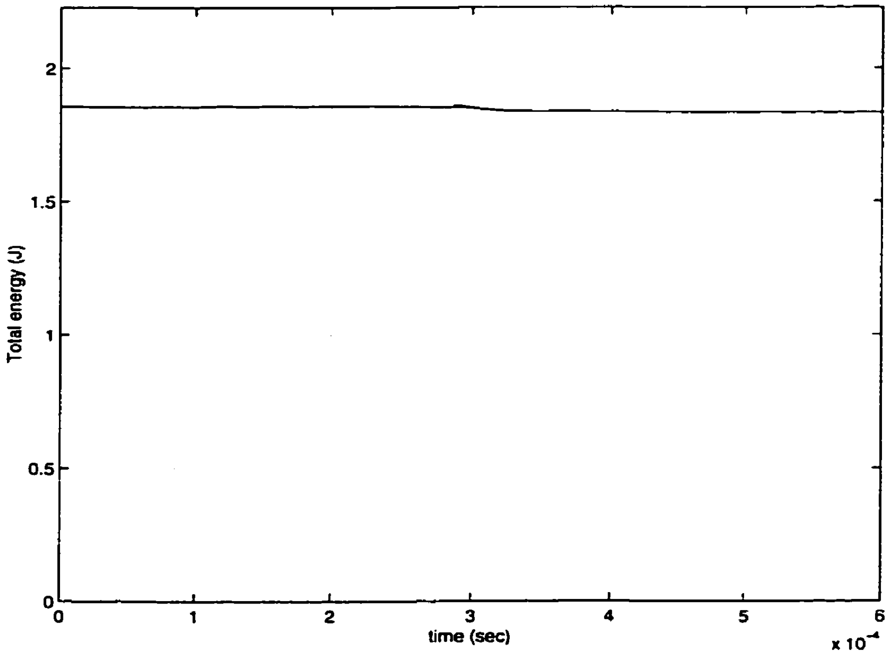

Figure 6.23: Total Energy: friction case.

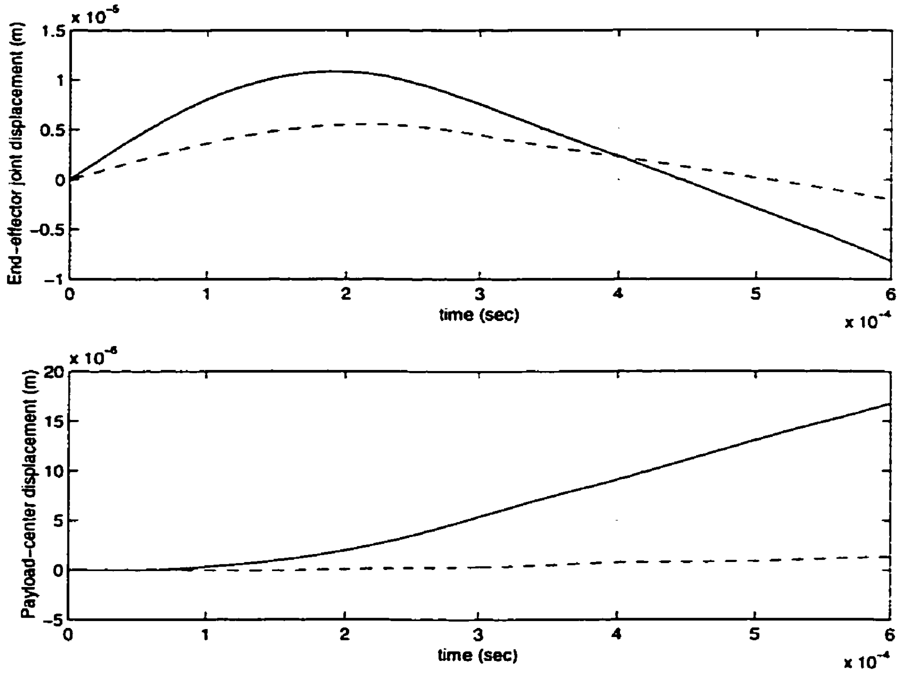

Figure 6.24: Displacements of contacting bodies: friction case. (— — x-dir, — y-dir)

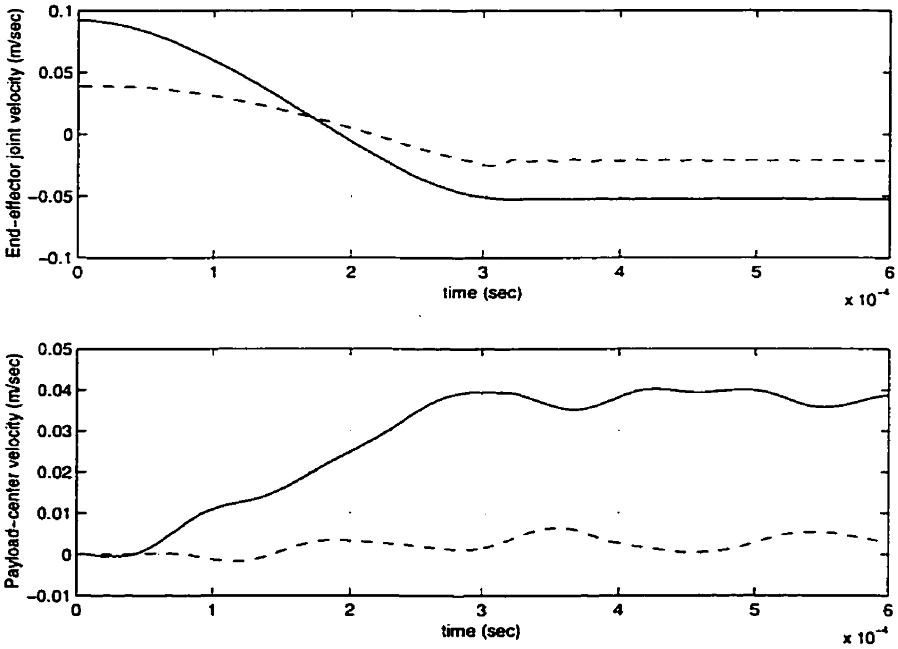

Figure 6.25: Velocities of contacting bodies: friction case. (— — x-dir, — y-dir)

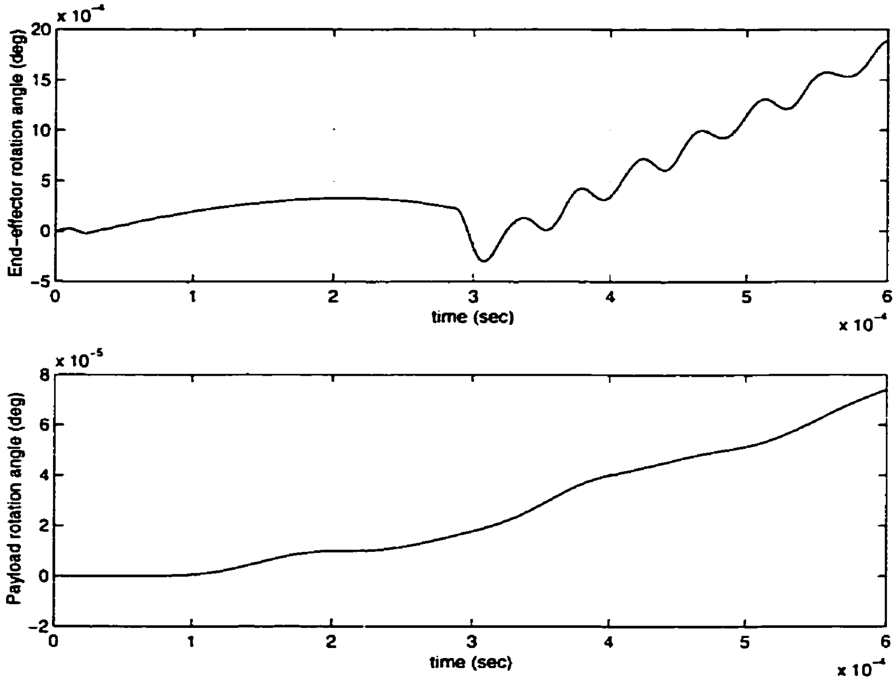

Figure 6.26: Rotation angles of contacting bodies: friction case.

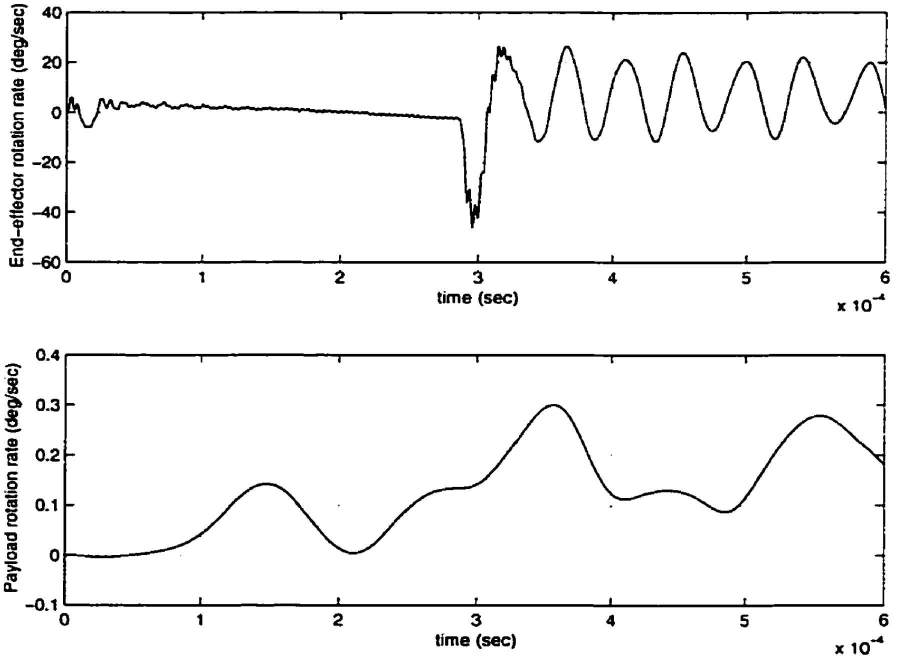

Figure 6.27: Rotation rates of contacting bodies: friction case.

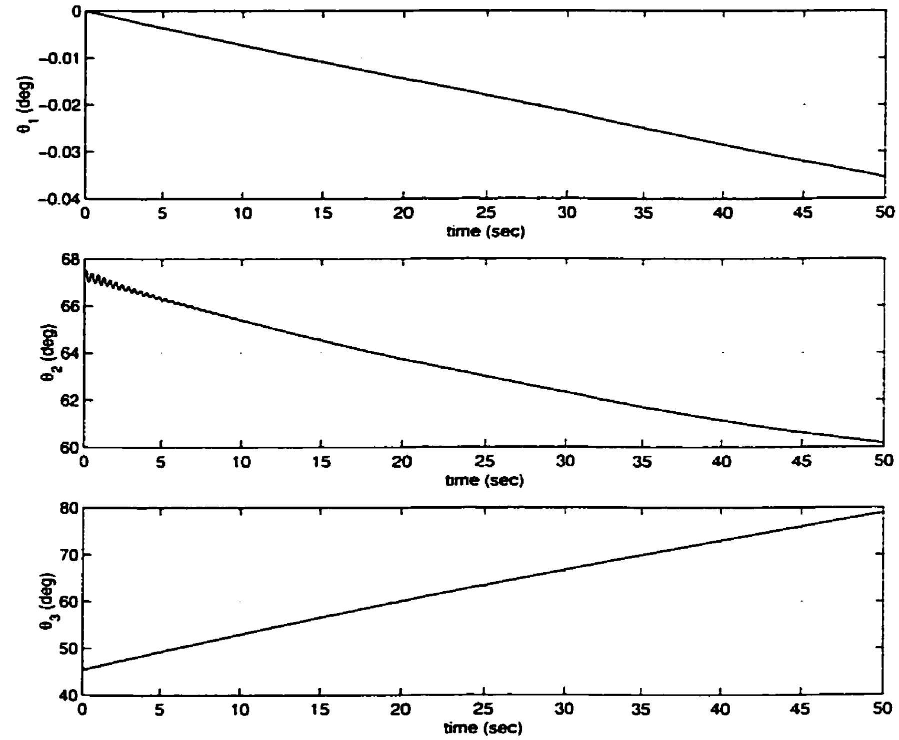

Figure 6.28: Joint angles of multi-body system vs. time: friction case.

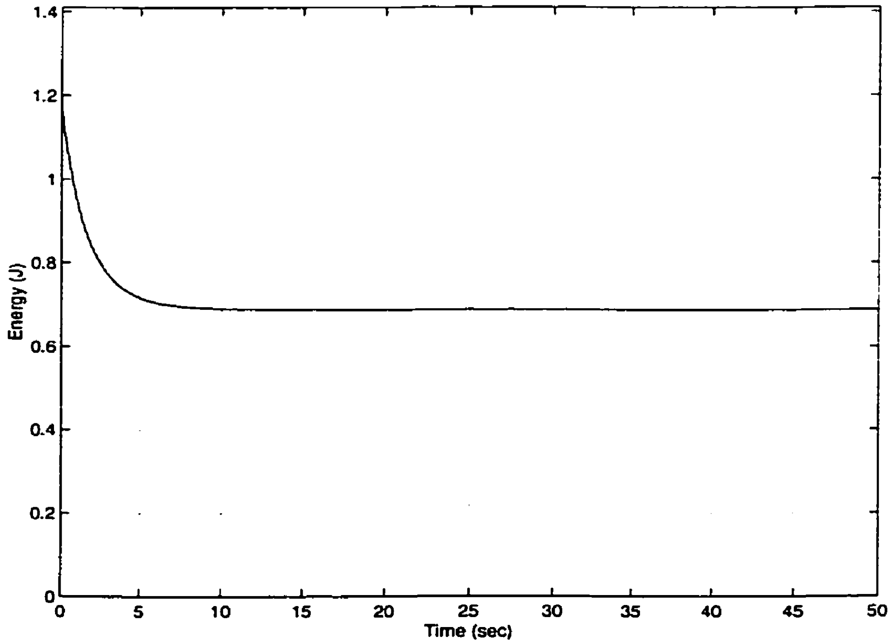

Figure 6.29: Total energy of multi-body system vs. time: friction case.

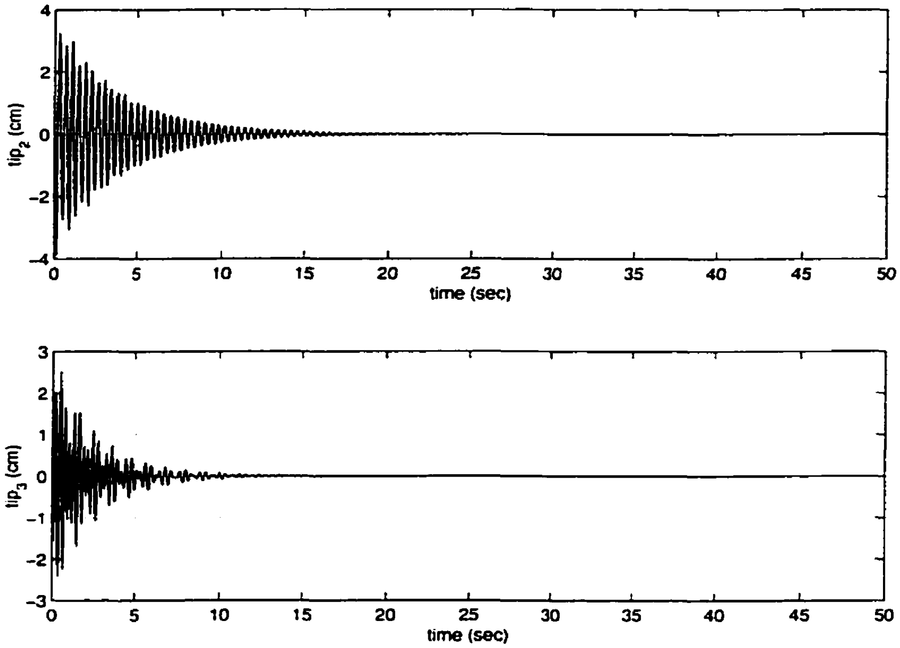

Figure 6.30: Tip deflections of manipulator links vs. time: friction case.

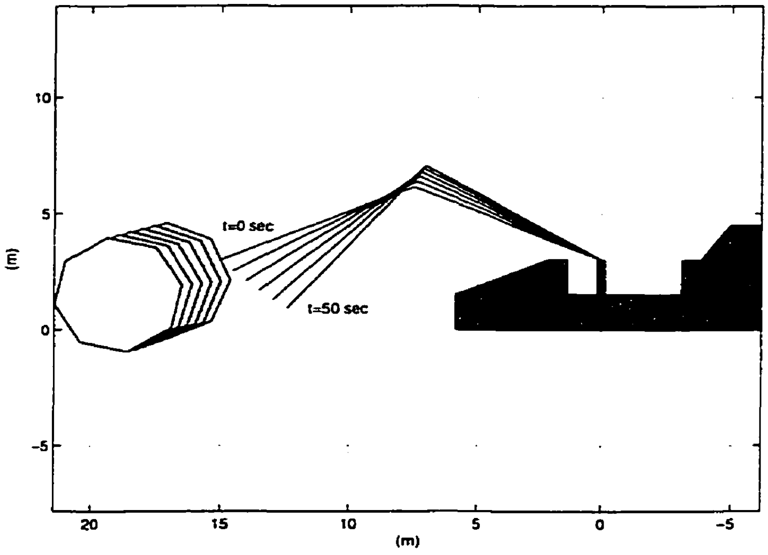

Figure 6.31: Configuration of the system from time = 0 to 50 sec: friction case.

6.3.3 Other Impact Scenarios

A few other impact scenarios are considered here. The same system parameters and initial conditions as in previous cases were used here except that two antennas, modelled as flexible beams, are added to the satellite to be captured, where the corresponding revolute joints may be either free or locked. The two antennas are identical and have the following material properties: mass (m) = 50 kg, length (l) = 5 m, flexural stiffness (EI) = $5 \times 10^3 N.m^2$, and moment of inertia about joint (J_{zz}) = 416.67 $kg.m^2$. To ease computational demands, softer elastic moduli were used to model the contacting bodies: $E_{ee} = 10^5 N/m^2$ and $E_p = 10^6 N/m^2$. In cases 1 and 2, the initial configuration of the system is as shown in Figure 6.32. In case 1 the antenna joints are free, and in case 2 they are locked. Figures 6.33–6.38 and 6.39–6.43 show the impact dynamics response of the system for cases 1 and 2 respectively. The tip deflections of the antennas in the two cases show drastic differences. The frequency of vibration in case 1 is much higher than in case 2, which is due to the coupling with the rigid-body rotational dynamics[‡]. On the other hand, larger amplitudes of vibration are observed in case 2. The translational and rotational motion of the payload in case 1 is greater that in case 2 which means that the locked antenna joints in case 2 provide greater resistance to the motion of the main payload body.

A different normal direction of the contact surface results in quite different post-impact dynamics. A vertical orientation of the payload at the beginning of impact as shown in Figure 6.44, results in the post-impact dynamics trajectory shown in Figure 6.45 for the free antenna joint case, and Figure 6.46 for the locked antenna joint case. It is interesting to note that the vertical orientation of the payload causes friction to act in the opposite direction to that of the two previous cases, which produces a clockwise rotation of the payload (as opposed to counterclockwise in cases 1 and 2; compare, for example, the respective payload rotations in Figures 6.38 and 6.45).

[‡] Another way of interpreting this result is that in case 1, the boundary conditions of the antennas correspond to those of a pinned-free beam, whereas in case 2 they correspond to a clamped-free beam. The natural frequencies of a clamped-free beam are lower than those of a pinned-free beam.

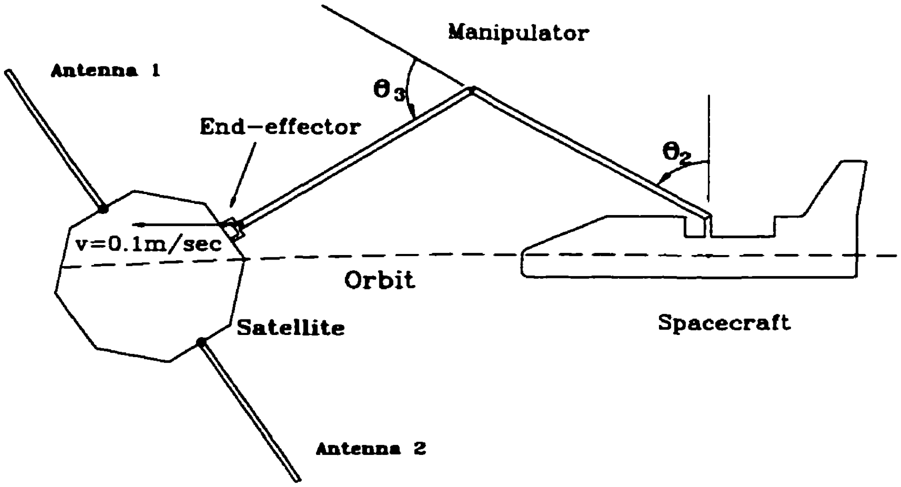

Figure 6.32: Impact scenario, with two satellite antennas

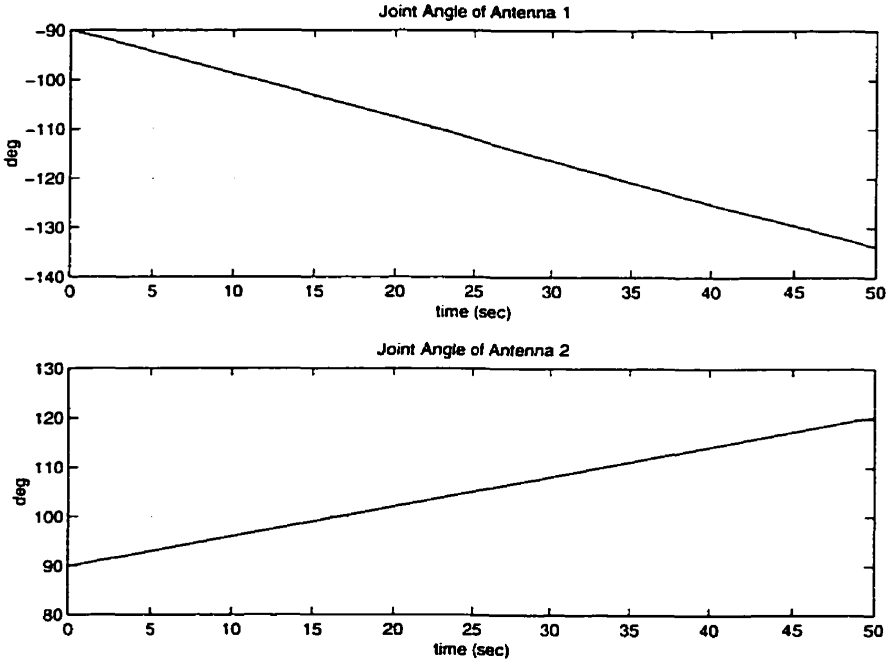

Figure 6.33: Joint angles of antennas vs. time. Case 1.

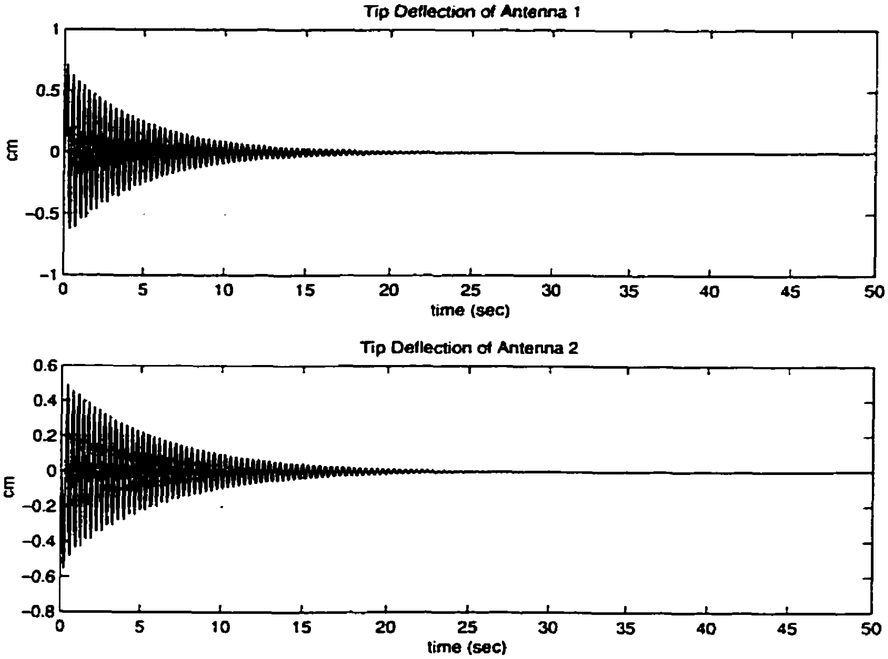

Figure 6.34: Tip deflections of antennas vs. time. Case 1.

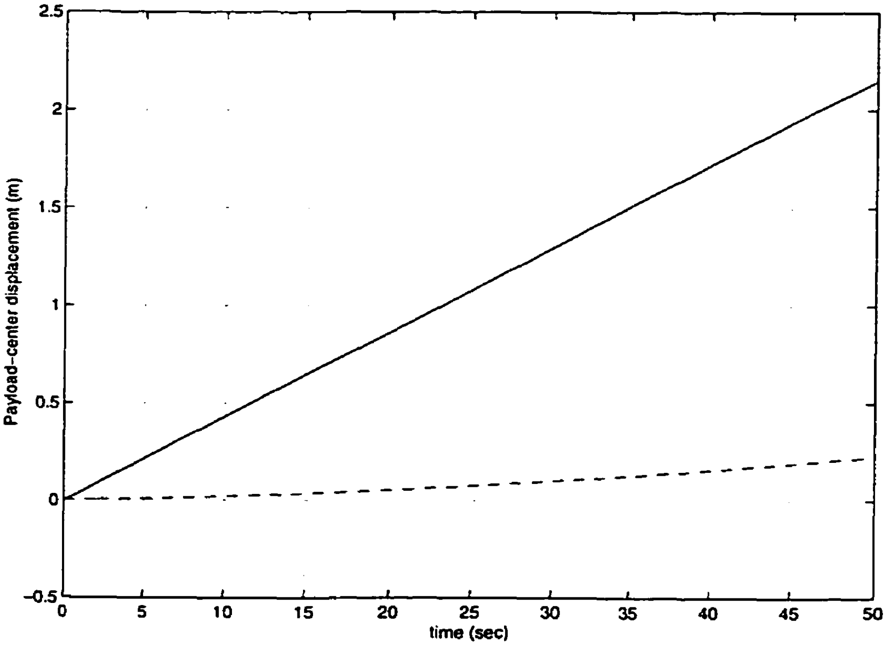

Figure 6.35: Displacement of payload. Case 1. (-- x-dir, — y-dir)

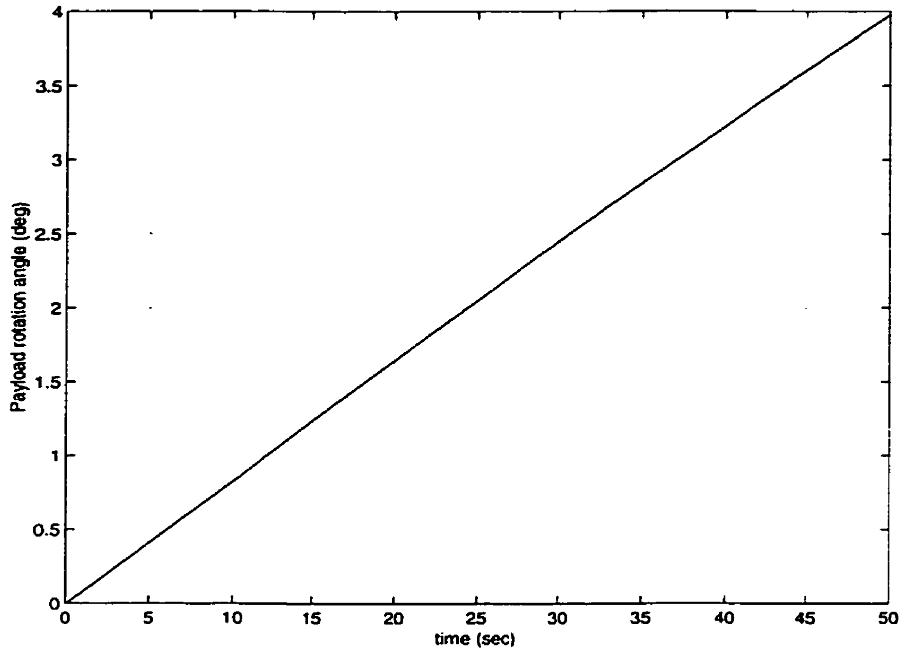

Figure 6.36: Rotation angle of payload. Case 1.

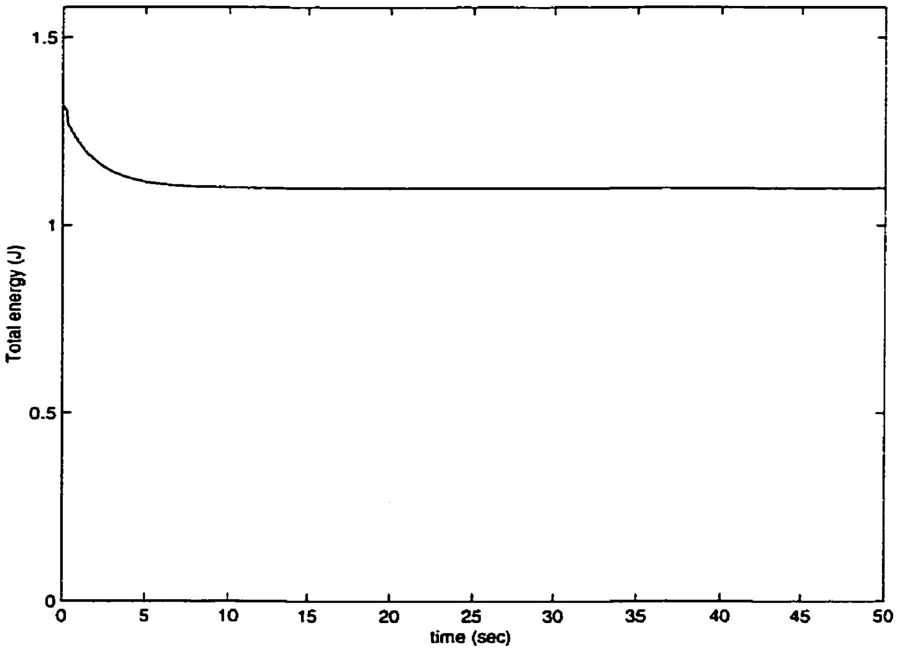

Figure 6.37: Total energy vs. time. Case 1.

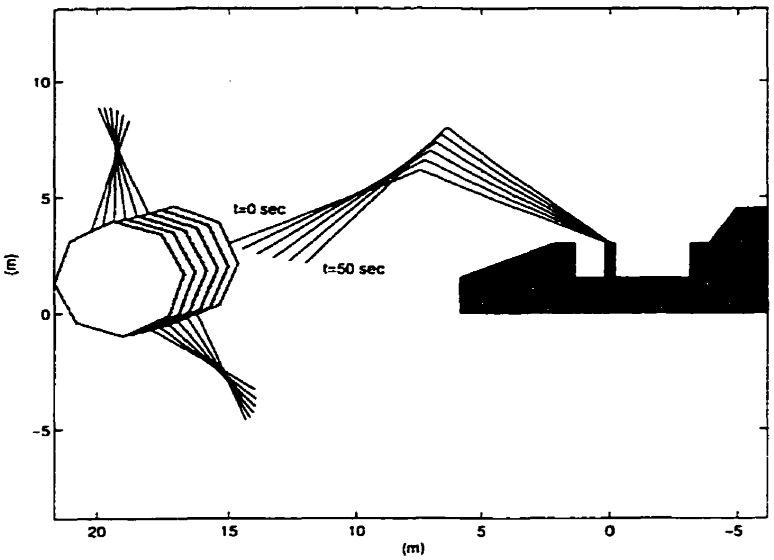

Figure 6.38: Configuration of the system from time = 0 to 50 sec. Case 1.

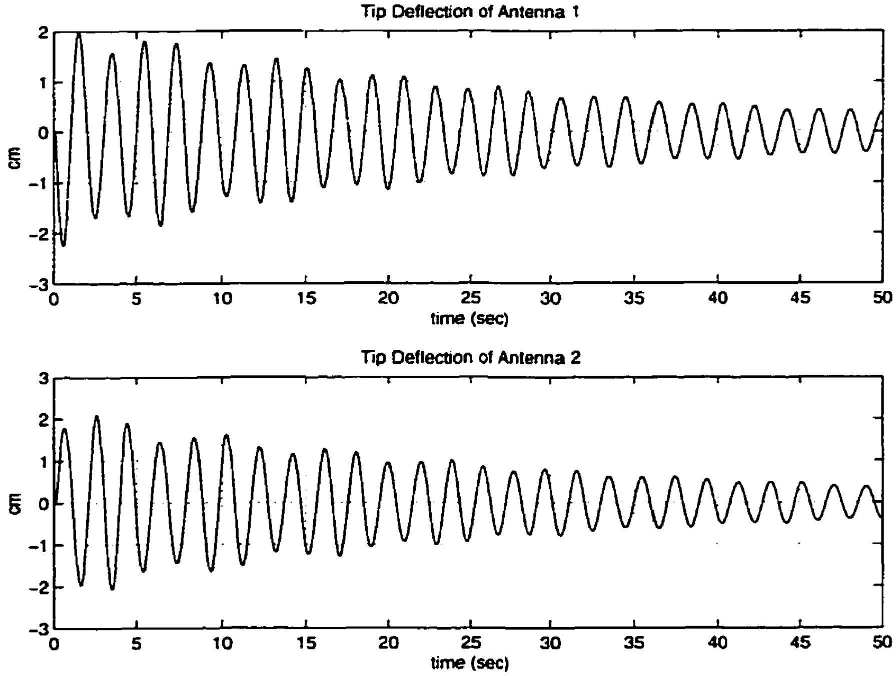

Figure 6.39: Tip deflections of antennas vs. time. Case 2.

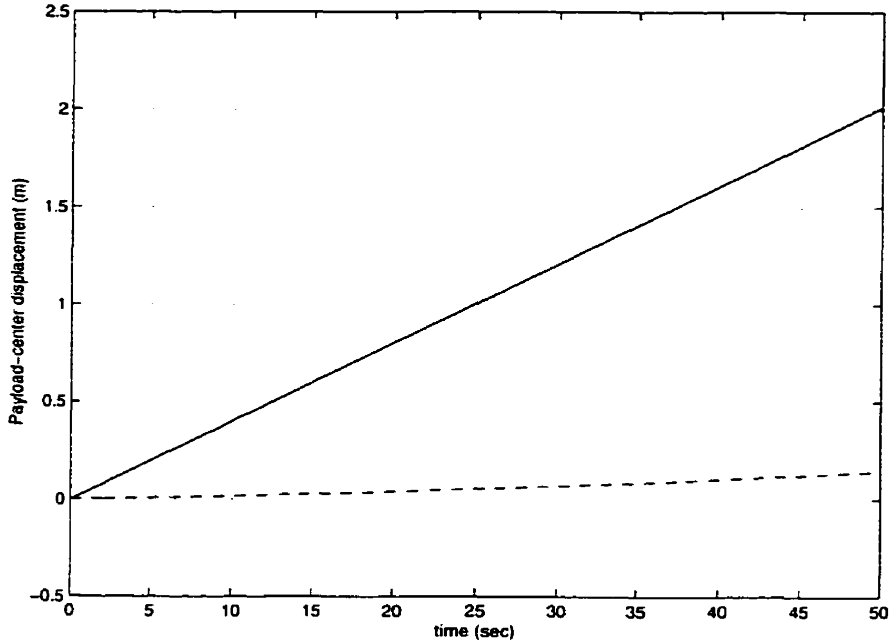

Figure 6.40: Displacement of payload. Case 2. (— — x-dir, — y-dir)

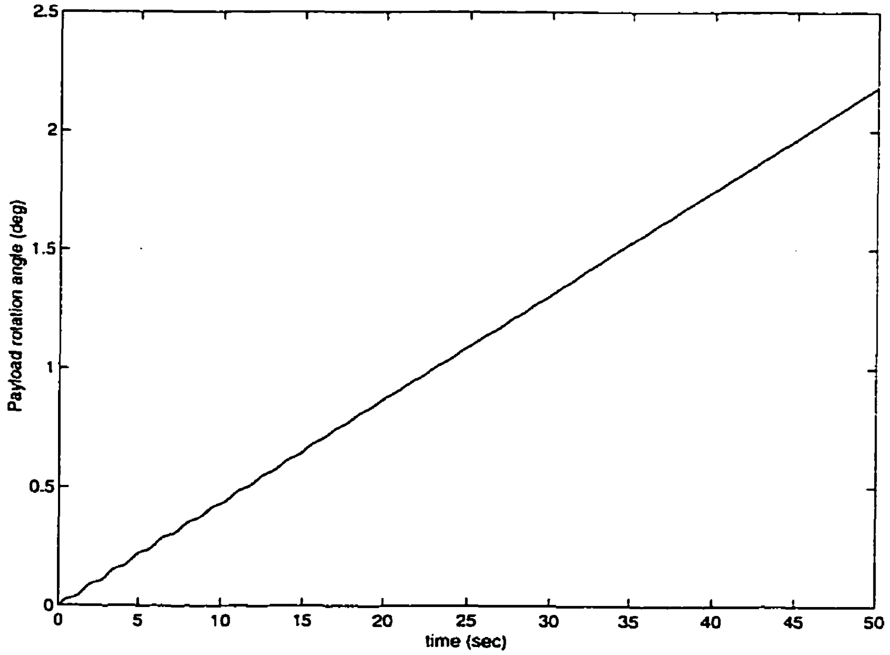

Figure 6.41: Rotation angle of payload. Case 2.

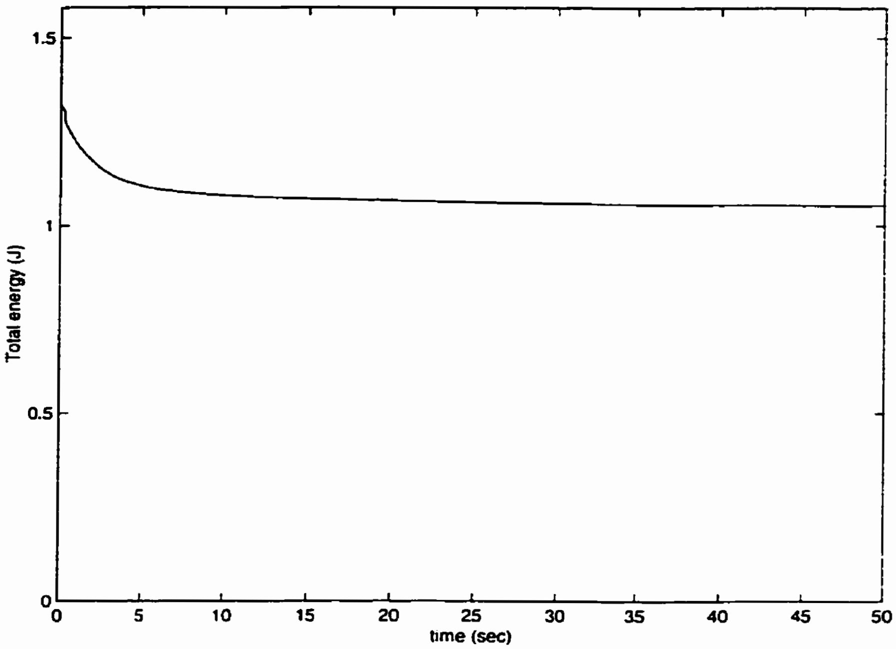

Figure 6.42: Total energy vs. time. Case 2.

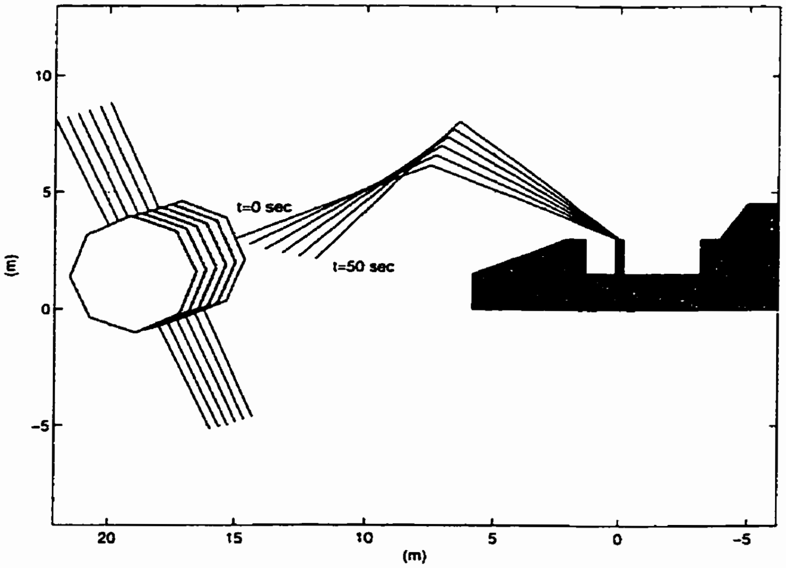

Figure 6.43: Configuration of the system from time = 0 to 50 sec. Case 2.

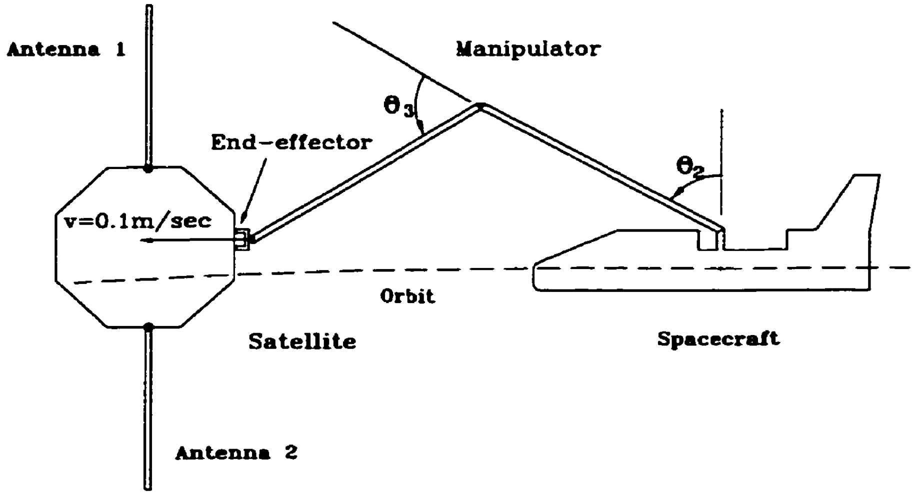

Figure 6.44: Impact scenario with a vertical contact surface

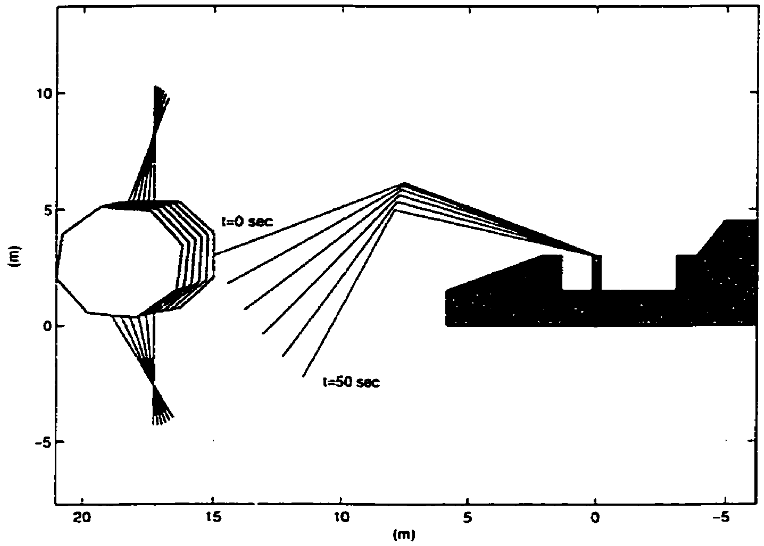

Figure 6.45: Configuration of the system from time = 0 to 50 sec. Free antenna joints, and vertical contact surface

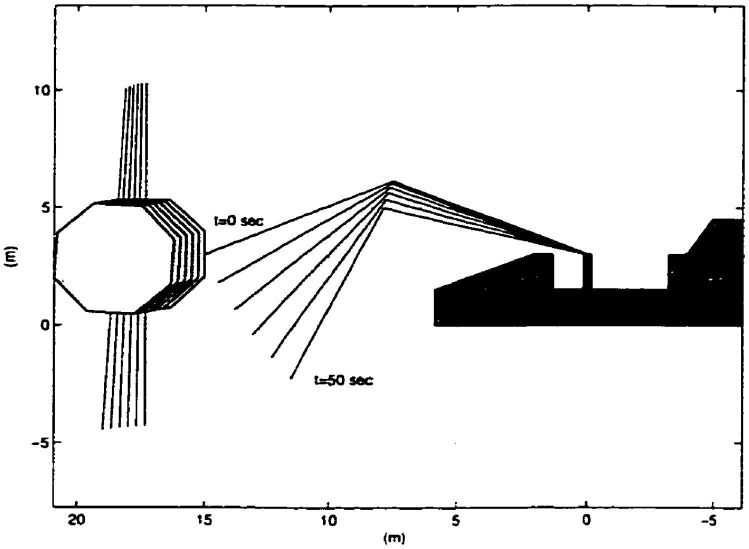

Figure 6.46: Configuration of the system from time = 0 to 50 sec. Locked antenna joints, and vertical contact surface

6.4 Capture Dynamics

In this section, the case where the end-effector successfully captures the satellite (as opposed to rebound) is considered. The contact scenario is illustrated in Figure 6.47. Coulomb friction, based on the model described in Sections 4.2.3 and 4.2.4, is applied on the contact surfaces with $\mu_s = 0.2$ and $\mu_d = 0.15$. An antenna, modelled as a flexible beam which has the same material specification as in Section 6.3.3, is attached to the satellite by a revolute joint.

The simulation of capture dynamics is dependent on the type of capture mechanism which is employed. But regardless of the type, the capture mechanism should essentially fulfill three functions: (*i*) the resulting dynamic forces must be reduced as much as possible; (*ii*) these forces must be damped out and; (*iii*) some type of latching or grasping mechanism must exist so that eventually the two impacting bodies become rigidly connected. With the purpose of keeping things as general and simple as possible, the following type of capture mechanism, illustrated in Figure 6.48, is

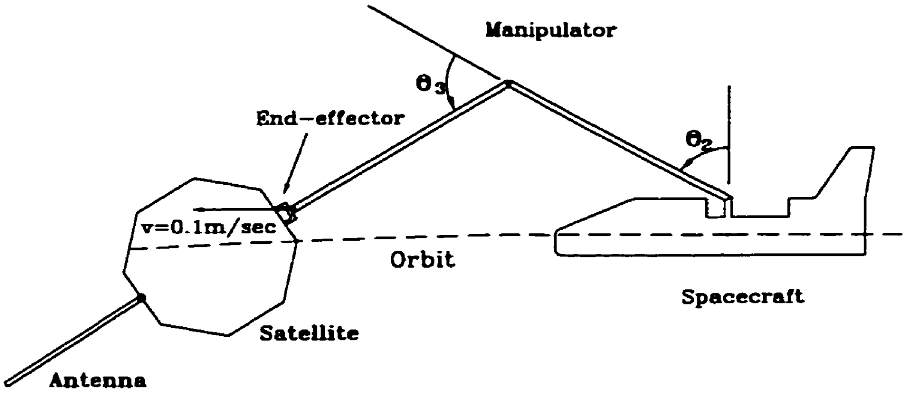

Figure 6.47: Initial capture scenario

assumed in this case: as soon as initial contact occurs, the grasping mechanism allows two spring-dashpot systems to join two pairs of grapple points, where for each pair one point is located on the end-effector and one on the payload. The spring component forces the two contacting bodies towards each other and the dashpot component damps out the resulting vibrations until eventual rigid attachment.

The forces produced by the capture mechanism must be accounted for in the dynamical model. Let the positions of the two pairs of grapple points on the end-effector and payload be $(\mathbf{r}_{e_1}, \mathbf{r}_{p_1})$ and $(\mathbf{r}_{e_2}, \mathbf{r}_{p_2})$. Then the forces being exerted by the capture mechanism are

$$\mathbf{f}_j^c = \mathbf{K}_c \Delta \mathbf{r}_j + \mathbf{C}_c \Delta \dot{\mathbf{r}}_j, \quad j = 1, 2 \tag{6.1}$$

where

$$\Delta \mathbf{r}_j = \mathbf{r}_{p_j} - \mathbf{r}_{e_j}, \quad j = 1, 2 \tag{6.2}$$

and $\mathbf{K}_c$ and $\mathbf{C}_c$ are diagonal matrices containing spring and damping constants. Then the following terms must be added to $\mathbf{f}_i$ of equation (4.1), where i corresponds to the end-effector and payload subsystems:

$$\mathbf{f}_e = \mathbf{J}_{e_1}^T \mathbf{f}_1^c + \mathbf{J}_{e_2}^T \mathbf{f}_2^c \tag{6.3}$$

$$\mathbf{f}_p = -\mathbf{J}_{p_1}^T \mathbf{f}_1^c - \mathbf{J}_{p_2}^T \mathbf{f}_2^c \tag{6.4}$$

where, if $\mathbf{q}_e$ and $\mathbf{q}_p$ are the generalized coordinates of the end-effector and payload respectively, then

$$\mathbf{J}_{e_j} = \frac{\partial \mathbf{r}_{e_j}}{\partial \mathbf{q}_e}, \quad j = 1, 2 \tag{6.5}$$

$$\mathbf{J}_{p_j} = \frac{\partial \mathbf{r}_{p_j}}{\partial \mathbf{q}_p}, \quad j = 1, 2 \tag{6.6}$$

The spring and damping constants used here are $K_c = 5 \times 10^4 N/m$ and $C_c = 4 \times 10^4 N.sec/m$ respectively.

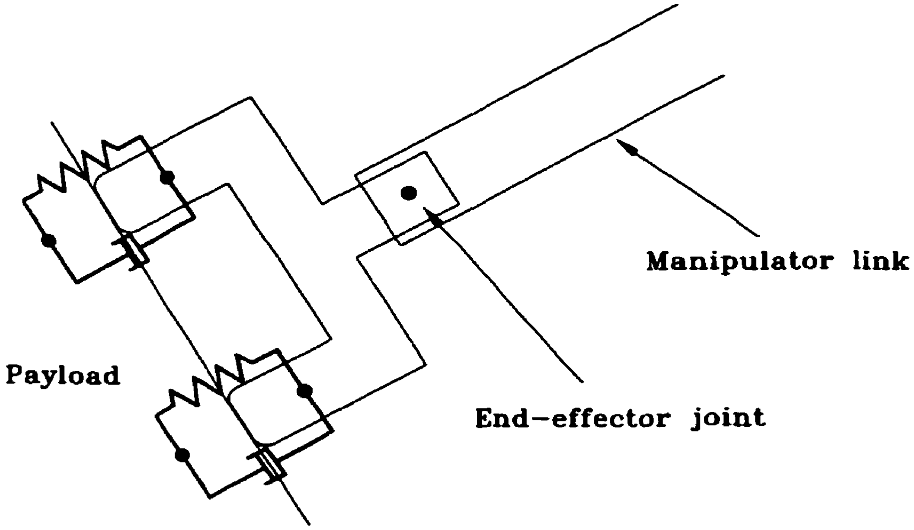

Figure 6.48: Capture mechanism

The simulation results during the capture operation are shown in Figures 6.49–6.52. The forces acting at the end-effector joint during capture are shown in Figure 6.49. As seen in Figure 6.50, which is an expanded view of Figure 6.49, five repeated impacts occur at A, B, C, D and E until eventual rigid attachment at about 3.5×10^{-3} seconds. This phenomena can be seen by the abrupt changes in an otherwise smooth oscillatory profile of the joint forces. The displacements of the end-effector joint and payload center are shown in Figure 6.51. The relative rotation angle between the end-effector and payload and the rotation angle of the payload are shown in Figure 6.52. Fluctuations in the relative angle are observed from the moment of contact because the mismatch in the rotations of the payload and end-effector cause misalignment between the two contacting surfaces and the torque which thus arises induces rotations of the end-effector joint. These phenomena complicate the whole capture operation as already seen by the abrupt changes in contact forces and rotation angles of the end-effector.

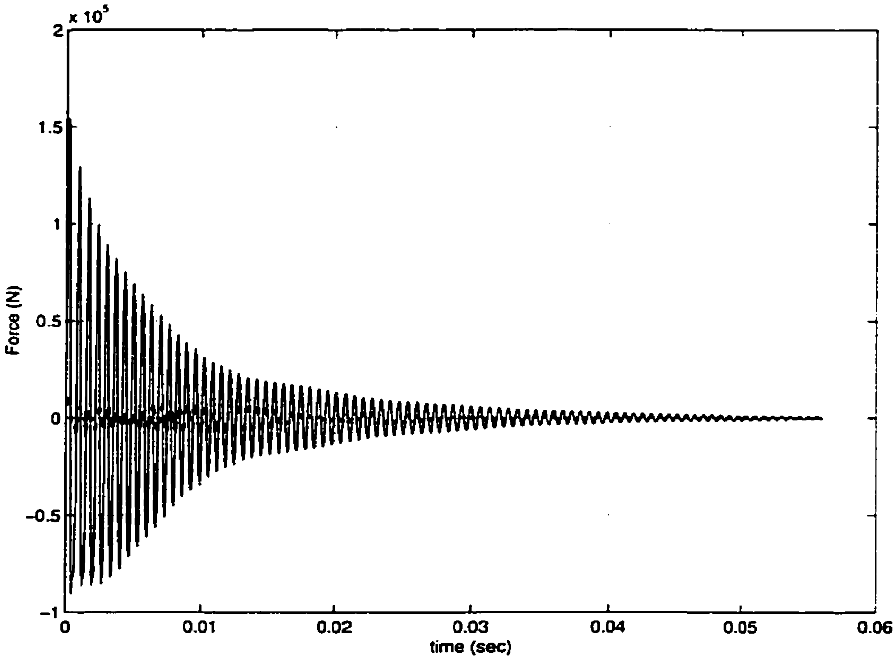

Figure 6.49: End-effector joint forces during capture. (-- x-dir, — y-dir)

The results for post-impact simulations ($0 \leq t \leq 100sec.$) are shown in Figures 6.53 to 6.56. The joint angles are plotted against time in Figure 6.53. The θ_1 plot shows the attitude drift of the spacecraft and the θ_p plot shows the rotation of both the end-effector and payload. The total energy of the system is shown in Figure 6.54. During the first 10 seconds, the energy is seen to decay gradually by a slight amount which is caused by loss of energy due to structural damping in the manipulator links. Afterwards, it maintains a steady value. The tip deflections of the two links of the manipulator and payload are shown in Figure 6.55. As predicted by the energy plot, the vibrations are seen to be almost damped out after about 10 seconds. It is interesting to note the smaller link tip deflections and energy decay here compared to those of impact scenarios in section 6.3, due to the extra constraints imposed by the payload inertia at the tip of the manipulator. The trajectory of the whole system for 100 seconds after impact is shown in Figure 6.56. The post-capture motion can be explained as follows: After successful rigid capture, the manipulator arms continue

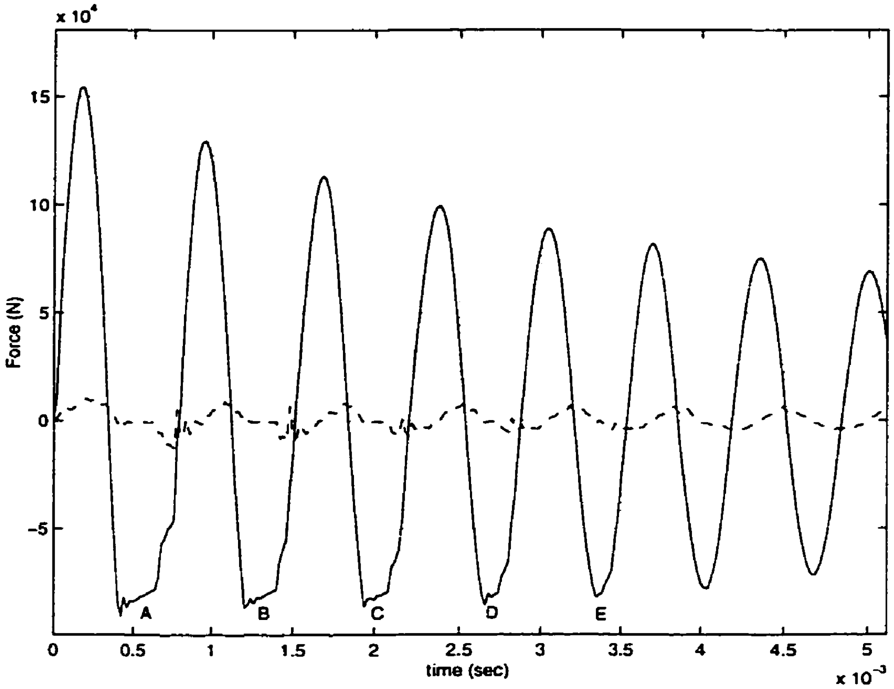

Figure 6.50: End-effector joint forces during capture. Expanded view (— — x-dir, — y-dir)

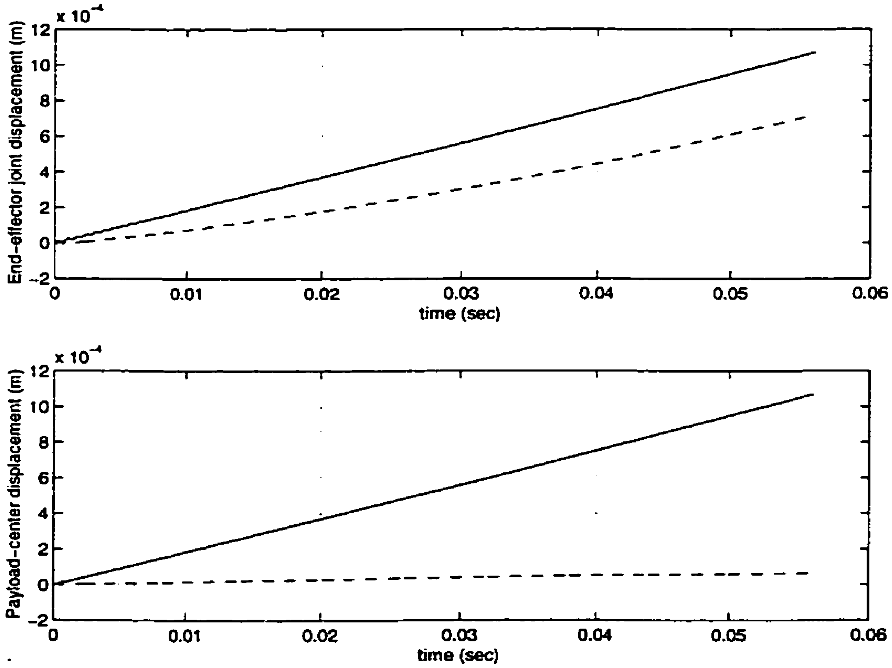

Figure 6.51: Displacements of contacting bodies during capture. (— — x-dir, — y-dir)

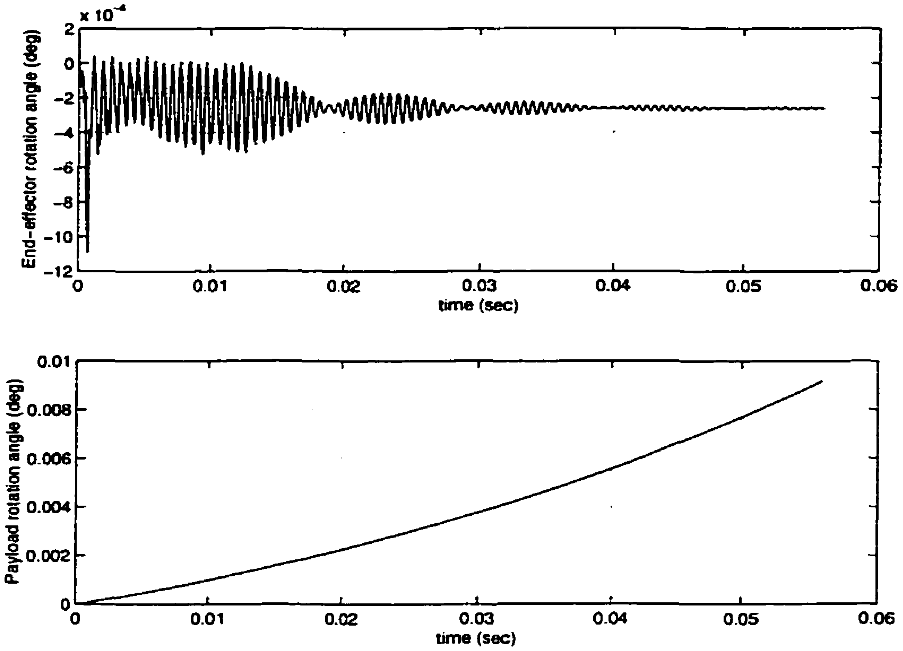

Figure 6.52: Rotation angles of contacting bodies during capture.

stretching until the singularity configuration (at about 50 *sec*), at which time a moment is induced in both the payload and the base of the spacecraft which causes the first to initiate a change in its direction of rotational and translational motion, and the second to experience significant attitude drift (note the larger attitude drift angle here compared to those of impact scenarios in section 6.3). The attitude drift of the spacecraft is an undesirable result, but the post-capture behaviour of the payload, which is shown to move towards the spacecraft, suggests that judicious approach conditions of the manipulator before capture may be advantageously used for uncontrolled satellite retrieval operations.

6.5 Trajectory, Force, and Vibration Control

The problem of a spacecraft-mounted flexible manipulator system applying desired amounts of force on desired locations of the payload is considered. The spacecraft can be thought of as the first link and its center as the base of the manipulator sys-

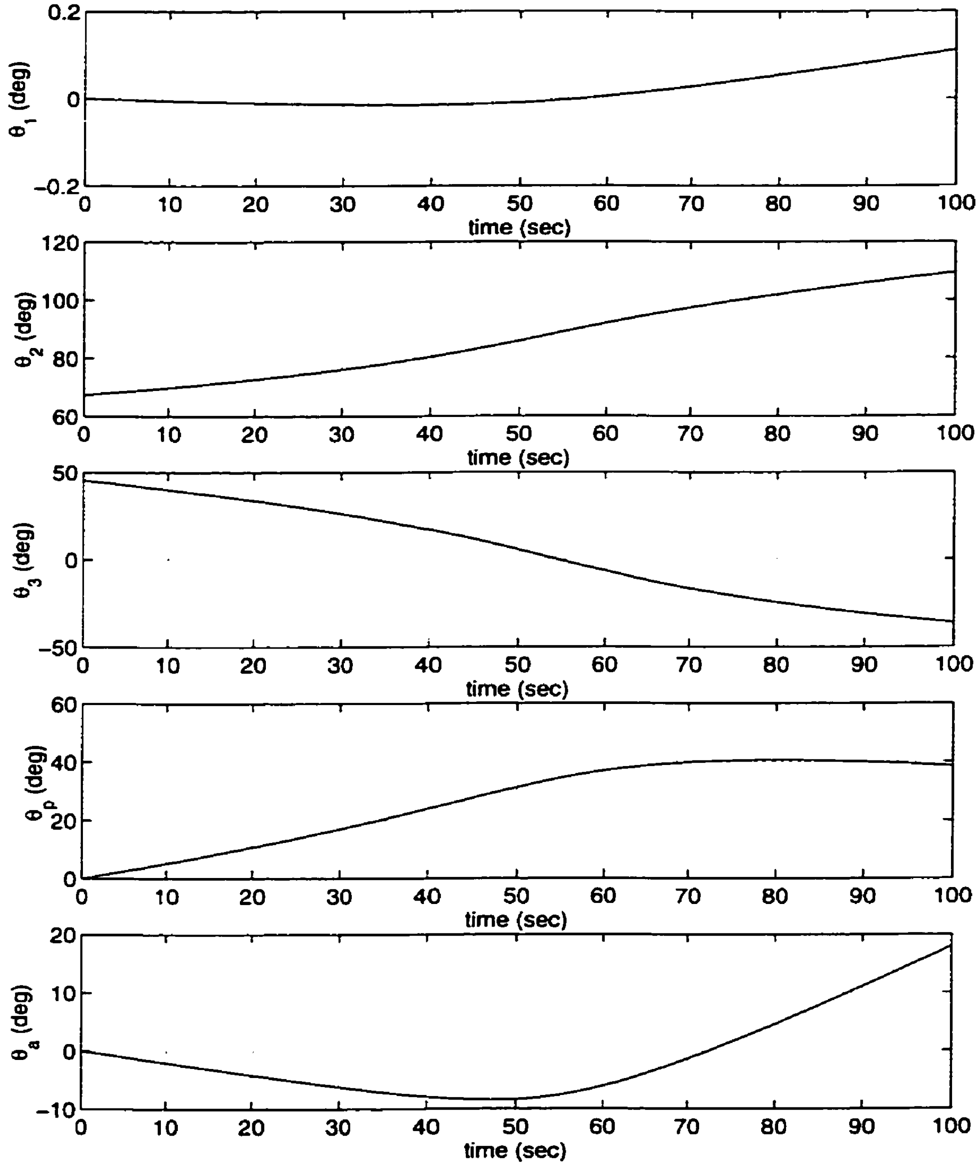

Figure 6.53: Joint angles vs. time after capture.

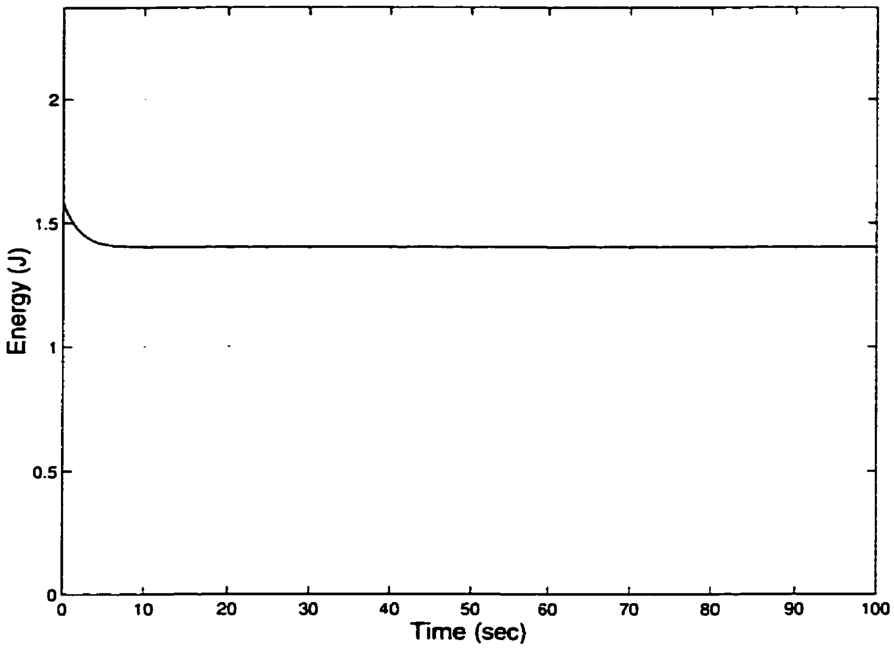

Figure 6.54: Total energy vs. time after capture.

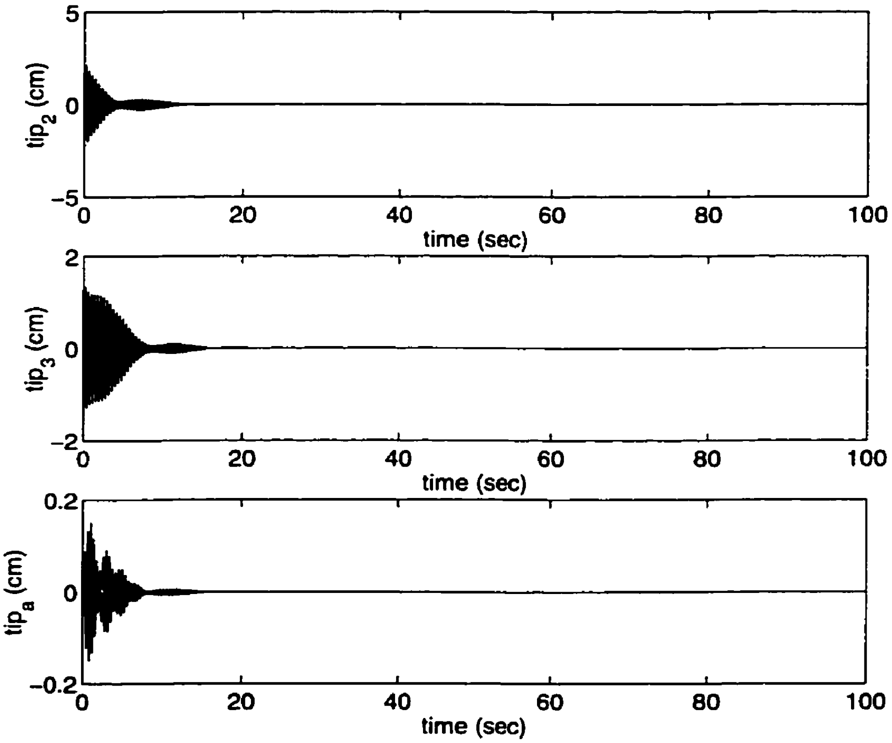

Figure 6.55: Tip deflections vs. time after capture.

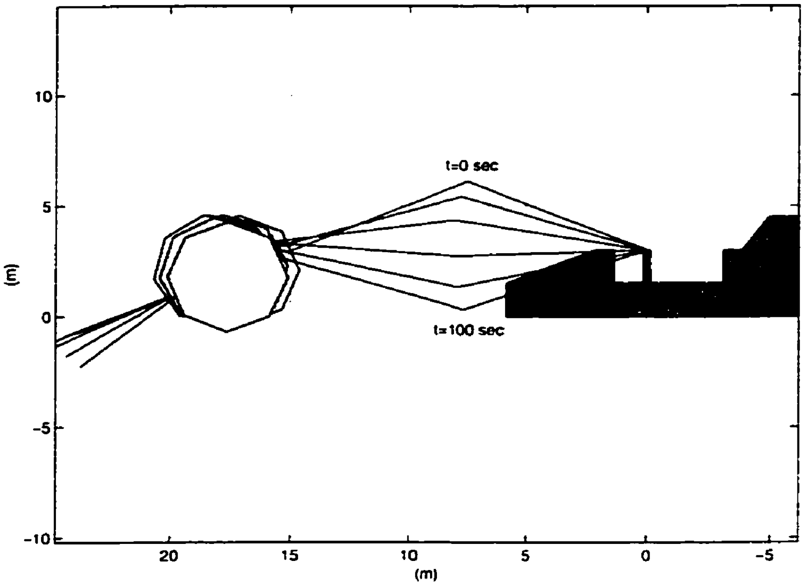

Figure 6.56: Configuration of the system from time = 0 to 100 sec after capture.

tem. Then the manipulator is redundant, so that the optimization method based on Khatib's (1987) *inertia-weighted pseudoinverse* is used here to obtain a path which minimizes the instantaneous kinetic energy of the system (section 5.3.1). The respective Young's modulus of the end-effector and payload material are taken as $E_{ee} = 1 \times 10^5 (N/m^2)$ and $E_p = 7 \times 10^6 (N/m^2)$. The mass and moment of inertia of the payload are 35,530 kg and 1.01×10^6 $kg.\,m^2$ respectively.

The manipulator is initially free and at rest with respect to the orbital frame, its joint angles being $\theta_1 = 0°$, $\theta_2 = 30°$, and $\theta_3 = 120°$. Subsequently, control is applied in 3 stages (see Figure 6.57). Stage (1): the end-effector attempts to make a smooth direct contact with the payload. To simulate the fact that in reality there is bound to be a small velocity differential between the contacting bodies just before contact, an error value of $2mm$ is added to the ideal final position of the end-effector (location of surface of payload), such that there is actually a small impact. Stage (2): a desired force of 15 N is slowly applied on the payload. Stage (3): the end-effector is commanded to follow a straight vertical line along the payload surface while maintaining the constant desired force. A difficulty with achieving this task is that the payload moves as load is applied to it, and its motion is not known *a priori*. Therefore, the nominal (reference) trajectory of the end-effector is divided into two parts as follows:

$$\mathbf{x}_r = \mathbf{x}_p + \mathbf{x}_{r/p} \tag{6.7}$$

where $\mathbf{x}_r$, $\mathbf{x}_p$, and $\mathbf{x}_{r/p}$ are the nominal trajectory of the end-effector, the location of the payload reference frame (engraved on the body, as in Figure 6.57), and the reference trajectory of the end-effector with respect to the payload reference frame, respectively. The trajectory $\mathbf{x}_p$ must be fed *online*, while $\mathbf{x}_{r/p}$ may be planned *offline*.

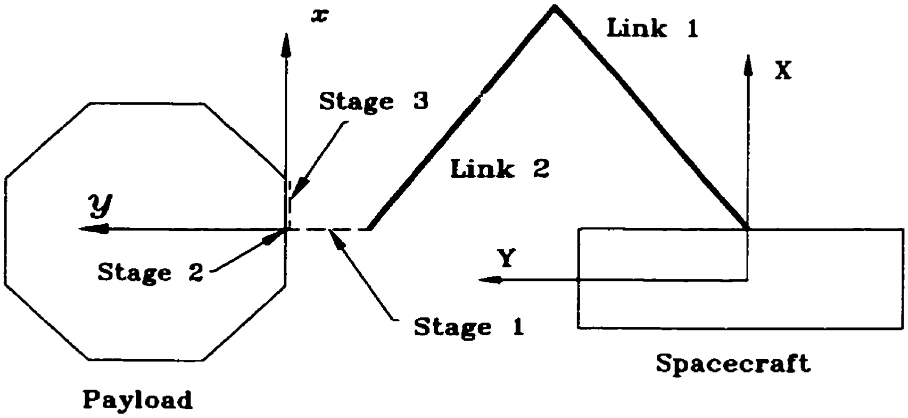

Figure 6.57: Controlled contact scenario

The following sinusoidal reference trajectory was chosen for $\mathbf{x}_{r/p}$:

$$\mathbf{x}_{r/p}(t) = \mathbf{c} + \mathbf{a}\{t_a - b sin(t_a/b)\} \tag{6.8}$$

where

$$t_a = t - t_m$$
$$\mathbf{a} = (\mathbf{x}_n - \mathbf{x}_m)/(t_n - t_m)$$
$$b = (t_n - t_m)/(2\pi)$$
$$\mathbf{c} = \mathbf{x}_m$$

and m and n denote the initial and final values of each stage, respectively.

The following values were used in the simulation:

$$\mathbf{A} = \begin{bmatrix} 80 & 0 \\ 0 & 80 \end{bmatrix} (kg); \ \mathbf{K}_d = \begin{bmatrix} 100 & 0 \\ 0 & 100 \end{bmatrix} (N.s/m);$$

$$\mathbf{K}_p = \begin{bmatrix} 80 & 0 \\ 0 & 80 \end{bmatrix} (N/m); \ \mathbf{x}_{p_0} = \left\{ \begin{array}{c} 1 \\ 8.63 \end{array} \right\} (m);$$

$$\mathbf{x}_0 = \left\{ \begin{array}{c} 0 \\ -0.5 \end{array} \right\} (m); \ \mathbf{x}_1 = \left\{ \begin{array}{c} 0 \\ 0.002 \end{array} \right\} (m);$$

$$\mathbf{x}_2 = \left\{ \begin{array}{c} 0 \\ 0.1875 \end{array} \right\} (m); \ \mathbf{x}_f = \left\{ \begin{array}{c} 0.5 \\ 0.1875 \end{array} \right\} (m);$$

$$t_0 = 0sec; \ t_1 = 6sec; \ t_2 = 14sec; \ t_f = 20sec.$$

Subscripts $0, 1, 2$, and f represent the initial, end of stage 1, end of stage 2 and final (end of stage 3) values of $\mathbf{x}_{r/p}$, respectively.

One of the conditions of applicability of the singular perturbation method is that the elastic vibration frequencies must be much greater than the frequency content of the rigid body motion (such as, ratio ≈ 10 (Boutin 1995)). Since in this particular case the lowest natural frequency of the manipulator is 16 rad/sec (final configuration) whereas the frequency content of the rigid body motion is 1 rad/sec (from equation (5.33)), the use of the singular perturbation method is valid.

The solution of the matrix Ricatti equation (5.44) can be computationally intensive such that it may not be possible to compute it online at each servo tick. But in most cases, the main purpose in vibration control is to damp out the deflections at steady state; thus, the LQR gain matrices can be designed also on the basis of the final joint configuration, provided that under that particular choice the fast variables will not go unstable along the slow trajectory. It was found through simulation results that this was indeed so in this case and in many others. In this way, the solution of the Ricatti equations for each joint configuration can be avoided (Siciliano & Book 1988).

When manipulator links are rigid, the controller is seen to achieve the desired trajectory and force with great precision (not shown). However, when links are flexible, basically two different controllers are at work: one which attempts to achieve the desired trajectory and force, and the other which attempts to suppress the induced vibrations. Since the same torques attempt to achieve both objectives, neither result is perfect during contact operations. The trajectory deviates slightly from the desired path, and a constant steady-state error appears in the applied force due to steady-state link deflections. This steady state error, however, can be circumvented by incorporating a corrective term to $\mathbf{x}_f$ as follows:

$$\mathbf{x}_{f_c} = \mathbf{x}_f + \mathbf{K}_p^{-1}(\mathbf{f}_d - \mathbf{f}_a) \tag{6.9}$$

where $\mathbf{x}_{f_c}$, $\mathbf{x}_f$, $\mathbf{f}_d$ and $\mathbf{f}_a$ are the corrected final trajectory, the pre-planned final trajectory, the desired force, and the actual force, respectively.

Figures 6.58 and 6.59 show the path of the end-effector in orbital and payload coordinates respectively. It can be seen that the end-effector traces the desired trajectory quite efficiently (Figure 6.59), even while in contact with the payload. In Figure 6.60 it can be seen that the force applied on the payload in the y-direction reaches a steady value of 15 N, as desired. Both Figures 6.59 and 6.60 show that the end-effector undergoes some bounces before reaching sustained contact. During this transitional phase, the end-effector is not able to track the desired trajectory; however, during the ensuing sustained-contact phase, the controller is seen to quickly regain its tracking capability.

Figure 6.61 shows the x and y displacements of the payload center of mass due to the applied contact forces, and the rotation of the payload caused by the end-effector moving along the payload surface, thus producing a counterclockwise moment about its center of mass. Figures 6.62 and 6.63 show respectively the applied torques and the joint angles of the spacecraft and manipulator links. The spacecraft is seen to undergo some attitude drift, which is due to the absence of an attitude controller. The spacecraft was simply treated as an additional link and was controlled to satisfy the redundancy optimization criteria based on Khatib's (1987) *inertia-weighted pseudoinverse*, which minimizes the instantaneous kinetic energy of the global spacecraft/manipulator system. Lastly, Figure 6.64 shows the tip deflections of the two links, where substantial steady-state deformations are observed in link 2, although oscillations have been damped out. In link 1, control torques act at both ends of the link, which have the effect of reducing its steady state deflection.

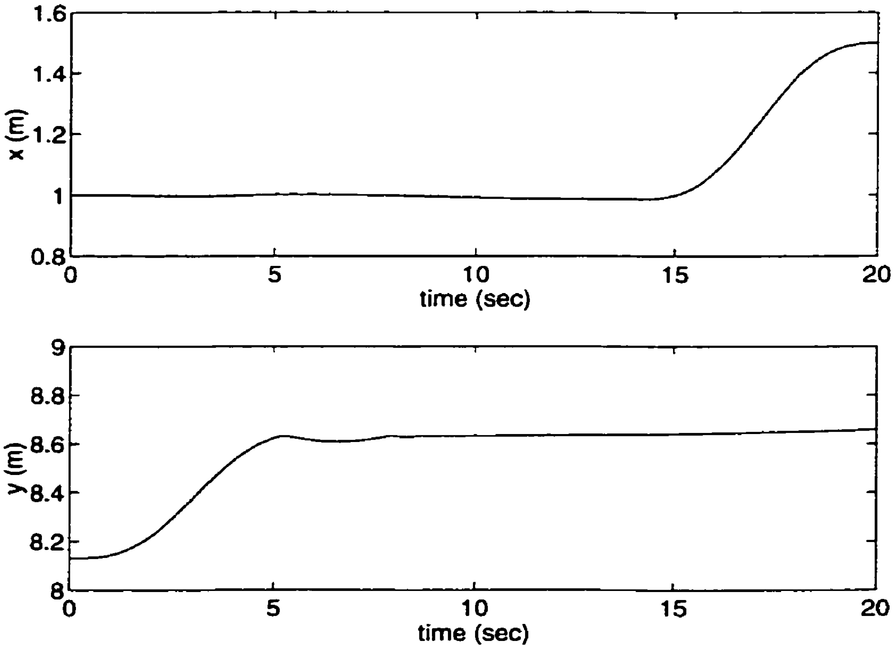

Figure 6.58: X and Y coordinates of the end-effector w.r.t. the orbital frame. Actual trajectory.

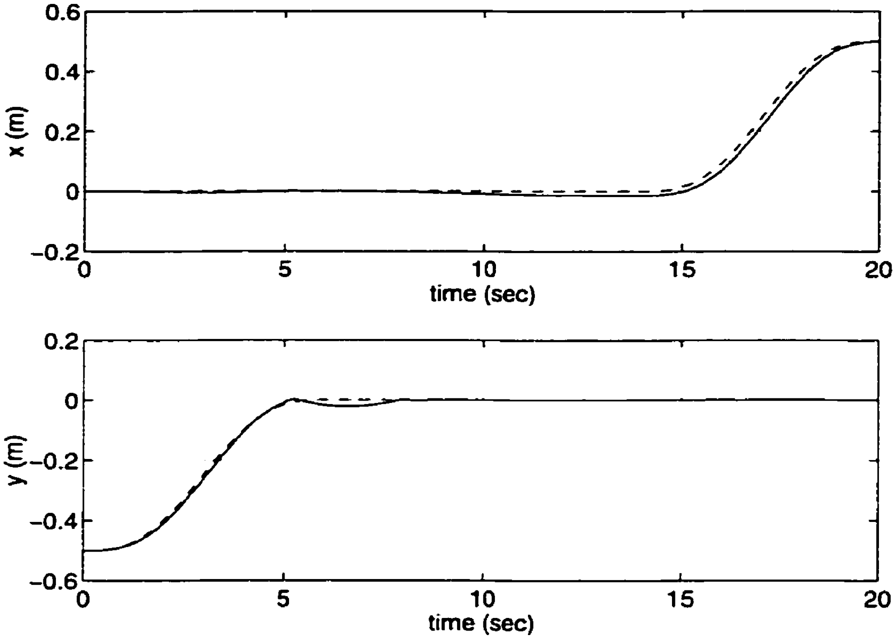

Figure 6.59: X and Y coordinates of the end-effector w.r.t. the local payload frame (—— desired, — actual)

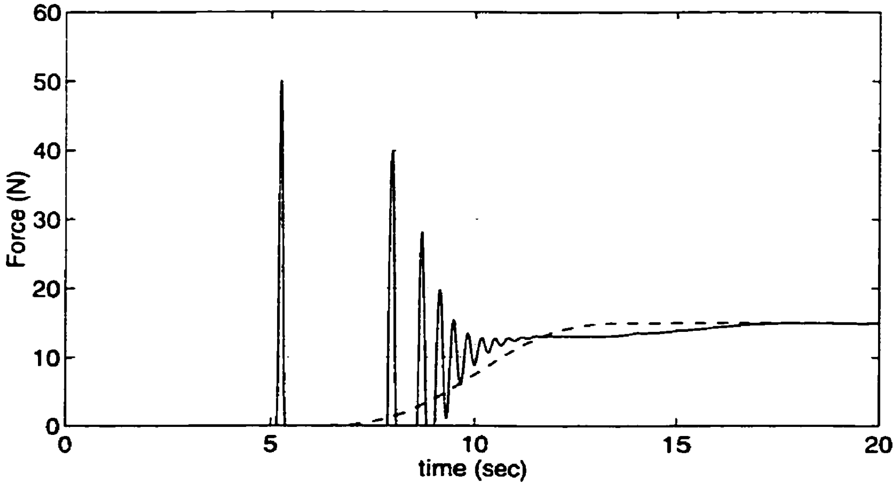

Figure 6.60: Normal force applied by the end-effector on payload (—— desired, — actual)

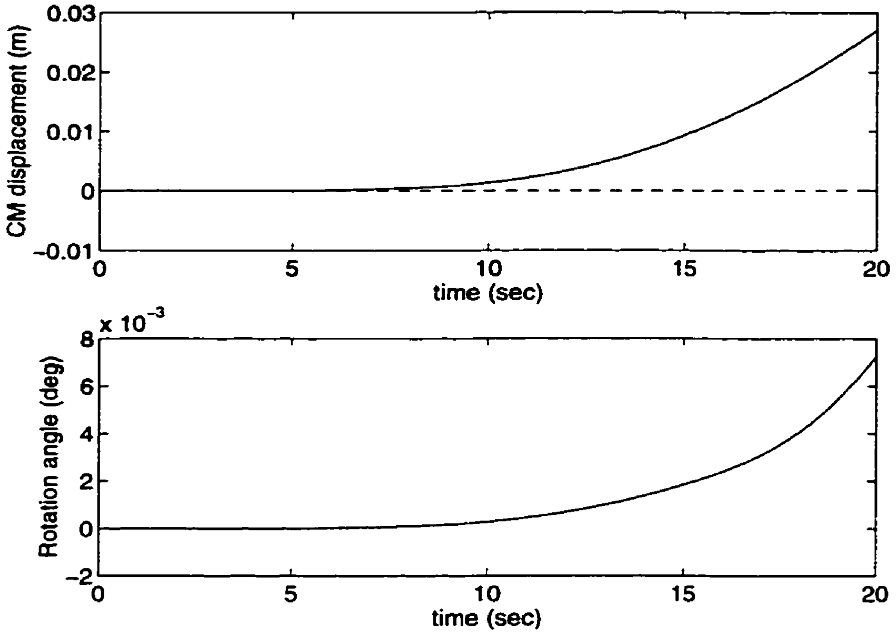

Figure 6.61: Payload displacements and rotation. (—— x-dir, — y-dir)

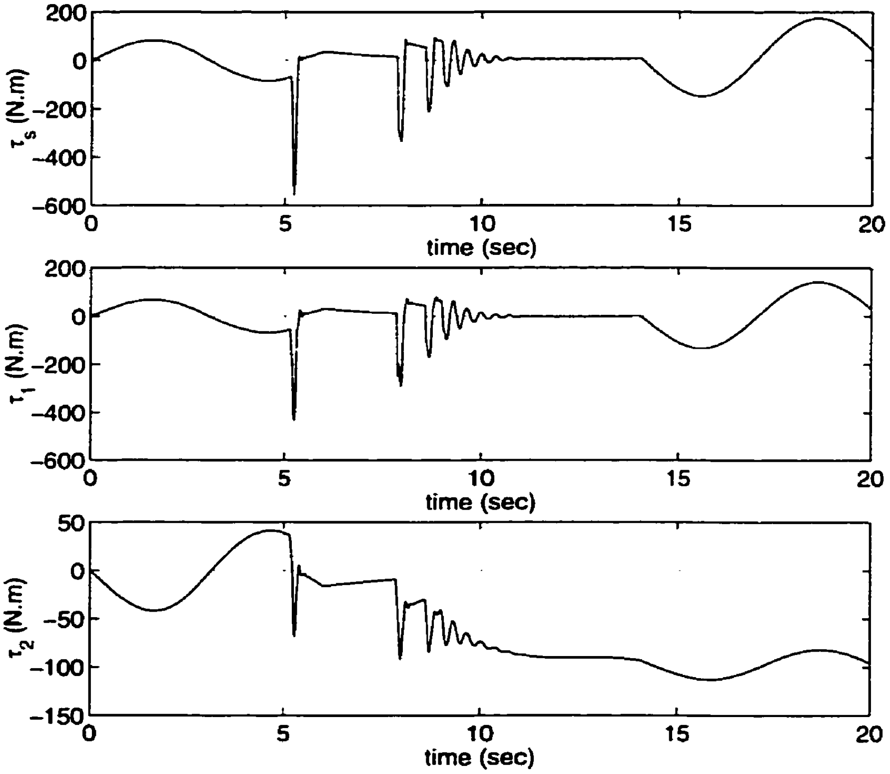

Figure 6.62: Torques applied at manipulator joints

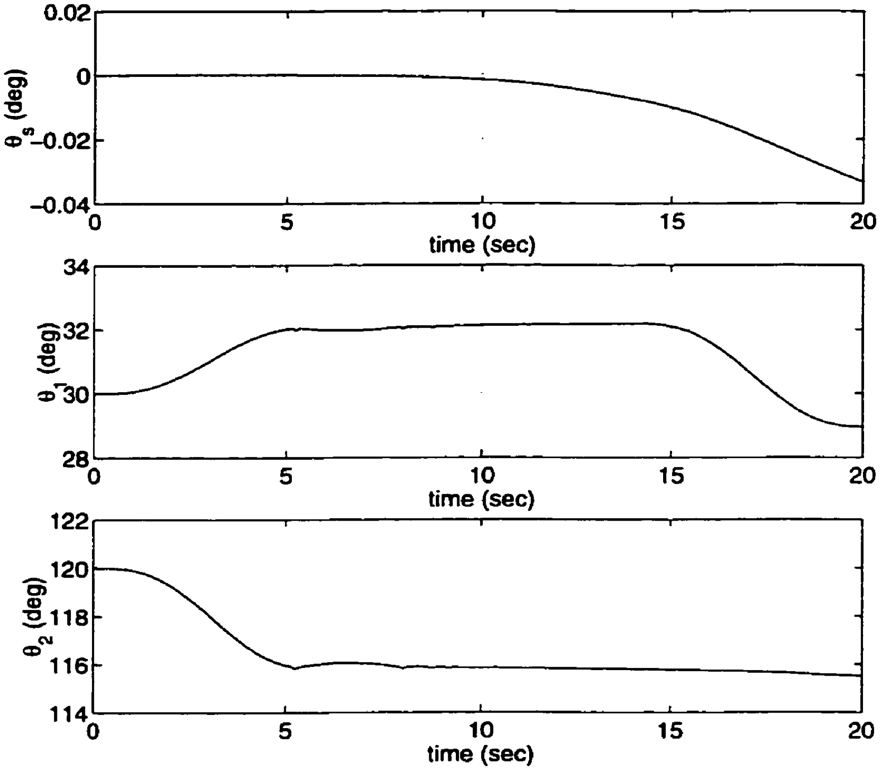

Figure 6.63: Manipulator joint angles

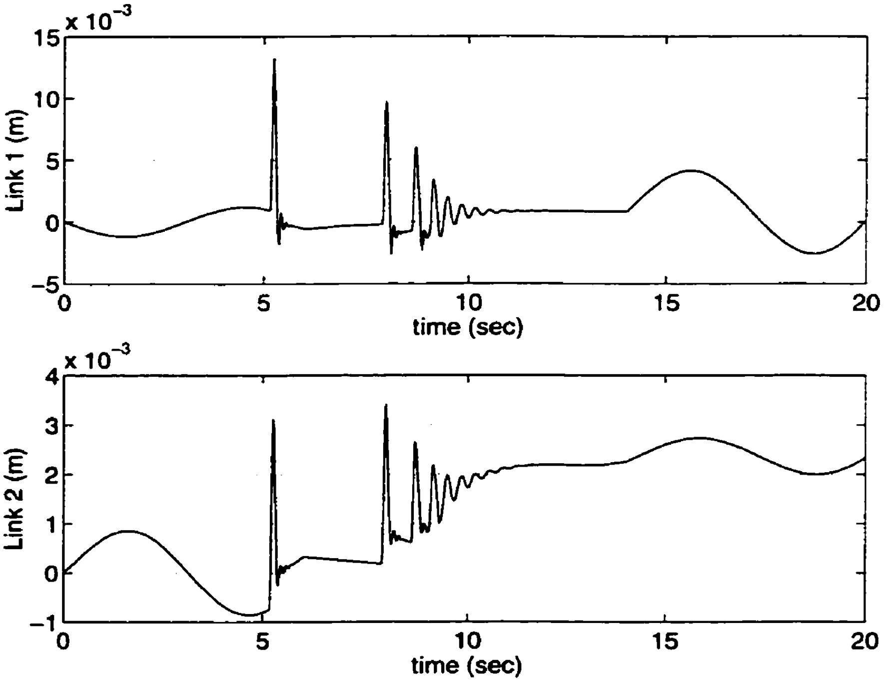

Figure 6.64: Link tip deflections

Chapter 7

Conclusions

In this chapter, a summary is presented of the work done in the thesis and conclusions are drawn based on its results. Some suggestions for future work are also put forward.

7.1 Summary and Conclusions

The main interest of this thesis was in the development of a dynamic formulation capable of simulating contact dynamics involving multi-body systems. The bodies which undergo direct contact, referred to as *contacting bodies*, were modelled using the finite element method and the Lagrange Multiplier technique for contact constraints, and multi-body systems were modelled using a modified Euler-Lagrange approach based on the method of Natural Orthogonal Complement. These systems are coupled due to kinematic and contact constraints acting between them. Thus, the overall system dynamics is composed of a set of differential equations (either multi-body formulations or finite element nodal displacement formulations of the contacting bodies) subjected to sets of algebraic equations expressing kinematic or contact constraints. A systematic and efficient procedure for solving this system of equations was presented. In this dynamic formulation, special attention was paid to:

- Dynamic fidelity of contact mechanics. Unlike the impulse-momentum approaches which neglect what happens during impact, and the Hertzian approaches which neglect effects of elastic structural vibrations, the approach presented in this thesis models the detailed mechanics of contact by using a finite element approach, analyses the contact geometric constraints and corresponding contact forces, and incorporates them into the dynamical equations. This method is capable of modeling such phenomena as structural deformations. elastic vibrations, friction, time-varying contact area, repeated contact/impact, and others, without making doubtful assumptions about the nature of the physical contact process.
- Computational efficiency. In order to render the dynamic simulation computationally efficient, the following solution procedures were used in this thesis. Firstly, the computationally straightforward and economical Newmark method was used for the time integration of the equations of motion, with which the second order dynamical equations can be converted into algebraic form. Secondly, algebraic manipulations were made of the resulting equations in order to exploit the positive definite and positive semi-definite character of the mass, damping and stiffness matrices and use the efficient Cholesky Decomposition method for the inversion of matrices. Thirdly, efficient methods of obtaining the inverse of a configuration-dependent and time-varying mass matrix of large size were considered and their relative merits analysed and weighed against compromises in modelling accuracy. Fourthly, the Guyan reduction method was applied to the sets of finite element equations in order to obtain a reduced set of equations. Finally, the flexible portion of the nonlinear forces of contacting bodies was analysed and its effects found to be negligible both during contact and no-contact phases (Section 4.3.3).

In order to control manipulator-type multi-body systems which may be required to handle maneuvers where the end-effector performs contact operations on the environment, it is necessary to design a controller capable of achieving trajectory, force and vibration control. Thus, the dynamic model was used to design a *composite* controller which must simultaneously achieve these three goals. The *singular perturbation method* was used to obtain two reduced order models. Subsequently, for the slow subsystem, impedance control was used along with an optimization method based on Khatib's (1987) *inertia-weighted pseudoinverse* to accommodate manipulator redundancy. For the fast subsystem, the LQR method was chosen to suppress link vibrations.

A FORTRAN program was developed to perform dynamic and control simulations involving contact of multi-body systems. Efficient solution methods for contacting bodies outlined previously were included and validated. The program was then used to run simulations on three different types of contact dynamics scenarios involving a spacecraft-mounted robotic system and a satellite system:

1. Impact dynamics: the manipulator end-effector hits the payload but rebounds after impact. It was observed that structural vibrations of contacting bodies are non-negligible factors (contrary to the assumption of Hertz theory) which should be taken into account for a detailed contact dynamics modelling. It was also found that friction has significant effects on the post-impact motion or trajectory of the system.
2. Capture dynamics: a capture mechanism was employed so that the manipulator achieves successful rigid capture of the payload. It was observed that surface misalignments between contacting bodies, friction effects, repeated impacts and structural vibrations all combine to substantially complicate the overall capture operation and dynamics. This suggests that simplified contact models such as the impulse-momentum and Hertzian approaches may not capture the complexity involved in a contact operation.
3. Controlled dynamics: torques were applied at manipulator joints to achieve trajectory, force, and vibration control. The controller was successfully tested in the presence of all previously mentioned factors which affect the overall contact

process. However, during contact a steady-state tracking and force error was observed due to elastic link deflections. A corrective action was proposed and used to remedy this problem. In general, it was found that contact maneuvers are much more difficult to control than no-contact maneuvers. It is concluded that a detailed contact model is essential for a rigorous validation of control systems.

7.2 Suggestions for Future Work

The following points may provide a platform for new research activities in the field of contact dynamics and force control of multi-body systems:

- Development of a three-dimensional simulation program for contact dynamics of multi-body systems. Although the formulations described in this thesis were for general spatial motion, the simulation program was restricted to planar dynamics.
- Investigation of alternative integration architectures. In this thesis, all systems of equations were integrated using the Newmark method at the same time step size. However, depending on the characteristics of each subsystem, different integration methods may be more suitable (e.g. Gear's method for stiff systems), and different time step sizes may be more appropriately used for greater computational efficiency (e.g. for slower varying systems, larger step sizes may be used. However, coupling between systems of equations must be accounted for by periodic exchanges of data). The ultimate objective of this investigation is to obtain an optimal tradeoff between accuracy and speed of execution.
- Inclusion of orbital dynamics. It was assumed here that the center of mass of the spacecraft follows a prescribed orbital trajectory. However, control maneuvers and contact operations may cause significant deviation from this assumed

orbital path. The base motion, in turn, is likely to affect the dynamic behaviour of the rest of the system due to dynamic coupling.

- Attitude control. In this thesis, the spacecraft was treated as an additional link, and was controlled to satisfy the optimization criteria of minimum instantaneous kinetic energy of the global spacecraft/manipulator system. However, this method results in a slight attitude drift of the spacecraft. which may be undesirable.

- Inclusion of alternate or additional control techniques. Alternate control methods should be investigated when vibration frequencies are not considerably greater than those of the rigid body motion, in which case the singular perturbation method is not suitable for successful control. The use of *integral manifolds* (Spong et al. 1987) to obtain a more accurate reduced order model, and the use of smart structures for active vibration control are possible options to be explored. Also, the implementations of force tracking strategies and state observers should be considered in the more realistic case where exact knowledge of environment parameters and full state feedback are not feasible.

Bibliography

Angeles, J. & Lee, S. (1988). The formulation of dynamical equations of holonomic mechanical systems using natural orthogonal complements, *ASME Journal of Applied Mechanics* **55**: 243–244.

Baruh, H. & Tadikonda, S. S. K. (1989). Issues in the dynamics and control of flexible robot manipulators, *Journal of Guidance, Control & Dynamics* **12**(5): 659–671.

Bathe, K.-J. (1982). *Finite Element Procedures In Engineering Analysis*, Prentice Hall Inc, New Jersey.

Bathe, K.-J. & Chaudhary, A. B. (1985). A solution method for planar and axisymmetric contact problems, *International Journal for Numerical Methods in Engineering* **21**: 65–88.

Bayo, E. (1988). Computed torque for the position control of open-chain flexible robots, *Proceedings of the 1988 IEEE International Conference on Robotics and Automation*, pp. 316–321.

Ben Souda, K. (1996). *Finite element formulation of the bone adaptation process following arthroplasty and application to the distal femur*, PhD thesis, Department of Mechanical Engineering, McGill University, Montreal, Quebec, Canada.

Boutin, B. (1995). *Dynamics and vibration control of articulating truss structures*, Master's thesis, Department of Mechanical Engineering, McGill University, Montreal, Quebec, Canada.

Caron, M., Modi, V. J., Pradhan, S., de Silva, C. W. & Misra, A. K. (1998). Planar dynamics of flexible manipulators with slewing deployable links, *Journal of Guidance, Control, and Dynamics* **21**(4): 572–580.

Carusone, J. & D'Eleuterio, G. M. T. (1993). Tracking control for end-effector position and orientation of structurally flexible manipulators, *Journal of Robotic Systems* **10**(6): 847–870.

Chaudhary, A. B. (1985). *A solution method for two- and three-dimensional contact problems*, PhD thesis, Department of Civil Engineering, Massachusetts Institute of Technology.

Chaudhary, A. B. & Bathe, K.-J. (1986). A solution method for static and dynamic analysis of three-dimensional contact problems with friction, *Computers and Structures* **24**(6): 855–873.

Chiou, B. C. & Shahinpoor, M. (1989). Effects of joint and link flexibilities on the dynamic stability of force-controlled manipulators, *Proceedings of the 1989 IEEE International Conference on Robotics and Automation*, pp. 398–403.

Cho, K.-S. (1995). *Feedback control of planar mechanisms with structurally-flexible links : theory and experiments*, PhD thesis, Department of Mechanical Engineering, McGill University, Montreal, Quebec, Canada.

Chung, W.-J., Chung, W.-K. & Youm, Y. (1993). Null torque-based dynamic control for kinematically redundant manipulators, *Journal of Robotic Systems* **10**(6): 811–833.

Cook, R. D. (1981). *Concepts and Applications of Finite Element Analysis*, 2 edn, John Wiley & Sons.

Craig, J. J. (1986). *Introduction to Robotics. Mechanics & Control*, Addison-Wesley Publishing Company.

Cyril, X. (1988). *Dynamics of flexible-link manipulators*, PhD thesis, Department of Mechanical Engineering, McGill University, Montreal, Quebec, Canada.

Cyril, X., Angeles, J. & Misra, A. K. (1989). Flexlink: A software package for the dynamic simulation of flexible-link robotic manipulators, *Proceedings 1989 ASME International Computers in Engineering Conference*, July 30–August 3, Anaheim, CA, pp. 453–459.

Cyril, X., Angeles, J. & Misra, A. K. (1991). Dynamics of flexible multibody mechanical systems, *Transactions of the CSME* **15**(3): 235–256.

de la Fuente, H. M. & Felippa, C. A. (1991). Ephemeral penalty functions for contact-impact dynamics, *Finite Elements in Analysis and Design* **9**: 177–191.

Fattah, A. (1995). *Dynamics of robotic manipulators with flexible links and kinematic loops*, PhD thesis, Department of Mechanical Engineering, McGill University, Montreal, Quebec, Canada.

Goldsmith, W. (1960). *Impact*, Edward Arnold Publishers Ltd.

Guyan, R. J. (1965). Reduction of stiffness and mass matrices, *AIAA J* **3**(2): 380.

Haessig, J. D. A. & Friedland, B. (1991). On the modeling and simulation of friction, *ASME Journal of Dynamic Systems, Measurement and Control* **113**(3): 354–362.

Hogan, N. (1987). Stable execution of contact tasks using impedance control, *Proceedings of the 1987 IEEE International Conference on Robotics and Automation*, pp. 1047–1054.

Hughes, T. J. R., Taylor, R. L., Sackman, J. L., Curnier, A. & Kanoknukulchai, W. (1976). A finite element method for a class of contact-impact problems, *Computer Methods In Applied Mechanics and Engineering* **8**: 249–276.

Jaar, G. (1993). *Dynamics and control of a spacecraft-mounted robot capturing a spinning satellite*, Master's thesis, Department of Mechanical Engineering, McGill University, Montreal, Quebec, Canada.

Jaar, G., Cyril, X. & Misra, A. K. (1995). Dynamical modelling and control of a spacecraft-mounted manipulator capturing a spinning satellite, *Acta Astronautica* **35**: 167–174.

James, M. L., Smith, G. M., Wolford, J. C. & Whaley, P. W. (1989). *Vibration of Mechanical and Structural Systems*, Harper and Row, Publishers, New York.

Johnson, K. L. (1985). *Contact Mechanics*, Cambridge University Press.

Junkins, J. L. & Schaub, H. (1997). An instantaneous eigenstructure quasivelocity formulation for nonlinear multibody dynamics, *The Journal of the Astronautical Sciences* **45**(3): 279–295.

Kalantzis, S., Modi, V. J., Pradhan, S. & Misra, A. K. (1998). Order-N formulation and dynamics of multibody tethered systems, *Journal of Guidance, Control & Dynamics* **21**(2): 277–285.

Kalaycioglu, S., Giray, M. & Asmer, H. (1997). Vibration control of flexible manipulators using smart structures, *Proceedings of the 12th IEEE International Symposium on Intelligent Control*, 16–18 July, Istanbul, Turkey, pp. 415–420.

Kane, T. R. & Levinson, D. A. (1983). The use of Kane's dynamical equations in robotics, *The International Journal of Robotic Research* **2**(3): 3–21.

Karnopp, D. (1985). Computer simulation of stick-slip friction in mechanical dynamic systems, *ASME Journal of Dynamic Systems, Measurement and Control* **107**: 100–103.

Khatib, O. (1987). A unified approach for motion and force control of robot manipulators: The operational space formulation, *IEEE Journal of Robotics and Automation* **3**(1): 43–53.

Kim, S.-W. (1994). *Dynamics of a spacecraft-mounted robotic manipulator impacting a rigid satellite*, M.Eng. Report, Department of Mechanical Engineering, McGill University, Montreal, Quebec, Canada.

Kim, S.-W. & Misra, A. K. (1997). Post-capture dynamics of space manipulator systems, *16th Canadian Congress of Applied Mechanics*, June 1–5, Quebec, Canada, pp. 525–526.

Kim, S.-W., Misra, A. K., Modi, V. J. & Cyril, X. (1997). Modelling of contact dynamics of two flexible multi-body systems, *48th International Astronautical Congress*, October 6–10, Turin, Italy. Paper No. IAF-97-A.3.04; also *Acta Astronautica* in press.

Kim, S.-W., Misra, A. K., Modi, V. J. & Cyril, X. (1998a). Contact dynamics and force control of space robotic systems, *First IFAC Workshop on Space Robotics*, October 19–22, Montreal, Canada, pp. 18–23.

Kim, S.-W., Misra, A. K., Modi, V. J. & Cyril, X. (1998b). Simulation of contact dynamics of flexible multi-body systems, *Proceedings of the AIAA/AAS Astrodynamics Specialist Conference*, August 10–12, Boston, MA, pp. 389–398.

Kokotovic, P. V. (1984). Applications of singular perturbation techniques to control problems, *SIAM Review* **26**(4): 501–550.

Lankarani, H. M. & Nikravesh, P. E. (1990). A contact force model with hysteresis damping for impact analysis of multibody systems, *Journal of Mechanical Design* **112**: 369–376.

Lasky, T. A. & Hsia, T. C. (1991). On force-tracking impedance control of robot manipulators, *Proceedings of the 1991 IEEE International Conference on Robotics and Automation*, pp. 274–280.

Ma, O. (1995). Contact dynamics modelling for the simulation of the space station manipulators handling payloads, *Proceedings of the 1995 IEEE International Conference on Robotics and Automation*, pp. 1252–1258.

Ma, O., Buhariwala, K., Roger, N., MacLean, J. & Carr, R. (1997). MDSF – a generic develpment and simulation facility for flexible, complex robotic systems, *Robotica* **15**: 49–62.

Ma, O. & Carr, R. (1998). Dynamics modelling and simulation of SPDM operations: Part I & II, *First IFAC Workshop on Space Robotics*, October 19–22, Montreal, Canada, pp. 167–178.

Matsuno, F. & Yamamoto, K. (1994). Dynamic hybrid position/force control of a two degree-of-freedom flexible manipulator, *Journal of Robotic Systems* **11**(5): 355–366.

Meirovitch, L. (1967). *Analytical Methods in Vibrations*, The Macmillan Company, New York.

Misra, A. K., Sadigh, M. J., Tyc, G. & Modi, V. J. (1998). Effect of nonlinearity on the dynamics of spinning spacecraft appendages with an offset, *AAS/AIAA Space Flight Mechanics Meeting*, 9–11 Feb. Monterey, CA. Paper N. AAS-98-175.

Modi, V. J., Karray, F. & Mah, H. (1993). A composite control scheme for joint tracking and active vibration suppression of mobile flexible manipulator systems, *44th Congress of the International Astronautical Federation*, Graz, Austria, pp. 16–22.

Nguyen, T., Wang, J., Hwang, J. & Alder, K. (1991). Force accomodation control of the space shuttle remote manipulator system: a unique problem, *Proceedings of the 1991 IEEE International Conference on Robotics and Automation*, Vol. 3, Sacramento, CA, USA, pp. 2510–2515.

Noor, A. K. (1994). Recent advances and applications of reduction methods, *Applied Mechanics Reviews* **47**(5): 125–145.

Noor, A. K. & Peters, J. M. (1980). Reduced basis technique for nonlinear analysis of structures, *AIAA J* **18**(4): 455–462.

Oden, J. T. & Kikuchi, N. (1982). Finite element methods for constrained problems in elasticity, *International Journal for Numerical Methods in Engineering* **18**: 701–725.

Parisch, H. & Lubbing, C. H. (1997). A formulation of arbitrarily shaped surface elements for three-dimensional large deformation contact with friction, *International Journal for Numerical Methods in Engineering* **40**: 3359–3383.

Pradhan, S., Modi, V. J. & Misra, A. K. (1997). Order N formulation for flexible multibody systems in tree topology: lagrangian approach, *Journal of Guidance, Control, and Dynamics* **20**(4): 665–672.

Raibert, M. H. & Craig, J. J. (1981). Hybrid position/force control of manipulators, *Journal of Dynamic Systems, Measurement, and Control* **102**(2): 126–133.

Readman, M. C. (1994). *Flexible Joint Robots*, CRC Press.

Seraji, H. & Colbaugh, R. (1993). Force tracking in impedance control, *Proceedings of the 1993 IEEE International Conference on Robotics and Automation*, pp. 499–506.

Shyu, S. C., Chang, T. Y. & Saleeb, A. F. (1989). Friction-contact analysis using a mixed finite element method, *Computers and Structures* **32**(1): 223–242.

Siciliano, B. & Book, W. J. (1988). A singular perturbation approach to control of lightweight flexible manipulators, *The International Journal of Robotics Research* **7**(4): 79–90.

Simo, J. C. & Laursen, T. A. (1992). An augmented Lagrangian treatment of contact problems involving friction, *Computers and Structures* **42**(1): 97–116.

Spong, M. W., Khorasani, K. & Kokotovic, P. V. (1987). An integral manifold approach to the feedback control of flexible joint robots, *IEEE Journal of Robotics and Automation* **3**(4): 291–300.

Stieber, M. E., Hunter, D. G. & Trudel, C. P. (1998). Control of robotic systems on the space station, *First IFAC Workshop on Space Robotics*, October 19–22, Montreal, Canada, pp. 90–95.

Tissakht, M. (1995). *Experimental and numerical investigations of the human knee joint with special emphasis on the menisci*, PhD thesis, Department of Mechanical Engineering, McGill University, Montreal, Quebec, Canada.

Vallejo, J. J. G., Benavente, J. E. & Taubmann, G. (1992). Efficient modelling of docking and berthing dynamics for flexible space structures, *Dynamics of Flexible Multibody Systems: Theory and Experiment, ASME* **141**: 207–214.

Wang, Y. & Mason, M. (1987). Modelling impact dynamics for robotic operations, *Proceedings of the 1987 IEEE International Conference on Robotics and Automation*, Vol. 2, pp. 686–695.

Wasfy, T. (1995). Modeling contact/impact of flexible manipulators with a fixed rigid surface, *Proceedings of the 1995 IEEE International Conference on Robotics and Automation*, pp. 621–626.

Whitney, D. E. (1969). Resolved motion rate control of manipulators and human prostheses, *IEEE Transactions on Man-Machine Systems* **10**(2): 47–53.

Wu, S. C. & Haug, E. J. (1990). A substructure technique for dynamics of flexible mechanical systems with contact-impact, *Journal of Mechanical Design* **112**: 390–398.

Yoshida, K., Kurazume, R., Sashida, N. & Umetani, Y. (1992). Modelling of collision dynamics for space free-floating links with extended generalized inertia tensor, *Proceedings 1992 IEEE Conference on Robotics and Automation*, Nice, France.

Zheng, Y. F. & Hemami, H. (1985). Mathematical modelling of robot collision with its environment, *Journal of Robotic Systems* **2**(3): 289–307.

Appendix A

Interpolating Functions of Finite Elements

A.1 Shape Functions of Isoparametric Elements

This section describes a few commonly used isoparametric elements and corresponding shape functions.

A.1.1 2D Elements

For a four-node quadrilateral element (QUAD4) shown in Figure A.1, the interpolation matrix in equations (2.8) and (2.9) is given by

$$\mathbf{N}_i = \begin{bmatrix} N_1 & 0 & N_2 & 0 & N_3 & 0 & N_4 & 0 \\ 0 & N_1 & 0 & N_2 & 0 & N_3 & 0 & N_4 \end{bmatrix} \tag{A.1}$$

where

$$\begin{aligned} N_1 &= \frac{1}{4}(\xi - 1)(\eta - 1) \\ N_2 &= -\frac{1}{4}(\xi + 1)(\eta - 1) \\ N_3 &= \frac{1}{4}(\xi + 1)(\eta + 1) \end{aligned}$$

$$N_4 = -\frac{1}{4}(\xi - 1)(\eta + 1)$$

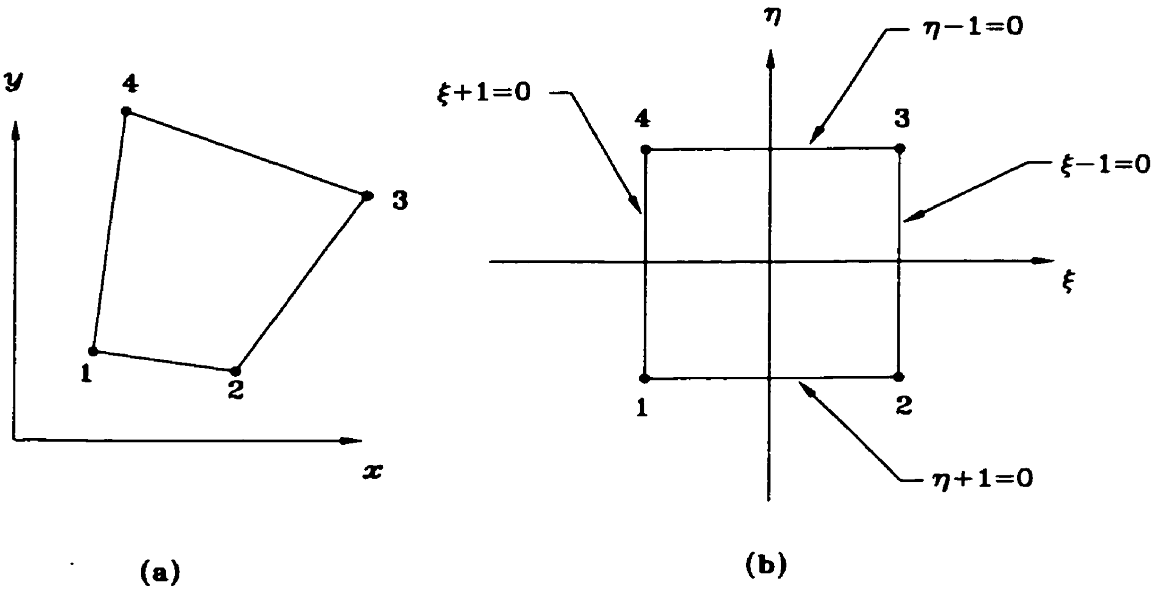

Figure A.1: A QUAD4 element in (a) xy space, (b) $\xi\eta$ space

A constant strain triangle element (CST) can be obtained by degradation of the QUAD4 element as

$$\mathbf{N}_i = \begin{bmatrix} N_1 & 0 & N_2 & 0 & N_{34} & 0 \\ 0 & N_1 & 0 & N_2 & 0 & N_{34} \end{bmatrix} \tag{A.2}$$

where

$$N_{34} = N_3 + N_4$$

A.1.2 3D Elements

A solid hexahedral or brick element is shown in Figure A.2. The corresponding interpolating matrix is given by

$$\mathbf{N}_i = \begin{bmatrix} N_1\mathbf{I}_{3\times3} & N_2\mathbf{I}_{3\times3} & N_3\mathbf{I}_{3\times3} & N_4\mathbf{I}_{3\times3} & N_5\mathbf{I}_{3\times3} & N_6\mathbf{I}_{3\times3} & N_7\mathbf{I}_{3\times3} & N_8\mathbf{I}_{3\times3} \end{bmatrix} \tag{A.3}$$

Here, $\mathbf{I}_{3\times3}$ is a 3×3 identity matrix and

$$N_i = \frac{1}{8}(1 + \xi\xi_i)(1 + \eta\eta_i)(1 + \zeta\zeta_i), \quad i = 1, \cdots, 8 \tag{A.4}$$

where ξ_i, η_i and ζ_i are natural coordinates of node i.

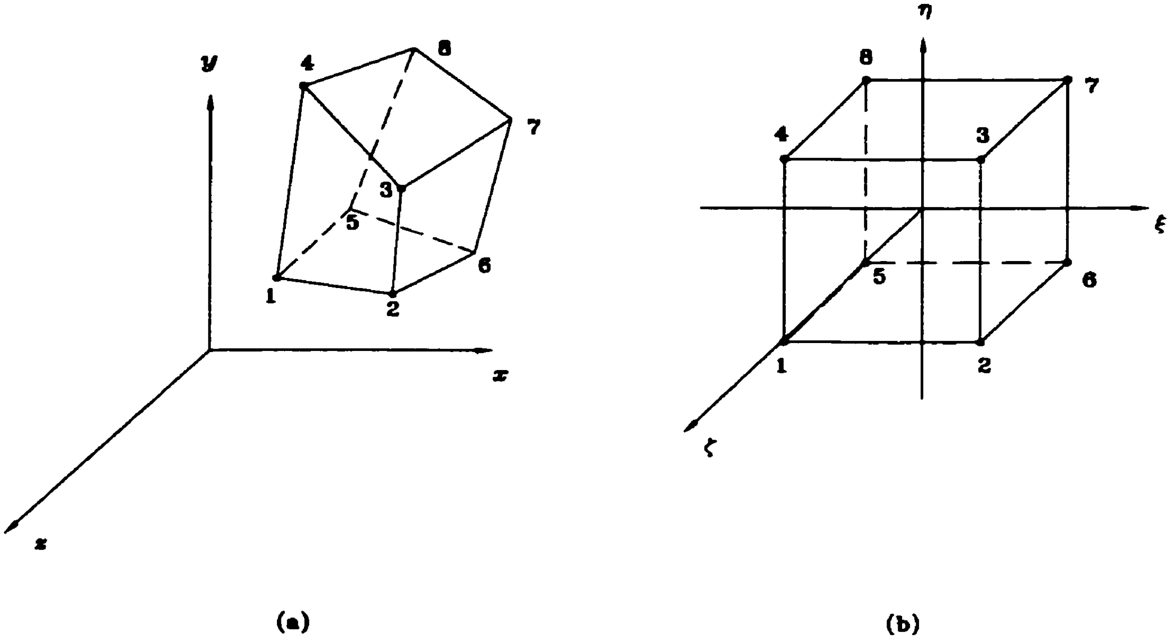

Figure A.2: A brick element in (a) xyz space, (b) $\xi\eta\zeta$ space

A.2 Kinematics of Contact for 3D Elements

This section describes, for 3D elements of *target* bodies, the interpolating functions used to obtain positions and elastic deformations of arbitary points with respect to those of segment nodes. This procedure is based on the work by Chaudhary & Bathe (1986).

Assume that the *target* surfaces are discretized using four-node quadrilateral segments as shown in Figure A.3. The equation relating the position and displacement of an arbitrary point p on segment s to those of the nodes A, B, C, and D of the segment is needed in the development of the constraint equations. A centroidal position O is defined within the segment such that

$$\mathbf{x}_O = \frac{1}{4}(\mathbf{x}_A + \mathbf{x}_B + \mathbf{x}_C + \mathbf{x}_D) \tag{A.5}$$

Assuming that point p lies in the triangle ABO as shown in Figure A.4, its position and displacement is linearly interpolated over the triangle as follows:

$$\mathbf{x}_p = \alpha\mathbf{x}_A + \beta\mathbf{x}_B + \gamma\mathbf{x}_O \tag{A.6}$$

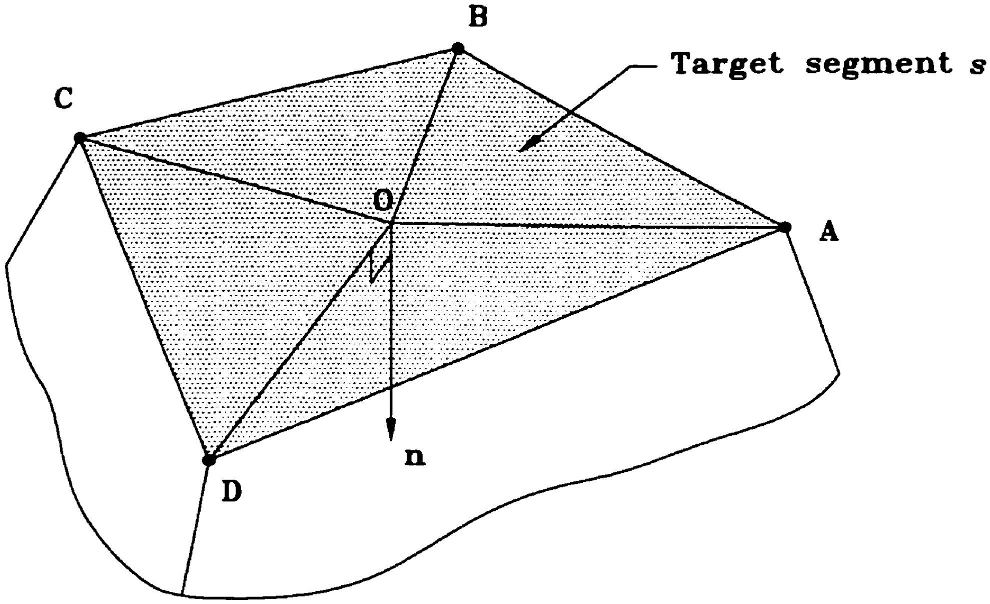

Figure A.3: Contact kinematics of a 3D element

where α, β, and γ are triangular area coordinates of point p satisfying the same relationship as equation (2.65), i.e.,

$$\alpha + \beta + \gamma = 1$$

In light of equation (A.5),

$$\mathbf{x}_p = \frac{1}{4}\{(4\alpha + \gamma)\mathbf{x}_A + (4\beta + \gamma)\mathbf{x}_B + \gamma\mathbf{x}_C + \gamma\mathbf{x}_D\} \tag{A.7}$$

where the new forms of interpolating functions also satisfy equation (2.65). Then, analogous to equation (2.68) for 2D cases, here we have

$$\mathbf{x}_s = \begin{Bmatrix} \mathbf{x}_A \\ \mathbf{x}_B \\ \mathbf{x}_C \\ \mathbf{x}_D \end{Bmatrix} \; ; \; \mathbf{u}_s = \begin{Bmatrix} \mathbf{u}_A \\ \mathbf{u}_B \\ \mathbf{u}_C \\ \mathbf{u}_D \end{Bmatrix} \tag{A.8}$$

$$\mathbf{C}_s = \frac{1}{4}\left[\begin{array}{cccc} (4\alpha + \gamma)\mathbf{I}_{3\times3} & (4\beta + \gamma)\mathbf{I}_{3\times3} & \gamma\mathbf{I}_{3\times3} & \gamma\mathbf{I}_{3\times3} \end{array}\right] \tag{A.9}$$

where $\mathbf{I}_{3\times3}$ is a 3 × 3 identity matrix.

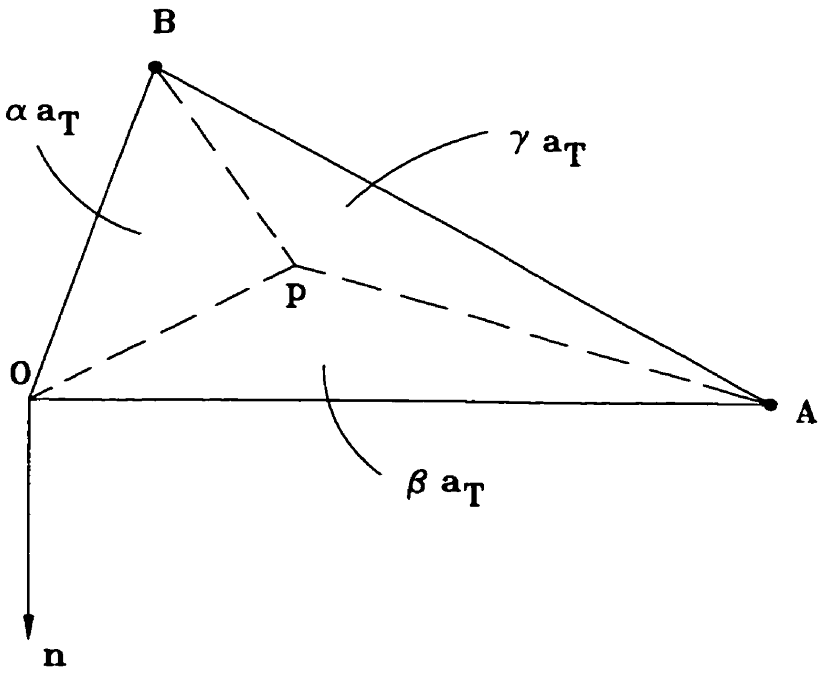

Figure A.4: An arbitrary triangle

Appendix B

Symmetry and Positive Definiteness of $\bar{\mathbf{R}}$ in Equation (4.21)

Symmetry of $\bar{\mathbf{R}}$

A matrix is symmetric if it is equal to its transpose. From equations (4.19) and (4.20), since matrix $\hat{\mathbf{K}}$ is symmetric, it follows that

$$\begin{aligned}
\bar{\mathbf{R}}_{kk}^T &= (\mathbf{P}_{kr_k}\hat{\mathbf{K}}_{r_k}^{-1}\mathbf{P}_{kr_k}^T + \mathbf{P}_{ks_k}\hat{\mathbf{K}}_{s_k}^{-1}\mathbf{P}_{ks_k}^T)^T \\
&= (\mathbf{P}_{kr_k}\hat{\mathbf{K}}_{r_k}^{-1}\mathbf{P}_{kr_k}^T)^T + (\mathbf{P}_{ks_k}\hat{\mathbf{K}}_{s_k}^{-1}\mathbf{P}_{ks_k}^T)^T \\
&= \mathbf{P}_{kr_k}\hat{\mathbf{K}}_{r_k}^{-1}\mathbf{P}_{kr_k}^T + \mathbf{P}_{ks_k}\hat{\mathbf{K}}_{s_k}^{-1}\mathbf{P}_{ks_k}^T = \bar{\mathbf{R}}_{kk} \\
\bar{\mathbf{R}}_{kj}^T &= (\mathbf{P}_{kc_{kj}}\hat{\mathbf{K}}_{c_{kj}}^{-1}\mathbf{P}_{jc_{kj}}^T)^T = \mathbf{P}_{jc_{kj}}\hat{\mathbf{K}}_{c_{kj}}^{-1}\mathbf{P}_{kc_{kj}}^T = \bar{\mathbf{R}}_{jk}
\end{aligned}$$

Positive definiteness of $\bar{\mathbf{R}}$

One way of proving positive definiteness of $\bar{\mathbf{R}}$ is by showing that for any nonzero vector $\mathbf{a}$

$$V = \mathbf{a}^T\bar{\mathbf{R}}\mathbf{a} > 0$$

Expanding V

$$V = \mathbf{a}^T\bar{\mathbf{R}}\mathbf{a} = \sum_{i=1}^{n}\sum_{j=1}^{n}\mathbf{a}_i^T\bar{\mathbf{R}}_{ij}\mathbf{a}_j$$

We may organize this series by collecting terms of the same subsystems as

$$V = \sum_{k=1}^{N} Q_k \tag{B.1}$$

where for a subsystem k, which is involved in constraint equations $c_1, \cdots, c_{m_k}$, we have

$$Q_k = \sum_{c_i=1}^{m_k}\sum_{c_j=1}^{m_k}\mathbf{a}_{c_i}^T\mathbf{P}_{c_ik}\hat{\mathbf{K}}_k^{-1}\mathbf{P}_{c_jk}^T\mathbf{a}_{c_j} \tag{B.2}$$

Letting

$$\tilde{\mathbf{a}}_{c_ik} = \mathbf{P}_{c_ik}^T\mathbf{a}_{c_i} \;\; ; \;\; \tilde{\mathbf{a}}_{c_jk} = \mathbf{P}_{c_jk}^T\mathbf{a}_{c_j}$$

equation (B.2) can be expressed as

$$\begin{aligned} Q_k &= \sum_{c_i=1}^{m_k}\sum_{c_j=1}^{m_k}\tilde{\mathbf{a}}_{c_ik}^T\hat{\mathbf{K}}_k^{-1}\tilde{\mathbf{a}}_{c_jk} \\ &= \left(\sum_{c_i=1}^{m_k}\tilde{\mathbf{a}}_{c_ik}^T\right)\hat{\mathbf{K}}_k^{-1}\left(\sum_{c_j=1}^{m_k}\tilde{\mathbf{a}}_{c_jk}^T\right) \end{aligned}$$

Letting

$$\mathbf{b}_k = \sum_{c_i=1}^{m_k}\tilde{\mathbf{a}}_{c_ik}$$

we have

$$Q_k = \mathbf{b}_k^T\hat{\mathbf{K}}_k^{-1}\mathbf{b}_k > 0$$

since $\hat{\mathbf{K}}_k^{-1}$ is positive definite. Now, from equation (B.1), since the individual Q_k's are positive, V is positive.

Appendix C

Updated Contact Forces After Iteration $l - 1$

This Appendix describes in detail the calculation of the updated contact nodal forces $\tilde{\gamma}$, discussed in Section 4.2.3. The procedure is based on the formulation presented by Chaudhary (1985).

C.1 Recovery of segment tractions

The traction recovery calculation assumes that the interpolation of tractions over each segment is linear and bilinear for 2D and 3D cases respectively, and that the tractions are continuous across the segment boundaries. Figures C.1 and C.2 show respectively for 2D and 3D cases the distribution of segment tractions over a generic *contactor* segment j. The consistent nodal loads corresponding to the distributed segment tractions are given by

$$\mathbf{\Gamma}_j = \mathbf{G}_j \mathbf{T}_j \tag{C.1}$$

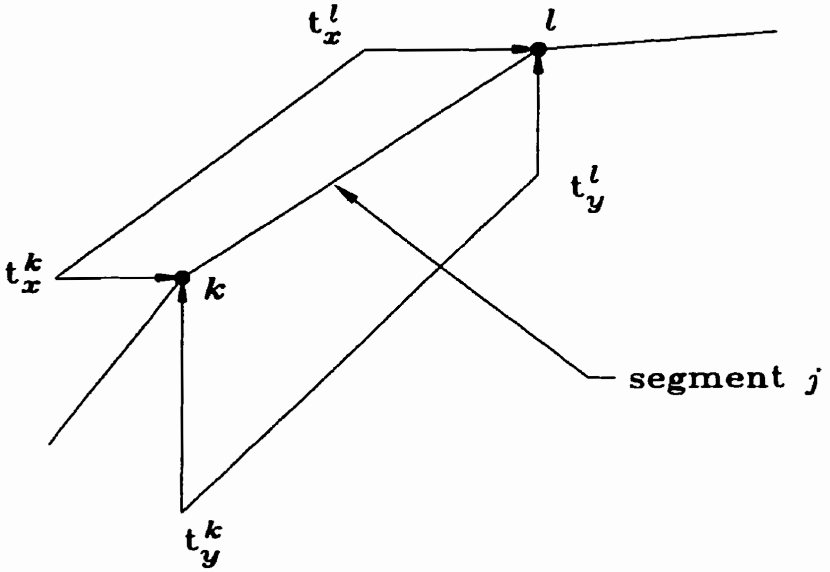

Figure C.1: 2D: *Contactor* traction distribution over segment j

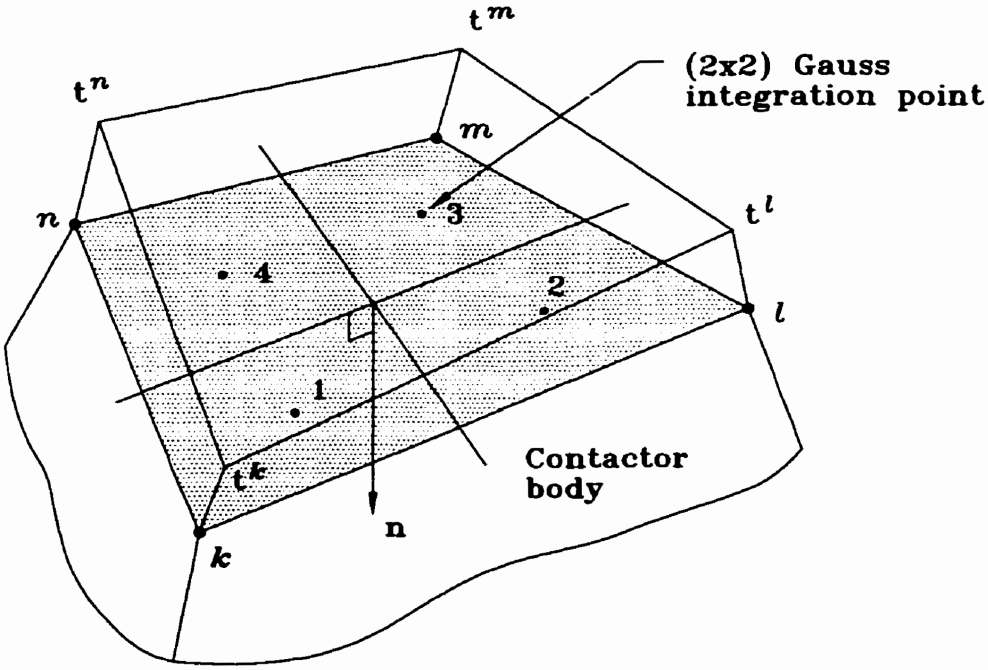

Figure C.2: 3D: *Contactor* traction distribution over segment j

where $\mathbf{T}_j$ is the matrix of nodal point values of the segment tractions given by

$$\underline{\text{2D}}: \ \mathbf{T}_j = \begin{bmatrix} t_x^k & t_y^k \\ t_x^l & t_y^l \end{bmatrix}, \quad \underline{\text{3D}}: \ \mathbf{T}_j = \begin{bmatrix} t_x^k & t_y^k & t_z^k \\ t_x^l & t_y^l & t_z^l \\ t_x^m & t_y^m & t_z^m \\ t_x^n & t_y^n & t_z^n \end{bmatrix}. \tag{C.2}$$

$\mathbf{\Gamma}_j$ is the matrix of consistent nodal forces corresponding to the segment tractions given by

$$\underline{\text{2D}}: \ \mathbf{\Gamma}_j = \begin{bmatrix} \gamma_x^k & \gamma_y^k \\ \gamma_x^l & \gamma_y^l \end{bmatrix}, \quad \underline{\text{3D}}: \ \mathbf{\Gamma}_j = \begin{bmatrix} \gamma_x^k & \gamma_y^k & \gamma_z^k \\ \gamma_x^l & \gamma_y^l & \gamma_z^l \\ \gamma_x^m & \gamma_y^m & \gamma_z^m \\ \gamma_x^n & \gamma_y^n & \gamma_z^n \end{bmatrix} \tag{C.3}$$

(e.g. γ_x^k is the x-component of the consistent nodal load at node k due to the distributed segment tractions over segment j only. The total force $\boldsymbol{\gamma}^k$ at node k is the sum of contributions from the tractions acting over all segments adjoining node k) and $\mathbf{G}_j$ is a coefficient matrix relating nodal values of segment tractions to the corresponding consistent nodal loads. For the 2D case, $\mathbf{G}_j$ is given by

$$\mathbf{G}_j = b\frac{d_j}{6}\begin{bmatrix} 2 & 1 \\ 1 & 2 \end{bmatrix} \tag{C.4}$$

where b is the width of the contact segments, and d_j is the length of segment j. For the 3D case, it is evaluated by (2 × 2) numerical integration (Bathe 1982) as

$$\mathbf{G}_j = \bar{\mathbf{H}}^T \mathbf{J}_j \bar{\mathbf{H}} \tag{C.5}$$

where $\bar{\mathbf{H}}$ is a symmetric matrix of the bilinear interpolation functions at the (2 × 2) Gauss integration points given by

$$\bar{\mathbf{H}} = \begin{bmatrix} \bar{h}_{11} & \bar{h}_{12} & \bar{h}_{13} & \bar{h}_{14} \\ . & \bar{h}_{22} & \bar{h}_{23} & \bar{h}_{24} \\ . & . & \bar{h}_{33} & \bar{h}_{34} \\ . & . & . & \bar{h}_{44} \end{bmatrix} \tag{C.6}$$

Specifically,

$$\bar{h}_{11} = \bar{h}_{22} = \bar{h}_{33} = \bar{h}_{44} = 0.62200847$$

$$\bar{h}_{12} = \bar{h}_{23} = \bar{h}_{34} = \bar{h}_{14} = 0.16666666$$

$$\bar{h}_{13} = \bar{h}_{24} = 0.04465820$$

Matrix $\mathbf{J}_j$ is a diagonal matrix of values of the Jacobian determinant at the (2 × 2) Gauss integration points, such that

$$\mathbf{J}_j = \begin{bmatrix} J_{j1} & 0 & 0 & 0 \\ 0 & J_{j2} & 0 & 0 \\ 0 & 0 & J_{j3} & 0 \\ 0 & 0 & 0 & J_{j4} \end{bmatrix} \tag{C.7}$$

Using equation (C.1) and summing the constributions from all *contactor* segments, a coefficient matrix relating the nodal values of segment tractions to the nodal contact forces is constructed:

$$\mathbf{\Gamma} = \hat{\mathbf{G}}\mathbf{T} \tag{C.8}$$

A Gauss elimination solution is performed on the above equation to obtain the unknown nodal values of the segment tractions $\mathbf{T}$.

C.2 Friction Update of Segment Tractions

Using the recovered segment tractions, the total segment contact force, $\boldsymbol{\kappa}_j$, is obtained from

$$\boldsymbol{\kappa}_j = [\mathbf{G}_T \mathbf{T}_j]^T \tag{C.9}$$

where

$$\underline{\text{2D}}:\ \mathbf{G}_T^T = b\frac{d_j}{2}\begin{Bmatrix} 1 \\ 1 \end{Bmatrix}, \quad \underline{\text{3D}}:\ \mathbf{G}_T^T = \begin{Bmatrix} \bar{h}_{11}J_1 + \bar{h}_{12}J_2 + \bar{h}_{13}J_3 + \bar{h}_{14}J_4 \\ \bar{h}_{12}J_1 + \bar{h}_{22}J_2 + \bar{h}_{23}J_3 + \bar{h}_{24}J_4 \\ \bar{h}_{13}J_1 + \bar{h}_{23}J_2 + \bar{h}_{33}J_3 + \bar{h}_{34}J_4 \\ \bar{h}_{14}J_1 + \bar{h}_{24}J_2 + \bar{h}_{34}J_3 + \bar{h}_{44}J_4 \end{Bmatrix} \tag{C.10}$$

Also,

$$\boldsymbol{\kappa}_j^n = [\boldsymbol{\kappa}_j^T \mathbf{n}_j]\mathbf{n}_j \tag{C.11}$$

$$\boldsymbol{\kappa}_j^t = \boldsymbol{\kappa}_j - \boldsymbol{\kappa}_j^n \tag{C.12}$$

where $\boldsymbol{\kappa}_j^n$ and $\boldsymbol{\kappa}_j^t$ are the total normal and tangential segment contact forces respectively. These values are used in the procedure for updating the segment tractions to enforce Coulomb's law of friction.

Now, the friction update of segment tractions is as follows:

- **Condition for tension release.** A *contactor* segment experiences tension release after iteration $l-1$ if the total normal segment contact force is tensile, or

  $$\boldsymbol{\kappa}_j^T \mathbf{n}_j < 0 \tag{C.13}$$

  The segment tractions are then updated to zero:

  $$\tilde{\mathbf{T}}_j = \mathbf{0} \tag{C.14}$$

  $$\tilde{\mathbf{\Gamma}}_j = \mathbf{0} \tag{C.15}$$

  where $\tilde{\mathbf{T}}_j$ is the matrix of updated nodal point values of segment tractions and $\tilde{\mathbf{\Gamma}}_j$ is the matrix of consistent segment nodal point forces corresponding to the updated tractions over segment j.

- **Condition of sliding contact.** A *contactor* segment experiences sliding contact after iteration $l-1$ if the total segment tangential force exceeds the total segment static frictional capacity, or

  $$\kappa_j^t > \kappa_j^{f_s} \tag{C.16}$$

  where

  $$\kappa_j^t = |\boldsymbol{\kappa}_j^t| \tag{C.17}$$

  $$\kappa_j^{f_s} = \mu_s \boldsymbol{\kappa}_j^T \mathbf{n}_j \tag{C.18}$$

The tangential components of the nodal point tractions of segment j are updated as follows:

$$\underline{\text{2D}}: \ \tilde{\mathbf{T}}_j^t = [\ \tilde{\mathbf{t}}_*^t \ \ \tilde{\mathbf{t}}_*^t\ ]^T, \quad \underline{\text{3D}}: \ \tilde{\mathbf{T}}_j^t = [\ \tilde{\mathbf{t}}_*^t \ \ \tilde{\mathbf{t}}_*^t \ \ \tilde{\mathbf{t}}_*^t \ \ \tilde{\mathbf{t}}_*^t\ ]^T \tag{C.19}$$

where

$$\tilde{\mathbf{t}}_*^t = \left(\frac{\kappa_j^{f_d}}{\kappa_j^t} \right) \frac{\boldsymbol{\kappa}_j^t}{A_j}, \tag{C.20}$$

$\kappa_j^{f_d}$ is the dynamic sliding frictional force (see Section 4.2.4) given by

$$\kappa_j^{f_d} = \mu_d \boldsymbol{\kappa}_j^T \mathbf{n}_j, \tag{C.21}$$

and A_j is the area of segment j given by

$$\underline{\text{2D}}: \ A_j = bd_j, \quad \underline{\text{3D}}: \ A_j = J_1 + J_2 + J_3 + J_4 \tag{C.22}$$

The updated segment tractions and nodal forces are obtained as

$$\tilde{\mathbf{T}}_j = \mathbf{T}_j^n + \tilde{\mathbf{T}}_j^t \tag{C.23}$$

$$\tilde{\mathbf{\Gamma}}_j = \mathbf{G}_j \tilde{\mathbf{T}}_j \tag{C.24}$$

where

$$\mathbf{T}_j^n = [\mathbf{T}_j \mathbf{n}_j] \mathbf{n}_j^T \tag{C.25}$$

Note that the direction of the updated tangential force is the same as for the force $\mathbf{\Gamma}_j^t$.

- **Condition of sticking contact.** A *contactor* segment experiences sticking contact after iteration $l-1$ if the total segment tangential force is less than the total segment static frictional capacity, or

$$\kappa_j^t \leq \kappa_j^{f_s} \tag{C.26}$$

The segment tractions satisfy Coulomb's law of friction and thus

$$\tilde{\mathbf{T}}_j = \mathbf{T}_j \tag{C.27}$$

$$\tilde{\mathbf{\Gamma}}_j = \mathbf{\Gamma}_j \tag{C.28}$$

Table C.1: State of *contactor* node as decided by states of adjoining *contactor* segments

One adjoining segment	Other adjoining segments	State of *contactor* node
Sticking	Sticking	Sticking
Sticking	Sliding	Sticking
Sticking	Tension Release	Sticking
Sticking	Not in contact	Sticking
Sliding	Sliding	Sliding
Sliding	Tension Release	Sliding
Sliding	Not in contact	Sliding
Tension Release	Tension Release	Tension Release
Tension Release	Not in contact	Tension Release

By summing the updated segment nodal forces, the total updated contact forces at the *contactor* nodes, $\bar{\gamma}$, are obtained. After the friction update calculation for the *contactor* segments, the algorithm determines the conditions of sticking, sliding and tension release at the *contactor* nodes as shown in Table C.1.

Appendix D

Hertz Theory of Elastic Impact

According to the Hertz theory of quasi-static elastic and collinear impact of two spheres or bodies which make contact over a circular area (Johnson 1985), the compression-time relationship is given by

$$t = \frac{\delta^*}{v_0} \int \frac{d(\delta/\delta^*)}{\{1 - (\delta/\delta^*)^{5/2}\}^{1/2}} \tag{D.1}$$

Here, δ is the relative displacement of the sphere centers and v_0 is the relative speed of approach immediately before impact:

$$\delta = |u_2 - u_1| \tag{D.2}$$

$$v_0 = |\dot{u}_2 - \dot{u}_1|_{t=0} \tag{D.3}$$

where u_1 and u_2 are the displacements of the center of mass of body 1 and 2 respectively. The maximum compression, δ^*, is given by

$$\delta^* = \left(\frac{15 m v_0^2}{16 R^{1/2} E^*}\right)^{2/5} \tag{D.4}$$

where, if m_1, R_1, E_1 and m_2, R_2, E_2 are the mass, radius and Young's modulus of body 1 and 2 respectively, then

$$\frac{1}{m} = \frac{1}{m_1} + \frac{1}{m_2} \tag{D.5}$$

$$\frac{1}{R} = \frac{1}{R_1} + \frac{1}{R_2} \tag{D.6}$$

$$\frac{1}{E^*} = \frac{1 - \nu_1^2}{E_1} + \frac{1 - \nu_2^2}{E_2} \tag{D.7}$$

Since the impact is perfectly elastic and frictionless, and the energy absorbed in wave motion is neglected, the deformation is perfectly reversible. The total time of impact T_c, is therefore twice the time of maximum compression t^*, and is given by

$$T_c = 2t^* = 2\frac{\delta^*}{v_0}\int_0^1 \frac{d(\delta/\delta^*)}{\{1-(\delta/\delta^*)^{5/2}\}^{1/2}} = 2.94\frac{\delta^*}{v_0} \tag{D.8}$$

The relationship between the deformation and contact force is given by

$$f = \frac{4}{3}R^{1/2}E^*\delta^{3/2} \tag{D.9}$$

and the speed of compression is given by

$$\frac{d\delta}{dt} = \{v_0^2 - \frac{16}{15m}R^{1/2}E^*\delta^{5/2}\}^{1/2} \tag{D.10}$$

The pressure distribution along the contact surface proposed by the Hertz theory is

$$p = p_0\{1-(r/a)^2\}^{1/2} \tag{D.11}$$

where p_0 is the pressure at the center of the contact circle given by

$$p_0 = \left(\frac{6fE^{*2}}{\pi^3R^2}\right)^{1/3}, \tag{D.12}$$

r is the distance of a point from the center and a is the radius of the contact circle.